Chemical structures of protoplanetary disks and possibility to locate the position of the H_2O snowline using spectroscopic observations

Shota Notsu (野津 翔太)[1]

[1] *Department of Astronomy, Graduate School of Science, Kyoto University;*

Kitashirakawa-Oiwake-cho, Sakyo-ku, Kyoto 606-8502, Japan;

snotsu@kusastro.kyoto-u.ac.jp

ORCID: 0000-0003-2493-912X

A thesis submitted for the degree of Doctor of Science (Ph.D.), Kyoto University

January 2019

ABSTRACT

Observationally locating the position of the H_2O snowline in protoplanetary disks is crucial for understanding the planetesimal and planet formation processes, and the origin of water on the Earth. The velocity profiles of emission lines from disks are usually affected by doppler shift due to Keplerian rotation. Therefore, the line profiles are sensitive to the radial distribution of the line emitting regions. However, water lines which have been obtained by previous infrared spectroscopic observations mainly traced the disk surface and the cold water resevoir outside the H_2O snowline. Thus, they are not good direct tracer of the H_2O snowline.

In our studies, first we calculated the chemical structures of the disk using the self-consistent physical models of a typical T Tauri disk and a typical Herbig Ae disk, and investigate the abundance distributions of H_2O gas and ice, and the positions of the H_2O snowline. We confirm that the abundance of H_2O gas is high not only in the hot disk midplane within the H_2O snowline but also in the hot surface layer and photodesorption region of the outer disk. Next, on the basis of our calculations of disk chemical structures and water line profiles, we proposed how to identify the position of the H_2O snowline directly by analyzing the Keplerian profiles of water lines which can be obtained by high-dispersion spectroscopic observations across a wide range of wavelengths (from mid-infrared to sub-millimeter wavelengths). We selected candidate water lines to locate the H_2O snowline based on specific criteria. We concluded that lines which have small Einstein A coefficients (A_{ul}=10^{-6} $\sim$ 10^{-3} s^{-1}) and relatively high upper state energies ($E_{up}\sim$ 1000K) trace the hot water reservoir within the H_2O snowline, and can locate the position of the H_2O snowline. In these candidate water lines, the contribution of the optically thick hot midplane inside the H_2O snowline is large compared with that of the outer optically thin surface layer. This is because the intensities of lines from the optically thin region are proportional to the Einstein

A coefficient. Moreover, the contribution of the cold water reservoir outside the H_2O snowline is also small, because lines with high excitation energies are not emitted from the regions at a low temperature.

The position of the H_2O snowline of a Herbig Ae disk exists at a larger radius compared with that around less massive and cooler T Tauri stars. In addition, the position of H_2O snowline migrates closer to the star as the disk becomes older and mass accretion rate to the central star becomes smaller. Therefore, it is expected to be easier to observe the candidate water lines, and thus identify the location of the H_2O snowline, in Herbig Ae disks and younger T Tauri stars.

In addition, since the number densities of the ortho- and para-$H_2{}^{18}O$ molecules are about 1/560 times smaller than their ^{16}O analogues, they trace deeper into the disk than the ortho-$H_2{}^{16}O$ lines (down to $z = 0$), and lines with relatively smaller upper state energies ($\sim$ a few 100K) can also locate the position of the H_2O snowline. Thus these $H_2{}^{18}O$ lines are potentially better probes of the position of the H_2O snowline at the disk midplane, depending on the dust optical depth.

There are several candidate water lines that trace the position of the H_2O snowline observable in ALMA Bands 5−10 and by SPICA. Finally, we have proposed the water line observations for the protoplanetary disk around the Herbig Ae star HD 163296, and partial data were delivered. We analyzed the upper limit fluxes of sub-millimeter ortho-$H_2{}^{16}O$ 321 GHz, para-$H_2{}^{18}O$ 322 GHz, and HDO 335 GHz lines, which are considered to be the best candidate water lines available at sub-millimeter wavelengths to locate the position of the H_2O snowline, on the basis of our model calculations. We compared the upper limit fluxes with the values calculated by our models with dust emission included, and we constrained the line emitting region and the dust opacity

from the observations. We conclude that, if the outer edge of the water vapor abundant region and also the position of the water snowline is beyond 8 au, the mm dust opacity $\kappa_{\rm mm}$ will have a value larger than 2.0 cm^2 g^{-1}. In addition, the position of the water snowline will be inside 20 au, if the mm dust opacity $\kappa_{\rm mm}$ is 2.0 cm^2 g^{-1}. We also report multiple ring and gap patterns in 0.9 mm (Band 7) dust continuum emission with 15 au resolution. The positions of bright rings and dust depleted dark gaps are consistent with those indicated by the previous observations.

In our future work, we will discuss the possibility of future observations (e.g., ALMA, SPICA) in detail on the basis of our further modeling studies, and conduct the further observations to locate the positions of the H_2O snowline for various types of protoplanetary disks using several water lines.

Contents

1. INTRODUCTION

1.1. *The overview of the protoplanetary disks*

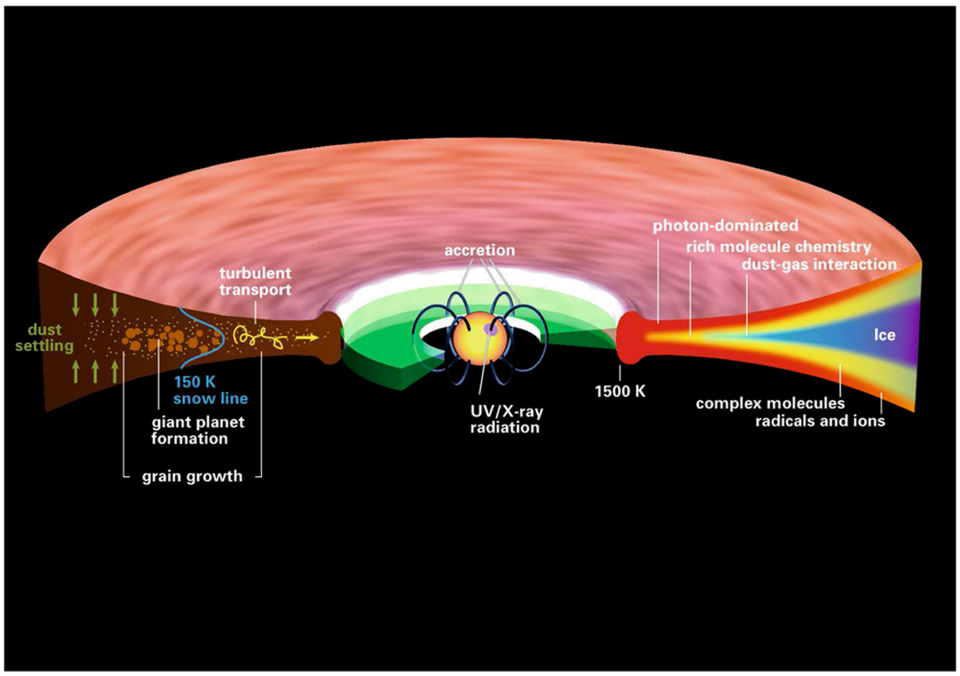

Figure 1. The sketch of the physical and chemical structure of a $\sim 1 - 5$ Myr old protoplanetary disk around a T Tauri star. This figure is originally reported in Henning & Semenov (2013).

Protoplanetary disks are rotating accretion disks surrounding young newly formed stars (e.g., T Tauri stars, Herbig Ae/Be stars). They are composed of dust grains and gas, and contain all the material which will form planetary systems orbiting main-sequence stars (e.g., Armitage 2011). They are also active environments for the creation of simple and complex molecules, including organic matter and H_2O (e.g., Caselli & Ceccarelli 2012; Henning & Semenov 2013; Pontoppidan et al. 2014). Figure 1 shows the sketch of the physical and chemical structure of a protoplanetary disk (Henning & Semenov 2013). The physical and chemical environments of protoplanetary disks determine the properties of various planets, including mass and chemical composition (e.g., Öberg et al. 2011; Pontoppidan et al. 2014). Among all molecules in disks, water is one of the most important molecules in determining physical and chemical properties.

1.2. *The definition of the* H_2O *snowline in the protoplanetary disks*

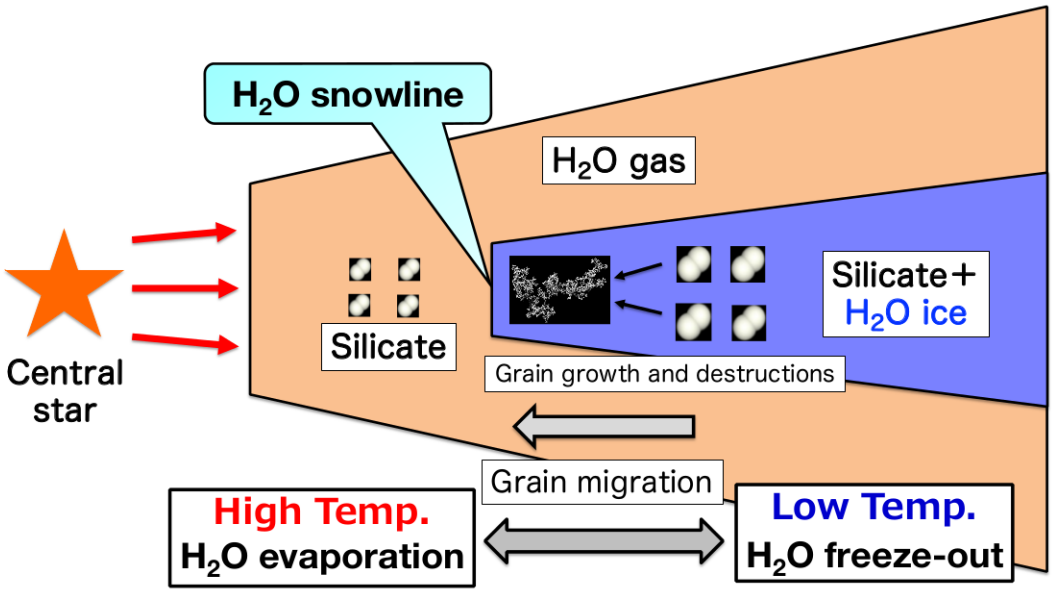

Figure 2. The outline picture of the disk physical and chemical structures and grain evolutions around the H_2O snowline

H_2O gas and ice likely carries most of the oxygen that is available, the only competitors are CO and possibly CO_2 (Pontoppidan & Blevins 2014; Walsh et al. 2015). In the hot inner regions of protoplanetary disks, H_2O ice evaporates from the dust-grain surfaces into the gas phase. On the other hand, it is frozen out on the dust-grain surfaces in the cold outer parts of the disk. The H_2O snowline is the surface that divides the disk into these two different regions (Hayashi 1981). H_2O ice enhances the solid material in the cold region beyond the H_2O snowline, and H_2O ice mantles on dust grains beyond the H_2O snowline allow dust grains to stick at higher collisional velocities and promote efficient coagulation compared with collisions of silicate grains (e.g., Wada et al. 2013). As a result, the formation of the cores of gaseous planets are promoted in such regions. In the disk midplane, we can thus regard the H_2O snowline as the line that divides the regions of rocky planet and gas-giant planet formation (e.g., Hayashi 1981, 1985, Öberg et al. 2011). Figure 2 summarizes the disk physical and chemical structures and grain evolutions around the H_2O snowline.

1.3. *The positions of the* H_2O *snowline and the roles of water molecules*

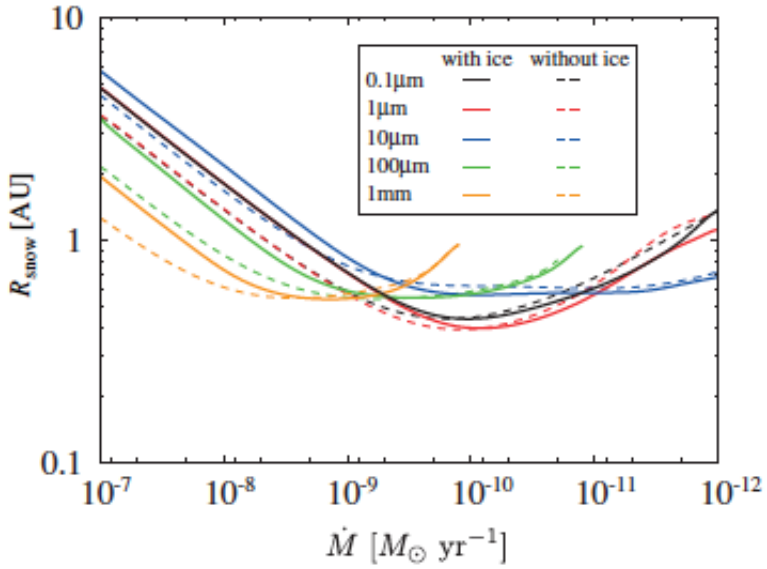

Figure 3. Heliocentric distance of the snow line ($R_{\rm snow}$) as a function of the mass accretion rate with various dust grain sizes for a typical T Tauri disk. The black, red, blue, green, and orange curves represent the results with dust grain sizes of 0.1, 1, 10, 100μm, and 1mm, respectively. The solid and dashed curves represent the results with and without icy grain opacity, respectively. This figure is originally reported in Oka et al. (2011).

Icy planetesimals, comets, and/or icy pebbles coming from outside the H_2O snowline may bring water to rocky planets including the Earth (e.g., Morbidelli et al. 2000, 2012, 2016; Walsh et al. 2011; Ida & Guillot 2016; Sato et al. 2016; Matsumura et al. 2015; Raymond & Izidoro 2017). In the case of disks around solar-mass T Tauri stars, the H_2O snowline is calculated to exist at a few au from the central T Tauri star (e.g., Hayashi 1981; Hayashi et al. 1985). However, if we change the physical conditions such as the luminosity of the central star, the mass accretion rate, and the dust-grain size distribution in the disk, the location of the H_2O snowline will change (e.g., Du & Bergin 2014, Piso et al. 2015). Recent studies (Davis 2005; Garaud & Lin 2007; Min et al. 2011; Oka et al. 2011; Harsono et al. 2015; Mulders et al. 2015; Piso et al. 2015) calculate the evolution of the H_2O snowline in optically thick disks, and show that it migrates as the mass accretion rate in the disk decreases and as the dust grains grow in size (see also Figure 3). In some cases the line may lie within the

current location of Earth's orbit (1 au), meaning that the formation of water-devoid planetesimals in the terrestrial planet region becomes more difficult as the disk evolves. Sato et al. (2016) estimated the amount of icy pebbles accreted by terrestrial embryos after the H_2O snowline has migrated inwards to the distance of Earth's orbit (1 au). They argued that the fractional water content of the embryos is not kept below the current Earth's water content (0.023 wt%) unless the total disk size is relatively small (< 100 au) and the disk has a stronger value of turbulence than that suggested by recent work, so that the pebble flow decays at early times. In contrast, other studies (Martin & Livio 2012, 2013) model the evolution of the H_2O snowline in a time-dependent disk with a dead zone and self-gravitational heating, and suggest that there is sufficient time and mass in the disk for the Earth to form from water-devoid planetesimals at the current location of Earth's orbit (1 au).

Ros & Johansen (2013) showed that around the H_2O snowline, dust-grain growth due to the condensation from millimeter to at least decimeter sized pebbles is possible on a timescale of only 1000 years. The resulting particles are large enough to be sensitive to concentration by streaming instabilities, pressure bumps and vortices, which can cause further growth into planetesimals, even in young disks (<1 Myr, e.g., Zhang et al. 2015). Moreover, Banzatti et al. (2015) recently showed that the presence of the H_2O snowline leads to a sharp discontinuity in the radial profile of the dust emission spectral index, due to replenishment of small grains through fragmentation because of the change in fragmentation velocities across the H_2O snowline (see also Figure 4). Furthermore, Okuzumi et al. (2016) argued that dust aggregates collisionally disrupt and pile up at the region slightly outside the snowlines due to the effects of sintering. These mechanisms of condensation (Ros & Johansen 2013; Zhang et al. 2015), fragmentation (Banzatti et al. 2015), and sintering (Okuzumi et al. 2016) of dust grains have been invoked to explain the multiple bright and dark ring patterns in the dust spectral index of the young disk HL Tau (ALMA Partnership et al. 2015, see also Figure 5). Zhang et al. (2015) argued that the center radius of the prominent innermost gap at 13 au is coincident with the expected midplane condensation front of water ice. Here we pointed out that Banzatti et al. (2015) and Okuzumi et al. (2016) reported the position of the H_2O snowline of HL Tau is < 10 au. It is

because disk temperature distributions of Zhang et al. (2015) is higher than those of Banzatti et al. (2015) and Okuzumi et al. (2016).

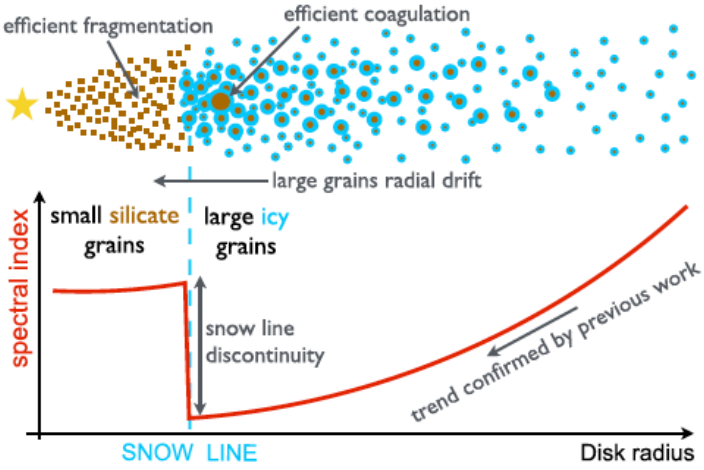

Figure 4. The illustrative sketch of the change in the dust emission spectral index as linked to the change in dust-grain properties across the H_2O snowline, in the case of optically thin disk emission at millimeter wavelengths. This figure is originally reported in Banzatti et al. (2015).

Here we noted that Pinte et al. (2016) presented a radiative transfer model of HL Tau accounting for the observed gaps and bright rings (see also Figure 5) and the radial changes of dust-grain emission spectral index. They estimated that the gaps are devoid of dust grains by at least a factor of 10 compared to the adjacent bright rings, and that if the disk originally had a smooth radial distribution, up to $40 M_{\rm earth}$ of dust grains has been removed to create each of the two largest gaps in HL Tau. Some works indicated that the dust grains in such gaps were considered to be removed through the creation of planets (e.g., Akiyama et al. 2016; Kanagawa et al. 2015a,b; Pinte et al. 2016). Takahashi & Inutsuka (2014, 2016) and Tominaga et al. (2017) investigated the secular gravitational instability in protoplanetary disks due to gas-dust friction, and argued that the instability is a candidate for the formation mechanism of observed ring-like structures in disks.

Therefore, measuring the position of the water snowline (which corresponds to the sublimation front

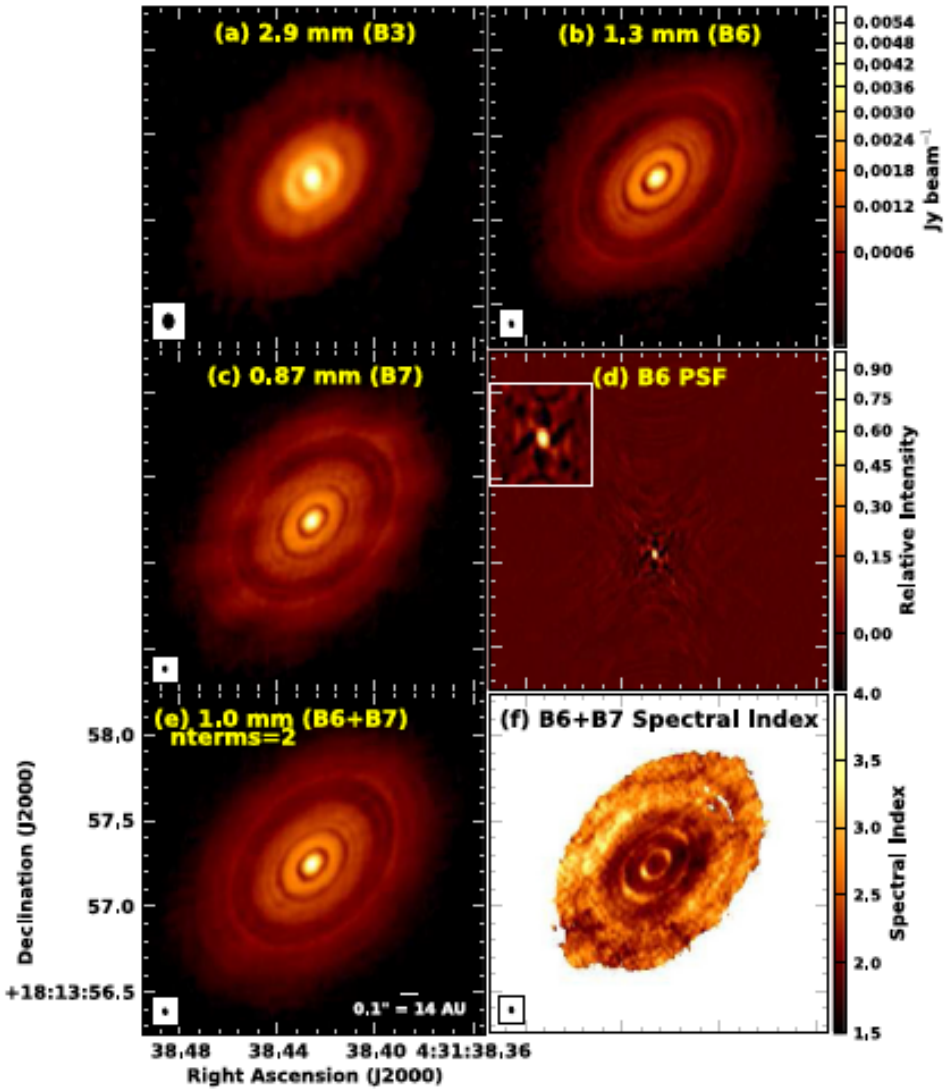

Figure 5. Panels (a), (b), and (c) show 2.9, 1.3, and 0.87 mm ALMA continuum images of HL Tau. Panel (d) shows the 1.3 mm PSF for the same Focus of view as the other panels. Panels (e) and (f) show the image and spectral index maps resulting from the combination of the 1.3 and 0.87 mm data. The synthesized beams are shown in the lower left of each panel. This figure is originally reported in ALMA Partnership et al. (2015).

of water molecules, e.g., Hayashi 1981; Hayashi et al. 1985) by observations in protoplanetary disks is important because it will constrain the dust-grain evolution and planet formation (e.g., Öberg et al. 2011; Oka et al. 2011; Okuzumi et al. 2012; Ros & Johansen 2013; Banzatti et al. 2015; Piso et al. 2015, 2016; Cieza et al. 2016; Pinilla et al. 2017; Schoonenberg et al. 2017), and the origin of water

on terrestrial planets (e.g., Morbidelli et al. 2000, 2012, 2016; Walsh et al. 2011; Ida & Guillot 2016; Sato et al. 2016; Raymond & Izidoro 2017). van Dishoeck et al. (2013, 2014) reviewed important features, roles and distribution of water in solar system, protoplanetary disks and planets.

1.4. *Previous direct imaging observations of protoplanetary disks*

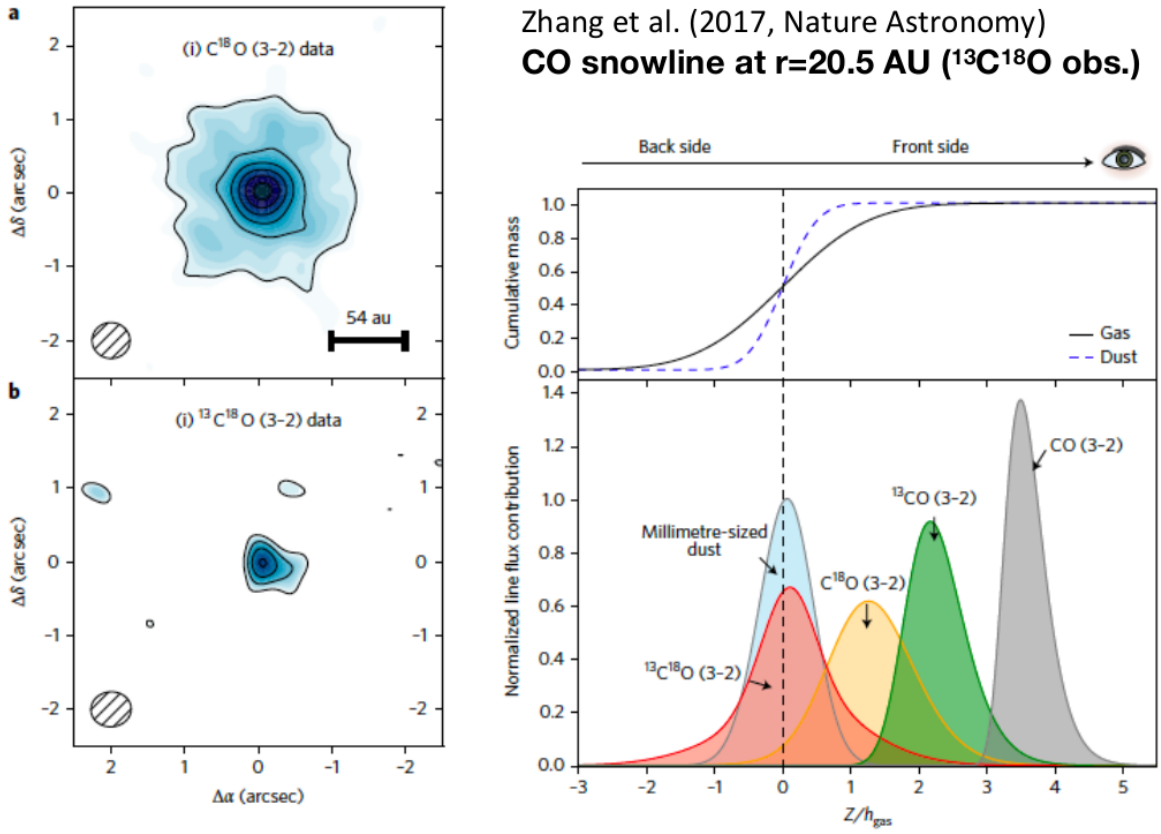

Figure 6. ALMA observations of the $C^{18}O$ and $^{13}C^{18}O$ $(3-2)$ line emission in the TW Hya protoplanetary disk. Left panels show the observed moment zero maps of these CO lines. Right panels show the vertical contributions of four CO isotopologues in the J = 3 − 2 line and 0.93 mm dust continuum emission in the inner region of the TW Hya disk. This figure is originally reported in Zhang et al. (2017).

Recent high spatial resolution direct imaging of protoplanetary disks at infrared wavelength (e.g., Subaru/HiCIAO, VLT/SPHERE, Gemini South/GPI) and sub-millimeter wavelengths (e.g., the

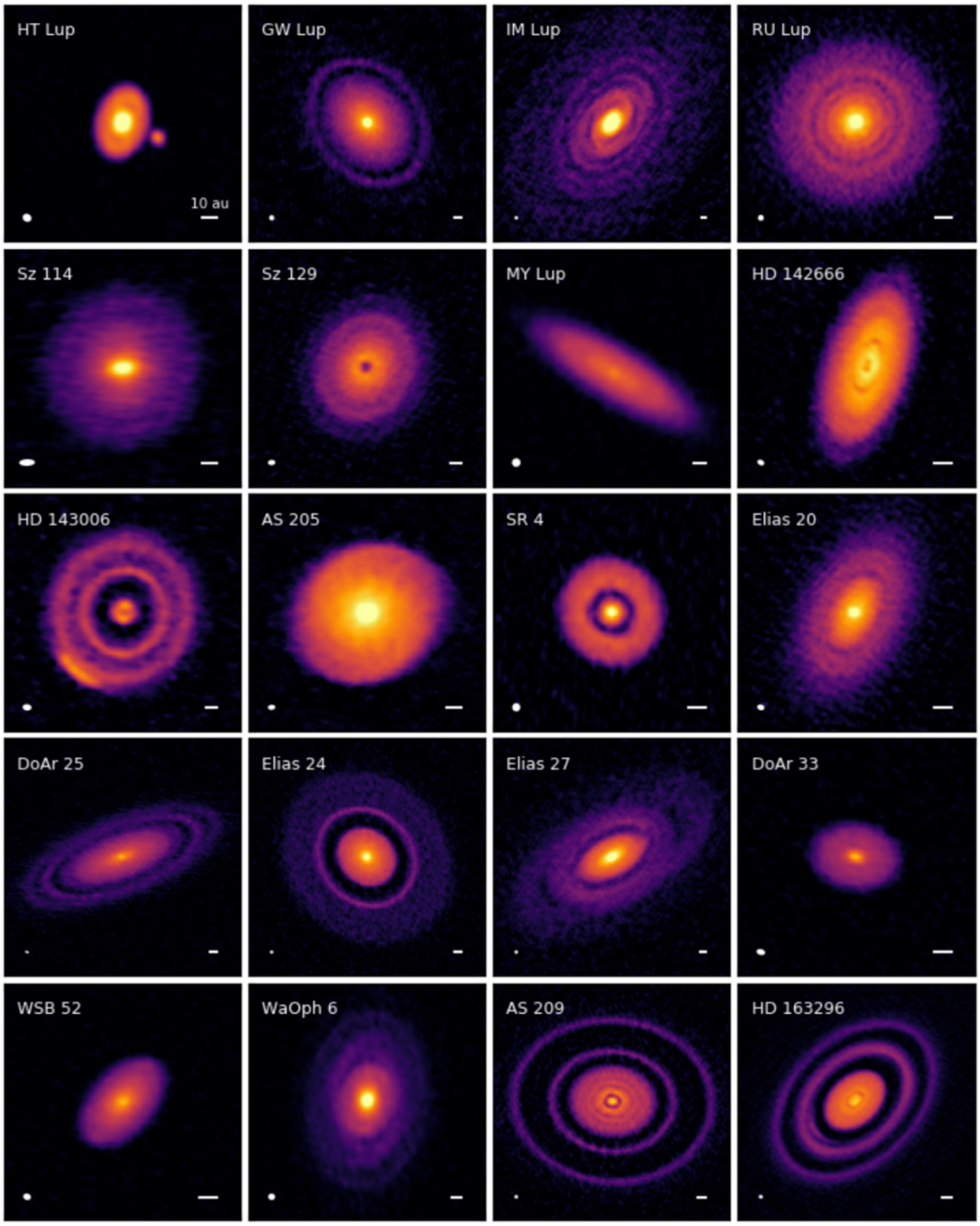

Figure 7. Gallery of 240 GHz (1.25 mm) continuum emission images for the disks in the ALMA DSHARP sample. Beam sizes and 10 au scalebars are shown in the lower left and right corners of each panel, respectively. All images are shown with an asinh stretch to reduce the dynamic range (accentuate fainter details without oversaturating the bright emission peaks). This figure is originally reported in Andrews et al. (2018).

Atacama Large Millimeter/sub-millimeter Array (ALMA), the Sub-Millimeter Array (SMA)) have revealed detailed structures of disks, such as the CO snowline (e.g., Mathews et al. 2013; Qi et al.

2013a,b, 2015; Öberg et al. 2015; Zhang et al. 2017, see also Figure 6), spiral structures (e.g., Muto et al. 2012; Benisty et al. 2015), strong azimuthal asymmetries in the dust continuum (e.g., Fukagawa et al. 2013; van der Marel et al. 2013, 2016; Muto et al. 2015), one or multiple gaps and rings (e.g., Walsh et al. 2014b; Akiyama et al. 2015; Nomura et al. 2016; Rapson et al. 2015; ALMA Partnership et al. 2015; Andrews et al. 2016, 2018; Isella et al. 2016, 2018; Schwarz et al. 2016). Recently, according to the observations of the DSHARP (Disk Substructures at High Angular Resolution Project)[1], the continuum substructures are ubiquitous in disks (see also Figure 7). The most common substructures are narrow emission rings and depleted gaps, although large-scale spiral patterns and small arc-shaped azimuthal asymmetries are also present in some cases (e.g., Andrews et al. 2018; Huang et al. 2018b,c; Isella et al. 2018). The origins of multiple gap and ring patterns are still under-discussion (for more details, see Section 5.3 of this thesis).

H_2O ice in disks has been detected by conducting low dispersion spectroscopic observations including the 3 μm H_2O ice absorption band (Pontoppidan et al. 2005; Terada et al. 2007; Terada & Tokunaga 2017), and crystalline and amorphous H_2O ice features at far-infrared wavelengths (e.g., McClure et al. 2012, 2015; Min et al. 2016). Multi-wavelength imaging including the 3 μm H_2O ice absorption band (Inoue et al. 2008) detected H_2O ice grains in the surface of the disks around the Herbig Ae/Be star, HD142527 (Honda et al. 2009). Figure 8 shows the observational result of this 3 μm H_2O ice absorption band in HD142527 disk (Honda et al. 2009). More recently, Honda et al. (2016) report the detection of H_2O ice in the HD 100546 disk, and postulate that photodesorption of water ice from dust grains in the disk surface can help explain the radial absorption strength at 3 μm. As we described previously, the H_2O snowline around a solar-mass T Tauri star is thought to exist at only a few AU from the central star. Therefore, the required spatial resolution

[1] DSHARP is one of the initial Large Programs conducted with ALMA. The primary goal of DSHARP is to find and characterize substructures in the spatial distributions of solid particles for a sample of 20 nearby protoplanetary disks, using very high resolution (0.”035, or 5 au, FWHM) observations of their 240 GHz (1.25 mm) continuum emission (e.g., Andrews et al. 2018; Huang et al. 2018b,c; Isella et al. 2018).

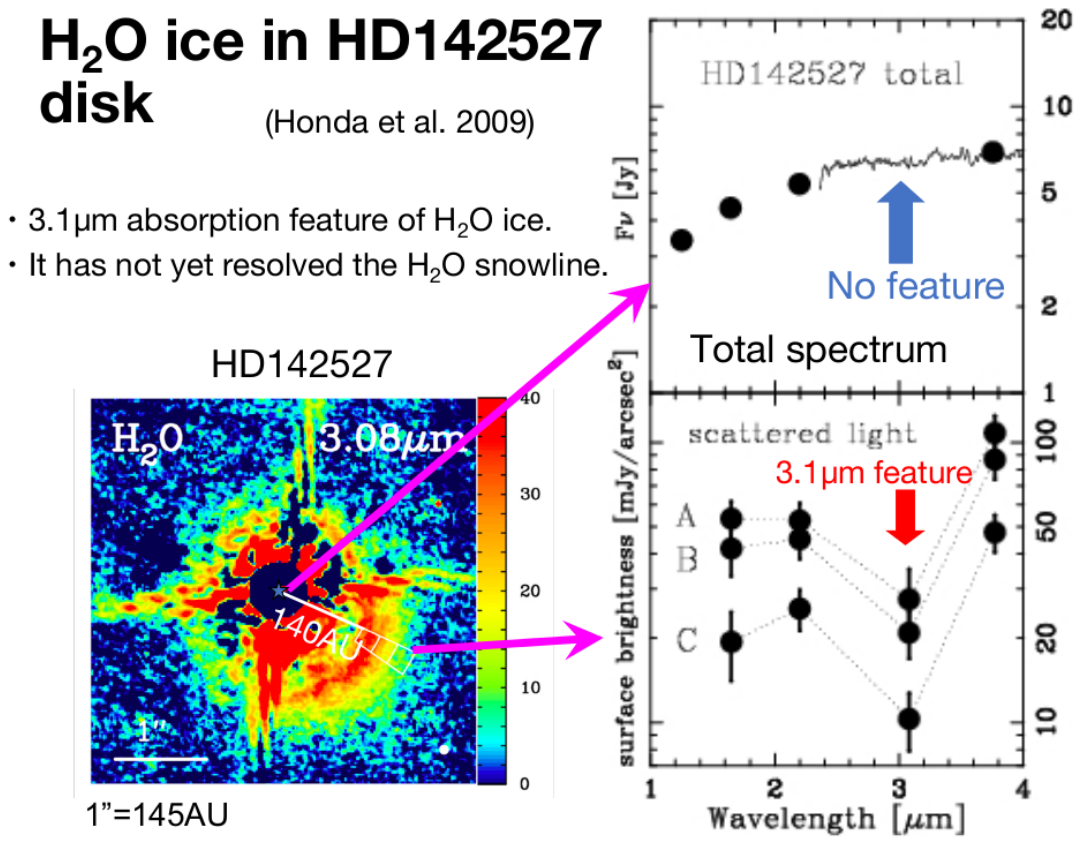

Figure 8. The observational result of the multi-wavelength imaging including 3 μm H_2O ice absorption band in HD142527 disk (Honda et al. 2009). This figure is created by using the figures of Honda et al. (2009).

to directly locate the H_2O snowline is on the order of 10 mas (milliarcsecond) around nearby disks ($\sim$100-200pc), which remains challenging for current facilities.

1.5. *Previous spectroscopic observations of strong water lines from protoplanetary disks*

In contrast, H_2O vapor has been detected through recent space spectroscopic observations of infrared rovibrational and pure rotational lines from protoplanetary disks by using *Spitzer*/IRS (e.g., Carr & Najita 2008, 2011; Salyk et al. 2008, 2011; Pontoppidan et al. 2010a; Najita et al. 2013; Antonellini et al. 2017; Banzatti et al. 2017), *Herschel*/PACS (e.g., Fedele et al. 2012, 2013; Meeus et al. 2012; Dent et al. 2013; Riviere-Marichalar et al. 2012; Kamp et al. 2013; Blevins et al. 2016, see also Figure 9), and *Herschel*/HIFI (Hogerheijde et al. 2011; van Dishoeck et al. 2014;

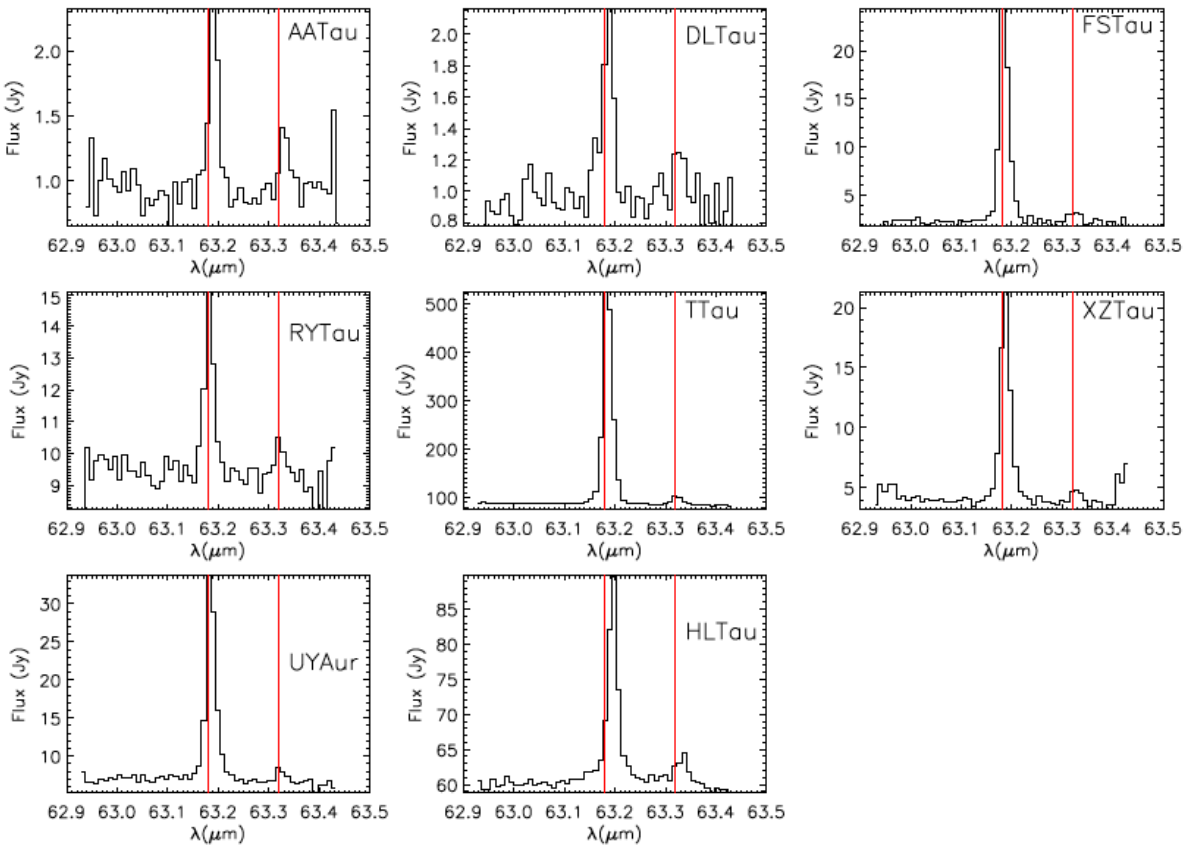

Figure 9. Spectra between λ=62.9-63.5μm, obtained with Herschel/PACS toward several T Tauri disks. The red lines indicate the rest wavelength of the [O I] $^3P_1$-$^3P_2$ 63.184 μm line and a pure rotational ortho-$H_2{}^{16}O$ line of λ=63.37μm ($J_{K_aK_c}$=8_{18}-7_{07}). The total integrated line flux of each T Tauri disk is observed to be $\sim 10^{-17}$ W m^{-2} (e.g., Riviere-Marichalar et al. 2012). This figure is originally reported in Riviere-Marichalar et al. (2012).

Podio et al. 2013; Du et al. 2017, see also Figure 10). van Dishoeck et al. (2013, 2014) reviewed the results of these recent space spectroscopic observations. These observations using *Spitzer*/IRS and *Herschel*/PACS are typically spatially unresolved and at low spectral resolution, leaving large uncertainty about the spatial distribution of H_2O gas in the protoplanetary disk. In addition, the lines they observed using *Spitzer*/IRS (Carr & Najita 2008, 2011; Salyk et al. 2008, 2011; Pontoppidan et al. 2010a; Najita et al. 2013; Banzatti et al. 2017) and *Herschel*/PACS (Fedele et al. 2012, 2013; Dent et al. 2013; Meeus et al. 2012; Riviere-Marichalar et al. 2012; Kamp et al. 2013; Blevins et al. 2016) are sensitive to the disk surface temperature and are potentially polluted by

slow disk winds, and they do not probe the midplane where planet formation occurs. Although the observations using *Herschel*/HIFI (Hogerheijde et al. 2011; van Dishoeck et al. 2014; Podio et al. 2013; Du et al. 2017) have high spectral resolution (allowing some constraints on the radial location), they mainly probe the cold water vapor in the outer disk (beyond 100 AU). The lines they detected correspond to the ground state rotational transitions which have low upper state energies. Zhang et al. (2013) estimated the position of the H_2O snowline in the transitional disk around TW Hya by using the intensity ratio of different H_2O lines that have various wavelengths and excitation energies (see also Figure 11). They used archival spectra obtained by *Spitzer*/IRS, *Herschel*/PACS, and *Herschel*/HIFI. Blevins et al. (2016) investigated the surface water vapor distribution in four disks using data obtained by *Spitzer*/IRS and *Herschel*/PACS, and found that they have critical radii of $3-11$ au, beyond which the surface gas-phase water abundance decreases by at least 5 orders of magnitude. The measured values for the critical radius are consistently smaller than the location of the surface H_2O snowline, as predicted by temperature profiles derived from the observed spectral energy distribution.

Here we also mention that millimeter and sub-millimeter H_2O, $H_2{}^{18}O$, and HDO thermal emission lines are also detected with high spatial and spectral resolution in the disks and outflows around massive protostar candidates such as Source I in Orion KL (e.g., Hirota et al. 2014), and around low mass deeply-embedded Class 0 protostellar binaries such as IRAS 16293-2422 (Persson et al. 2013). Such observations are conducted using ground telescopes of ALMA and SMA.

Studies investigating the structures of the inner disks from the analyses of velocity profiles of emission lines have been conducted by using some useful lines, such as 4.7 μm rovibrational lines of CO gas (e.g., Goto et al. 2006; Pontoppidan et al. 2008, 2011). Studies investigating the structure of the inner disk from the analyses of velocity profiles of emission lines have been conducted using lines, such as the 4.7 μm rovibrational lines of CO gas (e.g., Goto et al. 2006; Pontoppidan et al. 2008, 2011).

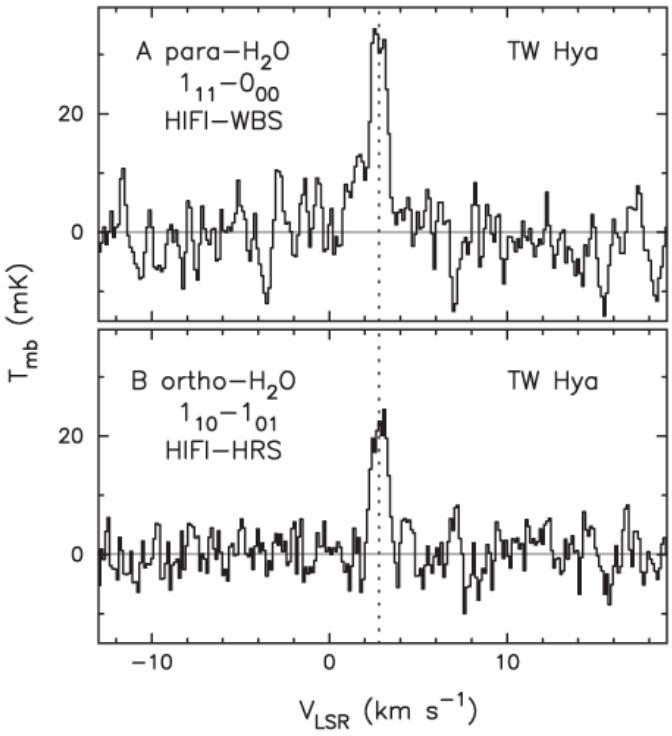

Figure 10. Spectra of a pure rotational para-$H_2{}^{16}O$ line of λ=269.47μm ($J_{K_aK_c}$=1_{11}-0_{00}) and ortho-$H_2{}^{16}O$ line of λ=538.66μm ($J_{K_aK_c}$=1_{10}-1_{01}) obtained by Herschel /HIFI toward the disk around TW Hya after subtraction of the continuum emission. The vertical dotted lines show the system's velocity of +2.8 km s^{-1} relative to the Sun's local environment (local standard of rest). This figure is originally reported in Hogerheijde et al. (2011).

Profiles of emission lines from protoplanetary disks are usually affected by Doppler shift due to Keplerian rotation, and thermal broadening. Therefore, the velocity profiles of lines are sensitive to the radial distributions of molecular tracers in disks. Follow-up ground-based near- and mid-infrared (L, N band) spectroscopic observations of H_2O emission lines for some of the known brightest targets have been conducted using VLT/VISIR, VLT/CRIRES, Keck/NIRSPEC, and TEXES (a visitor instrument on Gemini North), and the velocity profiles of the lines have been obtained (e.g., Salyk et al. 2008, 2015; Pontoppidan et al. 2010b; Fedele et al. 2011; Mandell et al. 2012). These observations suggested that the water vapor resides in the inner disk, but the spatial and spectroscopic resolution

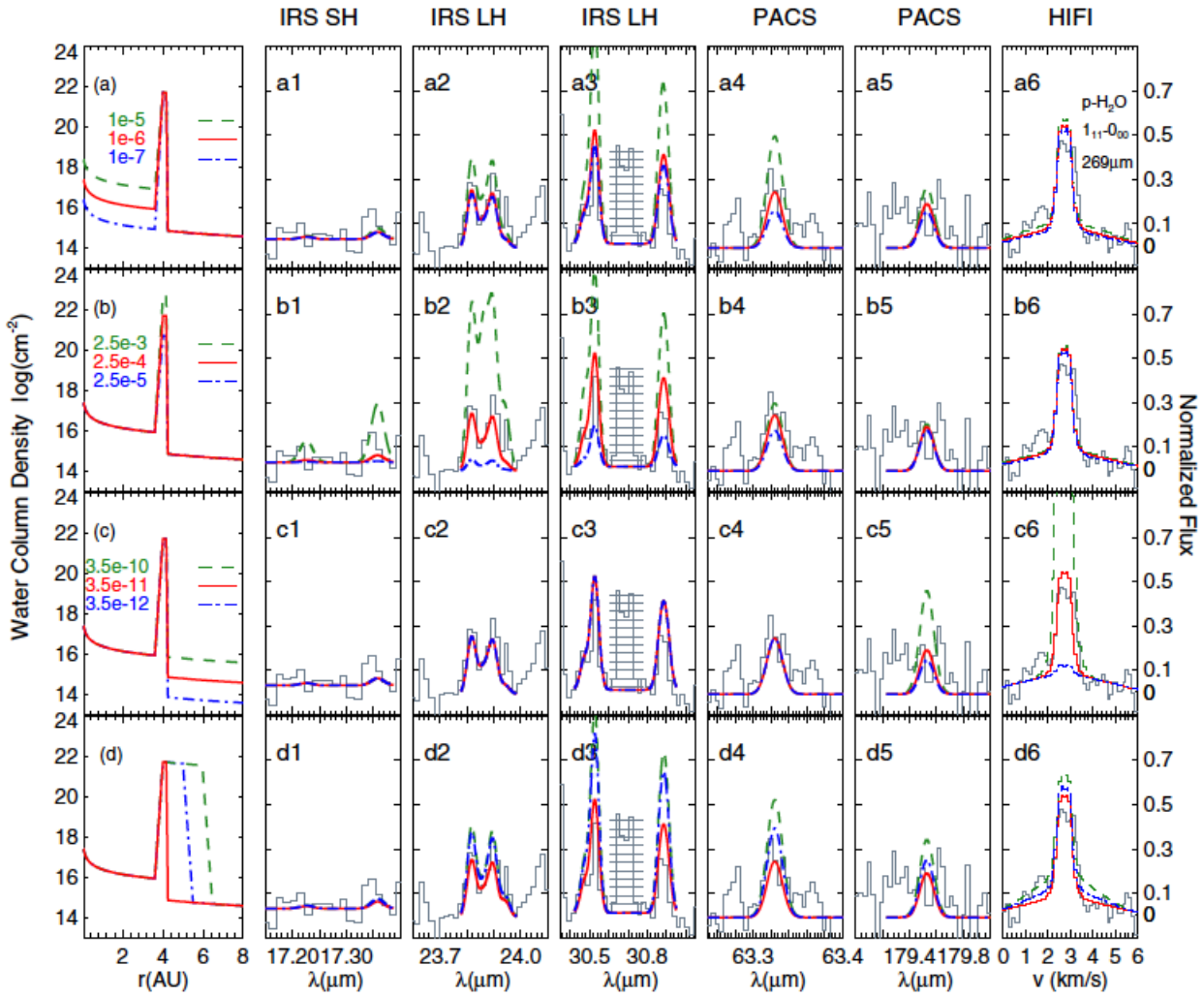

Figure 11. Sensitivity of selected water line fluxes of TW Hya to variations in the water vapor column density distribution. The first column shows the model water vapor distributions. The best-fit model is the solid red curve, while the green and blue curves are models calculated to illustrate the sensitivity of the various lines to changes in the water abundance at different disk radii. The numbers in the first column indicate the fractional (per hydrogen molecule) water abundance in (a) the optically thin inner disk, (b) the ring at the transition radius and (c) the outer disk. The final panel (d) shows the sensitivity of the model to the radius of the H_2O snow line. The following six columns show model line spectra compared to the observed spectra for TW Hya obtained by *Spitzer*/IRS, *Herschel*/PACS, and *Herschel*/HIFI. This figure is originally reported in Zhang et al. (2013).

is not sufficient to investigate the detailed structure, such as the position of the H_2O snowline. In addition, the lines they observed are sensitive to the disk surface temperature and are potentially polluted by slow disk winds, and they do not probe the midplane where planet formation occurs (e.g., Salyk et al. 2008; Pontoppidan et al. 2010b; Mandell et al. 2012; van Dishoeck et al. 2014). This is because these lines have large Einstein A coefficients and very high upper state energies (> 3000K), and exist in the near- to mid-infrared wavelength region where dust emission becomes optically thick in the surface regions.

1.6. *Purposes and structure of this thesis*

In this thesis, we proposed a means to identify the location of the H_2O snowline more directly by analyzing the Keplerian profiles of H_2O lines which can be obtained by high dispersion spectroscopic observations across a wide range of wavelengths (from mid-infrared to sub-millimeter, e.g., ALMA, SPICA) and selected based on specific criteria.

First, we calculated the chemical structures of protoplanetary disks using self-consistently derived physical models of a typical T Tauri disk (Notsu et al. 2016) and a typical Herbig Ae disk (Notsu et al. 2017) to investigate the abundance and distribution of H_2O gas and ice, as opposed to assuming the position of the H_2O snowline. Second, we calculated the velocity profiles of ortho-$H_2{}^{16}O$ emission lines from these disks ranging from near-infrared to sub-millimeter wavelengths, and investigate the properties of ortho-$H_2{}^{16}O$ lines that locate the position of the H_2O snowline. The method, results, and discussions of the T Tauri disk case (paper I, Notsu et al. 2016) and the Herbig Ae disk (paper II, Notsu et al. 2017) case are described in Sections 2 and 3, respectively.

In Section 4 (paper III, Notsu et al. 2018), we extend our water line calculations beyond ortho-$H_2{}^{16}O$ lines only to sub-millimeter para-$H_2{}^{16}O$ and ortho- and para-$H_2{}^{18}O$ lines. We discuss the possibility of detecting such candidate water lines to locate the position of the H_2O snowline with future observations with the Atacama Large Millimeter/Submillimeter Array (ALMA). We also investigate the effects of dust emission on water line profiles.

In Section 5 (paper IV, Notsu et al. 2019), we also report our ALMA observations of sub-millimeter water lines (ortho-$H_2{}^{16}O$ 321 GHz, para-$H_2{}^{18}O$ 322 GHz, and HDO 335 GHz) from the protoplanetary disk around Herbig Ae star HD163296. These lines are considered to be the prime candidate water lines available at sub-millimeter wavelengths to locate the position of the H_2O snowline (Notsu et al. 2015, 2016, 2017, 2018). We also report the dust continuum emission from the disk around HD 163296 at a spatial resolution of around 15 au, that confirms the multi-ringed and gapped structure which was originally found in previous observations (e.g., Isella et al. 2016, 2018; Andrews et al. 2018; Dent et al. 2019).

Most contents of this thesis is based on our refereed papers which have been published (Notsu et al. 2016, 2017, 2018), and was submitted recently (Notsu et al. 2019), and our unrefereed paper (Notsu et al. 2015).

2. MODELING STUDIES I. THE CASE OF THE T TAURI STAR (NOTSU ET AL. 2016)

2.1. *Methods*

2.1.1. *The physical model of the protoplanetary disk*

The physical structure of a protoplanetary disk model is calculated using the methods outlined in Nomura & Millar (2005) including X-ray heating as described in Nomura et al. (2007). In this subsection, we provide a brief overview of the physical model we adopt. A more detailed description of the background theory and computation of this physical model is described in the original papers (Nomura & Millar 2005; Nomura et al. 2007). Walsh et al. (2010, 2012, 2014a, 2015), Heinzeller et al. (2011), and Furuya et al. (2013) used the same physical model to study various chemical and physical effects, and they explain the treatment of the physical structure in detail.

We adopt the physical model of a steady, axisymmetric Keplarian disk surrounding a T Tauri star with mass M_*=0.5$M_\odot$, radius R_*=2.0$R_\odot$, and effective temperature T_*=4000K (Kenyon & Hartmann 1995). The α-disk model (Shakura & Sunyaev 1973) is adopted to obtain the radial surface density, assuming a viscous parameter α=10^{-2} and an accretion rate $\dot{M}$=$10^{-8}M_\odot$ yr^{-1}. The steady gas temperature and density distributions of the disk are computed self-consistently by solving the equations of hydrostatic equilibrium in the vertical direction and the local thermal balance between gas heating and cooling. The heating sources of the gas are grain photoelectric heating by UV photons and heating due to hydrogen ionization by X-rays. The cooling mechanisms are gas-grain collisions and line transitions (for details, see Nomura & Millar 2005 and Nomura et al. 2007). The dust temperature distribution is obtained by assuming radiative equilibrium between absorption and reemission of radiation by dust grains. The dust heating sources adopted are the radiative flux produced by viscous dissipation (α-disk model) at the midplane of the disk, and the irradiation from the central star. The radial range for which the calculations are conducted is r $\sim$0.04 au to 305 au.

The dust properties are important because they affect the physical and chemical structure of protoplanetary disks in several ways (for details, see, e.g., Nomura & Millar 2005). Since dust grains are

the dominant opacity source, they determine the dust temperature profile and the UV radiation field throughout the disk. Photodesorption, photodissociation, and photoionization processes are affected by the UV radiation field. The dust properties affect the gas temperature distribution, because photoelectric heating by UV photons is the dominant source of gas heating at the disk surface. The total surface area of dust grains has an influence on the chemical abundances of molecules through determining the gas and ice balance.

We adopt the model X-ray spectrum of a T Tauri star created by fitting the observed *XMM-Newton* spectrum of TW Hya (Kastner et al. 2002), the classical T Tauri star, with a two-temperature thin thermal plasma model (MEKAL model; see, e.g., Liedahl et al. 1995). The best-fit parameters are $kT_1 = 0.8$ keV and $kT_2 = 0.2$ for the plasma temperatures and $N_{\rm H} = 2.7 \times 10^{20}$ cm^{-2} for the foreground interstellar hydrogen column density. Figure 12 shows the X-ray spectrum of our adopted model of the T Tauri star. This is the same model that is adopted in Nomura et al. (2007).

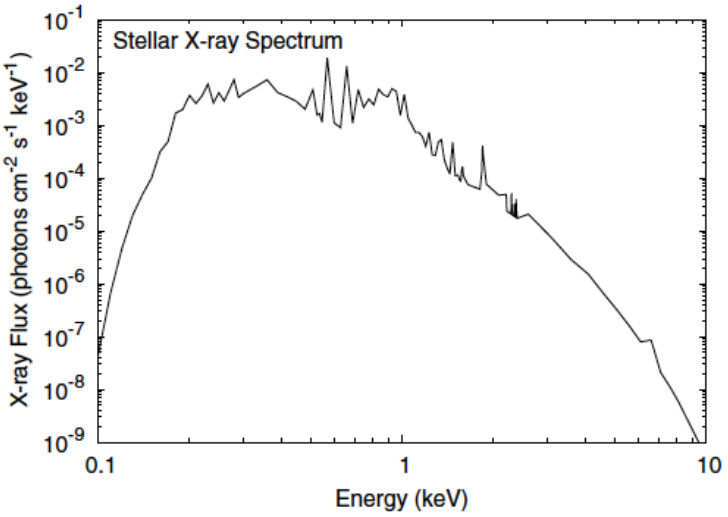

Figure 12. The X-ray spectrum of our adopted model of the T Tauri star. This spectrum assumes a distance to source of 56 pc ($\sim$ TW Hya). This figure is originally reported in Walsh et al. (2012).

The stellar UV radiation field model we use is based on the observational data of TW Hya, with

a stellar UV radiation field that has three components: photospheric blackbody radiation, optically thin hydrogenic bremsstrahlung radiation, and strong Lyα line emission (for details, see Appendix C of Nomura & Millar 2005, Walsh et al. 2015). For the UV extinction, we include absorption and scattering by dust grains. The interstellar UV radiation field is taken into account, but its contribution is negligible since the UV irradiation of the central star is strong (Nomura & Millar 2005). The total stellar FUV radiation fields at 1 au of our adopted models of T Tauri star and Herbig Ae star (see Section 3, Notsu et al. 2017) are shown in Figure 13.

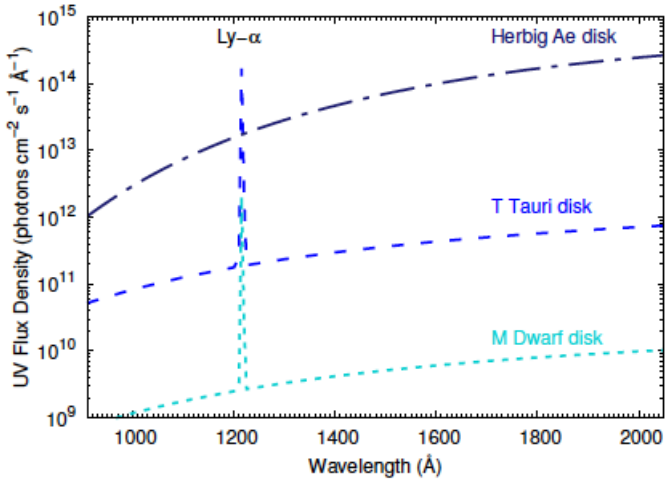

Figure 13. The total stellar FUV (912−2100 $\AA$) radiation fields at 1 au of the model of M type star and our adopted models of T Tauri star and Herbig Ae star. This figure is originally reported in Walsh et al. (2015).

We adopt the same dust grain model of Nomura & Millar (2005). They assume that the dust grains are compact and spherical, and consist of silicate grains, carbonaceous grains, and water ices. The optical properties of the carbonaceous grains are assumed to have a continuous distribution of graphite-like properties for larger sizes and PAH-like properties in the small size limit (Li & Draine 2001). The sublimation temperatures are assumed to be $T_{\rm silicate} = 1500$K, $T_{\rm carbon} = 2300$K, and $T_{\rm ice} = 150$K (Adams & Shu 1986). The mass fractional abundances are taken to be consistent with the solar elemental abundances: $\zeta_{\rm silicate} = 0.0043$, $\zeta_{\rm carbon} = 0.0030$, and $\zeta_{\rm ice} = 0.0094$ (Anders & Grevesse 1989).

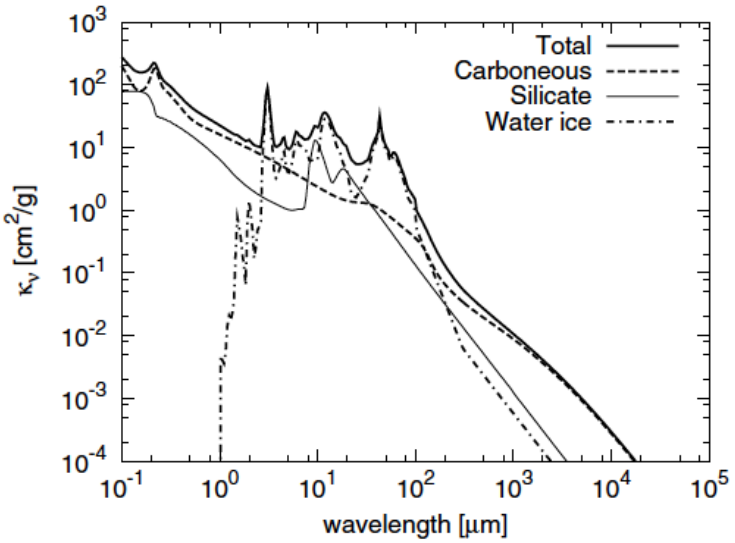

Figure 14. The monochromatic absorption coefficient (thick solid line) of dust grains consisting of carboneceous (dashed line), silicate (thin solid line), and water ice (dot-dashed line). This figure is originally reported in Appendix D of Nomura & Millar (2005).

Their bulk densities are set to be $\rho_{\rm silicate} = 3.5$ g cm^{-3}, $\rho_{\rm graphite} = 2.24$ g cm^{-3}, and $\rho_{\rm ice} = 0.92$ g cm^{-3}. They assume that the dust and gas are well mixed. They use the dust grain size distributions of silicate and carbonaceous grains obtained by Weingartner & Draine (2001), which reproduces the extinction curve observed in dense clouds with the ratio of visual extinction to reddening $R_V \equiv A(V)/E(B-V) = 5.5$. They adopt the value of $b_{\rm C} = 3.0\times10^{-5}$, which is the total C abundance per H nucleus in the log-normal size dust-grain distribution, in order to reproduce the distribution of very small hydrocarbon molecules including PAHs (see also Fig. 6 of Weingartner & Draine 2001). It is assumed that the water ice has the simple size distribution of $dn/da \propto a^{-3.5}$, where a is the radius of the dust particles (Mathis et al. 1977). The maximum radius of dust grains $a_{\rm max}$ is $\sim10\mu$m. The calculated monochromatic absorption coefficient is shown in Figure 14.

In Figure 15, we display the gas number density in cm^{-3} (top left), the gas temperature in K (top right, T_g), the dust-grain temperature in K (bottom left, T_d), and the wavelength-integrated UV flux in erg cm^{-2} s^{-1} (bottom right), as a function of disk radius in au and height (scaled by the radius,

z/r). The density decreases as a function of disk radius and disk height with the densest region of the disk found in the disk midplane close to the star ($\sim 10^{14}$ cm^{-3}) and the most diffuse, in the disk surface at large radii ($\sim 10^{5}$ cm^{-3}), so that the density range in our adopted disk model covers almost 10 orders of magnitude. The gas temperature increases as a function of disk height and decreases as a function of disk radius with the hottest region found in the disk surface ($> 10^3$K), and the coldest region found in the outer disk ($\sim$10K). In addition, due to the influence of viscous heating at the disk midplane, the temperature increases within several au from the central T Tauri star. In the disk surface, the dust-grain temperature is more than ten times lower than the gas temperature. At low densities, gas-grain collisions become ineffective so the gas cools via radiative line transitions. In contrast, the gas and dust-grain temperatures are similar in the midplane region with high densities. Moreover, the disk surface closest to the parent star is subjected to the largest flux of both UV and X-ray photons, although the disk midplane is effectively shielded from UV and X-ray photons over the radial extent of our disk model.

2.1.2. *Overview of chemical structure of the protoplanetary disk*

In order to investigate the chemical structure of the protoplanetary disk, we use a large chemical network which includes gas-phase reactions and gas-grain interactions (freezeout of gas molecules on dust grains, and thermal and non-thermal desorption from dust grains). The non-thermal desorption mechanisms we adopt include cosmic-ray-induced desorption, and photodesorption by UV photons. Walsh et al. (2010, 2012, 2014a, 2015), Heinzeller et al. (2011), Furuya et al. (2013), Furuya & Aikawa (2014), Ishimoto et al. (2013), and Du & Bergin (2014) used similar chemical networks to calculate chemical structure of a protoplanetary disk, and they, and the reviews of Henning & Semenov (2013) and Dutrey et al. (2014), explain the background theories and procedures in detail. Here we outline the key points of the chemical network we use.

The addition of grain-surface chemistry (e.g., Hasegawa et al. 1992) is expected to aid the synthesis of complex organic molecules in the outer disk where significant freezeout has occurred. Some previous works on chemical modeling of disks (e.g., Willacy 2007; Semenov & Wiebe 2011; Walsh et al. 2012,

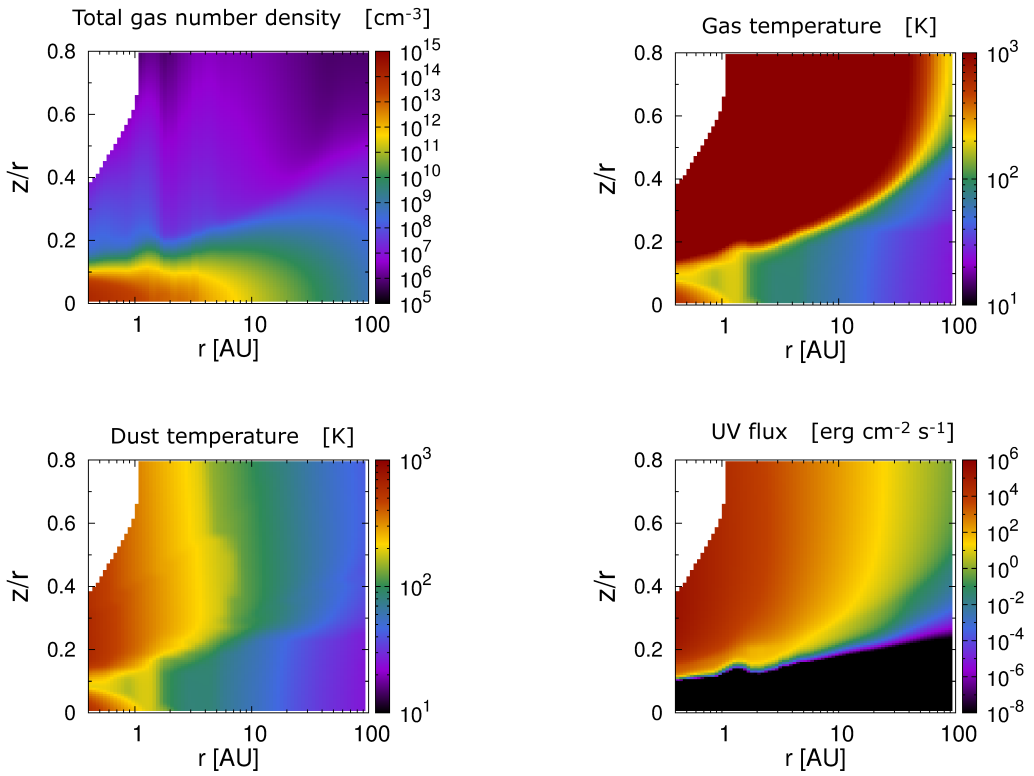

Figure 15. The total gas number density in cm^{-3} (top left), the gas temperature in K (top right), the dust temperature in K (bottom left), and the UV flux in erg cm^{-2} s^{-1} (bottom right) of a disk around a T Tauri star as a function of the disk radius in au and height (scaled by the radius, z/r) up to maximum radii of r =100au.

2014a, 2015; Furuya et al. 2013; Furuya & Aikawa 2014; Drozdovskaya et al. 2014) have contained grain-surface reactions. However, the chemical network we adopt in this work does not contain such grain-surface reactions, and is equivalent to one of models in Walsh et al. (2010), which includes the same freezeout and desorption processes as considered here. This is because we are primarily interested in the hot inner disk region where molecular line emission originates from the thermally desorbed gas reservoir. Figure 16 shows the summary of the main gas-phase and solid-state chemical reactions leading to the formation and destruction of water molecules, though the chemical network we adopt does not include the grain-surface chemistry.

2.1.3. *Gas-phase reactions*

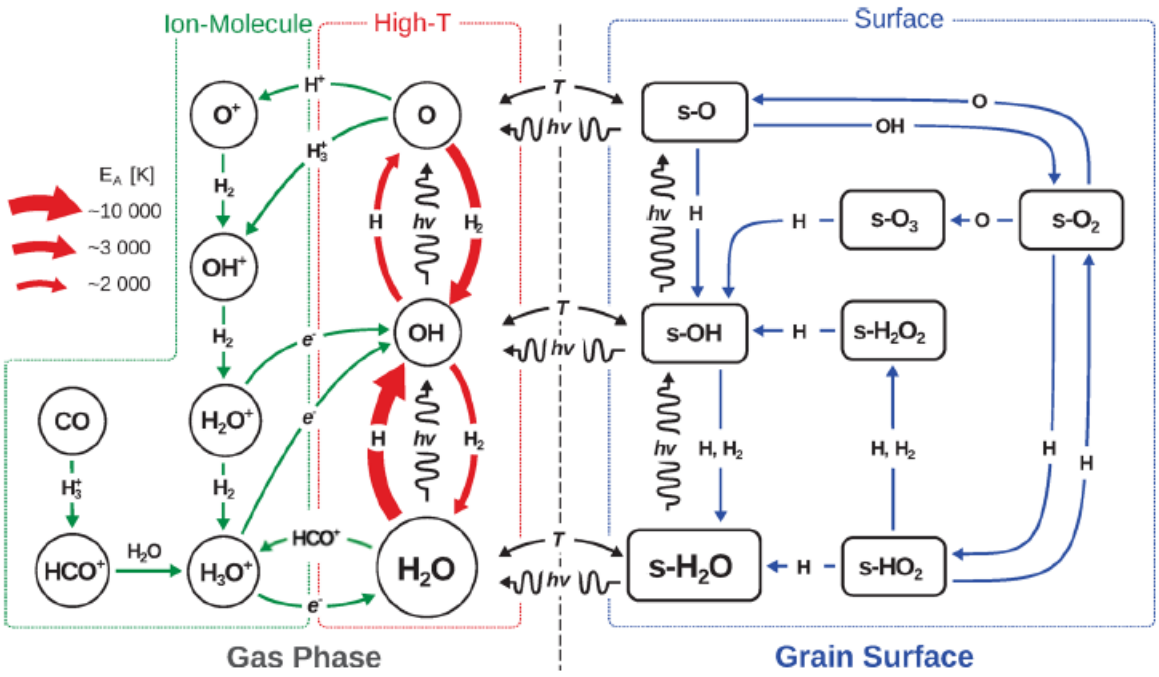

Figure 16. Summary of the main gas-phase and solid-state chemical reactions leading to the formation and destruction of H_2O. Three different chemical regimes can be distinguished:(i) ion-neutral chemistry, which dominates gas-phase chemistry at low T_g (green); (ii) high-temperature neutral-neutral chemistry (red); and (iii) solid-state chemistry (blue). s-X denotes species X on the ice surfaces. This figure is originally reported in van Dishoeck et al. (2013).

Our gas-phase chemistry is extracted from the UMIST Database for Astrochemistry (UDfA), henceforth referred to as "RATE06" (Woodall et al. 2007). Walsh et al. (2010, 2012), and Heinzeller et al. (2011) used RATE06 to calculate the chemical structure of a protoplanetary disk. We include almost the entire RATE06 gas-phase network removing only those species (and thus reactions) which contain fluorine, F, and phosphorus, P, in order to reduce computation time. We have confirmed that the loss of F- and P-containing species have a minimal impact on the remaining chemistry (Walsh et al. 2010; Heinzeller et al. 2011). Our gas-phase network thus contains 375 atomic, molecular, and ionic species composed of the elements H, He, C, N, O, Na, Mg, Si, S, Cl, and Fe. Table 1 in the online material from Woodall et al. (2007) shows the list of these 375 species. The initial elemental fractional abundances (relative to total hydrogen nuclei density) we use are the set of oxygen-rich low-metallicity abundances from Graedel et al. (1982), listed in Table 8 of Woodall et al. (2007) and

also in Table 1. The chemical evolution is run for 10^6 years. By this time, the chemistry in the inner regions of the disk midplane inside the H_2O snowline is close to steady state, at which time the chemistry has forgotten its origins, justifying our use of initial elemental abundances, instead of ambient cloud abundances.

Table 1. Initial elemental abundances relative to total hydrogen nuclei

Element	Abundance
He	0.14
C^+	7.30×10^{-5}
N	2.14×10^{-5}
O	1.76×10^{-4}
Na^+	3.00×10^{-9}
Mg^+	3.00×10^{-9}
Si^+	3.00×10^{-9}
S^+	2.00×10^{-8}
Cl^+	3.00×10^{-9}
Fe^+	3.00×10^{-9}

Our adopted reaction network consists of 4336 reactions including 3957 two-body reactions, 214 photoreactions, 154 X-ray/cosmic-ray-induced photoreactions, and 11 reactions of direct X-ray/cosmic-ray ionization. The adopted equations that give the reaction rates of two-body reactions, X-ray/cosmic-ray-induced photoreactions, and reactions of X-ray/cosmic-ray ionization are described in Section 2.1 of Woodall et al. (2007).

Here we mention that we use the previous version of the UDfA RATE06 (Woodall et al. 2007), instead of the latest version of UDfA, "RATE12" (McElroy et al. 2013). There are some updates in RATE12 such as reactions related to some complex molecules, and McElroy et al. (2013) described that the

major difference between RATE12 and RATE06 is the inclusion of anion reactions. Although this has an influence on the abundances of carbon-chain molecules (Walsh et al. 2009; McElroy et al. 2013), it has little effect on the chemistry of main simple molecules, such as H_2O.

In our calculations of the chemistry, we have approximated our photoreaction rates at each point in the disk, $k^{\rm ph}(r,z)$, by scaling the rates of RATE06 which assume the interstellar UV field, k_0, using the wavelength integrated UV flux calculated at each point (see also Figure 15),

$$G_{\rm FUV}(r,z) = \int_{912{\rm \AA}(13.6{\rm eV})}^{2068{\rm \AA}(6{\rm eV})} G_{\rm FUV}(\lambda,r,z){\rm d}\lambda. \quad (1)$$

Using this value of $G_{\rm FUV}(r,z)$, the rate for a particular photoreaction at each (r,z) is given by

$$k^{\rm ph}(r,z) = \frac{G_{\rm FUV}(r,z)}{G_0} k_0 \ {\rm s}^{-1}, \quad (2)$$

where G_0 is the interstellar UV flux (2.67×10^{-3} erg cm^{-2} s^{-1}, van Dishoeck et al. 2006).

2.1.4. *Gas-grain interactions*

In our calculations, we consider the freezeout of gas-phase molecules on dust grains, and the thermal and non-thermal desorption of molecules from dust grains. For the thermal desorption of a molecule to occur, the dust-grain temperature must exceed the freezeout (sublimation) temperature of each molecule. Non-thermal desorption requires an input of energy from an external source and is thus independent of dust-grain temperature. The non-thermal desorption mechanisms we investigate are cosmic-ray-induced desorption (Leger et al. 1985; Hasegawa & Herbst 1993) and photodesorption from UV photons (Westley et al. 1995; Willacy & Langer 2000; Öberg et al. 2007), as adopted in some previous studies (e.g., Walsh et al. 2010, 2012). First we explain the mechanisms of freezeout and thermal desorption we use in detail. Then we introduce the detailed mechanisms of non-thermal desportion we adopt (cosmic-ray-induced desorption and photodesorption from UV photons).

The freezeout (accretion) rate, k_i^a [s^{-1}], of species i onto the dust-grain surface is treated using the standard equation (e.g., Hasegawa et al. 1992; Woitke et al. 2009a; Walsh et al. 2010),

$$k_i^a = \alpha\sigma_d\langle v_i^{th}\rangle n_d \ {\rm s}^{-1}, \quad (3)$$

Table 2. Molecular Binding Energies

Species	Binding Energy $E_d^{\rm K}(i)$ [K]	References
CO	855	a
CO_2	2990	b
H_2O	4820	c
CH_4	1080	d
N_2	790	a
NH_3	2790	e
HCN	4170	d
H_2CO	1760	f
C_2H_2	2400	d

[a] Öberg et al. (2005); [b] Edridge (2010); [c] Sandford & Allamandola (1993); [d] Yamamoto et al. (1983); [e] Brown & Bolina (2007); [f] Hasegawa & Herbst (1993)

where α is the sticking coefficient, here assumed to 0.4 for all species, which is in the range of high gas temperature cases ($T_g \sim 100 - 200$K) reported in Veeraghattam et al. (2014). Previous theoretical and experimental studies suggested that the sticking coefficient tends to be lower as the gas and dust-grain temperature become higher (e.g., Masuda et al. 1998; Veeraghattam et al. 2014). $\sigma_d = \pi a^2$ is the geometrical cross section of a dust grain with radius, a, $\langle v_i^{th} \rangle$ is the thermal velocity of species i with mass m_i at gas temperature T_g, k_B is the Boltzmann's constant, and n_d is the number density of dust grains. We adopt the value of $\langle v_i^{th} \rangle = (k_B T_g / m_i)^{1/2}$ as Walsh et al. (2010) adopted. In this work, for our gas-grain interactions, we assume a constant grain radius $a = 0.1 \mu m$ and a fixed dust-grain fractional abundance ($x_d = n_d / n_{\rm H}$[2]) of 2.2×10^{-12}, as previous studies adopted (e.g., Walsh et al. 2012). From the viewpoint of dust-grain surface area per unit volume, the adopted value

[2] $n_{\rm H}$ is the total gas atomic hydrogen number density.

of a constant grain radius a is consistent with the value from the dust-grain size distributions in the disk physical model adopted in this work. This adopted value of x_d is consistent with a gas-to-dust ratio of 100 by mass.

The thermal desorption rate, k_i^d [s^{-1}], of species i from the dust-grain surface is given by (e.g., Hasegawa et al. 1992; Woitke et al. 2009a; Walsh et al. 2010),

$$k_i^d = \nu_0(i) \exp\left(\frac{-E_d^{\rm K}(i)}{T_d}\right) \ {\rm s}^{-1}, \tag{4}$$

where $E_d^{\rm K}(i)$ is the binding energy of species i to the dust-grain surface in units of K. The values of $E_d^{\rm K}(i)$ for several important molecules are listed in Table 2. Most of these values are adopted in Walsh et al. (2010) or Walsh et al. (2012). T_d is the dust-grain temperature in units of K. The characteristic vibrational frequency of each adsorbed species i in its surface potential well, $\nu_0(i)$, is represented by a harmonic oscillator relation (Hasegawa et al. 1992),

$$\nu_0(i) = \sqrt{\frac{2 n_{surf} E_d^{\rm erg}(i)}{\pi^2 m_i}} \ {\rm s}^{-1}, \tag{5}$$

where, $E_d^{\rm erg}(i)$ is in units of erg here, m_i is the mass of each absorbed species i, and $n_{surf} = 1.5 \times 10^{15}$ cm^{-2} is the surface density of absorption sites on each dust grain.

The non-thermal desorption mechanisms we adopt are cosmic-ray-induced desorption (Leger et al. 1985; Hasegawa & Herbst 1993) and photodesorption from UV photons (Westley et al. 1995; Willacy & Langer 2000; Öberg et al. 2007), in common with some previous studies (e.g., Walsh et al. 2010, 2012). In this subsection, we explain the details of these non-thermal desorption mechanisms.

In order to calculate the cosmic-ray-induced desorption rate for each species, $k_i^{\rm crd}$, we assume that dust grains with a radius of 0.1 μm are impulsively heated by the impact of relativistic Fe nuclei with energies of 20-70 MeV $nucleon^{-1}$ which deposit an energy of 0.4 MeV on average into each dust grain (Leger et al. 1985; Hasegawa & Herbst 1993). Assuming that the majority of molecules desorb

around 70 K, the cosmic-ray-induced desorption rate can be approximated by

$$k_i^{\rm crd} = f(70{\rm K}) k_i^d(70{\rm K}) \frac{\zeta_{\rm CR}}{1.36 \times 10^{-17} {\rm s}^{-1}} \ {\rm s}^{-1}, \quad (6)$$

where $\zeta_{\rm CR}$ is the cosmic-ray ionization rate of H_2, $k_i^d(70{\rm K})$ is the thermal desorption energy of species i at a dust temperature of 70K computed using Equation. (4). $f(70{\rm K})$ is the fraction of time spent by dust grains around 70K and is defined as the ratio of the desorption cooling time (10^{-5} s) to the time interval between successive heatings to 70K. The latter value is estimated to be $3.16{\times}10^{13}$ s from the Fe cosmic-ray flux, then $f(70{\rm K})$ is $3.16{\times}10^{-19}$ (Leger et al. 1985; Hasegawa & Herbst 1993). We mention that like cosmic-ray particles, X-ray photons can penetrate deep inside the disk and locally heat dust grains. However, X-ray desorption is not yet included in our chemical code unlike previous studies (e.g., Walsh et al. 2012, 2014a, 2015). This is because X-ray desorption is the least theoretically or experimentally constrained of all the non-thermal desorption mechanisms, and thus there remains significant uncertainties in the reaction rates (e.g., Najita et al. 2001; Walsh et al. 2010).

Absorption of a UV photon by a dust-grain surface species can increase the species internal energy enough to induce desorption. The photodesorption rate of species i is given by

$$k_i^{\rm pd} = F_{\rm UV} Y_{\rm UV}^i \sigma_d \frac{n_d}{n_{act}} \ {\rm s}^{-1}, \quad (7)$$

where $F_{\rm UV}$ is the wavelength integrated UV radiative flux calculated at each (r, z) in units of photons cm^{-2} s^{-1}. $Y_{\rm UV}^i$ is the experimentally determined photodesorption yield in units of molecules photon^{-1}. Woitke et al. (2009a) and Heinzeller et al. (2011) used a similar method to calculate $k_i^{\rm pd}$. $F_{\rm UV}$ is calculated from the density profile and the dust opacity in our adopted disk physical model (Nomura & Millar 2005; Nomura et al. 2007; Walsh et al. 2015). We assume that $Y_{\rm UV}^i$ is 3.0×10^{-3} for all species, which is the same value determined for pure water ice by Westley et al. (1995) and for pure CO ice by Öberg et al. (2007). Walsh et al. (2010) use the same value of $Y_{\rm UV}^i$. $n_{act} = 4\pi a^2 n_d n_{surf} N_{Lay}$ is the number of active surface sites in the ice mantle per unit volume. N_{Lay} is the number of surface layers to be considered as "active", and we adopt the value of Aikawa et al.

(1996), $N_{Lay} = 2$. Recent experiments by Öberg et al. (2009a,b,c) suggest that photodesorption rates are dependent on ice composition and the depth of the ice layer on a dust grain.

Considering these processes of freezeout, thermal desorption, cosmic-ray-induced desorption, and photodesorption, the total formation rate of ice species i is

$$\dot{n}_{i,\mathrm{ice}} = n_i k_i^a - n_{i,\mathrm{ice}}^{\mathrm{desorb}}(k_i^d + k_i^{\mathrm{crd}} + k_i^{\mathrm{pd}}). \tag{8}$$

where k_i^{crd} is the cosmic-ray-induced thermal desorption rate for each species i, k_i^{pd} is the photodesorption rate for a specific species i, $n_{i,\mathrm{ice}}$ denotes the number density of ice species i, and $n_{i,\mathrm{ice}}^{\mathrm{desorb}}$ is the fraction of $n_{i,\mathrm{ice}}$ located in the uppermost active surface layers of the ice mantles. The value of $n_{i,\mathrm{ice}}^{\mathrm{desorb}}$ is given by (Aikawa et al. 1996; Woitke et al. 2009a)

$$n_{i,\mathrm{ice}}^{\mathrm{desorb}} = \begin{cases} n_{i,\mathrm{ice}} & (n_{\mathrm{ice}} < n_{act}), \\ n_{act}\frac{n_{i,\mathrm{ice}}}{n_{\mathrm{ice}}} & (n_{\mathrm{ice}} \geq n_{act}), \end{cases} \tag{9}$$

where n_{ice} is the total number density of all ice species, $n_{act} = 4\pi a^2 n_d n_{surf} N_{Lay}$ is the number of active surface sites in the ice mantle per volume. N_{Lay} is the number of surface layers to be considered as "active", and we adopt the value from Aikawa et al. (1996), $N_{Lay} = 2$.

2.1.5. *Profiles of water emission lines from the protoplanetary disk*

Using the H_2O gas abundance distribution obtained from our chemical calculations, we calculate the profiles of water emission lines ranging from near-infrared to sub-millimeter wavelengths, and investigate which lines are the best candidates for probing emission from the inner thermally desorbed water reservoir, i.e., within the H_2O snow line. We also study how the line flux and profile shape depends upon the location of the H_2O snowline. In the following paragraphs, we outline the calculation methods used to determine the water emission line profiles (based on Rybicki & Lightman (1986), Hogerheijde & van der Tak (2000), and Nomura & Millar (2005)).

Here we define the transition frequency of each line as ν_{ul}, where the subscript ul means the transition

from the upper level (u) to the lower level (l). The intensity of each line profile at the frequency ν, $I_{ul}(\nu)$, is obtained by solving the radiative transfer equation in the line-of-sight direction of the disk,

$$\frac{\mathrm{d}I_{ul}(\nu)}{\mathrm{d}s} = -\chi_{ul}(\nu)(I_{ul}(\nu) - S_{ul}(\nu)). \tag{10}$$

The source function, $S_{ul}(\nu)$, and the total extinction coefficient, $\chi_{ul}(\nu)$, are given by

$$S_{ul}(\nu) = \frac{1}{\chi_{ul}(\nu)} n_u A_{ul} \Phi_{ul}(\nu) \frac{h\nu_{ul}}{4\pi}, \tag{11}$$

and

$$\begin{aligned} \chi_{ul}(\nu) =& \rho_d \kappa_{ul} \\ &+ (n_l B_{lu} - n_u B_{ul}) \Phi_{ul}(\nu) \frac{h\nu_{ul}}{4\pi}, \end{aligned} \tag{12}$$

where the symbols A_{ul} and B_{ul} are the Einstein A and B coefficients for the transition $u \to l$, the symbol B_{lu} is the Einstein B coefficient for the transition $l \to u$, h is the Planck constant, and n_u and n_l are the number densities of the upper and lower levels, respectively. The energy difference between the levels u and l corresponds to $h\nu_{ul}$. ρ_d is the mass density of dust grains which we calculate from the values of total gas mass density ρ_g and gas-to-dust mass ratio ($\rho_g/\rho_d = 100$). κ_{ul} is dust absorption coefficient at the frequency ν_{ul} as described in Section 2.1.1.

The symbol $\Phi_{ul}(\nu)$ is the line profile function at the frequency ν, and we consider the Doppler shift due to Keplerian rotation, and thermal broadening, in calculating the emission line profiles. This function is given by,

$$\Phi_{ul}(\nu) = \frac{1}{\Delta\nu_D \sqrt{\pi}} \exp\left[-\frac{(\nu + \nu_K - \nu_{ul})^2}{\Delta\nu_D^2} \right], \tag{13}$$

where $\Delta\nu_D = (\nu_{ul}/c)(\sqrt{2kT_g/m})$ is the Doppler width, c is the speed of light, T_g is the gas temperature, k is the Boltzmann constant, m is the mass of a water molecule, and ν_K is the Doppler-shift due to projected Keplerian velocity for the line-of-sight direction and is given by,

$$\nu_K = \frac{\nu_{ul}}{c} \sqrt{\frac{GM_*}{r}} \sin\phi \sin i, \tag{14}$$

where G is the gravitational constant, M_* is the mass of central star, r is the distance from the central star, ϕ is the azimuthal angle between the semimajor axis and the line which links the point

in the disk along the line-of-sight and the center of the disk.

The observable profiles of flux density are obtained by integrating Eq. (8) in the line-of-sight direction and summing up the integrals in the plane of the projected disk, (x, y), as,

$$\begin{aligned} F_{ul}(\nu) =& \frac{1}{4\pi d^2} \int d\Omega \int \int \mathrm{d}x\mathrm{d}y \\ & \times \int_{-s_\infty}^{s_\infty} j_{ul}(s, x, y, \nu)\mathrm{d}s, \end{aligned} \tag{15}$$

where d is the distance of the observed disk from the Earth. $j_{ul}(s, x, y, \nu)$ is the emissivity at (s, x, y) and the frequency ν considering the effect of absorption in the upper disk layer and it is given by the following equation,

$$\begin{aligned} j_{ul}(s, x, y, \nu) =& n_u(s, x, y) A_{ul} \frac{h\nu_{ul}}{4\pi} \Phi_{ul}(s, x, y, \nu) \\ & \times \exp(-\tau_{ul}(s, x, y, \nu)), \end{aligned} \tag{16}$$

and $\tau_{ul}(s, x, y, \nu)$ is the optical depth from s to the disk surface s_∞ at the frequency ν given by,

$$\tau_{ul}(s, x, y, \nu) = \int_s^{s_\infty} \chi_{ul}(s', x, y, \nu)\mathrm{d}s'. \tag{17}$$

Hence, the observable total flux of the lines, F_{ul}, are given by the following equation,

$$F_{ul} = \int F_{ul}(\nu)\mathrm{d}\nu \tag{18}$$

Here, we use a distance $d = 140$ pc for calculating the line profiles since this is the distance to the Taurus molecular cloud, one of the nearest star formation regions with observable protoplanetary disks.

The code for ray tracing which we have built for calculating emission line profiles from the protoplanetary disk is a modification of the original 1D code called RATRAN[3] (Hogerheijde & van der Tak 2000). We adopt the data for the ortho- and para-$H_2{}^{16}O$ energy levels from Tennyson et al. (2001),

[3] http://home.strw.leidenuniv.nl/~michiel/ratran/

the radiative rates (Einstein A coefficients A_{ul}) from the BT2 water line list (Barber et al. 2006), and the collisional rates, $< \sigma v >$, for the excitation of H_2O by H_2 and by electrons from Faure & Josselin (2008). We use the collisional rates to determine the critical densities of transitions of interest. These data are part of Leiden Atomic and Molecular Database called LAMDA[4] (Schöier et al. 2005). The level populations of the water molecule (n_u and n_l) are calculated under the assumption of local thermal equilibrium (LTE). In Section 2.3.2, we discuss the validity of the assumption of LTE in our work. We do not include dust-grain emission nor emission from disk winds and jet components in calculating the emission line profiles. However, we do include the effects of the absorption of line emission by dust grains (as described above).

The nuclear spins of the two hydrogen atoms in each water molecule can be either parallel or anti-parallel, and this results in a grouping of the H_2O energy levels into ortho ($K_a + K_c$ =odd) and para ($K_a + K_c$ =even) ladders. The ortho to para ratio (OPR) of water in the gas gives information on the conditions, formation, and thermal history of water in specific regions, such as comets and protoplanetary disks (e.g., Mumma & Charnley 2011; van Dishoeck et al. 2013, 2014). An alternative way to describe the OPR is through the "spin temperature", defined as the temperature that characterizes the observed OPR if it is in thermal equilibrium. The OPR becomes zero in the limit of low temperature and 3 in the limit of high temperature ($\gtrsim$60K). The original definition of OPR of water vapor in thermal equilibrium is described in Mumma et al. (1987). In our calculations, we set the OPR=3 throughout the disk to calculate values of n_u and n_l from the H_2O gas abundance distribution. The lines we calculate in order to locate the position of the H_2O snowline mainly trace the hot water vapor for which the temperature is higher than the water sublimation temperature ($\sim 150 - 160$K). The disk physical structure of our adopted model is steady, and thermal and chemical equilibrium is mostly achieved throughout the disk. In addition, previous observational data on warm water detected at mid-infrared wavelengths in the inner regions of protoplanetary disks are

[4] http://home.strw.leidenuniv.nl/~moldata/

consistent with OPR= 3 (e.g., Pontoppidan et al. 2010a).

Here we also mention that Hama et al. (2016) reported from their experiments that water desorbed from the icy dust-grain surface at 10K shows the OPR=3, which invalidates the assumed relation between OPR and the formation temperature of water. They argue that the role of gas-phase processes which convert the OPR to a lower value in low temperature regions is important, although the detailed mechanism is not yet understood.

2.2. *Results*

2.2.1. *The distributions of* H_2O *gas and ice*

Figure 17 shows the fractional abundances (relative to total gas hydrogen nuclei density, $n_{\rm H}$) of H_2O gas and H_2O ice in a disk around a T Tauri star as a function of disk radius r and height scaled by the radius (z/r). The radial range over which the chemistry is computed is r ∼0.5au and 100au in order to reduce computation time. Here we mention that at small radii, due to the high densities found in the midplane, there is a significant column density of material shielding this region from the intense UV and X-ray fields of the star. Therefore, molecules are expected to survive in the midplane at radii within ∼0.1 au, unless there are cavities in the dust and gas. Thus the actual total amount of molecular gas in the inner disk may be larger than that of our chemical calculation results.

According to this figure, the fractional abundance with respect to H_2 of H_2O gas is high ($\sim 10^{-4}$) in the midplane region inside the H_2O snowline, and in contrast, it is low ($\lesssim 10^{-12}$) in the midplane outside the H_2O snowline. The fractional abundance of H_2O ice has the opposite distribution. It is low ($\lesssim 10^{-9}$) in the midplane region inside the H_2O snowline, and in contrast, it is high ($\sim 10^{-5}$) in the midplane outside the H_2O snowline. The H_2O snowline in the T Tauri disk that we adopt in this work exists at a radius of $\sim$ 1.6 au in the midplane ($T_g \sim 150 - 160$K), consistent with the binding energy we adopt.

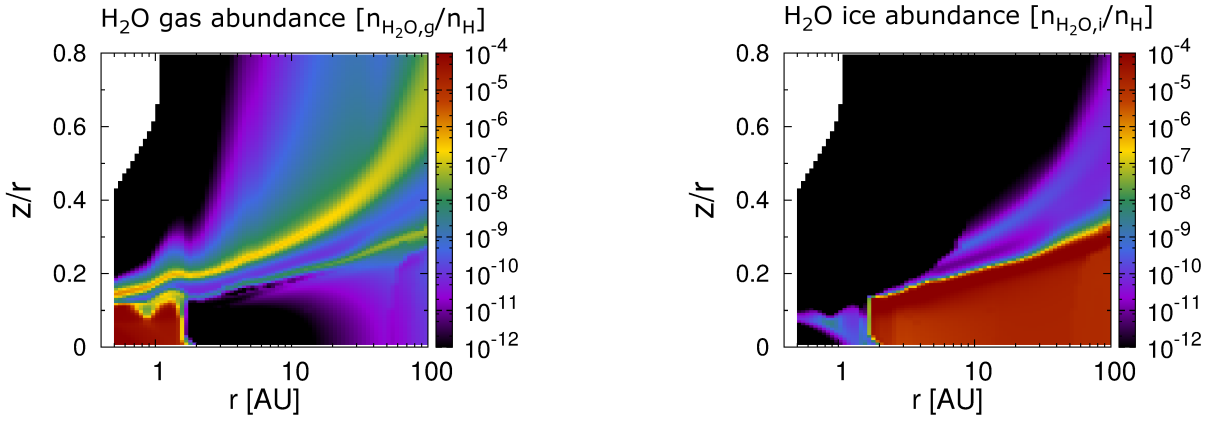

Figure 17. The fractional abundance (relative to total hydrogen nuclei density) distributions of H_2O gas (top) and H_2O ice (bottom) of a disk around a T Tauri star as a function of disk radius and height (scaled by the radius, z/r) up to maximum radii of r =100au.

Inside the H_2O snowline, the temperature exceeds the sublimation temperature under the pressure conditions of the midplane ($T_g \sim 150 - 160$K) and most of the H_2O is released into the gas-phase through thermal desorption. In addition, this region is almost completely shielded from intense the UV and X-ray fields of the star and interstellar medium (Nomura & Millar 2005; Nomura et al. 2007, see also Figure 2 of Walsh et al. 2012), has a high temperature ($>$ 150K) and large total gas particle number density ($> 10^{11}$ cm^{-3}), and thermal equilibrium between the gas and dust is achieved ($T_g \sim T_d$). Under these conditions, the gas-phase chemistry is close to thermochemical equilibrium and most of the oxygen atoms will be locked up into H_2O (and CO) molecules (e.g., Glassgold et al. 2009; Woitke et al. 2009a,b; Walsh et al. 2010, 2012, 2015; van Dishoeck et al. 2013, 2014; Du & Bergin 2014; Antonellini et al. 2015). Therefore, the H_2O gas abundance of this region is approximately given by the elemental abundance of oxygen (1.76×10^{-4}, Woodall et al. 2007) minus the fraction bound in CO.

In addition, the fractional abundance of H_2O gas is relatively high in the hot surface layer of the outer disk. First, at z/r of $0.1 - 0.3$ between $r \sim 0.5{-}100$ au, the fractional abundance H_2O gas

is $\sim 10^{-8} - 10^{-7}$. This region can be considered as the sublimation (photodesorption) front of H_2O molecules, driven by the relatively strong stellar UV radiation. This so-called photodesorbed layer (Dominik et al. 2005) allows H_2O to survive in the gas phase where it would otherwise be frozen out on the dust-grain surfaces. The abundance and extent of gas-phase H_2O in this layer is mediated by absorption back onto the dust grain, destruction by the stellar UV photons and by chemical reactions with other species.

Second, at z/r of 0.15-0.7 between r $\sim$0.5$-$100 au, the H_2O abundance is relatively high ($\sim 10^{-7}$) compared with the cold midplane region of the outer disk ($\lesssim 10^{-12}-10^{-10}$). Since the gas temperature is significantly higher than the dust temperature (typically $T_g \sim 200 - 2000$K) and the gas density is low compared to the disk midplane, the water chemistry is controlled by chemical kinetics as opposed to thermodynamic (or chemical) equilibrium. Due to the very high gas temperature (>200K), the energy barriers for the dominant neutral-neutral reactions of $O+H_2 \rightarrow OH+H$ and $OH+H_2 \rightarrow H_2O+H$ are readily surpassed and gaseous H_2O is produced rapidly. This route will drive all the available gas-phase oxygen into H_2O, unless strong UV or a high atomic hydrogen abundance is able to convert some water back to OH and O (e.g., Glassgold et al. 2009; Woitke et al. 2009b; Meijerink et al. 2012; van Dishoeck et al. 2013, 2014; Walsh et al. 2015). In the uppermost surface layers, H_2O is even more rapidly destroyed by photodissociation and reactions with atomic hydrogen than it is produced, so there is little water at the very top of the disk. The OH gas abundance in our calculations and others (e.g., Walsh et al. 2012) is high in this hot surface region. It is consistent with the above discussions that neutral-neutral reactions including OH and H_2O are dominant and strong UV or a high atomic hydrogen abundance converts some water back to OH and O (Walsh et al. 2012, 2015).

Figure 18 shows the radial column density profile of H_2O gas (*red solid line*) and ice (*blue dashed line*). The column density of H_2O gas and ice in the disk midplane flips across the H_2O snowline ($\sim$1.6 au). The column density of H_2O gas is high ($\sim 10^{21}$ cm^{-2}) inside the H_2O snowline, and, in contrast, is low outside the H_2O snowline ($\sim 10^{14} - 10^{15}$ cm^{-2}). The column density profile of

H_2O ice is roughly opposite. The column density of H_2O ice in the outer disk is $\sim 10^{20} - 10^{21}$ cm^{-2}. Previous chemical modeling calculations (e.g., Walsh et al. 2012, 2015; Du & Bergin 2014) gave a column density of H_2O gas inside the H_2O snowline of around $10^{21} - 10^{22}$ cm^{-2}. This value is slightly higher than in our calculations, possibly due to the inclusion of grain surface reactions. However, since gas-phase H_2O in the disk midplane is likely obscured by dust grains at near- to mid-infrared wavelengths (Walsh et al. 2015), the "visible" H_2O gas column density at these wavelength is much smaller than the actual amount. For example in Walsh et al. (2015), the visible value is on the order of a few times 10^{19} cm^{-2} within the H_2O snowline. Previous infrared low dispersion spectroscopic observations using *Spitzer*/IRS for classical T Tauri stars derive the H_2O gas column densities ranging from 4×10^{17} to 7.9×10^{20} cm^{-2} (Carr & Najita 2011; Salyk et al. 2011). Despite the model T Tauri disk being a generic model which is not representative of any particular source, there is significant overlap between the calculated "visible" column densities and these observed values, although it should be acknowledged that there is a three orders-of-magnitude spread in the observed values.

Previous analytical models and numerical simulations derived the position of the H_2O snowline of an optically thick disk for given parameters, such as mass (M_*) and temperature (T_*) of the central star, a viscous parameter α, an accretion rate $\dot{M}$, a gas-to-dust mass ratio g/d, and the average dust grain size a and opacity (e.g., Davis 2005; Garaud & Lin 2007; Min et al. 2011; Oka et al. 2011; Du & Bergin 2014; Harsono et al. 2015; Mulders et al. 2015; Piso et al. 2015), and suggested that the position of the H_2O snowline changes, as these parameters change. In the case of T Tauri disks with $M_* \sim 0.5 - 1 M_\odot$, $\dot{M} \sim 10^{-8} M_\odot$ yr^{-1}, and $a \sim 0.1\mu$m, the position of the H_2O snowline is $\sim 1.5 - 2$ au. In our calculations, we use similar parameters for M_*, $\dot{M}$ and a, and the H_2O snowline appears at a radius of around 1.6 au in the midplane ($T_g \sim 150 - 160$K), which is in the range of previous works.

Heinzeller et al. (2011) investigated the effects of physical mass transport phenomena in the radial

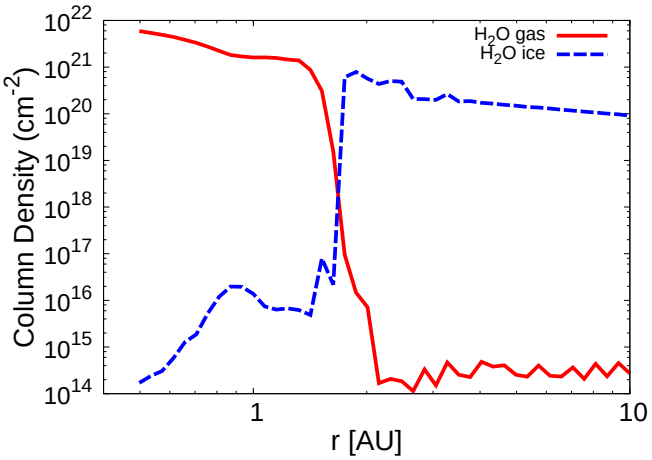

Figure 18. The radial profile of the vertically integrated column density cm^{-2} of H_2O gas (*red solid line*) and ice (*blue dashed line*).

direction by viscous accretion and in the vertical direction by diffusive turbulent mixing and disk winds. They showed that the gas-phase H_2O abundance is enhanced in the warm surface layer due to the effects of vertical mixing. In contrast, they mentioned that the gas-phase H_2O abundance in the midplane inside the H_2O snowline is not affected by the accretion flow, since the chemical reactions are considered to be fast enough in this region to compensate for the effects of the accretion flow.

2.2.2. *The overview of ortho-$H_2{}^{16}O$ emission lines from the T Tauri disk*

We perform ray-tracing calculations and investigate the profiles of $H_2{}^{16}O$ emission lines for a protoplanetary disk in Keplerian rotation, using the methods described in Section 2.1.5 and next paragraph. We include rovibrational and pure rotational ortho- and para- $H_2{}^{16}O$ lines at near-, mid-, and far-infrared and sub-millimeter wavelengths, and find that water lines which have small Einstein A coefficients ($A_{ul} \sim 10^{-3} - 10^{-6}\mathrm{s}^{-1}$) and relatively high upper energy levels (E_{up} ~1000K) are most promising for tracing emission from the innermost hot water reservoir within the H_2O snowline.

Here we describe how we find 50 candidate lines which are selected from the LAMDA database of ortho-$H_2{}^{16}O$ transition lines. First of all, we proceeded by selecting about 20 ortho-$H_2{}^{16}O$ lines

Table 3. Calculated ortho-$H_2{}^{16}O$ line parameters and total line fluxes

$J_{K_aK_c}$	λ [μm]	Freq. [GHz]	A_{ul} [s^{-1}]	E_{up} [K]	$n_{\rm cr}$ [cm^{-3}]	total flux[1] [W m^{-2}]
6_{43}-5_{50}	682.926	439.286	2.816×10^{-5}	1088.7	1.0×10^{6}	3.12×10^{-22}
8_{18}-7_{07}	63.371	4733.995	1.772	1070.6	1.5×10^{10}	5.66×10^{-18}
1_{10}-1_{01}	538.664	556.933	3.497×10^{-3}	61.0	2.9×10^{7}	1.13×10^{-20}

[a] In calculating total flux of these H_2O lines, we use a distance $d = 140$pc and the inclination angle of the disk i =30 deg.

from the LAMDA database which have various wavelengths (from near-infrared to sub-millimeter), Einstein A coefficients ($A_{ul} \sim 10^{-1} - 10^{-7}s^{-1}$), and upper state energies ($E_{up} < 3000$K). In making this initial selection we ignored lines with very small Einstein A coefficients and very high upper state energies, since the emission fluxes of these lines are likely to weak to detect. When we calculated the profiles of these lines, we noticed that $H_2{}^{16}O$ lines with small Einstein A coefficients ($A_{ul} \sim 10^{-3} - 10^{-6}s^{-1}$) and relatively large upper state energies ($E_{up} \sim 700 - 2100$K) are the best candidates to trace emission from the hot water reservoir within the H_2O snowline. The number of these candidate lines is 10 lines within originally selected 20 lines. Then we searched all other ortho-s$H_2{}^{16}O$ transition lines which satisfy these conditions, and found an additional 40 ortho-$H_2{}^{16}O$ candidate water lines. In the reminder of this thesis, we sometimes describe the $H_2{}^{16}O$ lines as H_2O lines.

In the remaining part of this section, we describe the detailed properties of three characteristic pure rotational ortho-$H_2{}^{16}O$ lines (λ=682.93, 63.37, 538.66μm). These three lines have different values of A_{ul} and E_{up}. We find that the $H_2{}^{16}O$ 682.93μm line, which falls in ALMA Band 8, is a candidate for tracing emission from the innermost hot water reservoir within the H_2O snowline. The 63.37 and 538.66μm lines are examples of lines which are less suited to trace emission from water vapor within the H_2O snowline. We consider these two particular lines to test the validity of our model calculations, since the fluxes of these two lines from protoplanetary disks are observed with *Herschel*

(see Sections 2.2.4 and 2.2.5). The list of suitable lines from mid-infrared (Q band) to sub-millimeter, and their properties, especially the variation in line fluxes with wavelength, are described in detail in our companion paper (paper II, Notsu et al. 2017, see also Section 3).

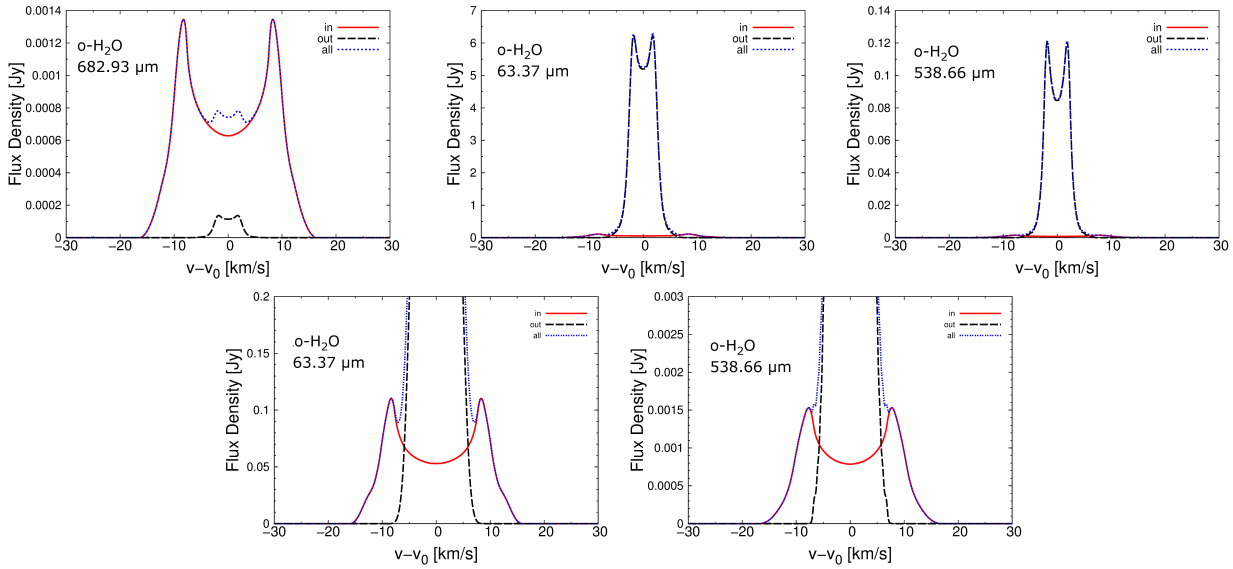

Figure 19. Top: the velocity profiles of three characteristic pure rotational ortho-$H_2{}^{16}O$ lines at λ=682.93μm ($J_{K_aK_c}$=6_{43}-5_{50}, top left), 63.37μm ($J_{K_aK_c}$=8_{18}-7_{07}, top middle), and 538.66μm ($J_{K_aK_c}$=1_{10}-1_{01}, top right), which have various Einstein A coefficients A_{ul} and upper state energies E_{up}. Bottom: the velocity profiles of the ortho-$H_2{}^{16}O$ 63.37μm line (bottom left) and 538.66μm line (bottom right), which enlarge the inner components. *Red solid lines* are the emission line profiles from inside 2 au (∼inside the H_2O snowline), *black dashed lines* are those from 2 − 30 au (∼outside the H_2O snowline), and *blue dotted lines* are those from the total area inside 30 au. In calculating these profiles, we assume that the distance to the object d is 140 pc (∼ the distance of Taurus molecular cloud), and the inclination angle of the disk i is 30 deg.

2.2.3. *The case of a candidate ortho-$H_2{}^{16}O$ emission line*

The top panels in Figure 19 show the emission profiles of three pure rotational ortho-$H_2{}^{16}O$ lines at λ=682.93μm ($J_{K_aK_c}$=6_{43}-5_{50}, top left), 63.37μm ($J_{K_aK_c}$=8_{18}-7_{07}, top middle), and 538.66μm ($J_{K_aK_c}$=1_{10}-1_{01}, top right), which have various Einstein A coefficients (A_{ul}) and upper state energies (E_{up}). The detailed parameters, such as transitions ($J_{K_aK_c}$), wavelength, frequency, A_{ul}, E_{up},

critical density $n_{\rm cr}$, and total line fluxes of these three ortho-$H_2{}^{16}O$ lines are listed in Table 3. In calculating these profiles, we assume that the distance d to the object is 140pc ($\sim$ the distance of Taurus molecular cloud), and the inclination angle i of the disk is 30 degs. The total fluxes of these three lines (λ=682.93, 63.37, 538.66μm) are 3.12×10^{-22}, 5.66×10^{-18}, 1.13×10^{-20} W m^{-2}, respectively. The bottom panels in Figure 19 show the velocity profiles of the ortho-$H_2{}^{16}O$ 63.37μm line (bottom left) and the 538.66μm line (bottom right), which enlarge the inner components.

Since the H_2O lines at λ=682.93 and 63.37μm have large upper state energies (E_{up}=1088.7K and 1070.6K), these lines trace the hot water vapor ($T_g \gtrsim$ a few hundred K). On the basis of the results of our chemical calculations, the abundance of H_2O gas is high in the optically thick hot inner region within the H_2O snowline near the equatorial plane ($T_g > 150$K) and in the hot optically thin surface layer of the outer disk.

In the top left panel of Figure 19, we show the $H_2{}^{16}O$ line emission at 682.93μm. The contribution from the optically thin surface layer of the outer disk (*black dashed line*, 2$-$30 au, "out" component) is very small compared with that from the optically thick region near the midplane of the inner disk (*red solid line*, 0$-$2 au, "in" component). This is because this ortho-$H_2{}^{16}O$ 682.93μm line has a small A_{ul} ($=2.816 \times 10^{-5}$ s^{-1}). On the basis of Eqs. (13)$-$(16), the observable flux density is calculated by summing up the emissivity at each point ($j_{ul}(s,x,y,\nu)$) in the line-of-sight direction. In the optically thin ($\tau_{ul} << 1$) region (e.g., the disk surface layer), the flux density is roughly characterized by integrating the values of $n_u(s,x,y)A_{ul}$ at each point. On the other hand, in the optically thick ($\tau_{ul} \geq 1$) region (e.g., the disk midplane of the inner disk), the flux density is independent of $n_u(s,x,y)$ and A_{ul} at each point, and it becomes similar to the value of the Planck function at T_g around the region of $\tau_{ul} \sim 1$. Therefore, the emission profile of the 682.93μm line which has a small A_{ul} and a relatively high E_{up} mainly traces the hot H_2O gas inside the H_2O snowline, and shows the characteristic double-peaked profile due to Keplerian rotation. In this profile, the position of the two peaks and the rapid drop in flux density between the peaks gives information on the distribution of hot

H_2O gas within the H_2O snowline. This profile potentially contain information which can be used to determine the H_2O snowline position. The spread in the wings of the emission profile (high velocity regions) represents the inner edge of the H_2O gas distribution in the disk. This is because emission from each radial region in the disk is Doppler-shifted due to the Keplerian rotation. Because the area near the outer emitting region is larger than that of the inner region ($\propto r^2$), the contribution to the emission from the region near the outer edge is larger if the emissivity at each radial point is similar. Figure 20 also shows the detailed properties of the line from the disk which rotates with Keplerian velocity.

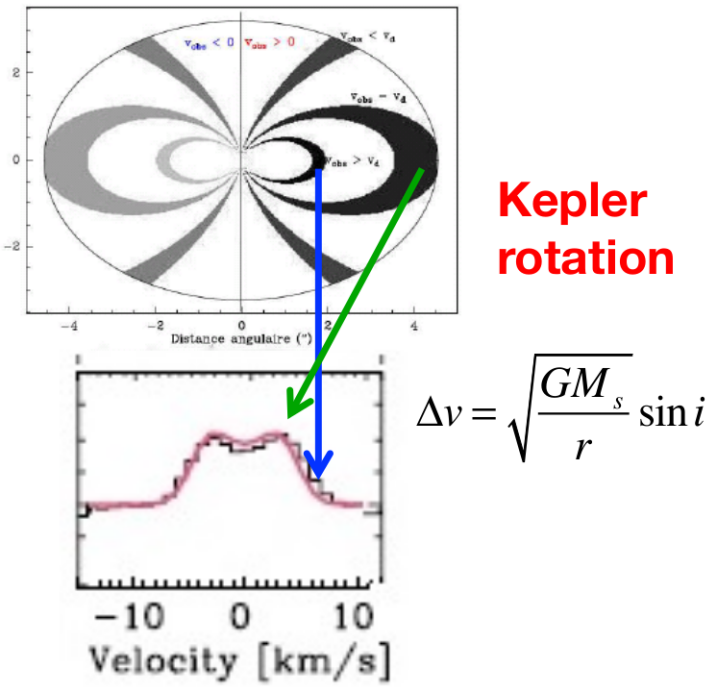

Figure 20. (Top): The map which shows the regions of the disk that have equal projected velocities v_{obs} (black painted regions). The ellipse is the projection of the outer edge of the disk observed by each line. (Bottom): The example of an emission line profile from an disk which rotates with Keplerian velocity. In the profile of this line, the position of the two peaks and the rapid drop in flux density between the peaks gives information on the distribution of gas and especially the position of the outer edge of the disk observed by the this line (e.g., the snowline). The spread in the wings of the emission profile (high velocity regions) will constrain the inner limit of the gas in the disks. This figure is created by using the panel originally reported in Guilloteau et al. (2012).

Figure 21 shows the line-of-sight emissivity distributions of these three pure rotational ortho-$H_2{}^{16}O$ lines. Figure 22 shows the total optical depth (gas emission and dust) distributions for the same transitions. We assume that the inclination angle, i, of the disk is 0 deg in making these figures, and thus the line-of-sight direction is from z=+∞ to -∞ at each disk radius. According to the top panels of Figures 21 and 22, the values of the emissivity at r <1.6 au (= the position of the H_2O snowline) and $z/r \sim 0.1$ are stronger than that of the other regions including the optically thin hot surface layer of the outer disk and the photodesorbed layer. Although we cannot detect the emission from $z \sim 0$ because of the high optical depth of the inner disk midplane due to the absorption by dust grains and excited H_2O molecules, we can get information about the distribution of hot H_2O gas within the H_2O snowline. This is because the H_2O gas fractional abundance is close to constant within r <1.6 au (= the position of the H_2O snowline) and $z/r \sim$ 0-0.1 (see also Figure 17).

2.2.4. *The case of a ortho-$H_2{}^{16}O$ emission line that traces the hot surface layer*

The top middle panel of Figure 19 where we show the line profile for the ortho-$H_2{}^{16}O$ 63.37μm line, the contribution from the optically thin surface layer of the outer disk (*black dashed line*, 2−30 au, "out" component) is large compared with that of the optically thick region near the midplane of the inner disk (*red solid line*, 0−2 au, "in" component), and the shape of the line profile is a much narrower double peaked profile. This is because this ortho-$H_2{}^{16}O$ 63.37μm line has a large A_{ul} (=1.772 s^{-1}), although E_{up} (=1070.6K) is similar to that of the ortho-$H_2{}^{16}O$ 682.93μm line (=1088.7K), and thus the flux density from the hot surface layer of the outer disk becomes strong. Here we note that since the peak velocities of the "in" and "out" components are different, water lines with large A_{ul} at infrared wavelengths, such as the 63.37μm line, can in principal trace the hot H_2O gas within the H_2O snowline. However, there is no current or future instrument with enough sensitivity and spectral resolution to distinguish the peaks of the "in" component from the "out" component in these lines. For example, SPICA/SAFARI is a future instrument with far-infrared spectrograph, but its spectral resolution is low (R ∼3000) and is not enough to distinguish the peaks of these line profiles. The difference in the peak flux density is very large ($\gtrsim$ several tens) and the wings of both components

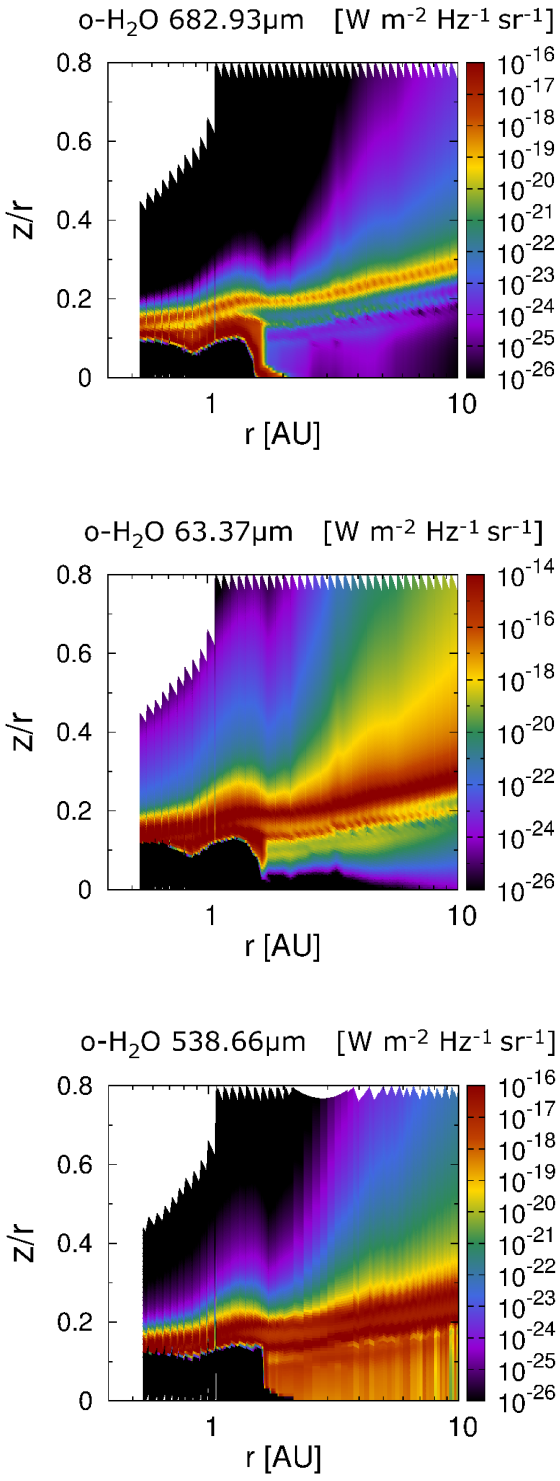

Figure 21. The line of sight emissivity distributions of the three characteristic pure rotational ortho-$H_2{}^{16}O$ lines with λ=682.93μm (top), 63.37μm (middle), and 538.66μm (bottom). The dimension is W m^{-2} Hz^{-1} sr^{-1}. We assume that the inclination angle of the disk i is 0 degree in making these figures, and thus the direction of line-of-sight is from z=+∞ to -∞ at each disk radius.

are blended (see also the bottom left panel of Figure 19).

According to the middle panels of Figures 21 and 22, the values of the emissivity at each (r, z) point in the optically thin hot surface layer of the outer disk and the photodesorbed layer are as strong as that of the optically thick region inside the H_2O snowline. For similar reasons as the case for the 682.93μm line, emission from the outer disk dominates. In addition, the outer disk midplane opacity of this line is larger than that of the ortho-$H_2{}^{16}O$ 682.93μm line, because the dust opacity becomes large at shorter wavelengths (e.g, Nomura & Millar 2005).

We mention that previous space far-infrared low dispersion spectroscopic observations with *Herschel*/PACS (R ∼1500) detected this line from some T Tauri disks and Herbig Ae disks (e.g., Fedele et al. 2012, 2013; Dent et al. 2013; Meeus et al. 2012; Riviere-Marichalar et al. 2012). Although the profiles of these lines are unresolved, comparison with models indicates that the emitting regions of these observations are thought to originate in the hot surface layer (e.g., Fedele et al. 2012; Riviere-Marichalar et al. 2012). In addition, the total integrated line flux of classical T Tauri objects in the Taurus molecular cloud are observed to be $\sim 6 \times 10^{-18} - 3 \times 10^{-16}$ W m^{-2} (e.g., Riviere-Marichalar et al. 2012). These values have a dispersion factor of 50. Riviere-Marichalar et al. (2012) suggested that the objects with higher values of line flux have extended emission from outflows, in contrast to those with lower values which have no extended emissions (e.g., AA Tau, DL Tau, and RY Tau). The latter lower values are of the same order as the value we calculate here assuming a T Tauri disk model with no outflow and envelope.

2.2.5. *The case of a ortho-$H_2{}^{16}O$ emission line that traces the cold water*

In the top right panel of Figure 19 where we show the line profile for the ortho-$H_2{}^{16}O$ 538.66μm line, the contribution from the outer disk (*black dashed line*, 2−30 au, "out" component) is large compared with that of the optically thick region near the midplane of the inner disk (*red solid line*, 0−2 au, "in" component) and the shape of the profile is a much narrower double peaked profile (closer to a single peaked profile), although the A_{ul} is not so high (=3.497×10^{-3}s^{-1}). This is because

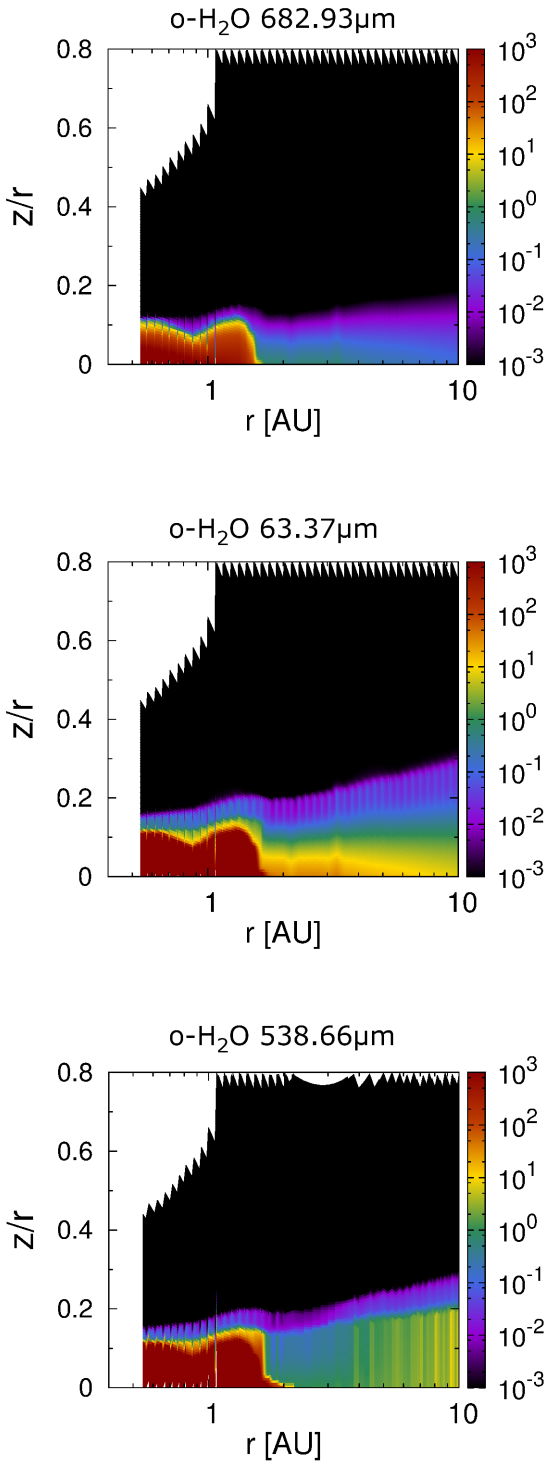

Figure 22. The line of sight optical depth $\tau_{ul}(s, x, y, \nu)$ distributions of three characteristic pure rotational ortho-$H_2{}^{16}O$ lines at λ=682.93μm (top), 63.37μm (middle), and 538.66μm (bottom). We assume that the inclination angle of the disk i is 0 degree in making these figures, and thus the direction of line-of-sight is from z=+∞ to -∞ at each disk radius.

this ortho-$H_2{}^{16}O$ 538.66μm line is the ground-state rotational transition and has low E_{up} (=61.0K) compared with the other lines. The flux of this line comes mainly from the outer cold water reservoir in the photodesorbed layer (see also Section 2.2.1). We propose that this line is not optimal to detect emission from the innermost water reservoir within the H_2O snowline for the same reasons explained in Section 2.2.4 for the 63.37μm line (see also the bottom right panel of Figure 19).

According to the bottom panels of Figure 21 and 22, the value of the emissivity at each (r, z) point in the photodesorbed layer is comparable to that of the optically thick region inside the H_2O snowline. The larger surface area of the outer disk, however, means that most disk-integrated emission arises from this region. In addition, the outer disk midplane opacity of this line is larger than that of the 682.93μm line, although the wavelength and thus the dust opacity is similar. This is because the abundance of cold water is relatively high, and because this line has low E_{up}.

We mention that previous space high dispersion spectroscopic observations with *Herschel*/HIFI detected the profiles of this line from disks around one Herbig Ae star (HD100546) and TW Hya (e.g., Hogerheijde et al. 2011; van Dishoeck et al. 2014). The number of detections is small since the line flux is low compared with the sensitivity of that instrument (Antonellini et al. 2015). The detected line profiles and other line modeling work (e.g., Meijerink et al. 2008; Woitke et al. 2009b; Antonellini et al. 2015; Du et al. 2015) suggested that the emitting region arises in the cold outer disk, consistent with the results of our model calculations. In addition, the total integrated line flux of TW Hya is observed to be $(1.7 \pm 1.1) \times 10^{-19}$ W m^{-2} (Hogerheijde et al. 2011; Du et al. 2015). Considering the difference in distance between TW Hya ($\sim$51pc, e.g., Zhang et al. 2013; Du et al. 2015) and our assumed value, 140 pc, the observed flux is within about a factor ≈ 2 of our estimated value (see also Table 3).

We note that previous observations suggested that the OPR of the emitting region is 0.77 for TW Hya (Hogerheijde et al. 2011) derived using the observed para-$H_2{}^{16}O$ ground state 1_{11}-0_{00} 269.47μm

line (A_{ul}=1.86×10^{-2} and E_{up}=53.4K) and the observed ortho-$H_2{}^{16}O$ ground state 538.66μm line. Since we define OPR as 3 (=the value in the high temperature region) throughout the disk (see also Section 2.1.5), we likely overestimate the line flux of the ortho-H_2O 538.66μm line. In addition, since the flux of this line is controlled by the outer cold H_2O gas which is desorbed from the cold dust-grain surfaces, it is necessary to include grain-surface reactions (e.g., Hasegawa et al. 1992) to calculate the H_2O gas and ice abundance to more accurately model this region.

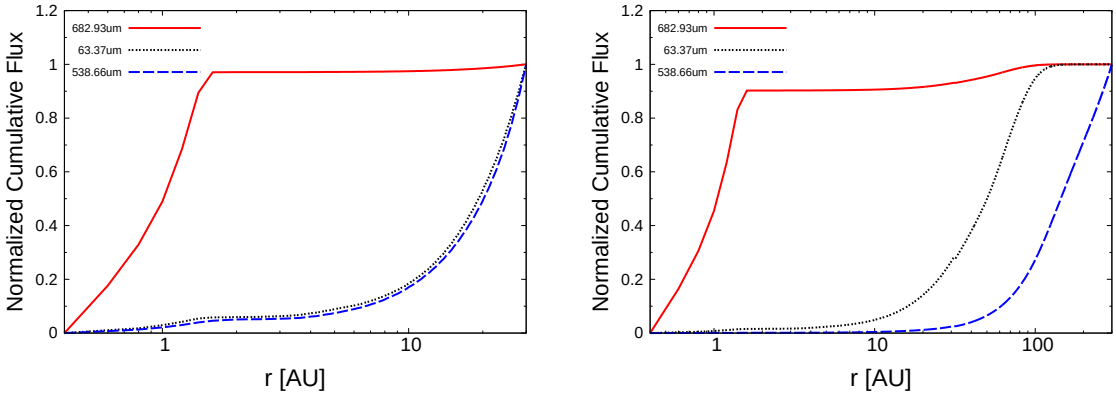

Figure 23. The radial distributions of the normalized cumulative flux for three pure rotational ortho-$H_2{}^{16}O$ lines at λ=682.93μm (*red solid line*), 63.37μm (*black dotted line*), and 538.66μm (*blue dashed line*). We normalized the cumulative flux of each line using the values at r = 30au (top panel) and at r = 300au (bottom panel). We assume that the inclination angle of the disk i is 0 degree in making these figures.

2.3. *Discussions*

2.3.1. *Influence of model assumptions*

Figure 23 shows the radial distributions of normalized cumulative fluxes for these three pure rotational ortho-$H_2{}^{16}O$ lines. We normalized the values of cumulative fluxes of these lines using the values at r = 30au (top panel) and at r = 300au (bottom panel). According to these panels, the 682.93μm line is emitted mostly from the region inside the H_2O snowline. In contrast, the 63.37μm line and the 538.66μm line are emitted mostly from the region outside the H_2O snowline. In addition, although the 63.37μm line is mainly emitted from the region between $r \sim 10 - 100$ au, the 538.66μm line is mainly emitted from a region much further out ($r \sim 50 - 300$ au). This is because the 682.93μm

line has a small A_{ul} and a relatively high E_{up}, and thus it mainly emits from the hot H_2O gas inside the H_2O snowline. In contrast, the 63.37μm line has a large A_{ul}, although E_{up} is similar to that of the 682.93μm line, and thus the flux density from the hot surface layer of the outer disk is strong (see also Section 2.2.4). Moreover, the flux density of the 538.66μm line from the outer cold water reservoir in the photodesorbed layer is strong, since this line is the ground-state rotational transition and has low E_{up} compared with the other lines (see also Section 2.2.5). These results suggest that the total fluxes of the 538.66μm line (and partly the 63.37μm line) will be influenced by the size of the disk which is included in the calculation of the line profiles, although the 682.93μm line does not have this problem because the line emitting region is sufficiently small.

Although we adopt a dust-grain size distribution with a maximum radius of $a_{\rm max}$ $\sim$10μm throughout the disk, dust grains are expected to grow in size due to settling and coagulation as the disk evolves and planet formation proceeds. Aikawa & Nomura (2006) calculated disk physical structures with various dust-grain size distributions. In addition, Vasyunin et al. (2011) and Akimkin et al. (2013) calculated the chemical structure of the outer disk ($\gtrsim$10 au) with grain evolution and discuss its features. They showed that the dust-grain settling and growth reduce the total dust-grain surface area and lead to higher UV irradiation rates in the upper disk. Therefore, the hot surface layer of the outer disk which contains abundant gas-phase molecules, including H_2O, gets wider and shifts closer to the disk midplane, thus the abundances and column densities of species are enhanced. However, they did not discuss the midplane structure of the inner disk including the position of the H_2O snowline, since they restricted their calculations to the outer disk ($\gtrsim$10 au). Here, we note that the position of the H_2O snowline in such an evolved disk is expected to be closer to the central star, since the total dust-grain surface area and thus dust opacity decreases as the size of dust grains becomes large, leading to a decrease in dust-grain and gas temperatures in the midplane of the inner disk (Oka et al. 2011). Moreover, Ros & Johansen (2013), Zhang et al. (2015), and Banzatti et al. (2015) discussed the effects of rapid dust-grain growth that leads to pebble-sized particles near the H_2O snowline.

As we explained in Section 2.1.1, the dominant dust heating source in the disk midplane of the inner disk is the radiative flux produced by viscous dissipation (α-disk model) which determines the dust and gas temperature of the region. Recent studies (e.g., Davis 2005; Garaud & Lin 2007; Min et al. 2011; Oka et al. 2011; Harsono et al. 2015; Piso et al. 2015) calculated the evolution of the position of the H_2O snowline in optically thick disks, and showed that it migrates as the disk evolves and as the mass accretion rate in the disk decreases, since the radiative flux produced by viscous dissipation becomes larger as the mass accretion rate increases. We suggest that younger protoplanetary disks like HL Tau (ALMA Partnership et al. 2015) are expected to have a larger mass accretion rate compared with that of our reference T Tauri disk model, and the position of the H_2O snowline will reside further out in the disk midplane. Zhang et al. (2015) argue that the center of the prominent innermost gap at 13 au is coincident with the expected midplane condensation front of water ice. Here we note that Banzatti et al. (2015) and Okuzumi et al. (2016) report the position of the H_2O snowline in HL Tau as $\lesssim$ 10 au. The difference occurs because the midplane radial temperature profile of Zhang et al. (2015) is larger than those of Banzatti et al. (2015) and Okuzumi et al. (2016).

As we described above, we adopt the wavelength integrated UV flux calculated at each point by Eqs. (1) and (2) to approximate the photoreaction rates $k^{\rm ph}(r,z)$ and photodesorption rate $k_i^{\rm pd}$. This UV flux is estimated by summing up the fluxes of three components: photospheric blackbody radiation, optically thin hydrogenic bremsstrahlung radiation, and strong Lyα line. Walsh et al. (2012) pointed out that using Eqs. (1) and (2), we may overestimate the strength of the UV field at wavelengths other than the Lyα ($\sim$ 1216Å). On the basis of their calculations, if we adopt the wavelength dependent UV flux to calculate photochemical reaction rates, the fractional abundance of H_2O vapor in the outer disk surface becomes larger because of the combination of increased gas phase production and decreased photodestruction. In contrast, the fractional abundance of H_2O vapor in the inner disk midplane is not expected to change, since the UV flux plays a minor role in determining physical and chemical structures around the H_2O snowline (see Figure 15). Walsh et al.

(2012) suggested that the column density of H_2O vapor in the outer disk can be enhanced by an order of magnitude depending on the method used to calculate the photodissociation rates.

In the remaining part of this subsection, we discuss the behavior of the H_2O lines for some cases in which we artificially change the distribution of H_2O vapor, the position of the H_2O snowline and the fractional abundance of H_2O gas in the outer disk surface, and test the validity of our model predictions. We explore different values of the H_2O snowline radius to simulate the effects of viscous heating and of different dust opacities due to dust evolution, and of the water abundance to simulate the effects of the strength of photo-reactions, as outlined above.

In Figure 24, we show the distributions of H_2O gas and profiles of the 682.93μm, 63.37μm, and 538.66 μm lines when we change the positions of the H_2O snowline ($r_{\rm snowline}$) to 1 au (top panels), 4 au (middle panels), 8 au (bottom panels) by hand. In the case of $r_{\rm snowline}$ =1 au, we change the fractional abundance of H_2O gas by hand to 10^{-12} in the regions of $r = 1 - 1.6$ au and $z/r \sim 0 - 1.5$. In the cases of $r_{\rm snowline}$ =4 au and 8 au, we change the fractional abundance to 5×10^{-5} in the regions of $r = 1.6 - 4$au and $z/r \sim 0 - 1.5$, and $r = 1.6 - 8$au and $z/r \sim 0 - 1.7$, respectively. In calculating these line profiles, we assume that the distance to the object d is 140pc ($\sim$ the distance of Taurus molecular cloud), and the inclination angle of the disk i is 30 deg. Here we note that the disk physical structure is the same as the original reference model (see Figure 15). As the position of the H_2O snowline moves outward, the flux of these three line from the inner disk becomes larger, that from the outer disk becomes weaker, and the line width, especially the width between the two peaks becomes narrower. In the case of the 682.93μm line, the emission flux inside the H_2O snowline is still larger than that outside the H_2O snowline, even when the H_2O snowline is artificially set at 1 au. In addition, the position of the H_2O snowline can be distinguished using the difference in the peak separations, although the sensitivity to its position will depend on the spectral resolution of the observations and the uncertainty of other parameters (e.g., inclination i). In the cases of the

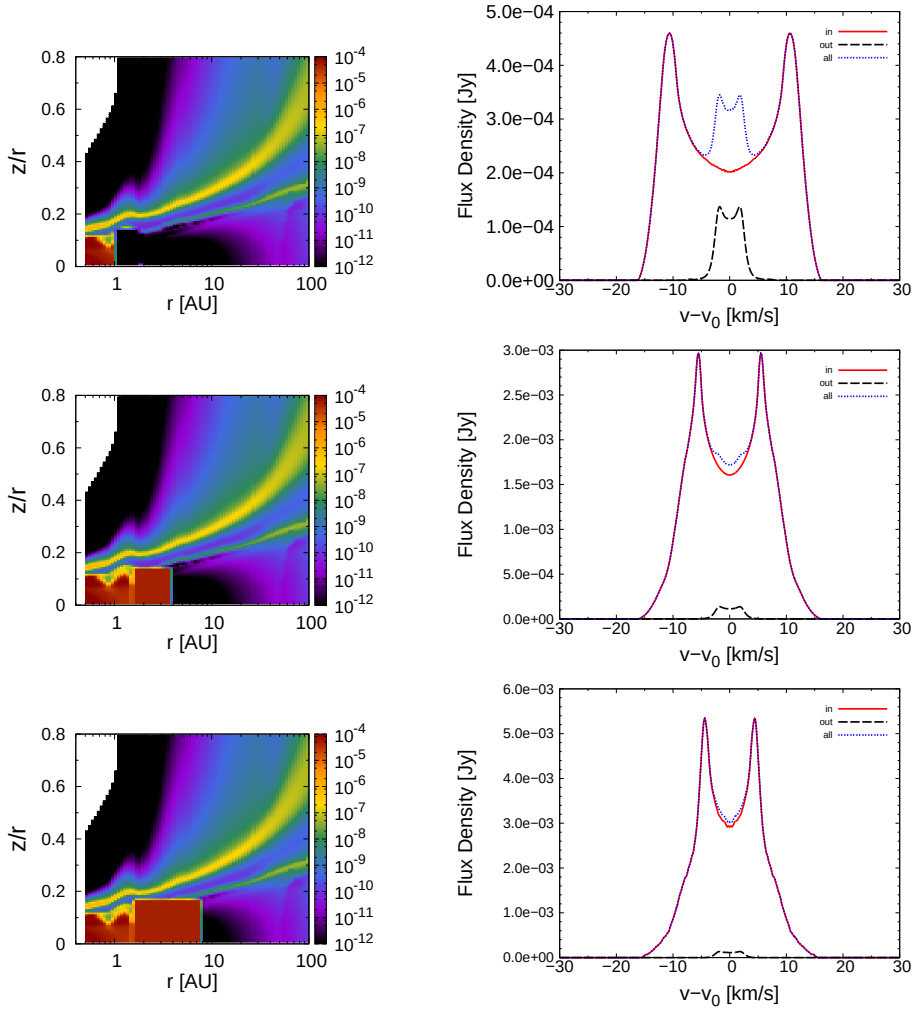

Figure 24. The left three panels: the fractional abundance (relative to total hydrogen nuclei density) distributions of H_2O gas of a disk around a T Tauri star as a function of disk radius and height (scaled by the radius, z/r) up to maximum radii of r =100au. We change the positions of the H_2O snowline to 1 au (top left), 4 au (middle left), 8 au (bottom left) by hand, in order to test the sensitivity for the position of the H_2O snowline. The right three panels: The velocity profiles of the pure rotational ortho-$H_2{}^{16}O$ lines at λ=682.93μm ($J_{K_aK_c}$=6_{43}-5_{50}). The three panels correspond to the cases that the H_2O snowline is assumed to be 1 au (top right) 4 au (middle right), 8 au (bottom right). *Red solid lines* are the emission line profiles from inside 1, 4, 8 au (∼inside the H_2O snowline), *black dashed lines* are those from 1-30, 4-30, 8−30 au (∼outside the H_2O snowline), and *blue dotted lines* are those from the total area inside 30 au, respectively. In calculating these profiles, we assume that the distance to the object d is 140pc (∼ the distance of Taurus molecular cloud), and the inclination angle of the disk i is 30 deg.

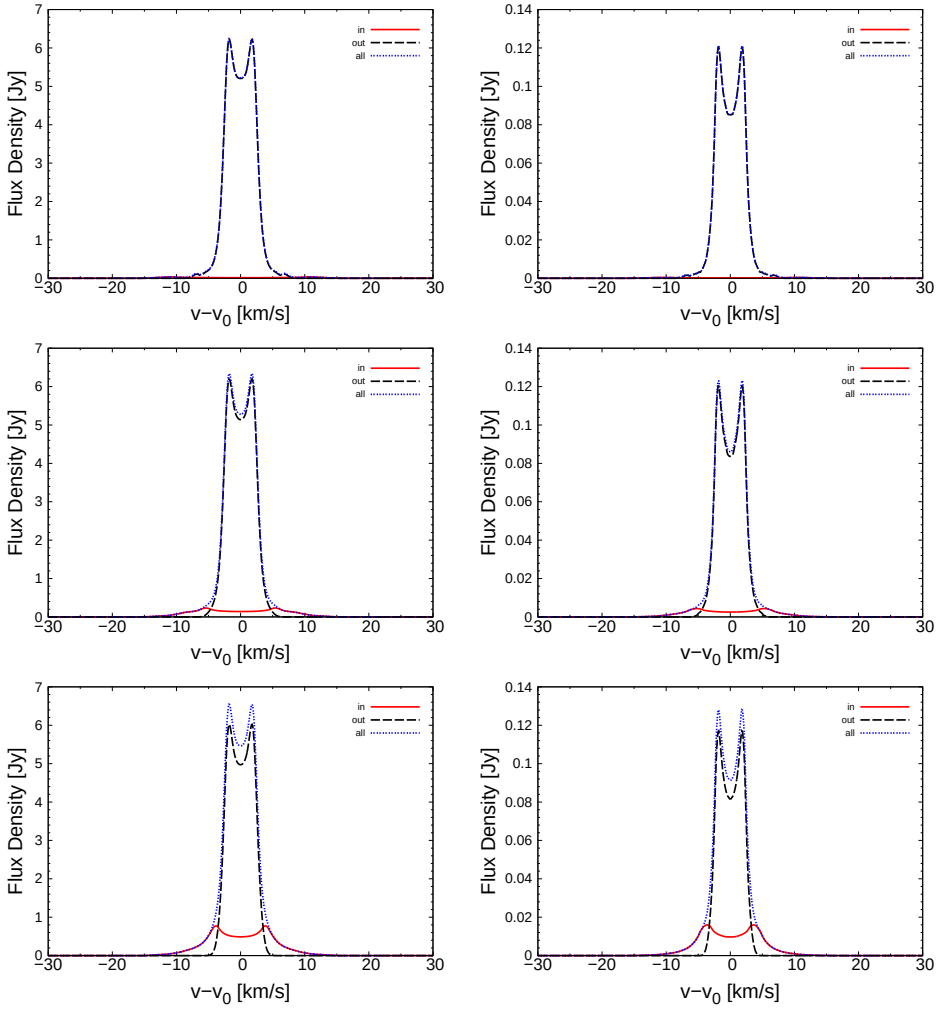

Figure 24. (Continued.) The left three panels: The velocity profiles of the pure rotational ortho-$H_2{}^{16}O$ lines at λ=63.37μm ($J_{K_aK_c}$=8_{18}-7_{07}). The right three panels: The velocity profiles of the pure rotational ortho-$H_2{}^{16}O$ lines at λ=538.66μm ($J_{K_aK_c}$=1_{10}-1_{01}). These panels correspond to the cases that the H_2O snowline is assumed to be 1 au (top left and right) 4 au (middle left and right), 8 au (bottom left and right).

63.37μm and 538.66 μm lines, the emission fluxes inside the H_2O snowline are still much smaller than that outside the H_2O snowline, even when the H_2O snowline is at 8 au. However, if we calculate the line fluxes using self-consistent physical models, the emission flux of the 63.37μm line inside the H_2O snowline is around ten times larger in the case of $r_{\rm snowline} = 8$ au, and its emission flux could be similar to that outside the H_2O snowline (see below).

We use the same disk physical structure as the original reference model, because calculating several different disk physical structures and chemical structures self-consistently using our method is computationally demanding and beyond the scope of this work. Even if we adopt self-consistent models, we expect that the line widths will not be affected; however, we do expect that the line fluxes will be affected since the temperature of line emitting regions will be different. In our original reference model, the gas and dust temperatures around the H_2O snowline are about 150−160K. In contrast, the temperatures of the line emitting regions around the H_2O snowline for the models with a snowline radius ($r_{\rm snowline}$) of 1 au, 4 au, and 8 au are 180−300K, 85−90K, and ∼65K, respectively. Therefore, estimation of blackbody intensities at λ ∼63−683μm suggests that the line peak flux densities could be ∼0.3−0.85 times lower for the model with $r_{\rm snowline}$ =1 au, and $\sim 2-4$ times and $\sim 2.5-10$ times higher for the models with $r_{\rm snowline}$=4 au and 8 au, respectively, if we calculate the line fluxes using self-consistent physical models. These differences in the peak flux densities are larger in the lines at shorter wavelengths.

In Figure 25, we show the distributions of H_2O gas and profiles of the 682.93μm, 63.37μm, and 538.66 μm lines when we change the fractional abundance of H_2O gas by hand in the hot disk surface of the outer disk to a larger value (10^{-5}, top panels), and to a smaller value (10^{-8}, bottom panels) compared to the original self-consistently calculated value (see also Figure 2), to test the sensitivity of the predictions to the disk surface abundance. If the fractional abundance of H_2O gas in the hot disk surface of the outer disk is larger, the flux of the 682.93μm line from the outer disk becomes larger. Here we note that since the peak velocities of the "in" and "out" components are different, we can separate both components with very high sensitivity and high dispersion spectroscopic observations, especially in the very high abundance case (top panels), although the wings of both components are blended. As the abundance in the hot surface of the outer disk becomes small, the fluxes of the 63.37μm and 538.66 μm lines from the outer disk become smaller. This effect is stronger in the case of the the 63.37μm line, since this line has a large Einstein A coefficient and high upper state energy compared to those of the 538.66μm line. However, the contributions of the fluxes of these two lines

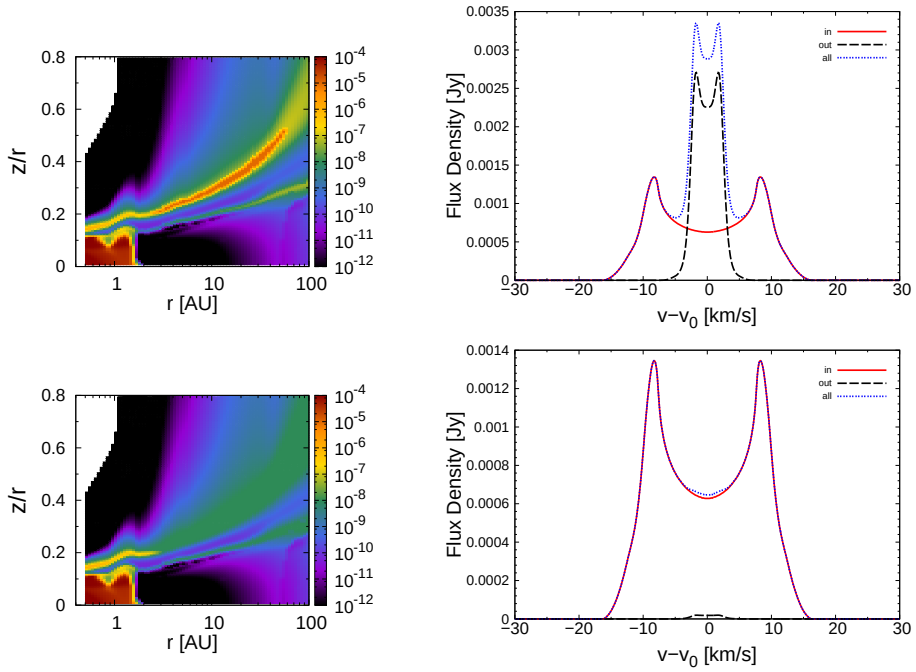

Figure 25. The left two panels: the fractional abundance (relative to total hydrogen nuclei density) distributions of H_2O gas of a disk around a T Tauri star as a function of disk radius and height (scaled by the radius, z/r) up to maximum radii of r =100au. We change the fractional abundance of H_2O gas in the hot disk surface of the outer disk to a larger value (10^{-5}, top left), and to a smaller value (10^{-8}, bottom left) compared with the original self-consistently calculated value (see also Figure 2). The right two panels: The velocity profiles of the pure rotational ortho-$H_2{}^{16}O$ lines at λ=682.93μm ($J_{K_aK_c}$=6_{43}-5_{50}). The two panels correspond to the case of the larger value (10^{-5}, top right), and to the case of the smaller value (10^{-8}, bottom right). *Red solid lines* are the emission line profiles from inside 2 au (∼inside the H_2O snowline), *black dashed lines* are those from 2−30 au (∼outside the H_2O snowline), and *blue dotted lines* are those from the total area inside 30 au, respectively. In calculating these profiles, we assume that the distance to the object d is 140pc (∼ the distance of Taurus molecular cloud), and the inclination angle of the disk i is 30 deg.

from the outer disk are still larger than that from the inner disk even when the abundance in the hot surface of the outer disk is small.

2.3.2. *Critical density and the assumption of LTE*

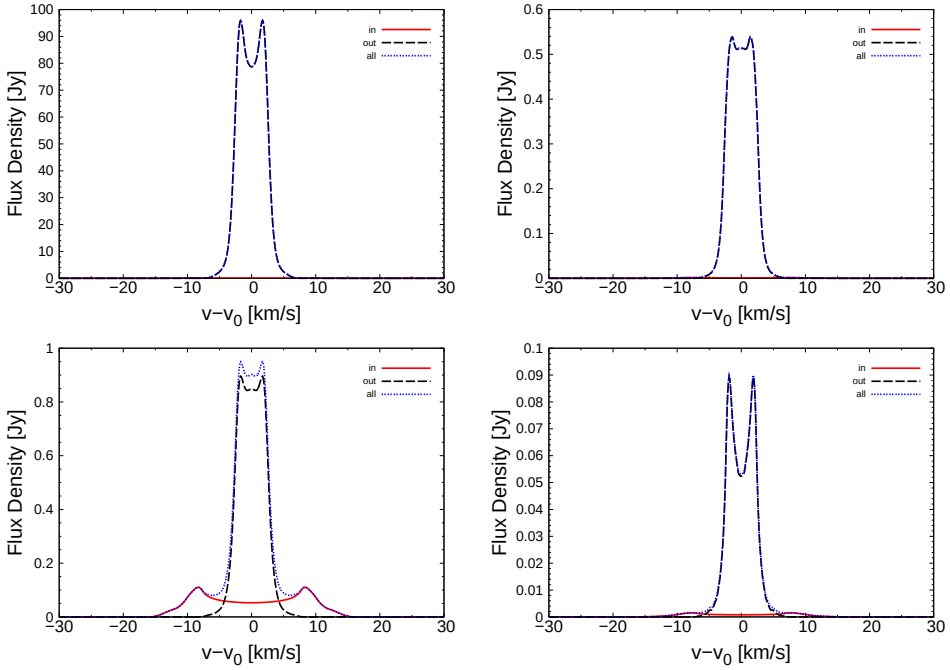

Figure 25. (Continued.) The left two panels: The velocity profiles of the pure rotational ortho-$H_2{}^{16}O$ lines at λ=63.37μm ($J_{K_aK_c}$=8_{18}-7_{07}). The right two panels: The velocity profiles of the pure rotational ortho-$H_2{}^{16}O$ lines at λ=538.66μm ($J_{K_aK_c}$=1_{10}-1_{01}). These panels correspond to the case of the larger value (10^{-5}, top left and right), and to the case of the smaller value (10^{-8}, bottom left and right).

As described in section 2.3, the level populations of the water molecule (n_u and n_l) are calculated under the assumption of local thermal equilibrium (LTE). In this subsection, we discuss the validity of the assumption of LTE within our work.

We calculate the critical density $n_{\rm cr} = A_{ul} < \sigma v >^{-1}$ of the three characteristic lines discussed here (ortho-H_2O 682.93, 63.37, 538.66μm lines, see Table 3). $< \sigma v >$ is the collisional rates for the excitation of H_2O by H_2 and electrons for a an adopted collisional temperature of 200K from Faure & Josselin (2008). The critical density $n_{\rm cr}$ of these three lines are 1.0×10^6, 1.5×10^{10}, 2.9×10^7 cm^{-3}, respectively. LTE is only realized when collisions dominate the molecular excitation/deexcitation, that is, when the total gas density is larger than $n_{\rm cr}$. In contrast, non-LTE allows for the fact that the levels may be sub-thermally excited, when $n_{\rm cr}$ is higher than the total

gas density, or when the emission (deexcitation) dominates collisions, as well as when the levels are super-thermally excited when the radiative excitation dominates the collisions. When a level is sub-thermally populated in a particular region of the disk, it has a smaller population than in LTE, thus the line flux in non-LTE is smaller than that for LTE (e.g., Meijerink et al. 2009; Woitke et al. 2009b). According to Meijerink et al. (2009), lines with small A_{ul} ($<10^{-2}$ s^{-1}) and low E_{up} ($<$2000K at $r = 1$au) are close to LTE, since collisions dominate the radiative excitation/deexcitation in those lines.

As described in Section 2.1.1 (see also Figure 15), the total gas density decreases as a function of disk radius and disk height. We found that the densest region of the disk is in the hot disk midplane inside the H_2O snowline ($\sim 10^{12} - 10^{14}$ cm^{-3}), where $n_{\rm cr}$ of the three characteristic lines are much smaller than the total gas density. In contrast, the total gas density in the hot surface layer of the outer disk is $\sim 10^7 - 10^8$ cm^{-3}, and that in the photodesorbed layer of water molecules is $\sim 10^8 - 10^{10}$ cm^{-3}. Therefore in these regions, the critical densities of the 63.37 and 538.66μm lines are similar to and larger than the values of the total gas density, while that of the 682.93μm line is smaller. In Section 2.2.2, we showed that the emission flux of the 682.93μm line which traces the H_2O snowline mainly comes from the hot disk midplane inside the H_2O snowline. Since the value of $n_{\rm cr}$ for this line is much smaller than the total gas density in the line emitting region, it is valid to use the LTE for this region.

On the other hand, in our LTE calculations it remains possible that we have overestimated the emission flux of strong H_2O lines with large A_{ul} which trace the hot surface layer of the outer disk (e.g., the 63.37 μm line) and lines which trace cold water vapor in the photodesorbed layer (e.g., the 538.66 μm line). Previous works which model such water lines (e.g., Meijerink et al. 2009; Woitke et al. 2009b; Banzatti et al. 2012; Antonellini et al. 2015) showed that non-LTE calculations are important for these lines. They suggest that non-LTE effects may, however, alter line fluxes by factors of only a few for moderate excitation lines. Moreover, current non-LTE calculations are likely to be

inaccurate, due to the incompleteness and uncertainty of collisional rates (e.g., Meijerink et al. 2009; Banzatti et al. 2012; Kamp et al. 2013; Zhang et al. 2013; Antonellini et al. 2015).

2.3.3. *Requirement for the observations*

Since the velocity width between the emission peaks is ∼20 km s^{-1}, high dispersion spectroscopic observations (R=$\lambda/\delta\lambda$> tens of thousands) of the identified $H_2{}^{16}O$ lines are needed to trace emission from the hot water reservoir within the H_2O snowline. Their profiles potentially contain information which can be used to determine the H_2O snowline position. Moreover, the lines that are suitable to trace emission from the hot water gas within the H_2O snowline (e.g., 682.93μm) tend to have a much smaller A_{ul} than those detected by previous observations (e.g, 63.37μm, 538.66μm). Since the area of the emitting regions are small (radii < 2 au for a T Tauri disk) compared with the total disk size, the total flux of each line is very small (3.12×10^{-22} W m^{-2} for the 682.93μm line). In addition, the sensitivity and spectral resolution (of some instruments) used for previous mid-infrared, far-infrared, and sub-millimeter observations (e.g., *Spitzer*/IRS, *Herschel*/PACS, *Herschel*/HIFI) were not sufficient to detect and resolve weak lines.

Among the various H_2O lines in ALMA Band 8, the ortho-$H_2{}^{16}O$ 682.93μm line is the most suitable to trace emission from the hot water reservoir within the H_2O snowline. Several suitable sub-millimeter H_2O lines exist in ALMA Bands 7, 9, and 10 ($\sim 300-1000$ μm), some of which have the same order-of-magnitude fluxes compared with that of the 682.93μm line. With ALMA, we can now conduct high sensitivity ($\sim 10^{-21}-10^{-20}$ W m^{-2} (5σ, 1 hour)), high dispersion (R> 100,000), and even high spatial resolution (< 100 mas) spectroscopic observations. Since the total fluxes of the candidate sub-millimeter lines to trace emission from the hot water reservoir within the H_2O snowline are small in T Tauri disks, they are challenging to detect with current ALMA sensitivity. However, in hotter Herbig Ae disks and in younger T Tauri disks (e.g., HL Tau), the H_2O snowline exists at a larger radius and the flux of these lines will be stronger compared with those in our fiducial T Tauri disk (∼1.6 au). Thus the possibility of a successful detection is expected to increase in these sources and could be achieved with current ALMA capabilities.

In addition, suitable lines for detection exist over a wide wavelength range, from mid-infrared (Q band) to sub-millimeter, and there are future mid-infrared instruments including the Q band which will enable high sensitivity and high-dispersion spectroscopic observations: Mid-Infrared Camera High-disperser & IFU spectrograph on the Thirty Meter Telescope (TMT/MICHI, e.g., Packham et al. 2012), and HRS of SPICA[5] Mid-Infrared Instrument (SPICA/SMI). Moreover, since SPICA/SMI has an especially high sensitivity, successful detection is expected even for a T Tauri disk with several hours of observation. In the next section (paper II, Notsu et al. 2017), we will discuss in detail the difference in flux between T Tauri and Herbig Ae disks in lines ranging from the mid-infrared to sub-millimeter wavelengths, and their possible detection with future instruments (e.g., ALMA, TMT/MICHI, SPICA/SMI-HRS).

2.4. *Conclusion*

In this section, we identify candidate H_2O lines to trace emission from the hot water reservoir within the H_2O snowline through high-dispersion spectroscopic observations in the near future. First, we calculated the chemical composition of a protoplanetary disk using a self-consistent physical model of a T Tauri disk, and investigated the abundance distributions of H_2O gas and ice. We found that the abundance of H_2O is high ($\sim 10^{-4}$) in the hot inner region within the H_2O snowline ($\sim$1.6 au) near the equatorial plane, and relatively high $\sim 10^{-7}$ in the hot surface layer of the outer disk, compared to its value in the regions outside the H_2O snowline near the equatorial plane ($\sim 10^{-12}$).

Second, we calculated the velocity profiles of H_2O emission lines, and showed that lines (e.g., the ortho-H_2O 682.93μm line) with small Einstein A coefficients ($A_{ul} \sim 10^{-3} - 10^{-6}$ s^{-1}) and relatively high upper state energies (E_{up} $\sim$1000K) are dominated by emission from the disk region inside the H_2O snowline, and therefore their profiles potentially contain information which can be used to determine the H_2O snowline position. This is because the water gas column density of the region inside

[5] http://www.ir.isas.jaxa.jp/SPICA/SPICA_HP/research-en.html

the H_2O snowline is sufficiently high that all lines emitting from this region are optically thick as long as $A_{ul} > 10^{-6}$ s^{-1}. Instead, the region outside the H_2O snowline has a lower water gas column density and lines with larger Einstein A coefficients have a more significant contribution to their fluxes since the lines are expected to be optically thin there. Therefore, we argue that the H_2O lines with small Einstein A coefficients and relatively high upper state energies are the most suitable to trace emission from the hot water reservoir within the H_2O snowline in disks through high-dispersion spectroscopic observations in the near future. The wavelengths of those lines suitable to trace emission from the hot water reservoir within the H_2O snowline range from mid-infrared (Q band) to sub-millimeter, and they overlap with the capabilities of ALMA and future mid-infrared high dispersion spectrographs (e.g., TMT/MICHI, SPICA/SMI-HRS).

In addition, we calculate the behavior of water lines which have been detected by previous spectroscopic observations (e.g., the ortho-H_2O 63.37μm line, the ortho-H_2O 538.66μm line). The fluxes calculated for these lines are consistent with those of previous observations and models. These lines are less suited to trace emission from water vapor within the H_2O snowline because they are mainly emitted from the region outside the snowline.

In the next section (paper II, Notsu et al. 2017), we will discuss the differences of fluxes in the suitable lines ranging from mid-infrared (Q band) to sub-millimeter, and the possibility of future observations (e.g., ALMA, TMT/MICHI, SPICA) to locate the position of the H_2O snowline.

3. MODELING STUDIES II. THE CASE OF THE HERBIG AE STAR (NOTSU ET AL. 2017)

3.1. *Methods*

The physical structures of the protoplanetary disk models used here are calculated using the methods in Nomura & Millar (2005) including X-ray heating (Nomura et al. 2007). A more detailed description of the background theory and computation of this physical model is described in the original papers (Nomura & Millar 2005; Nomura et al. 2007) and Section 2 of this thesis (see also paper I, Notsu et al. 2016). Walsh et al. (2010, 2012, 2014a, 2015), Heinzeller et al. (2011), Furuya et al. (2013), Notsu et al. (2015), and Notsu et al. (2016) used the same physical models for a T Tauri disk and a Herbig Ae disk to study various chemical and physical effects, and they also describe the calculation of the physical structures in detail.

In Section 2 of this thesis (see also paper I, Notsu et al. 2016), we adopted the physical model of a steady, axisymmetric Keplerian disk surrounding a T Tauri star with mass M_*=0.5$M_\odot$, radius R_*=2.0$R_\odot$, and effective temperature T_*=4000K (Kenyon & Hartmann 1995). In this section (paper II, Notsu et al. 2017), we adopt the physical model of a disk surrounding a Herbig Ae star with M_*=2.5$M_\odot$, R_*=2.0$R_\odot$, and T_*=10,000K (see also Walsh et al. 2015). In our disk physical models, we adopt a viscous parameter α=10^{-2}, a mass accretion rate $\dot{M}$=$10^{-8}M_\odot$ yr^{-1}, and gas-to-dust mass ratio g/d = 100. The values of total disk mass are $M_{\rm disk} \sim 2.4 \times 10^{-2} M_\odot$ for the T Tauri disk (Heinzeller et al. 2011), and $M_{\rm disk} \sim 2.5 \times 10^{-2} M_\odot$ for the Herbig Ae disk. We adopt the same compact and spherical dust-grain model of Nomura & Millar (2005). They assume that dust and gas are well mixed, and that the dust grains consist of silicate grains, carbonaceous grains, and water ices. They adopt the dust-grain size distribution which is consistent with the extinction curve observed in dense clouds (Mathis et al. 1977; Weingartner & Draine 2001). The stellar UV radiation field in our Herbig Ae disk model has no excess emission components (e.g., optically thin hydrogenic bremsstrahlung radiation and Lyman-α line emission), although that in our T Tauri disk model has such excess emission components (for more detail, see Nomura & Millar 2005, Walsh et al. 2015 and Notsu et al. 2016). In Figure 26, we display the gas number density in cm^{-3} (top left),

the gas temperature in K (top right, T_g), the dust-grain temperature in K (bottom left, T_d), and the wavelength-integrated UV flux in erg cm^{-2} s^{-1} (bottom right) of a Herbig Ae disk as a function of disk radius in au and height (scaled by the radius, z/r).

Here we focus on the differences between the physical structures of the T Tauri disk (see also Figure 15) and the Herbig Ae disk. The density in the atmosphere of the Herbig Ae disk (e.g., $n_{\rm H} = 6 \times 10^{10}$ cm^{-3} at $r = 5$ au and $z/r = 0.1$) is lower than that of the T Tauri disk (e.g., $n_{\rm H} = 2 \times 10^{11}$ cm^{-3} at $r = 5$ au and $z/r = 0.1$), because the scale height[6] H of the Herbig Ae disk (e.g., $H/r \sim 1.2$ at $r = 5$ au) is smaller than that for the disks around the T Tauri disk (e.g., $H/r \sim 1.7$ at $r = 5$ au). The gas density and temperature distributions of the disks are obtained self-consistently by iteratively solving the equations for hydrostatic equilibrium in the vertical direction and local thermal balance between heating and cooling of gas (Nomura & Millar 2005). The gas and dust temperatures throughout most of the Herbig Ae disk, and the strength of the UV flux in the disk surface of the Herbig Ae disk are higher compared with those of the T Tauri disk, although the stellar UV radiation field in our Herbig Ae disk model has no excess emission components, apart from that in our T Tauri disk model. This is because the photospheric blackbody radiative flux from the central Herbig Ae star is larger than that from the central T Tauri star. The strength of the X-ray flux in the disk surface of the Herbig Ae disk is lower compared with that of the T Tauri disk, since we adopted a smaller value of X-ray luminosity in the Herbig Ae disk ($L_{\rm X} \sim 3 \times 10^{29}$ erg s^{-1}) compared with that in the T Tauri disk ($L_{\rm X} \sim 10^{30}$ erg s^{-1}).

To investigate the chemical structure of the Herbig Ae disk, we use a large chemical network which includes gas-phase reactions and gas-grain interactions (freeze-out of gas molecules on dust grains, and thermal and non-thermal desorption from dust grains). The initial elemental fractional abundances (relative to total hydrogen nuclei density) we use are the set of atomic oxygen-rich low-metallicity

[6] $H = c_s/\Omega \propto M_*^{-0.5} T_g^{0.5}$, where c_s and Ω are the sound speed and Keplerian angular velocity, respectively.

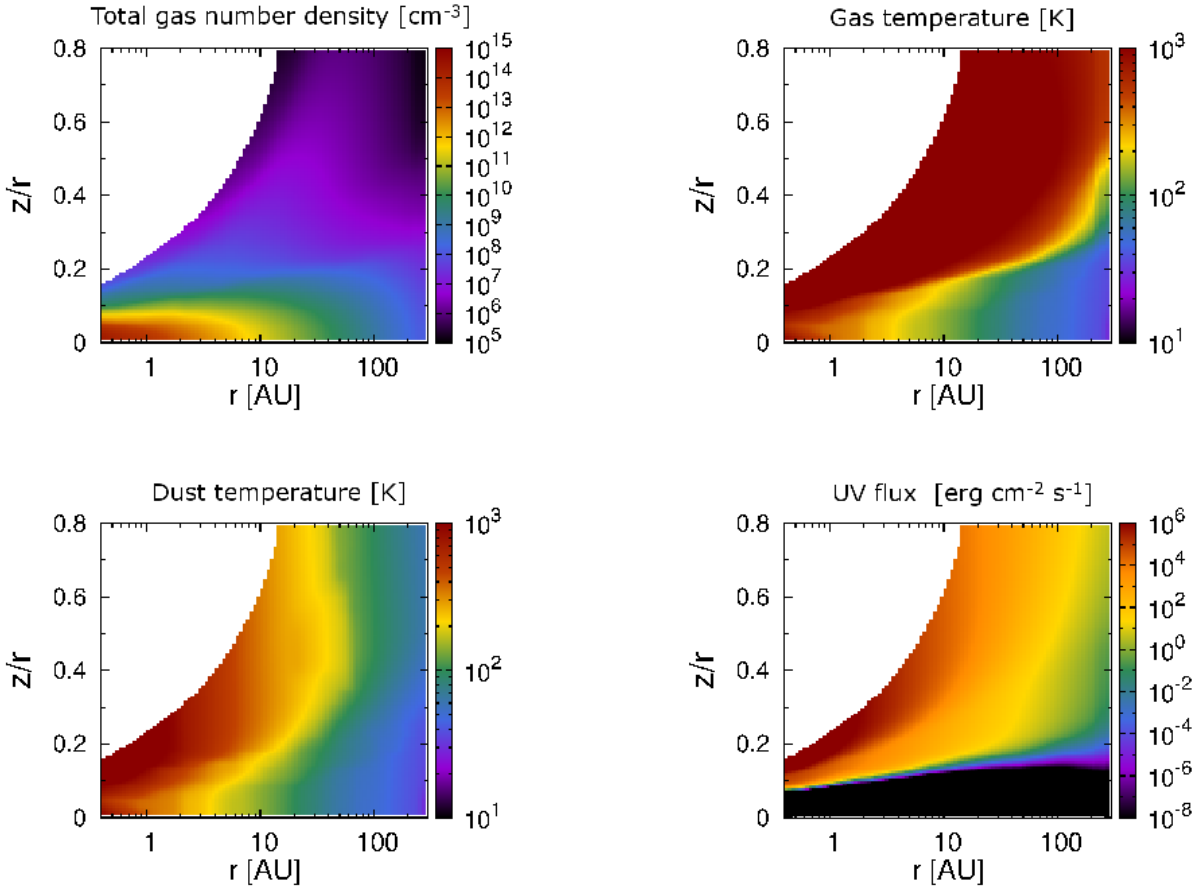

Figure 26. The total gas number density in cm^{-3} (top left), the gas temperature in Kelvin (top right), the dust temperature in Kelvin (bottom left), and the UV flux in erg cm^{-2} s^{-1} (bottom right) of a Herbig Ae disk as a function of the disk radius in au and height (scaled by the radius, z/r) up to maximum radius of r =300 au.

abundances from Graedel et al. (1982), listed in Table 8 of Woodall et al. (2007), which is the same set as used in Section 2 of this thesis (see Table 1). We adopt the same chemical network as described in Section 2 of this thesis (see also paper I, Notsu et al. 2016). Henning & Semenov (2013), Dutrey et al. (2014), and Haworth et al. (2016) reviewed the recent development of calculations for chemical structure in protoplanetary disks.

Using the H_2O gas abundance distribution obtained from our chemical calculation described in the

previous paragraph, we calculate the ortho-$H_2{}^{16}O$ emission line profiles ranging from near-infrared to sub-millimeter wavelengths from the Herbig Ae disk assuming Keplerian rotation, and identify the lines which are the best candidates for probing emission from the inner thermally desorbed water reservoir, i.e., within the H_2O snowline. We also study how the line fluxes and profile shapes depend on the position of the H_2O snowline. In Section 2 of this thesis (see also paper I, Notsu et al. 2016), we adopted the same calculation method to determine the water emission line profiles from a T Tauri disk (based on Rybicki & Lightman 1986, Hogerheijde & van der Tak 2000, Nomura & Millar 2005, and Schöier et al. 2005) The code which we have built for calculating emission line profiles is a modification of the original 1D code called RATRAN[7] (Hogerheijde & van der Tak 2000). We adopt the data of line parameters in the Leiden Atomic and Molecular Database LAMDA[8] (Schöier et al. 2005). Here we note that in our method, we adopt the assumption of local thermal equilibrium (LTE) to obtain the level populations of the water molecule (n_u and n_l). In Section 3.3.2, we discuss the validity of this assumption. In addition, we set the ortho to para ratio (OPR) of water to its high-temperature value of 3 throughout the disk (Hama & Watanabe 2013; Hama et al. 2016).

3.2. *Results*

3.2.1. *The distributions of* H_2O *gas and ice*

Figure 27 shows the fractional abundances (relative to total gas hydrogen nuclei density, n_H) of H_2O gas and ice in a Herbig Ae disk as a function of disk radius r and height scaled by the radius (z/r). Here we focus on the differences in H_2O distributions between the cases of a Herbig Ae disk (see also paper II, Notsu et al. 2017) and a T Tauri disk (see also paper I, Notsu et al. 2016).

The H_2O snowline of the Herbig Ae disk exists at a radius of $r \sim 14$ au in the midplane ($T_g \sim T_d \sim 120$K), which is significantly larger than that for the T Tauri disk model ($r \sim 1.6$ au, see

[7] http://home.strw.leidenuniv.nl/~michiel/ratran/
[8] http://home.strw.leidenuniv.nl/~moldata/

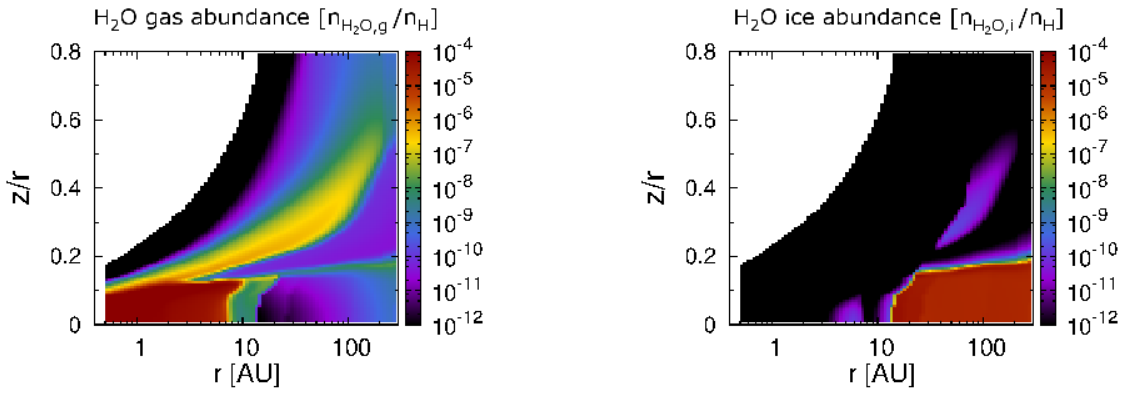

Figure 27. The fractional abundance (relative to total hydrogen nuclei density) distributions of H_2O gas (top) and H_2O ice (bottom) of a Herbig Ae disk as a function of disk radius and height (scaled by the radius, z/r) up to maximum radius of r =300au.

Figure 15 of this thesis). This is because the gas and dust temperatures, which are coupled in the midplane of the Herbig Ae disk, are higher than that of our T Tauri disk. Inside the H_2O snowline, the temperature exceeds the sublimation temperature under the pressure conditions in the midplane of the Herbig Ae disk ($T_g \sim T_d \sim 120$K), and most of the H_2O is released into the gas-phase by thermal desorption. Here we note that the sublimation temperature under the pressure conditions in the midplane of the Herbig Ae disk ($T_g \sim T_d \sim 120$K) is lower than that in the midplane of the T Tauri disk ($T_g \sim T_d \sim 150 - 160$K). The region in the midplane of the Herbig Ae disk where the temperature is around 100−200K is at a larger radius compared with that in the midplane of T Tauri disk, and the gas number density of such a region in the midplane of the Herbig Ae disk is lower ($n_{\rm H} \sim 10^{11} - 10^{12}$ cm^{-3}) versus ($n_{\rm H} \sim 10^{12} - 10^{13}$ cm^{-3}). According to Eq. (3)-(5) in Section 2 of this thesis, the sublimation temperature is higher if the gas number density is also higher.

The temperature of the region just inside the H_2O snowline in the Herbig Ae disk (between $7 - 8$ au and 14 au) is $T_g \sim 120 - 170$K; hence the gas-phase chemistry to form H_2O molecules (e.g., $O+H_2 \rightarrow OH+H$ and $OH+H_2 \rightarrow H_2O+H$) is not efficient compared with the inner region at a higher temperature ($T_g > 170$K, $r < 7 - 8$au). We point out that the radial temperature profile in the

midplane of the T Tauri disk is steeper than that in the midplane of the Herbig Ae disk, and this is another reason why the T Tauri disk does not have such a region with a relatively large fractional abundance of H_2O gas ($\sim 10^{-8}$). A similar distribution of gas-phase H_2O in the midplane of a Herbig Ae disk is reported in Figure 1 of Woitke et al. (2009b). Here we also note that Eistrup et al. (2016) calculated the chemical evolution of a disk midplane under both molecular and atomic initial conditions as initial chemical abundances. They showed that in the latter atomic conditions, the abundance of H_2O gas and ice around the H_2O snowline ($\sim 10^{-6}$) is smaller than that for molecular initial abundances ($\sim 10^{-4}$). This is because O_2 is formed in the gas-phase via O+OH→O_2+H and remains in the gas phase since its sublimation temperature is much lower than that of other molecules like H_2O. This reaction route competes with gas-phase H_2O formation.

In the outer disk, the fractional abundance of H_2O gas is also relatively high ($\sim 10^{-8} - 10^{-7}$) in the hot surface layer and at the H_2O sublimation (photodesorption) front compared with the cold midplane region of the outer disk ($\lesssim 10^{-12} - 10^{-10}$), as also shown in the T Tauri disk model.

Here we note that the region with a high H_2O gas abundance ($\sim 10^{-4}$) in the disk midplane extends to a larger radius ($r \sim$10 au) at $z/r \gtrsim 0.1$ than at $z/r \sim 0$ ($r \sim 7 - 8$ au). This is not seen in the T Tauri disk case (see Figure 2 of paper I, Notsu et al. 2016). This is because the scale height of the Herbig Ae disk (e.g., $H/r \sim 1.2$ at $r = 5$ au) is smaller than that for the T Tauri disk (e.g., $H/r \sim 1.7$ at $r = 5$ au) and the radiation from the central Herbig Ae star is stronger than that from the central T Tauri star, thus the gas temperature of the Herbig Ae disk around $z/r \sim 0.1$ is higher. In contrast, for the T Tauri disk case, since the disk scale height is larger than that of Herbig Ae disk, the values of gas temperature of the disk between $z/r \sim 0 - 0.1$ is constant.

The left panel of Figure 28 shows the radial column density profiles of H_2O gas and ice for both the T Tauri disk and the Herbig Ae disk. In the Herbig Ae disk case, the column density of H_2O gas and ice in the disk midplane flips across the H_2O snowline as expected ($r \sim 14$ au). The column density

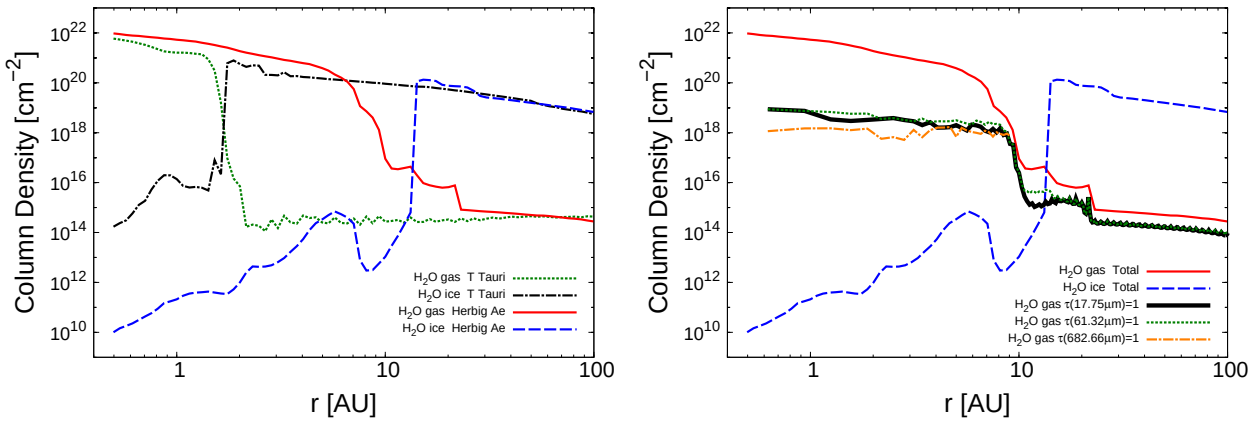

Figure 28. Left panel: The radial profiles of the vertically integrated column density in cm^{-2} of H_2O gas and ice in the T Tauri disk (*green dotted line* and *black dashed dotted line*) and the Herbig Ae disk (*red solid line* and *blue dashed line*). Right panel: The radial profiles of the column density in cm^{-2} of H_2O ice (*blue dashed line*) and gas in the Herbig Ae disk, which are vertically integrated from $z = \infty$ to $-\infty$ (*red solid line*), to $z(\tau_{17.75\mu m} = 1)$ (*black bold solid line*), to $z(\tau_{61.32\mu m} = 1)$ (*green dotted line*), and to $z(\tau_{682.66\mu m} = 1)$ (*orange dashed dotted line*). Since $\tau_{682.66\mu m}$ at $z = -\infty$ is lower than unity at $r \gtrsim 10$ au, the radial profile of this case is plotted only $r \lesssim 10$ au.

of H_2O gas is high ($\sim 10^{20} - 10^{22}$ cm^{-2}) in the inner high-temperature region of the disk midplane with $r < 7 - 8$ au, relatively high ($\sim 10^{16} - 10^{19}$ cm^{-2}) in the midplane between $7 - 8$ au and 14 au, and in contrast, low outside the H_2O snowline ($< 10^{16}$ cm^{-2}). The column density profile of H_2O ice is roughly opposite. In the T Tauri disk case, the column densities of H_2O gas and ice in the disk midplane flips across the H_2O snowline more steeply following the steeper temperature gradient. The right panel of Figure 28 shows the radial profiles of the column density in cm^{-2} of H_2O ice and gas in the Herbig Ae disk, which have been vertically integrated from $z = \infty$ to (i) $-\infty$, (ii) $z(\tau_{17.75\mu m} = 1)$, (iii) $z(\tau_{61.32\mu m} = 1)$, and (iv) $z(\tau_{682.66\mu m} = 1)$. τ_λ is the total optical depth value at each wavelength, λ, including gas and dust components. In Section 3.3.3, we discuss about this panel in detail.

Previous analytical models and numerical simulations derived the position of the H_2O snowline of

an optically thick disk for given parameters, such as mass (M_*) and temperature (T_*) of the central star, a viscous parameter α, an accretion rate $\dot{M}$, a gas-to-dust mass ratio g/d, and the average dust grain size a and opacity (e.g., Davis 2005; Garaud & Lin 2007; Min et al. 2011; Oka et al. 2011; Du & Bergin 2014; Harsono et al. 2015; Mulders et al. 2015; Piso et al. 2015; Sato et al. 2016), and suggested that the position of the H_2O snowline changes, as these parameters change. In the case of Herbig Ae disks with $M_* \sim 2.5 M_\odot$, $\dot{M} \sim 10^{-8} M_\odot$ yr^{-1}, $g/d = 100$, and $a \sim 0.1 \mu$m, the position of the H_2O snowline is $\sim 10 - 20$ au. In our calculations we use similar parameters for M_*, $\dot{M}$ and a, and the H_2O snowline appears at a radius of around 14 au in the midplane, within the range of previous studies.

3.2.2. *The overview of ortho-$H_2{}^{16}O$ emission lines from a Herbig Ae disk*

In this Section, we first describe the detailed properties of seven characteristic pure rotational ortho-$H_2{}^{16}O$ lines (see Table 4) for the Herbig Ae disk. These seven lines (including the ortho-$H_2{}^{16}O$ 682.66 μm line) are candidates for tracing emission from the hot water reservoir within the H_2O snowline. In Section 3.2.2, we describe the properties of the 63.32 and 538.29μm lines, which are examples of lines which are less suited to trace emission from the water reservoir within the H_2O snowline. We consider these two lines to test the validity of our model calculations, since the fluxes of these two lines from protoplanetary disks have been observed with *Herschel*. The properties of near-, and mid-infrared water emission lines which do not trace emission from the hot water vapor within the H_2O snowline are also described in this subsection. Since we investigated the profiles and properties of three lines (λ=682.66, 63.32, 538.29μm) for the T Tauri disk in paper I (Notsu et al. 2016), here we mainly focus on the differences between the line properties between the T Tauri disk and the Herbig Ae disk. In Sections 3.2.3 and 3.2.5, we show and discuss other candidate lines which trace the emission from the hot water vapor within the H_2O snowline from mid-infrared to sub-millimeter wavelengths, and their properties, especially the variation in line fluxes with wavelength. In Section 3.2.6, we show and discuss normalized radial cumulative line fluxes for the lines discussed in Sections 3.2.1-3.2.3.

In this work, we show and discuss only the results concerning ortho-$H_2{}^{16}O$ lines, since the number densities and the fluxes of ortho-$H_2{}^{16}O$ lines are larger than those of para-$H_2{}^{16}O$ and other water isotope lines, due to the assumption, OPR=3 (see also Section 4, Notsu et al. 2018). The line selection process is described in detail in Section 2.1.5 of this thesis.

3.2.3. *The case of candidate ortho-$H_2{}^{16}O$ emission lines*

Figure 29 shows the emission profiles of seven representative characteristic pure rotational ortho-$H_2{}^{16}O$ lines at λ=17.75μm (top left), 24.00μm (top center), 61.32μm (top right), 94.17μm (middle left), 482.99μm (middle center), 682.66μm (middle right), and 933.28μm (bottom), for the Herbig Ae disk. These lines have small values of A_{ul} ($\sim 10^{-3} - 10^{-6}$ s^{-1}) and relatively large values of upper E_{up} ($\sim 700 - 1900$K). They are representative candidate ortho-H_2O lines which trace emission from the hot water gas within the H_2O snowline. The ortho-$H_2{}^{16}O$ 933.28μm, 682.66μm, and 482.99μm lines fall in ALMA Bands 7, 8, and 9, respectively. The ortho-$H_2{}^{16}O$ 17.75μm line and 24.00μm line are Q band lines at mid-infrared wavelengths, and the ortho-$H_2{}^{16}O$ 17.75μm line falls in the wavelength coverage of SPICA/SMI-HRS (see Section 3.3.4). The detailed parameters, such as transitions ($J_{K_aK_c}$), wavelength λ, frequency, A_{ul}, E_{up}, critical density $n_{\rm cr} = A_{ul}/<\sigma v>$[9], and total line fluxes are listed in Table 4. In Table 4, we also show the values of the total fluxes from both the Herbig Ae disk and the T Tauri disk (see also paper I, Notsu et al. 2016). In calculating the values from the T Tauri disk, we use the same method as in Section 2 (see also paper I, Notsu et al. 2016). In calculating all line profiles in this work (see Figures 29, 33, 36, and 37), we assume that the distance d to the object is 140pc ($\sim$ the distance of Taurus molecular cloud), and the inclination angle i of the disk is 30 degs.

[9] $<\sigma v>$ is the collisional rates for the excitation of H_2O by H_2 and electrons for an adopted collisional temperature of 200K from Faure & Josselin (2008).

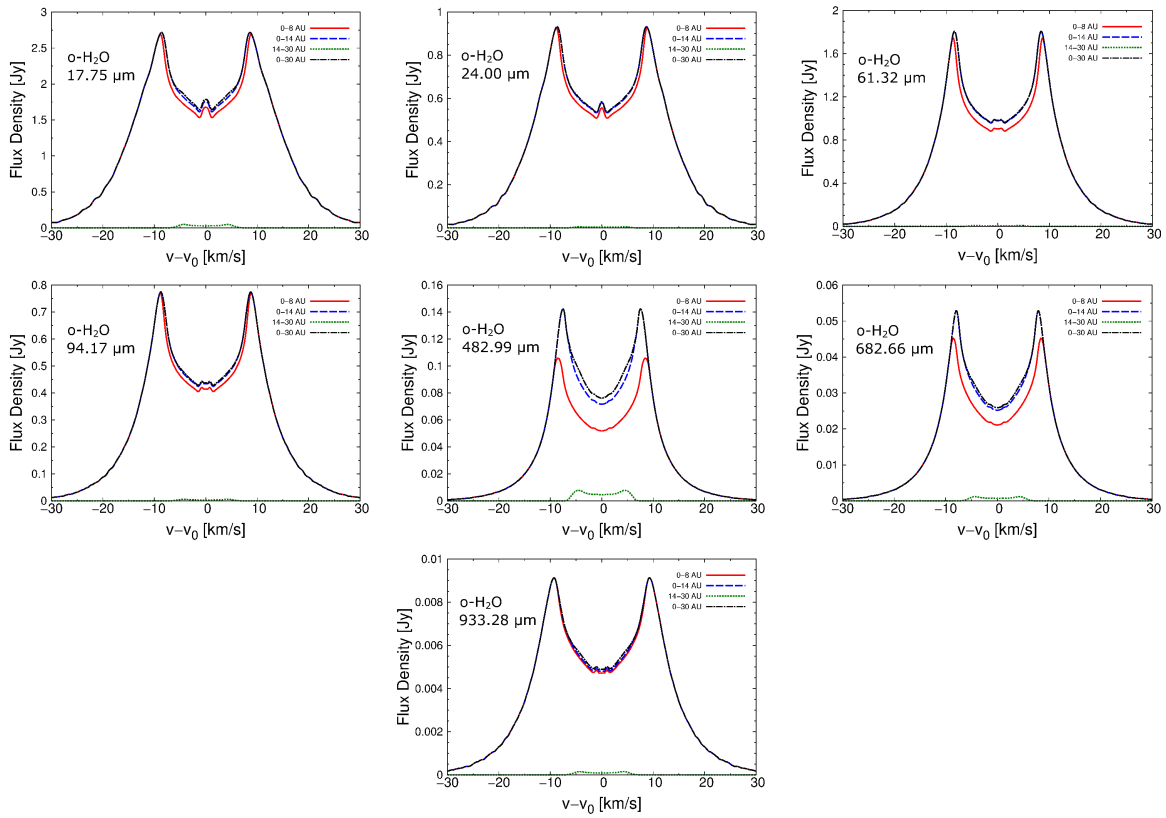

Figure 29. The velocity profiles of seven characteristic pure rotational ortho-$H_2{}^{16}O$ lines at λ=17.75μm (top left), 24.00μm (top center), 61.32μm (top right), 94.17μm (middle left), 482.99μm (middle center), 682.66μm (middle right), and 933.28μm (bottom), which have small A_{ul} and large E_{up}, from the Herbig Ae disk. These are candidate H_2O lines to trace the hot water vapor within the H_2O snowline. In calculating the line profiles in this work (see Figures 29, 33, 36, and 37), we assume that the distance to the object d is 140pc ($\sim$ the distance of Taurus molecular cloud), and the inclination angle of the disk, i, is 30 degree. The parameters and total fluxes of these lines are listed in Tables 4 and 5. *Red solid lines* are the emission line profiles from inside 8 au (=the inner high temperature region), *blue dashed lines* are those from inside 14 au ($\sim$inside the H_2O snowline), *green dotted lines* are those from 14−30 au ($\sim$outside the H_2O snowline), and *black dashed dotted lines* are those from the total area inside 30 au.

As shown in all panels in Figure 29, the contributions from the optically thin surface layer of the outer disk (r =14−30 au) are very small compared with those from the optically thick region near the midplane of the inner disk (r <14 au), and they show the characteristic double-peaked profile due to Keplerian rotation. This is because these lines, which have small Einstein A coefficients ($A_{ul} \sim 10^{-3} - 10^{-6}$ s^{-1}) and relatively large upper state energies (E_{up} $\sim$1000K), mainly trace the

Table 4. Calculated representative ortho-$H_2{}^{16}O$ line parameters and total line fluxes

$J_{K_aK_c}$	λ[1]	Freq.	A_{ul}	E_{up}	$n_{\rm cr}$	HAe flux[2,3]	TT flux[3,4]
	[μm]	[GHz]	[s^{-1}]	[K]	[cm^{-3}]	[W m^{-2}]	[W m^{-2}]
6_{52}-5_{05}	17.754	16885.840	2.909×10^{-3}	1278.5	8.3×10^{10}	4.1×10^{-17}	2.3×10^{-20}
5_{50}-5_{05}	23.996	12493.205	2.696×10^{-4}	1067.7	1.9×10^{9}	9.4×10^{-18}	6.4×10^{-21}
5_{41}-6_{16}	61.316	4889.280	2.686×10^{-4}	878.1	4.1×10^{8}	5.9×10^{-18}	3.5×10^{-20}
6_{52}-7_{25}	94.172	3183.464	3.387×10^{-4}	1278.5	3.1×10^{8}	1.8×10^{-18}	1.6×10^{-20}
5_{32}-4_{41}	482.990	620.701	1.106×10^{-4}	732.1	3.3×10^{6}	5.3×10^{-20}	1.1×10^{-21}
6_{43}-5_{50}	682.664	439.151	2.816×10^{-5}	1088.7	1.0×10^{6}	1.4×10^{-20}	3.1×10^{-22}
10_{29}-9_{36}	933.277	321.226	6.165×10^{-6}	1861.2	4.7×10^{6}	2.3×10^{-21}	7.8×10^{-23}
8_{18}-7_{07}	63.324	4734.296	1.772	1070.6	1.5×10^{10}	1.1×10^{-16}	5.7×10^{-18}
1_{10}-1_{01}	538.289	556.936	3.497×10^{-3}	61.0	2.9×10^{7}	7.2×10^{-20}	1.1×10^{-20}
17_{413}-16_{314}	12.396	24184.126	7.728	5780.8	1.1×10^{11}	6.7×10^{-17}	5.3×10^{-19}
13_{76}-12_{49}	12.453	24073.032	1.053	4212.6	1.1×10^{13}	6.9×10^{-17}	2.5×10^{-19}
7_{61}-6_{52}	4.958	60463.186	3.260	4180.4	1.6×10^{13}	2.2×10^{-16}	1.1×10^{-18}
7_{61}-6_{34}	4.432	67646.817	2.080×10^{-4}	4180.4	6.5×10^{11}	5.0×10^{-20}	8.1×10^{-23}

[a] In calculating the value of line wavelength from the value of line frequency, we use the value of speed of light c=2.99792458 $\times$ 10^8 m s^{-1}.

[b] The total flux of each emission line from the Herbig Ae disk.

[c] In calculating the total fluxes of these H_2O lines, we use a distance of d = 140pc and an inclination angle of i =30 degree.

[d] The total flux of each emission line from the T Tauri disk (see also paper I, Notsu et al. 2016).

hot H_2O vapor inside the H_2O snowline. In Sections 2.1.5 and 2.2.3 of this thesis (see also paper I, Notsu et al. 2016), we explained the reason why these lines have such properties.

In the cases of candidate ortho-$H_2{}^{16}O$ lines except the 482.99μm and 682.66μm lines (see Figure 29), almost all of the emission fluxes ($> 95\%$) come from the region with a high H_2O gas abundance ($\sim 10^{-4}$, r <8 au), and the position of the two peaks and the rapid drop in flux density between the peaks contains information on the position of the outer edge of this region. In contrast, in the cases of the 482.99μm and 682.66μm lines (see Figure 29), most of the emission fluxes ($\sim 80-90\%$) are emitted from the region with a high H_2O gas abundance ($\sim 10^{-4}$, r <8 au), and some fluxes ($\sim 10-20\%$) are emitted from the region with a relatively high H_2O gas abundance ($\sim 10^{-8}$, r =8-14 au). The position of the two peaks and the rapid drop in flux density between the peaks contains information on the distribution of hot H_2O gas within the H_2O snowline.

Figures 30 and 31 show the line-of-sight emissivity (emissivity times extinction, $\eta_{ul}e^{-\tau_{ul}}$; see Equation (16)) and the total optical depth, τ_{ul} (gas emission and dust) distributions of these seven ortho-$H_2{}^{16}O$ lines, respectively. We assume that the inclination angle, i, of the disk is 0 deg in making these figures (see Figures 30, 31, 34, 35, and 32), and thus the line-of-sight direction is from $z = +\infty$ to $-\infty$ at each disk radius. In the left panels of Figure 30, we overplot the total optical depth contours (τ_{ul} =0.1, 1, and 10) on top of these line emissivity panels (see also Figure 31). In the right panels, we overplot the gas temperature T_g contours (T_g =120, 170, and 300K, see also Figure 26). Figure 32 in shows the vertical distributions of the normalized cumulative line emissivity at r =5 au (top two panels), r =10 au (middle two panels), and r =30 au (bottom two panels), and of the gas temperature T_g. The left three panels show the distributions for these seven lines. We normalize the cumulative emissivity of each line using the values at $z = -\infty$. According to Figures 30, 31, and 32, the values of emissivity at $r \lesssim 14$ au (= the position of the H_2O snowline), $T_g \gtrsim$120K, and $z/r \sim 0.05-0.12$ are larger than those of the optically thin hot surface layer and the photodesorbed layer of the outer disk, and in particular those in the region with a higher H_2O gas abundance ($\sim 10^{-4}$, $r < 7-8$ au, and $T_g \gtrsim$170K) and $z/r \sim 0.05-0.12$ are much larger. Emission from $z \sim 0$ at $r \lesssim 7$ au is not possible to detect, because the optical depth of the inner disk midplane is high due to absorption by dust grains and excited H_2O molecules in the upper disk layer. Nevertheless,

we can extract information on the distribution of hot H_2O vapor inside the H_2O snowline. This is because within r <14 au (= the position of the H_2O snowline), the H_2O gas fractional abundance is relatively constant over $z/r \sim$ 0-0.1 for the same disk radius r (see also Figure 27). Strictly speaking, as we described in Section 3.2.1, the region with a high H_2O gas abundance ($\sim 10^{-4}$) extends to a radius of r ~10 au at $z/r \sim 0.1$ compared with that at $z \sim 0$ (r ~7-8 au), and is reflected in the emissivity distribution. However, since the radial shift in the distribution is small (a few au), its influence is not so serious for obtaining information on the general trend of the H_2O distribution in the inner disk within the H_2O snowline.

The differences in the properties of the line profiles (see Figures 29, 30, 31, and 32) come from the differences in A_{ul}, E_{up}, and wavelengths among lines. For the lines with similar wavelengths, the values of optical depth tend to be larger as values of A_{ul} of the lines become larger, since the absorption by excited H_2O molecules increases. In addition, the values of optical depth become larger as values of E_{up} become smaller, since the line absorption become stronger even in the colder region of the disk.

For the lines at shorter wavelengths, the opacity of the dust grains becomes larger (e.g., Nomura & Millar 2005). In the cases of shorter wavelength (mid- and far-infrared) lines, the absorption by the dust grains mainly determines total optical depth profiles (including gas and dust components) and line emitting regions in the both inner and outer disk. In contrast, for the lines with longer wavelengths, the values of the line absorption by excited molecules become larger (see also Equation (12)) even if the values of A_{ul} and E_{up} are similar. In the case of longer wavelength lines (sub-millimeter lines), the line absorption by excited molecules mainly determines the total optical depth profiles and line emitting regions in the inner disk midplane with a high H_2O gas abundance ($\sim 10^{-4}$, $r < 7 - 8$ au), although the absorption by dust grains mainly determines those in the disk surface and outer colder disk midplane.

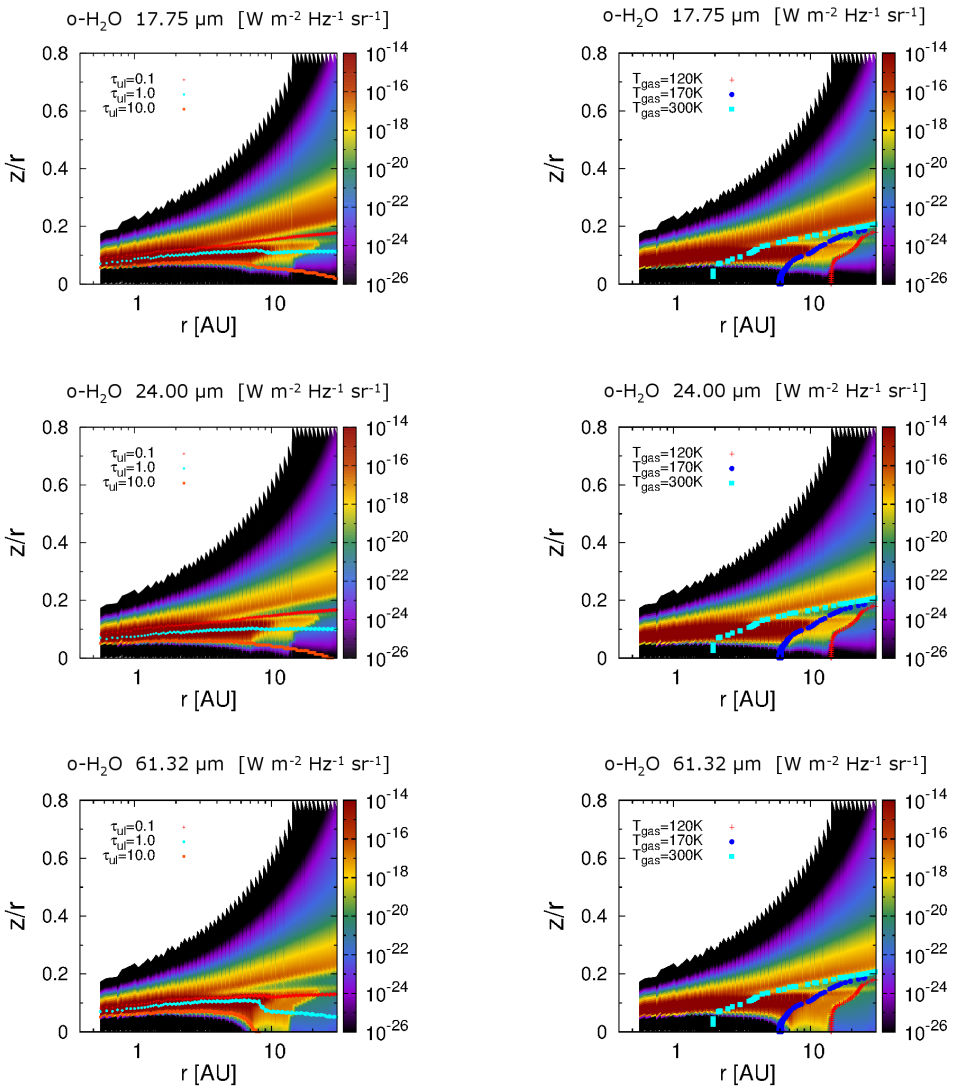

Figure 30. The line-of-sight emissivity distributions of the ortho-$H_2{}^{16}O$ lines at λ=17.75μm (top left and right), 24.00μm (middle left and right), 61.32μm (bottom left and right), which have small A_{ul} and large E_{up}, from the Herbig Ae disk. In the left panels, we overplot the total optical depth contours $\left(\tau_{ul}\right.$ =0.1 (red cross points), 1 (cyan circle points), and 10 (orange square points)$\left.\right)$ on top of these line emissivity panels (see also Figure 31). In the right panels, we overplot the gas temperature T_g contours $\left(T_g\right.$ =120K (red cross points), 170K (blue circle points), and 300K (cyan square points), see also Figure 26$\left.\right)$. We assume that the inclination angle, i, of the disk is 0 deg in making these figures in this work (see Figures 30, and 34), and the emissivity is calculated along the line from z=+∞ to -∞ at each disk radius. The units are W m^{-2} Hz^{-1} sr^{-1}.

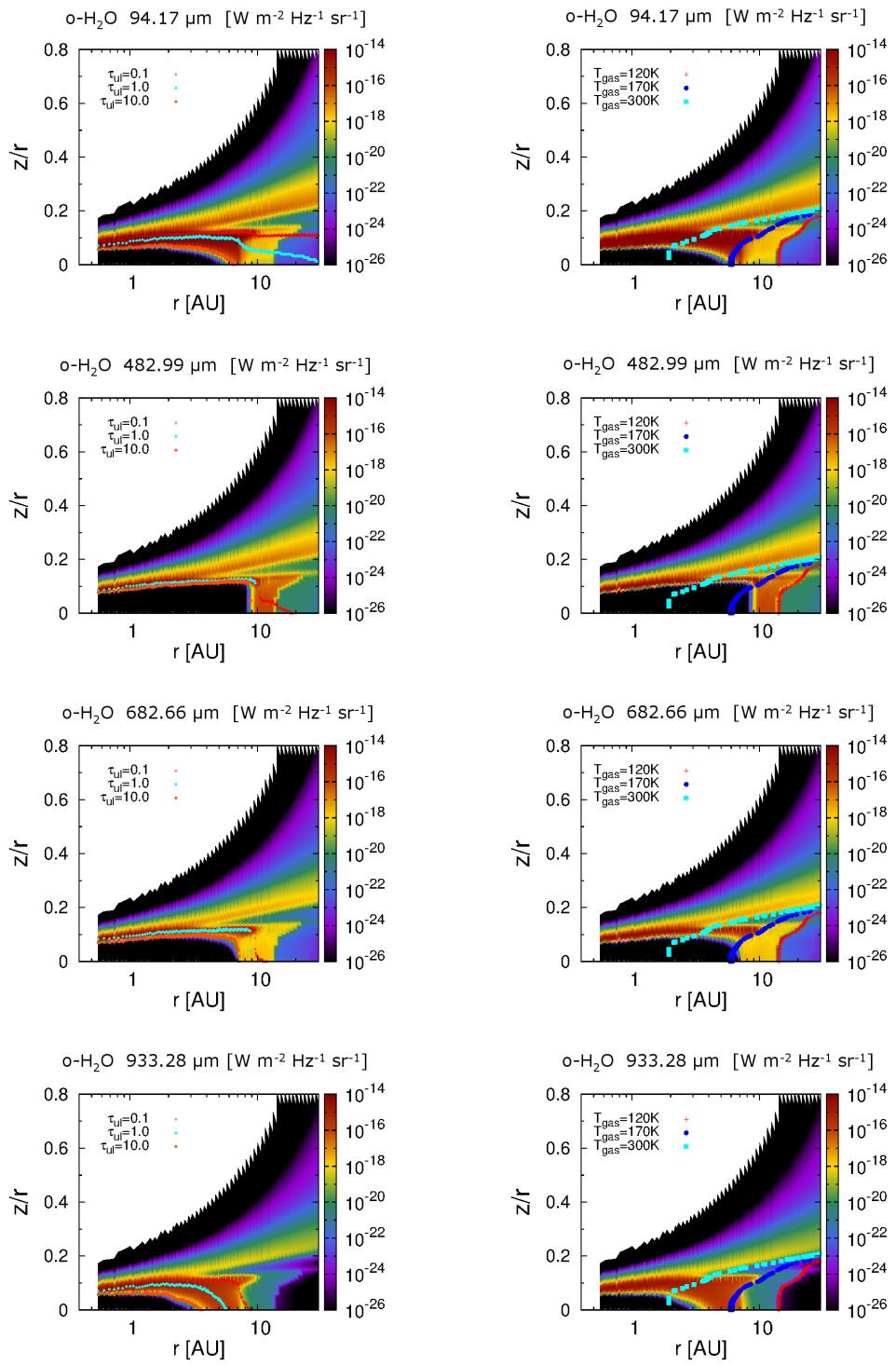

Figure 30. (Continued.) The line-of-sight emissivity distributions of the ortho-$H_2{}^{16}O$ lines at λ=94.17μm (top left and right), 482.99μm (second line left and right), 682.66μm (third line left and right), and 933.28μm (bottom left and right), which have small A_{ul} and large E_{up}, from the Herbig Ae disk.

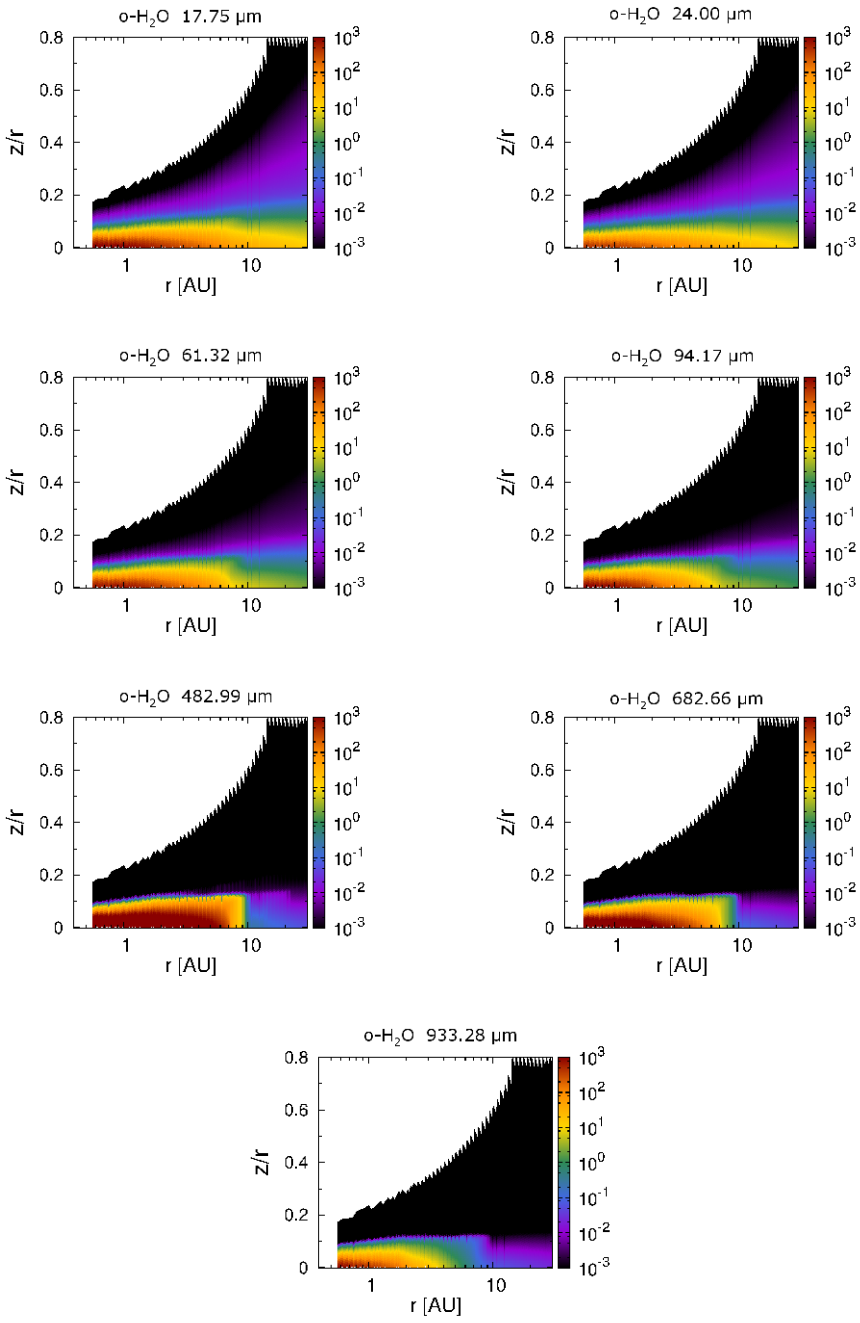

Figure 31. The line-of-sight total optical depth $\tau_{ul}(s, x, y, \nu)$ (gas emission and dust) distributions of the ortho-$H_2{}^{16}O$ lines at λ=17.75μm (top left), 24.00μm (top center), 61.32μm (top right), 94.17μm (middle left), 482.99μm (middle center), 682.66μm (middle right), and 933.28μm (bottom), which have small A_{ul} and large E_{up}, from the Herbig Ae disk. We assume that the inclination angle, i, of the disk is 0 deg in making these figures in this work (see Figure 31 and 35), and thus the optical depth is calculated along the line from z=+∞ to -∞ at each disk radius. In calculating the values of $\tau_{ul}(s, x, y, \nu)$, we consider the contributions of both absorption by dust grains and the line absorption by the H_2O gas.

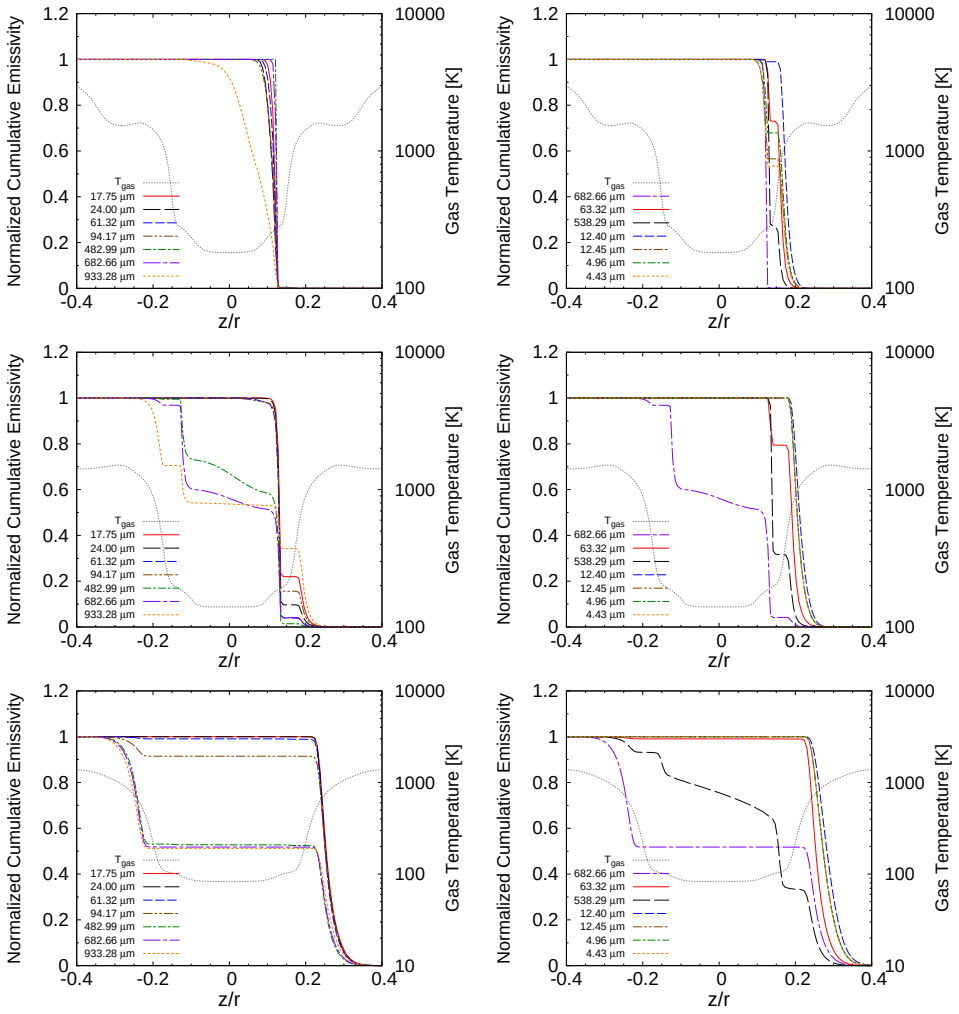

Figure 32. The vertical distributions of the normalized cumulative line emissivity at r =5 au (top two panels), r =10 au (middle two panels), and r =30 au (bottom two panels), and of the gas temperature T_g at Kelvin (*gray dotted line*). The left three panels show the distributions for seven pure rotational ortho-$H_2{}^{16}O$ lines at λ=17.75μm (*red solid line*), 24.00μm (*black long dashed line*), 61.32μm (*blue dashed line*), 94.17μm (*brown dashed two dotted line*), 482.99μm (*green dashed dotted line*), 682.66μm (*violet long dashed dotted line*), and 933.28μm (*orange dotted line*. The right three panels show the distributions for seven pure rotational ortho-$H_2{}^{16}O$ lines at λ=682.66μm (*violet long dashed dotted line*), 63.32μm (*red solid line*), 538.29μm (*black long dashed line*), 12.40μm (*blue dashed line*), 12.45μm (*brown dashed two dotted line*), 4.96μm (*green dashed dotted line*), and 4.43μm (*orange dotted line*). We normalized the cumulative emissivity of each line using the values at $z = -\infty$. We assume that the inclination angle of the disk i is 0 degree in making these figures.

The ortho-$H_2{}^{16}O$ 482.99μm and 682.66μm lines have relatively smaller values of E_{up} (<1100K), and thus they can also trace outer colder region compared to lines with larger values of E_{up}. In addition, they have longer wavelengths (> 400μm) compared with other lines, thus the dust opacity is smaller and they can trace the regions closer to the midplane in the outer disk. These are the reasons why emission fluxes from the region with a relatively high H_2O gas abundance ($\sim 10^{-8}$, r =8-14 au) are not so small ($\sim 10-20\%$ of total emission fluxes) compared to the region with a high H_2O gas abundance ($\sim 10^{-4}$, r <8 au). Although the ortho-$H_2{}^{16}O$ 933.28 μm line resides in the sub-millimeter region, this line has a larger E_{up}(=1861.2K) than other lines, and thus most of the emission flux is emitted from the region with high temperature and a high H_2O gas abundance ($\sim 10^{-4}$, r <8 au).

Since the radial difference of the positions between the exact H_2O snowline location and the outer edge of the hot H_2O gas region is not so large (several au), the influence is not so serious when we want to get information on the overall H_2O distribution of the inner disk and roughly estimate the position of the H_2O snowline. However, if we observe several candidate ortho-$H_2{}^{16}O$ lines with small A_{ul} ($\sim 10^{-6}-10^{-3}$), various E_{up} (e.g., $\sim 700-2100$K), and at various wavelengths between mid-infrared and sub-millimeter, there is the possibility to confine the detailed distribution, not only the position of the H_2O snowline, but also the H_2O gas abundance and the gas temperature in the disk midplane. In addition, we could trace the water reservoir within the H_2O snowline from the Keplerian line profiles independently regardless of the assumption of the relation between disk gas temperature and radius, as adopted in previous works to get the H_2O distributions (e.g., Zhang et al. 2013; Blevins et al. 2016). We note that the previous observations of water lines with large A_{ul} ($\sim 10^{-1}-10^{0}$ s^{-1}) and very high E_{up} (>3000K) in many cases mainly trace the emission from the disk surface (e.g., Salyk et al. 2008; Pontoppidan et al. 2010a,b; Fedele et al. 2011; Mandell et al. 2012; van Dishoeck et al. 2014; Banzatti et al. 2017; Blevins et al. 2016, see also Section 3.2.4).

3.2.4. *The case of the less suited ortho-$H_2{}^{16}O$ emission lines*

In the top left panel of Figure 33, we show the line profile for the ortho-$H_2{}^{16}O$ 63.32μm line. The contribution from the optically thin surface layer of the outer disk (r =14−30 au) is large (three times larger in flux density) compared with that of the optically thick region near the midplane of inner disk (r <14 au), and the shape of the line profile is a narrower by around a factor of two compared to those of candidate H_2O lines which trace the emission from the hot water vapor within the H_2O snowline. This is because the H_2O 63.32μm line has a large A_{ul} (=1.772 s^{-1}), although E_{up} (=1070.6K) is similar to that of the candidate ortho-$H_2{}^{16}O$ lines (e.g., E_{up} =1088.7K for the 682.66μm line). The detailed parameters, such as transitions ($J_{K_aK_c}$), wavelength, frequency, A_{ul}, E_{up}, critical density $n_{\rm cr}$, and total line fluxes of the ortho-$H_2{}^{16}O$ lines discussed in this subsection are listed in Table 4.

According to Figures 32, 34, and 35, the values of emissivity of the ortho-$H_2{}^{16}O$ 63.32μm line in the optically thin hot surface layer of outer disk are as strong as that of the optically thick region inside the H_2O snowline. The area of the outer H_2O line emitting region is larger than that of the inner region for this line, and thus emission from the outer part dominates. Therefore, we propose that this line is not optimal to detect emission from the hot water vapor within the H_2O snowline in Herbig Ae disk case, as we also found for the T Tauri disk (Notsu et al. 2016).

We note that previous space far-infrared low-dispersion spectroscopic observations with *Herschel*/PACS (R ∼1500) detected some far-infrared H_2O emission lines with large A_{ul} ($\sim 10^{-1} - 10^{0}$ s^{-1}) and relatively large E_{up} ($\sim$ 1000K) including this 63.32μm line from the gas-rich Herbig Ae disk around HD163296, although the detections of these lines are only slightly above 3σ (e.g., Fedele et al. 2012, 2013; Meeus et al. 2012; Tilling et al. 2012; Dent et al. 2013). Although the profiles of these lines are spectrally unresolved, a comparison of line strength with models indicates that the emitting region of these observations originates in the hot surface layer of the outer disk (r>15 au, e.g., Fedele et al. 2012, 2013). The total integrated line flux of this H_2O 63.32μm line from the disk around HD163296 (at a distance d of $\sim$ 122 pc and inclination i of 44 deg) is observed to be $(2.0 \pm 0.6) \times 10^{-17}$ W m^{-2},

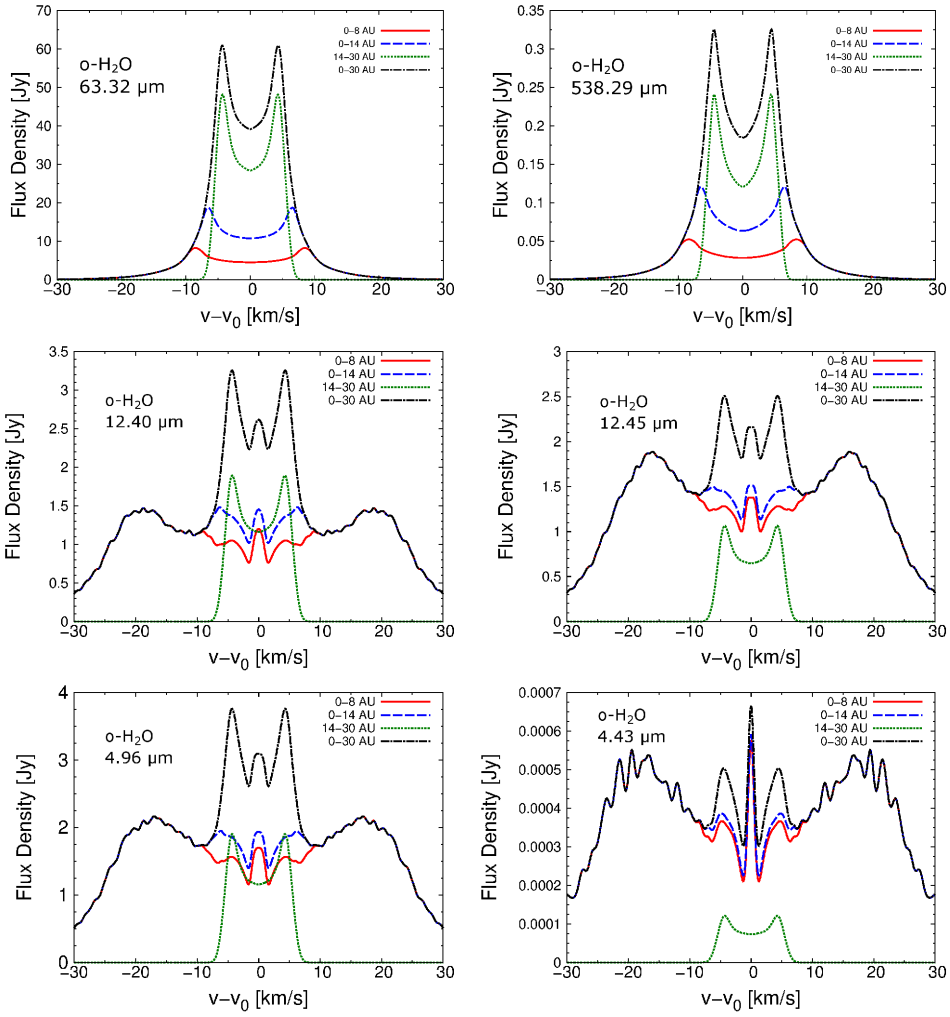

Figure 33. (Top two panels): The velocity profiles of two characteristic pure rotational ortho-$H_2{}^{16}O$ lines at $\lambda = 63.32\mu$m (top left) and 538.29μm (top right) from the Herbig Ae disk. They are examples of lines which are less suited to trace emission from water vapor within the H_2O snowline. (Middle two panels): The velocity profiles of mid-infrared ortho-$H_2{}^{16}O$ lines at λ=12.40μm (middle left), 12.45μm (middle right) from the Herbig Ae disk. Both lines have much larger values of A_{ul} and E_{up} than those of the candidate mid-infared H_2O lines to trace the emission from the H_2O vapor within the H_2O snowline. (Bottom two panels): The velocity profiles of near-infrared ortho-$H_2{}^{16}O$ lines at λ=4.96μm (bottom left), 4.43μm (bottom right) from the Herbig Ae disk. Both lines have the same values of E_{up} (=4180.4K), the former line has a larger value of A_{ul} and the latter line has a smaller value of A_{ul}. *Red solid lines* are the emission line profiles from inside 8 au (=the inner high temperature region), *blue dashed lines* are those from inside 14 au ($\sim$ inside the H_2O snowline), *green dotted lines* are those from 14−30 au ($\sim$ outside the H_2O snowline), and *black dashed dotted lines* are those from the total area inside 30 au.

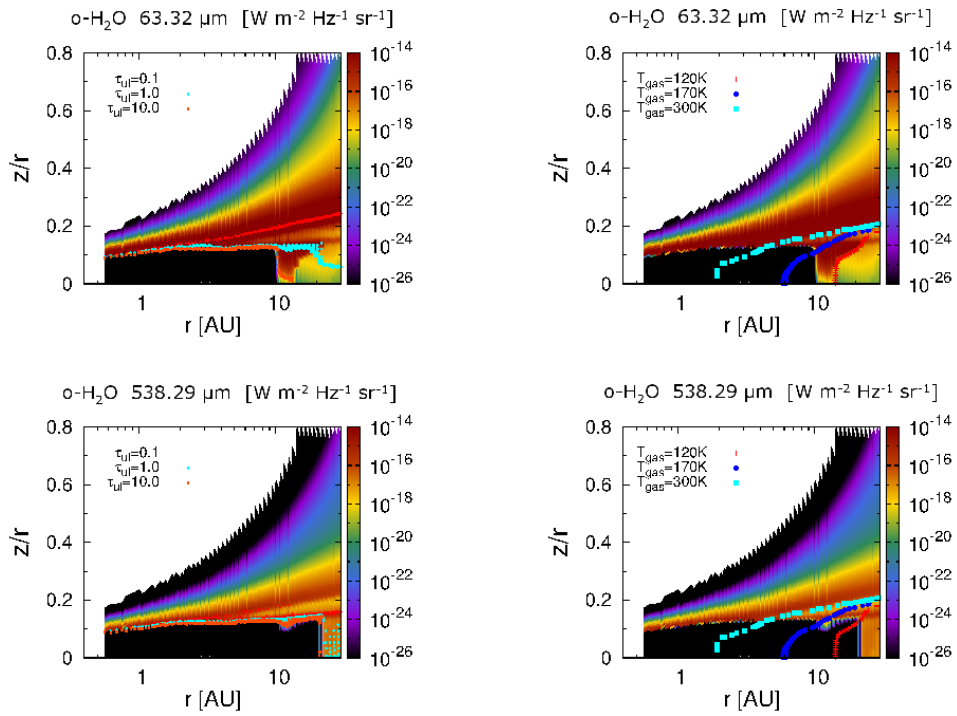

Figure 34. The line-of-sight emissivity distributions of the two characteristic ortho-$H_2{}^{16}O$ lines at λ=63.32μm (top left and right) and 538.29μm (bottom left and right), which have various A_{ul} and E_{up}, from the Herbig Ae disk. In the left panels, we overplot the total optical depth contours (τ_{ul} =0.1 (red cross points), 1 (cyan circle points), and 10 (orange square points)) on top of these line emissivity panels (see also Figure 35). In the right panels, we overplot the gas temperature T_g contours (T_g =120K (red cross points), 170K (blue circle points), and 300K (cyan square points), see also Figure 26).

and the values of the other lines (e.g., ortho-$H_2{}^{16}O$ 56.82μm and 71.95μm lines) are roughly similar (e.g., Fedele et al. 2012; Meeus et al. 2012). Meeus et al. (2012) and Fedele et al. (2013) determined that the upper limits of the total fluxes of such water emission lines, including the 63.32μm from other Herbig Ae disks ($d \sim 100 - 150$ pc), are between a few 10^{-18} and a few 10^{-17} W m^{-2}. These values are roughly several tens of times smaller than the value which we calculate in this work for this particular Herbig Ae disk model (see also Table 4, d =140 pc) if we consider the difference in the distances from the solar system. We note that our model disk is not intended to be representative of any particular source. We discuss this issue further in Section 3.3.3.

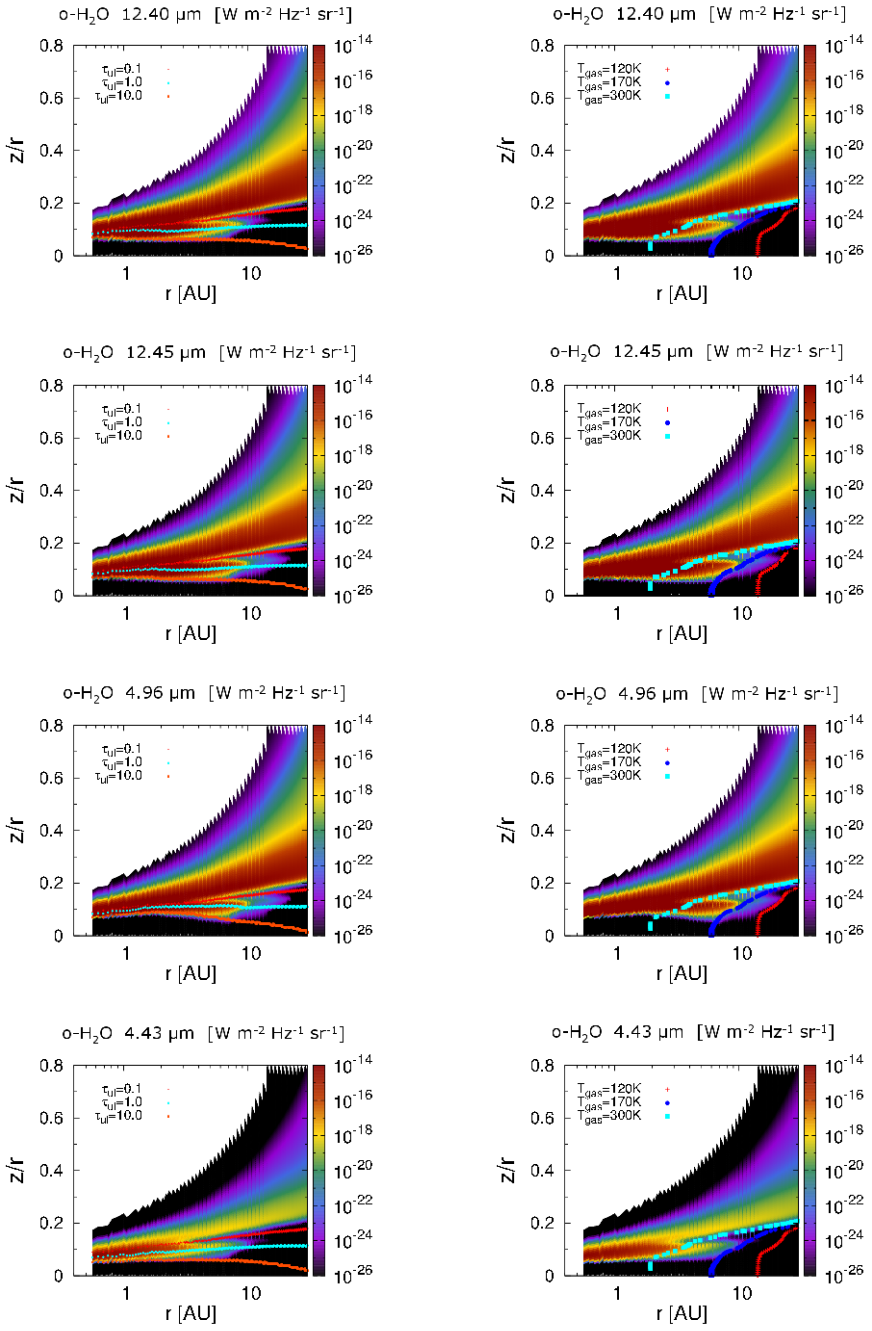

Figure 34. (Continued.) (Top and second line panels): The line-of-sight emissivity distributions of mid-infrared ortho-$H_2{}^{16}O$ lines at λ=12.40μm (top left and right), 12.45μm (second line left and right) from the Herbig Ae disk. Both lines have much larger values of A_{ul} and E_{up} than those of the candidate mid-infared H_2O lines which trace emission from the hot water vapor within H_2O snowline. (Third line and bottom panels): The line-of-sight emissivity distributions of near-infrared ortho-$H_2{}^{16}O$ lines at λ=4.96μm (third left and right), 4.43μm (bottom left and right) from the Herbig Ae disk. Both lines have the same values of E_{up} (=4180.4K), the former line has a larger value of A_{ul} and the latter line has a smaller value of A_{ul}.

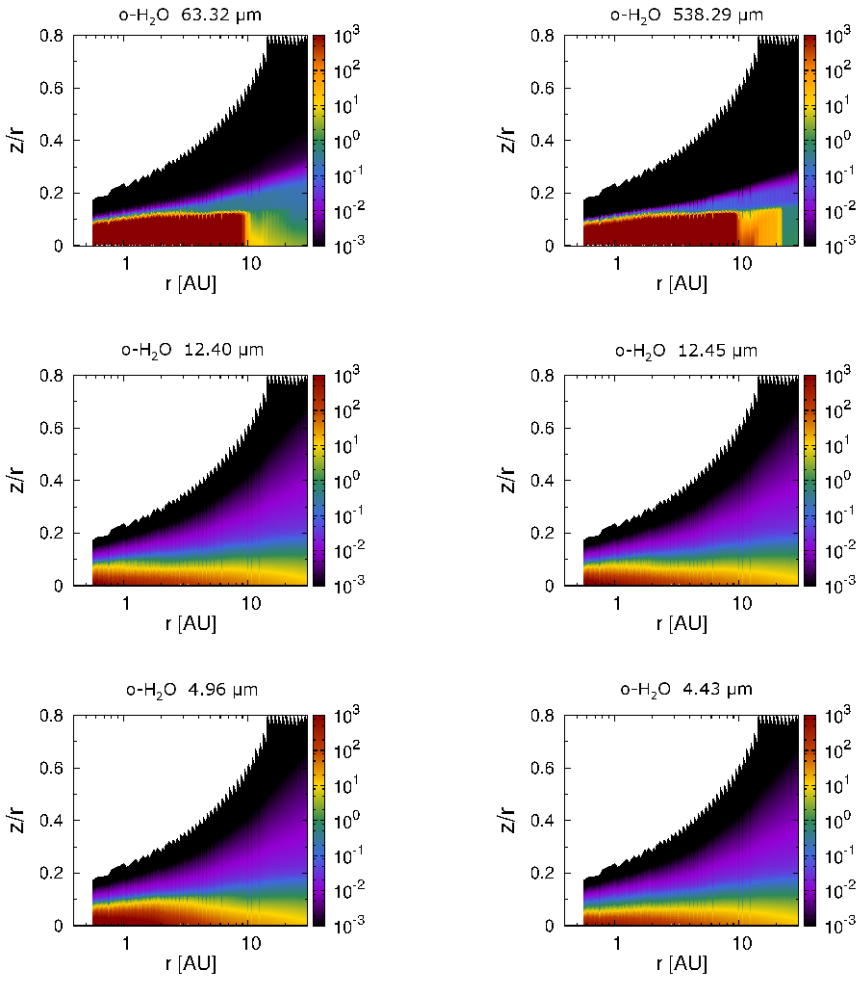

Figure 35. (Top two panels): The line-of-sight total optical depth $\tau_{ul}(s, x, y, \nu)$ (gas emission and dust) distributions of two characteristic ortho-$H_2{}^{16}O$ lines at 63.32μm (top left) and 538.29μm (top right) from the Herbig Ae disk. (Middle two panels): The line-of-sight optical depth distributions of mid-infrared ortho-H_2O lines at λ=12.40μm (middle left), 12.45μm (middle right) from the Herbig Ae disk. Both lines have much larger values of A_{ul} and E_{up} than those of the candidate mid-infared H_2O lines which trace emission from the hot water vapor within H_2O snowline. (Bottom two panels): The line-of-sight optical depth distributions of near-infrared ortho-$H_2{}^{16}O$ lines at λ=4.96μm (bottom left), 4.43μm (bottom right) from the Herbig Ae disk. Both lines have the same values of E_{up} (=4180.4K), the former line has a larger value of A_{ul} and the latter line has a smaller value of A_{ul}.

In the top right panel of Figure 33 we show the line profile for the ortho-$H_2{}^{16}O$ line at 538.29μm. The contribution from the outer disk (r =14−30 au) is large compared to that from the optically

thick region near the midplane of the inner disk (r <14 au) and the width between the double peaks of the line profile is around two times narrower than those of candidate water lines which trace the emission from the hot water vapor within the H_2O snowline, although the A_{ul} is not so high (=$3.497\times10^{-3}s^{-1}$). This is because this 538.29μm line is the ground-state rotational transition and has a low E_{up} (=61.0K) compared with the other lines discussed in this work. The flux of this line comes mainly from the outer cold water vapor in the photodesorbed layer.

According to Figures 32 and 34, the value of the emissivity of the ortho-$H_2{}^{16}O$ 538.29μm at each (r, z) in the photodesorbed layer is comparable inside and outside the H_2O snowline. However, because of the larger surface area of the outer disk most disk-integrated emission from this line arises from the outer disk. In addition, in the outer disk midplane opacity of this line (see Figure 35) is around $10^3 - 10^4$ times higher than those of the ortho-$H_2{}^{16}O$ 482.99μm and 682.66μm lines, although the wavelength and thus the dust opacity are similar. This is because this line has a small value of E_{up} and the level population of H_2O for this line is very high near the midplane of cold outer disk. On the basis of these properties, we propose that this line is not optimal to detect emission from the hot water vapor within the H_2O snowline in the Herbig Ae disk case, as also concluded for the T Tauri disk (Notsu et al. 2016).

We mention that previous space high-dispersion spectroscopic observations with *Herschel*/HIFI detected this line from disks around one Herbig Ae star HD100546 and two T Tauri stars TW Hya and DG Tau (e.g., Hogerheijde et al. 2011; Podio et al. 2013; van Dishoeck et al. 2014; Salinas et al. 2016). The number of detections is small because the line flux is low compared with the sensitivity of that instrument (Antonellini et al. 2015). The detected line profile and other line modeling work (e.g., Meijerink et al. 2008; Woitke et al. 2009b; Antonellini et al. 2015) suggested that the emitting region arises in the cold outer disk, consistent with the results of our model calculations.

Here we note that since we define OPR =3 (=the value in the high temperature region) throughout

the disk, we may be overestimating the line flux of the ortho-$H_2{}^{16}O$ 538.29μm line (for more details, see Section 2.1.5 of this thesis and paper I, Notsu et al. 2016). In addition, since the flux of this line is controlled by the outer cold H_2O gas which is desorbed from the cold dust-grain surfaces, it also may be necessary to include grain-surface reactions (e.g., Hasegawa et al. 1992) for accurate determination of the gas phase H_2O abundance in this region.

The middle two panels of Figure 33 show the profiles for the pure rotational mid-infrared ortho-$H_2{}^{16}O$ lines at λ=12.40μm (middle left), 12.45μm (middle right) from the Herbig Ae disk. Figures 32, 34, and 35 also show the line-of-sight emissivity, the total optical depth (gas emission and dust), and the vertical normalized cumulative emissivity distributions of these two mid-infrared ortho-$H_2{}^{16}O$ lines from the Herbig Ae disk, respectively. Both lines have much larger values of A_{ul} (>1 s^{-1}) and E_{up} (>4000K) than those of the candidate mid-infared water lines that trace emission from the H_2O vapor within the H_2O snowline in the disk midplane (see Tables 4 and 5), and thus they mainly trace emission from the hot surface of the inner and outer disk. The velocity profiles of these two lines were obtained by previous ground-based mid-infrared spectroscopic observations using VLT/VISIR (Pontoppidan et al. 2010b) from bright T Tauri disks (AS 205N and RNO 90). They show the Keplerian double-peaked or flat-topped (for low inclination objects) profiles, and the line emitting region is the hot disk surface.

The bottom two panels of Figure 33 show the profiles of pure rotational near-infrared ortho-$H_2{}^{16}O$ lines at λ=4.96μm (bottom left), 4.43μm (bottom right) from the Herbig Ae disk. Figures 34, 35, and 32 also show the line-of-sight emissivity, the total optical depth (gas emission and dust), and the vertical normalized cumulative emissivity distributions of these near-infrared lines for the Herbig Ae disk, respectively. Both lines have the same much larger values of E_{up} (=4180.4K), the former line has a larger value of A_{ul} (=3.260 s^{-1}) and the latter has a smaller value of A_{ul} (= 2.080×10^{-4} s^{-1}). For the former case, since it has much larger values of A_{ul} and E_{up} than those of the candidate ortho-$H_2{}^{16}O$ lines (see Tables 4 and 5), it mainly traces the emission from the hot surface of the

inner and outer disk. This line has similar values of A_{ul} and E_{up} with the observed near-infrared rovibrational water lines in L band (Mandell et al. 2012). For the latter smaller A_{ul} line case, since the value of E_{up} in this near-infrared line is much larger (>4000K) than those of the candidate water lines which trace the emission from the hot water vapor within the H_2O snowline from mid-infrared to sub-millimeter wavelengths, it only traces the very innermost region ($r < 3$ au for the 4.43μm line case). In addition, the widths between the two peaks of the Keplerian profiles of these near- and mid-infrared lines with large E_{up} are larger than those of candidate water lines which trace the emission from the hot water within the H_2O snowline (see Figures 29, 33, and 37). These are because they trace the innermost hot region compared with the region around the H_2O snowline.

Here we note that previous near- and mid-infrared spectroscopic observations using VLT/CRIRES and *Spitzer*/IRS for Herbig Ae disks (e.g., Pontoppidan et al. 2010a; Fedele et al. 2011; Salyk et al. 2011) have not detected any water lines regardless of the value of A_{ul}. We discuss this issue in Section 3.3.3. Moreover, as we described in Section 3.1, the level populations of the water molecule are calculated under LTE, as opposed to non-LTE. However, as we discuss further in Section 3.3.2, in our LTE calculations there is a possibility that we have overestimated the emission fluxes of strong H_2O lines with large A_{ul} which trace the hot surface layer, as found in previous studies (e.g., Meijerink et al. 2009; Woitke et al. 2009b; Banzatti et al. 2012; Antonellini et al. 2015).

3.2.5. *The total fluxes of candidate ortho-$H_2{}^{16}O$ emission lines*

Figure 36 shows the total fluxes of the various ortho-$H_2{}^{16}O$ lines which are the candidates for tracing emission from hot water vapor within the H_2O snowline for a Herbig Ae disk (top panel) and a T Tauri disk (bottom panel). We select those lines from the LAMDA database (see Section 2.1.5 of this thesis and paper I, Notsu et al. 2016) which have both small values of A_{ul} ($10^{-6} < A_{ul} < 10^{-2}$ s^{-1}) and relatively large values of E_{up} ($700 < E_{up} < 2100$K). The wavelengths of these lines range from mid-infrared to sub-millimeter, $\lambda \sim 11 - 1000\mu$m, because we do not have candidate lines which trace emission from the hot water vapor within H_2O snowline with wavelengths $\lambda < 10\mu$m on the

basis of our criteria for A_{ul} and E_{up}. The values of E_{up} of lines for wavelengths $\lambda < 10\mu$m are too large ($\gtrsim$3000K), and the opacity of the dust grains for wavelengths $\lambda < 10\mu$m is expected to be too large to trace the emission from the midplane of the disk (see Sections 3.2.2 and 3.3.4). The detailed parameters, such as transitions ($J_{K_aK_c}$), wavelength, frequency, A_{ul}, E_{up}, and total line fluxes of these candidate ortho-$H_2{}^{16}O$ lines shown in Figure 36 are listed in Table 5. In Figure 36 and Table 5, we show both values for the total fluxes from the Herbig Ae disk and the T Tauri disk. In addition, Figure 37 shows the profiles of mid-infrared candidate lines ($\lambda \sim 11 - 25\mu$m) for the Herbig Ae disk. All lines in this Figure are listed in Table 5.

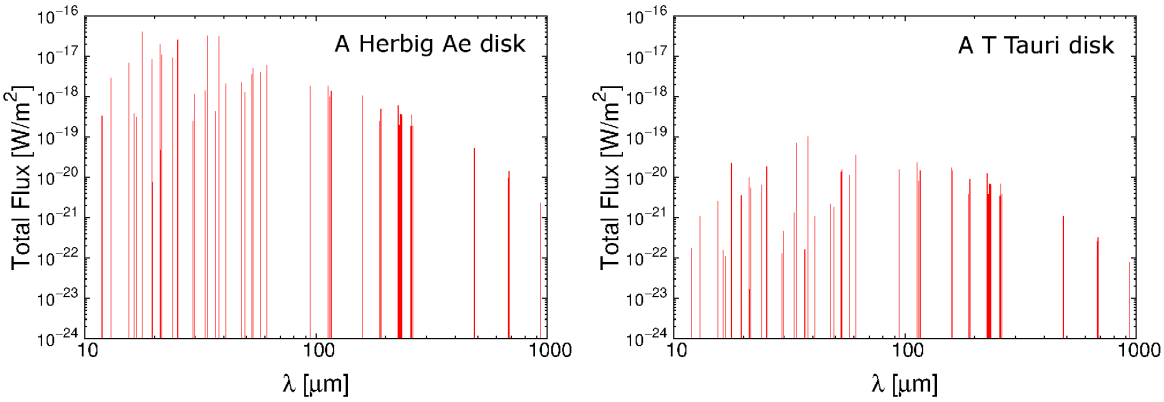

Figure 36. The total fluxes of the ortho-$H_2{}^{16}O$ lines which are best candidates to trace the emission from the water vapor within the H_2O snowline, for a Herbig Ae disk (top panel) and a T Tauri disk (bottom panel). We select these lines based on their small Einstein A coefficients of $10^{-6} < A_{ul} < 10^{-2}$ s^{-1} and relatively large excitation energies of $700 < E_{up} < 2100$K. The wavelengths of these lines range from mid-infrared to sub-millimeter, $\lambda \sim 11 - 1000\mu$m.

On the basis of Figures 36, 37, and Tables 4, 5, the values of fluxes of these lines from the Herbig Ae disk are around $10^2 - 10^3$ larger than those of the T Tauri disk. This is because the position of the H_2O snowline in the Herbig Ae disk exists at a larger radius from the central star than that in the T Tauri disk. In addition, the peak fluxes of these lines become larger as the values of A_{ul} become larger and E_{up} become smaller. Moreover, the values of total flux tend to be larger as the wavelengths of these water lines become shorter. This is because the peak wavelengths of the Planck function at

the gas temperatures around the H_2O snowline ($T_g \sim$ 100-200 K) are at mid-infrared wavelengths. In the cases of the Herbig Ae disk and the T Tauri disk, the values of total fluxes of the mid-infrared water lines which trace emission from the hot water vapor within H_2O snowline are $\sim 10^2 - 10^4$ and $\sim 10^1 - 10^2$ times larger than those of sub-millimeter lines, respectively, and there are differences in the line flux ratio of mid-infrared lines to sub-millimeter lines between the Herbig Ae and the T Tauri disks. These are because the amount of hot H_2O gas around the region at $\tau_{ul} \lesssim 1$ in mid-infrared lines and inside the H_2O snowline are higher in the Herbig Ae disk model than that in the T Tauri disk.

On the basis of Figure 37, most of the emission flux from these mid-infrared lines comes from the region with a high H_2O gas abundance ($\sim 10^{-4}$, r <8 au), and the position of the two peaks and the rapid drop in flux density between the peaks contains information on the position of the outer edge of this region. This is because they have shorter wavelengths ($\lambda \sim 11 - 25 \mu$m) and relatively larger values of E_{up} ($\sim$1500 − 2000K except for the ortho-$H_2{}^{16}O$ 17.75 and 24.00 μm lines) among all candidate lines which trace the emission from the hot H_2O vapor within the H_2O snowline (see Table 5).

Table 5. Candidate ortho-$H_2{}^{16}O$ line parameters and total line fluxes (11−1000μm)

$J_{K_aK_c}$	λ[1]	Freq.	A_{ul}	E_{up}	HAe flux[2,3]	TT flux[3,4]
	[μm]	[GHz]	[s^{-1}]	[K]	[W m^{-2}]	[W m^{-2}]
7_{70}-6_{25}	11.878	25239.615	6.653×10^{-3}	2006.8	3.4×10^{-19}	1.8×10^{-22}
7_{61}-6_{16}	13.005	23052.310	2.585×10^{-4}	1749.8	2.9×10^{-18}	1.1×10^{-21}
6_{61}-5_{14}	15.489	19354.618	4.138×10^{-4}	1503.6	6.9×10^{-18}	2.6×10^{-21}
7_{70}-7_{25}	16.329	18359.435	7.756×10^{-5}	2006.8	3.8×10^{-19}	1.6×10^{-22}
6_{61}-6_{16}	16.728	17921.765	2.153×10^{-5}	1503.6	3.2×10^{-19}	1.1×10^{-22}

Table 5 continued on next page

Table 5 *(continued)*

$J_{K_aK_c}$	λ^1 [μm]	Freq. [GHz]	A_{ul} [s^{-1}]	E_{up} [K]	HAe flux[2,3] [W m^{-2}]	TT flux[3,4] [W m^{-2}]
6_{52}-5_{05}	17.754	16885.840	2.909×10^{-3}	1278.5	4.1×10^{-17}	2.3×10^{-20}
7_{61}-7_{16}	19.532	15348.791	1.269×10^{-3}	1749.8	8.3×10^{-18}	3.5×10^{-21}
7_{70}-8_{27}	19.638	15265.853	1.900×10^{-6}	2006.8	7.6×10^{-21}	3.1×10^{-24}
7_{52}-7_{07}	21.115	14197.932	2.078×10^{-3}	1524.8	2.0×10^{-17}	9.9×10^{-21}
7_{61}-8_{18}	21.185	14151.161	6.154×10^{-6}	1749.8	4.8×10^{-20}	1.7×10^{-23}
7_{70}-7_{43}	21.571	13897.693	3.474×10^{-3}	2006.8	1.1×10^{-17}	5.5×10^{-21}
5_{50}-5_{05}	23.996	12493.205	2.696×10^{-4}	1067.7	9.4×10^{-18}	6.4×10^{-21}
6_{61}-6_{34}	25.247	11874.160	3.803×10^{-3}	1503.6	2.6×10^{-17}	1.9×10^{-20}
6_{61}-7_{16}	29.339	10218.246	1.859×10^{-5}	1503.6	2.5×10^{-19}	1.3×10^{-22}
8_{54}-9_{09}	29.851	10043.001	1.605×10^{-4}	1805.9	1.2×10^{-18}	4.7×10^{-22}
6_{52}-7_{07}	33.074	9064.381	5.942×10^{-5}	1278.5	1.4×10^{-18}	1.3×10^{-21}
5_{50}-5_{23}	33.833	8860.835	4.552×10^{-3}	1067.7	3.2×10^{-17}	7.1×10^{-20}
7_{70}-8_{45}	36.750	8157.523	1.123×10^{-4}	2006.8	4.3×10^{-19}	1.6×10^{-22}
4_{41}-4_{14}	37.984	7892.616	2.629×10^{-3}	702.3	3.1×10^{-17}	1.0×10^{-19}
9_{45}-10_{110}	40.702	7365.464	4.815×10^{-4}	1957.1	2.1×10^{-18}	1.1×10^{-21}
7_{61}-8_{36}	47.601	6297.997	4.268×10^{-4}	1749.8	2.3×10^{-18}	2.2×10^{-21}
6_{61}-7_{34}	49.334	6076.834	1.195×10^{-4}	1503.6	1.3×10^{-18}	1.8×10^{-21}
5_{50}-6_{25}	52.864	5671.021	1.442×10^{-4}	1067.7	3.7×10^{-18}	1.4×10^{-20}
7_{43}-8_{18}	53.455	5608.351	5.030×10^{-4}	1339.8	5.2×10^{-18}	1.6×10^{-20}
7_{52}-8_{27}	57.394	5223.441	7.203×10^{-4}	1524.8	4.1×10^{-18}	1.1×10^{-20}
5_{41}-6_{16}	61.316	4889.280	2.686×10^{-4}	878.1	5.9×10^{-18}	3.5×10^{-20}
6_{52}-7_{25}	94.172	3183.464	3.387×10^{-4}	1278.5	1.8×10^{-18}	1.6×10^{-20}
4_{41}-5_{14}	112.803	2657.666	1.670×10^{-4}	702.3	1.8×10^{-18}	2.3×10^{-20}

Table 5 continued on next page

Table 5 *(continued)*

$J_{K_aK_c}$	λ[1]	Freq.	A_{ul}	E_{up}	HAe flux[2,3]	TT flux[3,4]
	[μm]	[GHz]	[s^{-1}]	[K]	[W m^{-2}]	[W m^{-2}]
9_{27}-10_{110}	114.454	2619.334	6.768×10^{-4}	1729.3	1.0×10^{-18}	8.1×10^{-21}
8_{36}-9_{09}	116.350	2576.644	7.255×10^{-4}	1447.5	1.4×10^{-18}	1.5×10^{-20}
8_{45}-7_{52}	159.051	1884.888	7.403×10^{-3}	1615.3	1.1×10^{-18}	1.7×10^{-20}
6_{34}-7_{07}	159.400	1880.753	3.911×10^{-4}	933.7	9.0×10^{-19}	1.5×10^{-20}
8_{54}-9_{27}	187.810	1595.252	2.947×10^{-4}	1805.9	2.5×10^{-19}	3.8×10^{-21}
6_{43}-7_{16}	190.437	1574.232	2.927×10^{-4}	1088.7	4.9×10^{-19}	8.9×10^{-21}
6_{25}-5_{32}	226.761	1322.065	2.334×10^{-3}	795.5	6.0×10^{-19}	1.2×10^{-20}
8_{45}-9_{18}	229.206	1307.963	2.599×10^{-4}	1615.3	2.0×10^{-19}	3.9×10^{-21}
8_{27}-7_{34}	231.248	1296.411	1.074×10^{-3}	1274.1	3.7×10^{-19}	6.8×10^{-21}
7_{43}-6_{52}	234.531	1278.266	1.552×10^{-3}	1399.8	3.6×10^{-19}	6.7×10^{-21}
8_{54}-7_{61}	256.593	1168.358	9.459×10^{-4}	1805.9	1.8×10^{-19}	3.5×10^{-21}
6_{34}-5_{41}	258.816	1158.324	1.417×10^{-3}	933.7	3.5×10^{-19}	7.0×10^{-21}
7_{25}-8_{18}	261.457	1147.621	1.087×10^{-4}	1125.7	1.9×10^{-19}	3.9×10^{-21}
5_{32}-4_{41}	482.990	620.701	1.106×10^{-4}	732.1	5.3×10^{-20}	1.1×10^{-21}
7_{52}-6_{61}	676.704	443.018	2.231×10^{-5}	1524.8	9.4×10^{-21}	2.6×10^{-22}
6_{43}-5_{50}	682.664	439.151	2.816×10^{-5}	1088.7	1.4×10^{-20}	3.1×10^{-22}
10_{29}-9_{36}	933.277	321.226	6.165×10^{-6}	1861.2	2.3×10^{-21}	7.8×10^{-23}

[1]In calculating the value of line wavelength from the value of line frequency, we use the value of speed of light c=2.99792458 $\times$ 10^8 m s^{-1}.

[2]The total flux of each emission line from the Herbig Ae disk.

[3]In calculating the total fluxes of these ortho-$H_2{}^{16}O$ lines, we use a distance d = 140pc and an inclination angle of i =30 degree.

[4]The total flux of each emission line from the T Tauri disk (see also paper I, Notsu et al. 2016).

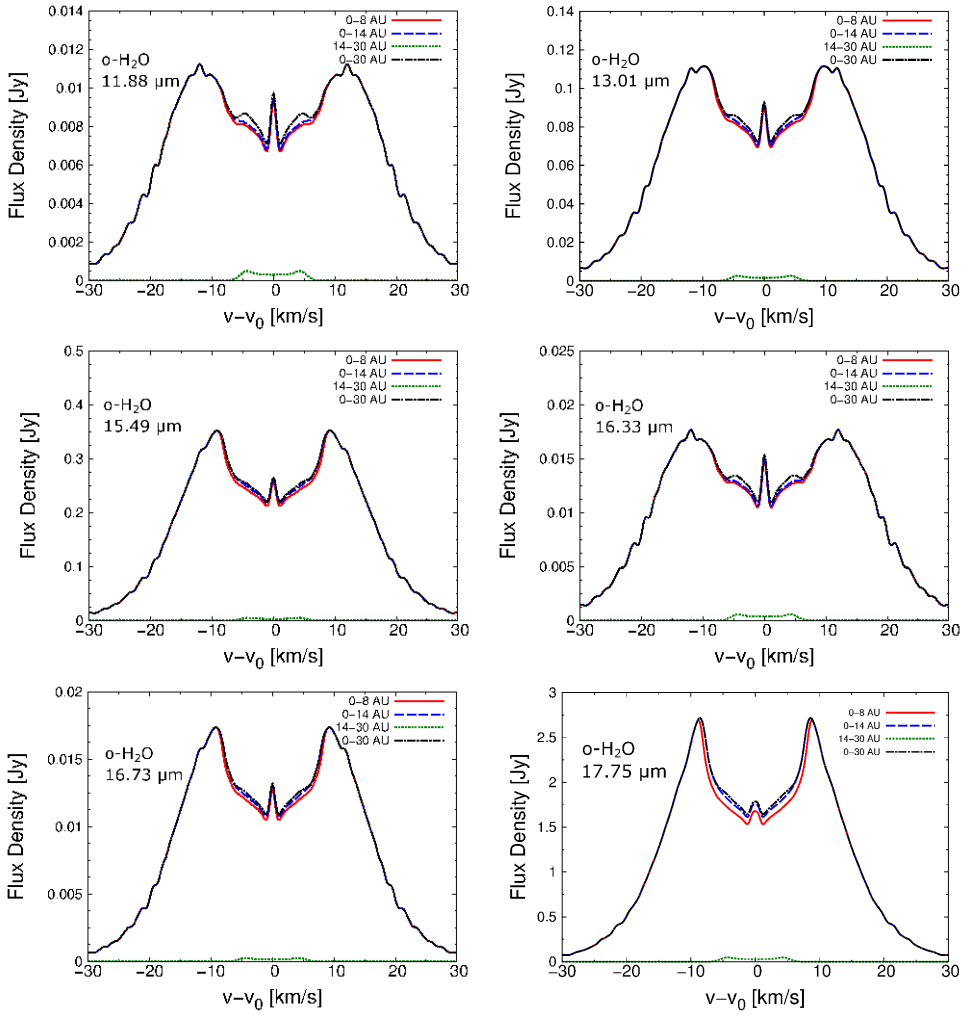

Figure 37. The velocity profiles of mid-infrared ortho-$H_2{}^{16}O$ lines at λ=11.88μm (top left), 13.01μm (top right), 15.49μm (middle left), 16.33μm (middle right), 16.73μm (bottom left), and 17.75μm (bottom right), from the Herbig Ae disk. These exist between 11-25μm and are also the best mid-infrared candidate ortho-H_2O lines to trace the hot water vapor within the H_2O snowline. The parameters and total fluxes of these ortho-H_2O lines are reported in Table 5. *Red solid lines* are the emission line profiles from inside 8 au (=the inner high temperature region), *blue dashed lines* are those from inside 14 au (∼inside the H_2O snowline), *green dotted lines* are those from 14−30 au (∼outside the H_2O snowline), and *black dashed dotted lines* are those from the total area inside 30 au.

3.2.6. *The radial distributions of normalized cumulative line fluxes*

Figure 38 shows the normalized radial cumulative fluxes for seven $H_2{}^{16}O$ lines at λ=682.66μm, 63.32μm, 538.29μm, 12.40μm, 12.45μm, 4.96μm, and 4.43μm. We discussed the properties of these

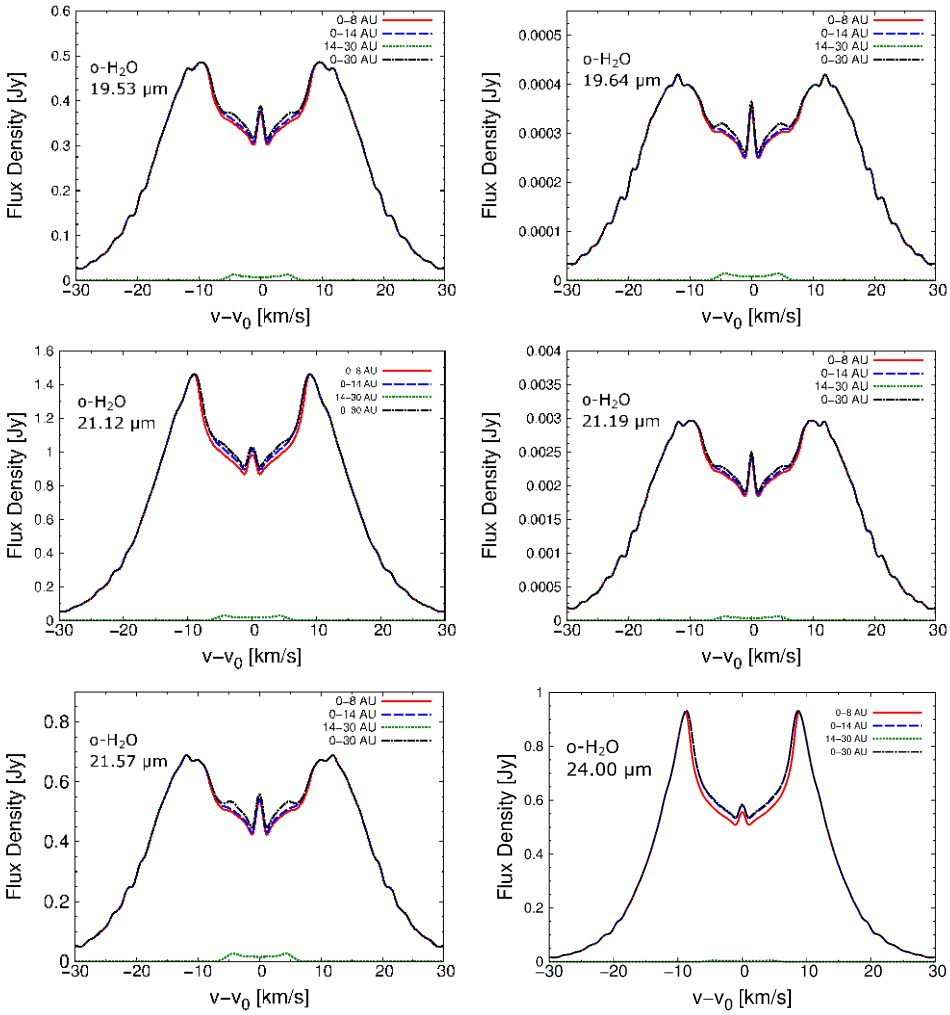

Figure 37. (Continued.) The velocity profiles of mid-infrared ortho-$H_2{}^{16}O$ lines at λ=19.53μm (top left), 19.64μm (top right), 21.12μm (middle left), 21.19μm (middle right), 21.57μm (bottom left), and 24.00μm (bottom right), from the Herbig Ae disk.

seven lines in Sections 3.2.3 and 3.2.4. According to these figures, around 90% of the flux of the 682.66μm line is emitted from the region inside the H_2O snowline (r <14 au). In contrast, emission from the 63.32μm and the 538.29μm lines is emitted mostly from the region outside the H_2O snowline. In addition, although the 63.32μm line is mainly emitted from the region between $r \sim 25 - 200$ au, the 538.29μm line is mainly emitted from a region much further out ($r \sim 50 - 300$ au). The properties of these three lines for the Herbig Ae disk are similar to those for the T Tauri disk which we showed and discussed in Sections 2.2.3−2.2.5 in this thesis (see also paper I, Notsu et al. 2016).

The 12.40μm, 12.45μm, and 4.96μm lines are mainly emitted both from the regions within 3 au and outside the H_2O snowline (r >14 au). The emission from the region between 3-14 au (= the H_2O snowline) is much smaller. The 4.43μm line is mainly emitted from the innermost region of the disk ($r < 3$ au). These are because these four lines have much larger values of E_{up} (>4000K) than both the candidate ortho-$H_2{}^{16}O$ lines that trace the hot water vapor within the H_2O snowline and the 63.32μm line. Thus, the values of flux densities from the hot surface layer of the inner disk are larger. The 4.43μm line has a smaller value of A_{ul} ($= 2.080 \times 10^{-4}$ s^{-1}) and thus the values of flux densities from the hot surface layer of the outer disk are much smaller, but the other three lines have larger values of A_{ul} (>1 s^{-1}) and thus the values of flux densities from the hot surface layer of the outer disk are larger.

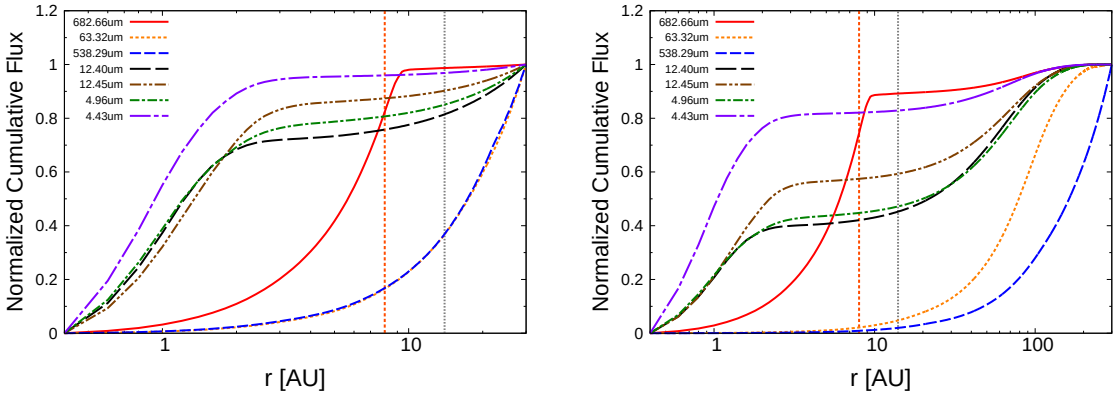

Figure 38. The radial distributions of the normalized cumulative flux for seven pure rotational ortho-H_2O lines at λ=682.66μm (*red solid line*), 63.32μm (*orange dotted line*), 538.29μm (*blue dashed line*), 12.40μm (*black long dashed line*), 12.45μm (*brown dashed two dotted line*), 4.96μm (*green dashed dotted line*), and 4.43μm (*violet long dashed dotted line*). The vertical straight lines display the positions of r=8 au (*orange dotted line*) and 14 au (*grey dotted line*), respectively. We normalized the cumulative flux of each line using the values at $r = 30$ au (top panel) and at $r = 300$ au (bottom panel). We assume that the inclination angle of the disk i is 0 degree in making these figures.

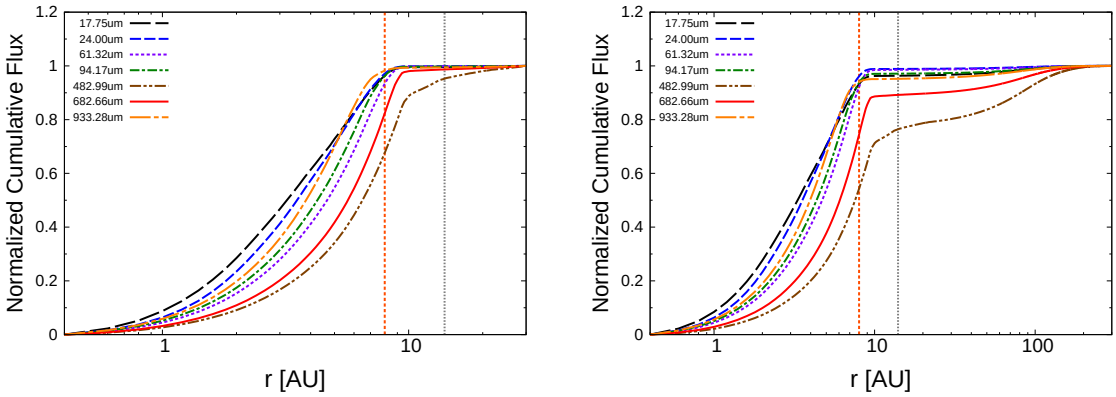

Figure 39. The radial distributions of the normalized cumulative flux for seven pure rotational ortho-$H_2{}^{16}O$ lines at λ=17.75μm (*black long dashed line*), 24.00μm (*blue dashed line*), 61.32μm (*violet dotted line*), 94.17μm (*green dashed dotted line*), 482.99μm (*brown dashed two dotted line*), 682.66μm (*red solid line*), and 933.28μm (*orange long dashed dotted line*). These are candidate ortho-$H_2{}^{16}O$ lines to trace the emission from the hot water vapor within the H_2O snowline. The vertical straight lines display the positions of r=8 au (*orange dotted line*) and 14 au (*grey dotted line*), respectively. We normalized the cumulative flux of each line using the values at r = 30 au (top panel) and at r = 300 au (bottom panel). We assume that the inclination angle of the disk i is 0 degree in making these figures.

Figure 39 shows the normalized radial cumulative fluxes for seven rotational ortho-$H_2{}^{16}O$ lines that trace the hot water vapor within the H_2O snowline: λ=17.75μm, 24.00μm, 61.32μm, 94.17μm, 482.99μm, 682.66μm, and 933.28μm. We discussed the properties of these seven lines in Sections 3.2.3 and 3.2.5. In the cases of the 482.99μm and 682.66μm lines, most of the flux is emitted from the region with a high H_2O gas abundance ($\sim10^{-4}$, r <8 au), with some emission flux emitted from the region with a relatively high H_2O gas abundance ($\sim10^{-8}$, r =8-14 au). On the other hand, for the other lines, almost all of the emission flux comes from the region with a high H_2O gas abundance ($\sim10^{-4}$, r <8 au). Such differences in line properties come from the differences in E_{up} and the dust opacity at different wavelengths. The 482.99μm and 682.66μm lines have relatively smaller values of E_{up} (<1100K) and longer wavelengths (>400μm), as discussed in Section 3.2.3. In Figure 39, lines which have larger E_{up} and shorter wavelengths tend to be emitted from the innermost region within

the H_2O snowline.

3.3. *Discussions*

3.3.1. *Influence of model assumptions on the line properties*

In Section 2.3.1 of this thesis (see also paper I, Notsu et al. 2016), we discussed the uncertainties in our model predictions in detail, and we also discussed the behavior of the water lines for some cases in which we artificially changed the distribution of H_2O vapor, the position of the H_2O snowline, and the fractional abundance of H_2O gas in the outer disk surface layer (see Figures 8 and 9 of paper I, Notsu et al. 2016). We explored different values of the H_2O snowline radius to simulate the effects of (i) increased and decreased viscous heating (e.g., Oka et al. 2011; Harsono et al. 2015), (ii) using different dust opacities due to dust-grain growth (e.g., Aikawa & Nomura 2006; Oka et al. 2011). We varied the abundance of water vapor in the disk atmosphere to simulate the effects of (iii) increasing/decreasing the strength of UV photoreactions. We found that in the cases for which the H_2O snowline is more distant from the central star, and the fractional abundance of H_2O gas in the disk atmosphere is lower than that in the originally adopted T Tauri disk, the line fluxes from the hot inner disk midplane inside the H_2O snowline are more dominant from those from the outer disk (e.g., Walsh et al. 2012).

An analysis of spectral energy distributions (SEDs) classified Herbig Ae/Be stars into two groups (group I/II, Meeus et al. 2001). Group I sources show both power-law and blackbody components up to far-infrared wavelengths in their SEDs. SEDs of group II sources can be well modeled with only a single power law from mid- to far-infrared wavelengths. Meeus et al. (2001) suggested that group I sources have a flaring disk while the group II disks are geometrically flat. Meeus et al. (2001) proposed a possible evolutionary scenario where a group I flaring disk evolves into a group II flat disk through grain growth and settling of grains onto the disk midplane (see also Dominik et al. 2003; Dullemond & Dominik 2004).

However, recent high-spatial resolution observations at various wavelengths have revealed a more complex structure in disks, with inner holes and/or gaps toward many group I sources such as HD100546 (e.g., Benisty et al. 2010; Panić et al. 2014; Walsh et al. 2014b), HD142527 (e.g., Fujiwara et al. 2006; Fukagawa et al. 2006, 2013), and HD169142 (e.g., Benisty et al. 2010; Honda et al. 2012). On the other hand, there is little evidence for inner holes and/or gaps reported toward group II disks, and they seem to have a radially continuous structure (e.g., Honda et al. 2015). Honda et al. (2012) and Maaskant et al. (2013) suggested that most group I sources can be classified as (pre-)transitional disks. Transitional and pre-transitional disks are protoplanetary disks with an inner hole and/or gaps indicated by a lack of near-infrared/mid-infrared excess in their SEDs (e.g., Strom et al. 1989; Espaillat et al. 2007). They pointed out that there is no significant difference in age between groups I and II sources (Meeus et al. 2001; Honda et al. 2015). Therefore, recent studies (e.g., Maaskant et al. 2013; Honda et al. 2015) suggested that both group I and II sources had experienced different evolutionary paths from some common primordial and continuous flaring disks. Here we note that Menu et al. (2015), Isella et al. (2016), and Zhang et al. (2016) suggested that some geometrically flat disks (group II disk) have gaps. Menu et al. (2015) suggested flat disks with gaps are most likely descendants of flat disks without gaps. Banzatti et al. (2017) discovered a correlation between water line fluxes at λ =2.9μm and $10-33\mu$m and the size of inner disk gaps/holes as probed by 4.7μm CO rovibrational emission lines. They described that the lower detection frequency of near- and mid-infrared water vapor lines in disks around intermediate mass stars (M_*=1.5-4$M_\odot$) is linked to inner gaps/holes with depleted molecular gas content of the disks out to close to or beyond the H_2O snowline.

Our Herbig Ae disk model adopted in this work has a radially continuous structure with no inner hole and/or gap. If we adopt a disk model with an inner hole and/or gap, the emission fluxes of water lines, especially from the hot water vapor inside the H_2O snowline is expected to decrease. Recently ALMA observations with high spatial resolution have been conducted towards protoplane-

tary disks with various central star masses/ages (e.g., ALMA Partnership et al. 2015; Andrews et al. 2016; Isella et al. 2016; Tsukagoshi et al. 2016), and will help understand these evolutionary scenarios.

3.3.2. *Critical density and the assumption of LTE*

In this subsection, we discuss the validity of the assumption of LTE. As we discussed in paper I (Notsu et al. 2016), the assumption of LTE is valid in calculating the emission flux of the 682.66μm line. This is because this line mainly comes from the hot region around $z/r \sim 0.1$ within the H_2O snowline where the total gas density ($\sim 10^{11} - 10^{14}$ cm^{-3}) is much larger than the critical density for this line ($n_{cr}= 1.0 \times 10^6$ cm^{-3}, see also Table 4). On the other hand, in our LTE calculations it remains possible that we have overestimated the emission flux of strong water lines with large A_{ul} ($\sim 10^{-1} - 10^0$ s^{-1}) which trace the hot surface layer of the inner/outer disk (e.g., the 12.40 μm and the 63.32 μm lines) and lines which trace the cold water vapor in the photodesorbed layer (e.g., the 538.29 μm line). The values of n_{cr} of these lines (e.g., $n_{cr}= 1.1 \times 10^{11}$, 1.5×10^{10}, and 2.9×10^7 cm^{-3} for the 12.40 μm, the 63.32 μm, and the 538.29 μm lines, respectively) are larger than or similar to the total gas density in the hot surface layer of the inner/outer disk ($\sim 10^7 - 10^8$ cm^{-3}) and the photodesorbed layer ($\sim 10^8 - 10^{10}$ cm^{-3}). Previous studies which model such water lines (e.g., Meijerink et al. 2009; Woitke et al. 2009b; Banzatti et al. 2012; Antonellini et al. 2015, 2016) showed that non-LTE calculations are important for the latter lines. They suggested that non-LTE effects may, however, alter line fluxes by factors of only a few for moderate excitation lines (E_{up} < a few thousand K). Moreover, current non-LTE calculations are likely to remain inaccurate, due to the incompleteness and uncertainty of collisional rates (e.g., Meijerink et al. 2009; Banzatti et al. 2012; Kamp et al. 2013; Zhang et al. 2013; Antonellini et al. 2015).

We calculated the critical density n_{cr} of the six other lines discussed in Section 3.2.3 and Figures 29, 30, and 31 as probes interior to the H_2O snowline (the 17.75, 24.00, 61.32, 94.17, 482.99, and 933.28 μm lines, see Table 4). n_{cr} for the sub-millimeter lines at 482.99, 682.66, and 933.28 μm (3.3×10^6,

1.0×10^6, and 4.7×10^6 cm^{-3}, respectively) are lower than the values of the total gas density in the hot surface layer of the outer disk ($\sim 10^7-10^8$ cm^{-3}) and in the photodesorbed water layer ($\sim 10^8-10^{10}$ cm^{-3}). In contrast, $n_{\rm cr}$ for the mid- to far-infrared lines (8.3×10^{10}, 1.9×10^9, 4.1×10^8, and 3.1×10^8 cm^{-3} for the 17.75, 24.00, 61.32, and 94.17 μm lines, respectively) are similar to and larger than the values of the total gas density in those regions. This is because the latter infrared lines have larger Einstein A coefficients and shorter wavelengths compared with the aforementioned sub-millimeter lines. If the wavelength of a line is shorter, the energy difference between the upper and lower state is larger and the value of collisional rates $<\sigma v>$ tends to be smaller (Faure & Josselin 2008). However, emission from these lines mainly comes from the hot water vapor within the H_2O snowline where total gas density is much larger ($\sim 10^{11}-10^{14}$ cm^{-3}) than the values of $n_{\rm cr}$, and thus it is valid to use LTE to calculate their fluxes.

3.3.3. *Previous water line observations in Herbig Ae disks*

Since water line emission from the disk midplane is likely obscured by dust grains at near- to mid-infrared wavelengths (Walsh et al. 2015), the "visible" H_2O gas column density at these wavelengths is smaller than the total H_2O column density integrated over the disk in the vertical direction (see e.g., Figure 28). For example, in Walsh et al. (2015), the visible column density at 14μm in the Herbig Ae disk case is $\sim 10^{19}-10^{20}$ cm^{-2} within the H_2O snowline. In the bottom panel of Figure 28, the visible H_2O gas column densities at 17.75, 61.32, and 682.66μm in the Herbig Ae disk are $\sim 10^{18}-10^{19}$ cm^{-2} within the H_2O snowline, which are lower than those of Walsh et al. (2015). This is because the total integrated column density of water vapor in our model ($\sim 10^{20}-10^{22}$ cm^{-2}) is lower than that of Walsh et al. (2015) ($\sim 10^{21}-10^{23}$ cm^{-2}), and because absorption by dust grains is dominant in the disk midplane and the disk surface ($\tau_{ul}\lesssim 1$) compared to that by excited gas molecules, especially remarkable in the cases of infrared lines (see also Section 3.2.3). Previous near- and mid-infrared spectroscopic observations using instruments on ground and space telescopes (e.g., VLT/CRIRES and *Spitzer*/IRS) for Herbig Ae disks (Pontoppidan et al. 2010a; Fedele et al. 2011; Salyk et al. 2011) have not detected the H_2O lines, and they derive upper limits for H_2O gas column

densities ($\lesssim 10^{18}$ cm^{-2}). However, such near- and mid-infrared water lines are observed in many T Tauri disks (e.g., Pontoppidan et al. 2010a). Water lines at far-infrared wavelengths have been detected with *Herschel*/PACS only in the disk around HD163296, although this emission originates in the hot surface layer of the outer disk ($r > 15$ au), and it is farther out than that expected for emission at shorter wavelengths (Fedele et al. 2012, 2013; Meeus et al. 2012). From these observational results, there is an important question as to why the detection rate for near- and mid-infrared water lines for T Tauri disks is higher than that for Herbig Ae disks.

Previous studies (e.g., Woitke et al. 2009b; Pontoppidan et al. 2010a; Fedele et al. 2011; Meeus et al. 2012; Walsh et al. 2015; Antonellini et al. 2015, 2016) discussed some answers to the above question. Here we highlight some important ideas (see also Section 3.2.4). First, there may be additional destruction routes for gas-phase water in the inner disk atmosphere, not yet included in the chemical networks we have adopted, for example the reaction to produce OH via photodissociation of H_2O by Lyman-α photons (Walsh et al. 2015). Second, dust-grain settling and dust-grain growth can reduce the total dust-grain surface area and possibly increase the UV irradiation rates in the upper disk (e.g., Vasyunin et al. 2011; Akimkin et al. 2013), which can push the molecular layer deeper into the disk atmosphere. Hence, a higher fraction of the gas-phase water may be hidden from view (e.g., Walsh et al. 2015; Krijt et al. 2016). We note that HD100546, for which far-infrared water lines have not been detected, has very high UV flux from the central star and even at 30 au the UV field is expected to be too strong for gas-phase water to survive (Meeus et al. 2012). Tilling et al. (2012) modeled the disk of HD163296 and pointed out that the dust material is settled. Meanwhile, dust-grain growth and the dust-grain shape also affect the UV field through scattering efficiency in the disk atmosphere. If the dust-grain radius is large enough compared with the wavelength of radiation from the central star, forward scattering by dust grains becomes efficient and the UV field decreases in the disk atmosphere (e.g., Bethell & Bergin 2011). The gas temperature in the disk atmosphere, which affects the water line fluxes, is also controlled by the UV radiation field. If the UV radiation field increases/decreases, the gas temperature in the disk atmosphere will become higher/lower.

We have assumed isotropic dust scattering and the grain size distribution of the dark cloud model with compact and spherical dust grains (For more details, see Nomura & Millar 2005 and paper I, Notsu et al. 2016), and these assumptions will affect the resulting H_2O line fluxes. Third, if the disk is transitional and has a significant gap/hole in the inner disk (e.g., HD100546), the line fluxes from the inner disk atmosphere will be decreased (e.g., Banzatti et al. 2017, see also Section 3.3.1).

Fourth, in Herbig Ae disks the strong infrared excess of dust emission might veil the faint emission of molecular lines at infrared wavelengths (e.g., Lahuis et al. 2007; Pontoppidan et al. 2010a; Fedele et al. 2011; Antonellini et al. 2015, 2016). Previous line modeling calculations such as Du & Bergin (2014) and Antonellini et al. (2015, 2016) concluded the infrared and sub-millimeter water line fluxes are affected by many parameters related to disk physical structure, such as dust-size distribution, dust-to-gas mass ratio, disk gas mass, maximum dust size, and luminosity of the central star. Antonellini et al. (2015, 2016) showed that the sensitivity and spectral resolution of previous mid-infrared observations (e.g., *Spitzer*/IRS) were not sufficient to detect the detailed profiles of even strong H_2O lines (with large A_{ul}) in many disks, especially disks around high-mass Herbig Ae/Be stars. This was because of the presence of noise in the spectra which can mask the line emission, combined with the high dust continuum flux (the noise level is proportional to the dust continuum flux).

3.3.4. *Requirement for the observations of candidate ortho-$H_2{}^{16}O$ lines*

Since the velocity width between the emission peaks is $\sim$20 km s^{-1}, high-dispersion spectroscopic observations (R=$\lambda/\delta\lambda$> tens of thousands) of the water lines in Table 5 are needed to trace emission from the hot water vapor within the H_2O snowline. Their profiles contain information which can be used to locate the position of the H_2O snowline. The area of the emitting regions are small ($r<$ 2 au for a T Tauri disk and $r <$ 14 au for a Herbig Ae disk) compared with the total disk size. The spectral resolution (of many instruments) and sensitivity used for previous mid-infrared, far-infrared, and sub-millimeter observations (e.g., *Spitzer*/IRS, *Herschel*/PACS, *Herschel*/HIFI)

were not sufficient to detect and resolve the candidate lines we identified in Table 5 which trace emission from the hot water vapor within H_2O snowline.

Among the various water lines in ALMA Band 8, the ortho-$H_2{}^{16}O$ 682.66μm line is the most suitable to trace emission from the hot water vapor within the H_2O snowline. Other candidate sub-millimeter H_2O lines to trace the H_2O snowline, having the same order-of-magnitude fluxes, exist in ALMA Bands 7, 9 and 10 ($\sim 300 - 1000$ μm). The ortho-$H_2{}^{16}O$ 933.28μm and 482.99μm lines are the most suitable lines in ALMA Bands 7 and 9, respectively. Here we note that although there is no candidate ortho-$H_2{}^{16}O$ line in ALMA Band 10, some candidate para-$H_2{}^{16}O$ lines do fall in this band. With ALMA, we can now conduct high sensitivity $\left(\sim 10^{-21} - 10^{-20}\ \mathrm{W\ m^{-2}}\ (5\sigma,\ 1\ \mathrm{hour})\right)$, high-dispersion (R> 100,000), and even high spatial resolution (< 100 mas) spectroscopic observations. Since the total fluxes of the candidate sub-millimeter lines which trace the emission from hot water vapor within the H_2O snowline are low in T Tauri disks ($\sim 10^{-22} - 10^{-21}$ W m^{-2}), they remain challenging to detect with current ALMA sensitivity unless we have an unrealistically long integration time (see paper I, Notsu et al. 2016). However, in hotter Herbig Ae disks, in younger T Tauri disks (e.g., HL Tau, ALMA Partnership et al. 2015; Banzatti et al. 2015; Harsono et al. 2015; Zhang et al. 2015; Okuzumi et al. 2016), and in disks around FU Orionis type stars (e.g., V883 Ori, Cieza et al. 2016), the H_2O snowline exists at a larger radius and the fluxes of these lines will be stronger compared with those in our fiducial T Tauri disk.

Our calculations for a Herbig Ae disk predict the fluxes of the 482.99μm (band 9), 682.66μm (band 8), and 933.28μm (band 7) lines to be around $10^{-21} - 10^{-20}$ W m^{-2} if we assume that the distance to the object d is 140pc ($\sim$ the distance of Taurus molecular cloud), and the inclination angle of the disk i is 30 deg. Thus the possibility of a successful detection is expected to increase in such Herbig Ae disks and could be achieved with current ALMA capabilities. Here we mention that the 933.28 μm line has been detected with high spectral resolution in the disk and outflow around the massive protostar candidate, Source I in Orion KL (Hirota et al. 2014), using ALMA, and around the embedded low

mass protostar (Class I), HL Tau, using SMA (Kristensen et al. 2016). Kristensen et al. (2016) suggested that future observations at higher sensitivity and angular resolution with ALMA will clarify the origin of this water emission from HL Tau and resolve the disk structures.

Candidate H_2O lines to trace the H_2O snowline exist over a wide wavelength range, from mid-infrared to sub-millimeter. As we discuss in Section 3.2.5, the values of the total fluxes tend to increase as the wavelengths of the candidate water lines which trace emission from the hot water vapor within H_2O snowline become shorter (see Tables 4, 5, and Figure 36). There are future mid-infrared instruments covering the part of Q band which will enable high sensitivity and high-dispersion spectroscopic observations: the HRS on SPICA[10] Mid-infrared Instrument (SPICA/SMI) and Mid-Infrared Camera High-disperser & IFU spectrograph on the Thirty Meter Telescope (TMT/MICHI, e.g., Packham et al. 2012). HRS on SPICA/SMI will have a relatively high spectral resolution (R$\sim$ 28,000), and especially high sensitivity $\left(\sim 10^{-20}\ \mathrm{W\ m^{-2}}\ (5\sigma,\ 1\ \mathrm{hour})\right)$ compared with previous mid-infrared instruments at the same wavelengths. TMT/MICHI will have a high spectral resolution (R$\sim$ 60,000$-$120,000), high sensitivity $\left(\sim 10^{-19}\ \mathrm{W\ m^{-2}}\ (5\sigma,\ 1\ \mathrm{hour})\right)$. The ortho-$H_2{}^{16}O$ 17.75μm and 24.00 μm lines are in the Q band at mid-infrared wavelengths, and the former line falls in the wavelength coverage of SPICA/SMI-HRS and TMT/MICHI. Here we note that since TMT is a ground-based telescope, the effect of atmospheric absorption has to be considered carefully in selecting lines from the candidate line list. Figure 37 shows the profiles of mid-infrared candidate lines ($\lambda \sim 11-25\mu$m) which trace emission from the hot water vapor within H_2O snowline. All of the lines in this Figure are also listed in Table 5. Our calculations for a Herbig Ae disk suggest that the fluxes of the stronger candidate water lines in Q band (including ortho-$H_2{}^{16}O$ 17.75μm and 24.00μm lines) are $\sim 10^{-17} - 10^{-18}$ W m^{-2}. Since HRS on SPICA/SMI has a high sensitivity in Q band, we predict not only successful detections for some Herbig Ae disks, but also suggest the possibility of a survey of the locations of H_2O snowlines in Herbig Ae disks in nearby ($\lesssim$150 pc) star-forming regions

[10] http://www.ir.isas.jaxa.jp/SPICA/SPICA_HP/research-en.html

for the first time. Moreover, since HRS on SPICA/SMI has an especially high sensitivity, successful detections are expected even for T Tauri disks in nearby ($\lesssim$150pc) star-forming regions, as well as Herbig Ae disks in the Orion star-forming region ($\sim$410 pc), with several hours of observations. Our calculations for a T Tauri disk (see Tables 4 and 5) show that the fluxes of the strongest candidate water lines at Q band (including 17.75μm and 24.00μm lines) are $\sim 10^{-20} - 10^{-21}$ W m^{-2}.

We also expect to detect emission from those candidate lines (some of which are not accessible from the ground) which trace emission from the hot water vapor within the H_2O snowline using other high sensitivity mid-infrared and far-infrared instruments on future space telescopes, such as The Mid-Infrared Instrument on board the James Webb Space Telescope (JWST/MIRI[11]), SPICA FAR-infrared Instrument (SPICA/SAFARI), and MRS of SPICA/SMI. Since the spectral resolution of these instruments is not so high ($\sim$ a few thousands), we cannot resolve the velocity profiles of these candidate lines at sufficient resolution to locate the position of the H_2O snowline. However, it will be possible to detect the total fluxes of these candidate lines with these high sensitivity instruments. Our results suggest that these lines mainly trace emission from the hot water vapor within the H_2O snowline. Moreover, since the sensitivity of these instruments is very high, meaning that the time necessary for a detection is not very long, we expect to detect emission from the hot H_2O gas inside the H_2O snowline for various protoplanetary disks, which are suitable candidates for high-dispersion spectroscopic observations with future instruments (e.g., ALMA, SPICA/SMI-HRS).

3.4. *Conclusions*

In this work, we calculated the disk water vapor distribution and corresponding water line profiles for a Herbig Ae disk, and identified candidate water lines which can locate the position of the H_2O snowline across a wide wavelength range from mid-infrared to sub-millimeter.

[11] http://ircamera.as.arizona.edu/MIRI/index.htm

First we calculated the chemical composition using a self-consistent physical model of a Herbig Ae disk, and investigated the abundance distributions of H_2O gas and ice, and the position of the H_2O snowline. We found that the abundance of H_2O is high (up to 10^{-4}) in the inner region with higher temperature ($\gtrsim$ 170K) within $\sim 7-8$ au, relatively high ($\sim 10^{-8}$) between $7-8$ au and 14 au (= the position of the H_2O snowline, $\sim$120K) near the equatorial plane. In addition, it is relatively high ($\sim 10^{-8}-10^{-7}$) in the hot surface layer and the photodesorbed region of the outer disk, compared to its value ($\sim 10^{-12}$) in the regions outside the H_2O snowline near the equatorial plane. The position of the H_2O snowline in the Herbig Ae disk is further from the central star compared to that in the T Tauri disk, in agreement with previous studies (e.g., Woitke et al. 2009b).

Second, we calculated the ortho-$H_2{}^{16}O$ line profiles, and showed that ortho-$H_2{}^{16}O$ emission lines with small Einstein A coefficients ($A_{ul} \sim 10^{-3}-10^{-6}$ s^{-1}) and relatively high upper state energies ($E_{up} \sim$ 1000K) are dominated by emission from the region inside the H_2O snowline, and therefore their profiles potentially contain information which can be used to locate the position of the snowline. Since the fluxes of these lines from Herbig Ae disks are larger than those from T Tauri disks, the possibility of a successful detection is expected to increase for a Herbig Ae disk. The wavelengths of those lines which are the best candidates to locate the position of the H_2O snowline range from mid-infrared to sub-millimeter. The values of total fluxes tend to be larger as the wavelengths of the water lines become shorter. This is because the peak wavelength of the Planck function at the gas temperature around the H_2O snowline ($T_g \sim 100-200$ K) is in the mid-infrared region.

In addition, we investigated the properties of water lines which have been detected by previous spectroscopic observations (e.g., 63.32μm, 538.29μm). These lines are less suited to locate the H_2O snowline, because they are not dominated by emission from the region within the H_2O snowline. The properties of near-, and mid-infrared water emission lines which do not trace emission from the hot water vapor within the H_2O snowline are also discussed.

The wavelengths of such candidate lines which trace emission from the hot water vapor within H_2O snowline overlap with the capabilities of ALMA and future mid-infrared high-dispersion spectrographs (e.g., SPICA/SMI-HRS). The successful detection in a Herbig Ae disk could be achieved with current ALMA capabilities using several lines. Mid-infrared instruments such as HRS on SPICA/SMI would have a high sensitivity in the Q band (e.g., $\sim$ 16-18μm), and we predict not only successful detections for some Herbig Ae disks, but also suggest the possibility of a survey of H_2O snowline locations in many Herbig Ae disks in nearby ($\lesssim$150pc) star-forming regions for the first time.

4. MODELING STUDIES III. SUB-MILLIMETER $H_2{}^{16}O$ AND $H_2{}^{18}O$ LINES (NOTSU ET AL. 2018)

4.1. *Methods*

4.1.1. *The disk physical structures and molecular abundances*

In this work (paper III, Notsu et al. 2018), we adopt the molecular abundance distribution of a T Tauri disk and a Herbig Ae disk which were calculated in paper I (Notsu et al. 2016)[12] and paper II (Notsu et al. 2017), using self-consistent disk physical models. Here we briefly explain our disk model.

In our works (see also papers I and II), we used self-consistent physical models of steady, axisymmetric Keplerian disks surrounding a T Tauri star and a Herbig Ae star. They were calculated on the basis of the methods in Nomura & Millar (2005) with X-ray heating (Nomura et al. 2007). Walsh et al. (2010, 2012, 2014a, 2015), Heinzeller et al. (2011), Furuya et al. (2013), and Notsu et al. (2015) adopted the same physical models to study various physical and chemical effects. Table 6 shows the central star and disk parameters of our adopted models in detail.

The gas and dust are assumed to be mixed well. In this model, we adopt a size distribution of spherical, compact dust grains that replicates the extinction curve observed in dense clouds (Mathis et al. 1977; Weingartner & Draine 2001).

In Figures 15 and 26, we displayed the gas number densities, the gas temperatures $T_{\rm g}$, the dust-grain temperatures $T_{\rm d}$, and the wavelength-integrated UV fluxes in a T Tauri disk and a Herbig Ae disk, respectively. In Section 3.1 of this thesis (see also paper II), we discussed the differences between the physical structures of the T Tauri disk and the Herbig Ae disk in detail.

[12] In the remainder of this thesis, we often mention Notsu et al. (2016) and Notsu et al. (2017) as papers I and II, respectively.

Table 6. The central star and disk parameters of our adopted physical models

Star	M_*	R_*	T_*	$\dot{M}$	α	g/d	$M_{\rm disk}$	UV excess?
	$[M_\odot]$	$[R_\odot]$	[K]	$[M_\odot\ {\rm yr}^{-1}]$			$[M_\odot]$	
T Tauri	0.5	2.0	4000	10^{-8}	10^{-2}	100	2.4×10^{-2}	Yes
Herbig Ae	2.5	2.0	10,000	10^{-8}	10^{-2}	100	2.5×10^{-2}	No

Notes: M_*: central star mass, R_*: star radius, T_*: star effective temperature, $\dot{M}$: mass accretion rate, α: viscous parameter, g/d: gas to dust mass ratio, $M_{\rm disk}$: total disk mass

UV excess?: whether stellar UV radiation field has excess emission components, such as Lyman-α line emission and optically thin hydrogenic bremsstrahlung radiation.

The large chemical network we use to calculate the disk molecular abundances includes gas-phase reactions and gas-grain interactions (freeze-out, and thermal and non thermal desorption). We adopt the set of atomic oxygen-rich abundances (Graedel et al. 1982; Woodall et al. 2007) as the initial elemental fractional abundances. Figures 17 and 27, of papers I and II showed the fractional abundances (relative to total gaseous hydrogen nuclei density) of H_2O vapor ($n_{\rm H2O,gas}/n_{\rm H}$) and ice ($n_{\rm H2O,ice}/n_{\rm H}$) in a T Tauri disk and a Herbig Ae disk.

4.1.2. *Water emission line profiles from protoplanetary disks*

We calculate the Keplerian profiles of water emission lines from the T Tauri disk and the Herbig Ae disk, and identify those emission lines which are the best candidates for tracing emission from the inner gaseous water within the H_2O snowline. In papers I and II, we used the same method to calculate the profiles of water emission lines from a Herbig Ae disk and a T Tauri disk (based on Rybicki & Lightman 1986, Hogerheijde & van der Tak 2000, Nomura & Millar 2005, and Schöier et al. 2005, see also Section 2.1.5 of this thesis.). In this work, we extend our water line calculations beyond ortho-$H_2{}^{16}O$ lines only (papers I and II), to sub-millimeter para-$H_2{}^{16}O$ and ortho- and para-$H_2{}^{18}O$ lines. In addition, we focus on the sub-millimeter lines, in order to investigate more

thoroughly the possibility of observing the H_2O snowline with ALMA.

For the calculation of line profiles, we modified the 1D code RATRAN[13] (Hogerheijde & van der Tak 2000). The data for the line parameters are adopted from the Leiden Atomic and Molecular Database LAMDA[14] (Schöier et al. 2005) for the $H_2{}^{16}O$ lines and from the HITRAN Database[15] (e.g., Rothman et al. 2013) for the $H_2{}^{18}O$ lines. We also cross-referenced the values of line parameters with the Splatalogue database[16]. The value of the ortho-to-para ratio (OPR) of water is set to 3, which is the high-temperature value (Mumma et al. 1987; Hama & Watanabe 2013; Hama et al. 2016). Here we mention that Hama et al. (2016) reported from their experiments that water desorbed from the icy dust-grain surface at 10K shows the OPR = 3, which invalidates the assumed relation between OPR and the formation temperature of water (Mumma et al. 1987). They argue that the role of gas-phase processes that convert the OPR to a lower value in low temperature regions is important, though the detailed mechanism is not yet understood. We set the isotope ratio of oxygen $^{16}O/^{18}O$ to 560 throughout the disk, as Jørgensen & van Dishoeck (2010) and Persson et al. (2012) adopted. This $^{16}O/^{18}O$ value is determined by the observation of local interstellar medium (Wilson & Rood 1994). We do not include emission from jet components and disk winds in calculating the line profiles.

The assumption of local thermal equilibrium (LTE) is adopted in our calculations to obtain the level populations of the water molecule. In Sections 2.3.2 and 3.3.2, we discussed the validity of this assumption, and we concluded that the LTE assumption is valid when we calculate the candidate water lines which probe emission from hot gaseous water inside the H_2O snowline. This is because these lines mainly come from the dense region ($\sim 10^{11} - 10^{14}$ cm^{-3}) at $z/r < 0.1$ inside the H_2O snowline, while they have low values of Einstein A coefficients, such that their critical densities

[13] http://home.strw.leidenuniv.nl/~michiel/ratran/
[14] http://home.strw.leidenuniv.nl/~moldata/
[15] http://www.hitran.org
[16] http://www.cv.nrao.edu/php/splat/

Table 7. The regional classifications in the disk midplane with different water abundances

Region name	Star	r [au]	T_g [K]	$n_{\rm H2O,gas}/n_{\rm H}$	Comments
A_{TT}	T Tauri	0−2	> 150	$\sim 10^{-5} - 10^{-4}$	inside the H_2O snowline
B_{TT}		2−30	< 150	$\sim 10^{-12}$	outside the H_2O snowline
A_{HA}	Herbig Ae	0−8	> 170	$\sim 10^{-5} - 10^{-4}$	high H_2O abundance region
B_{HA}		8−14	$120 - 170$	$\sim 10^{-8}$	inside the H_2O snowline
C_{HA}		14−30	< 120	$\sim 10^{-12}$	outside the H_2O snowline

Notes: r: the disk radius from the central star, T_g: disk gas temperature, $n_{\rm H2O,gas}/n_{\rm H}$: the fractional abundances (relative to total gaseous hydrogen nuclei density) of water vapor

$n_{\rm cr} = A_{ul}/<\sigma v>$[17] are relatively small ($n_{\rm cr} \sim 10^5 - 10^7$ cm^{-3}, see also Table 4). Here we note that $n_{\rm cr}$ of the para-$H_2{}^{16}O$ 183 GHz and 325 GHz lines are 1.4×10^5 and 1.2×10^6 cm^{-3}, respectively. These values are lower than the values of the total gas density not only in the inner disk midplane, but also in the hot surface water layer of the outer disk ($\sim 10^7 - 10^8$ cm^{-3}) and in the photodesorbed water layer ($\sim 10^8 - 10^{10}$ cm^{-3}). In contrast, non-LTE effects are important for strong water lines which have large $A_{\rm ul}$ ($\sim 10^{-1} - 10^0$ s^{-1}), and trace the inner/outer hot surface layers (e.g., the ortho-$H_2{}^{16}O$ 63.32 μm line) or the cold photodesorbed layer (e.g., the ortho-$H_2{}^{16}O$ 557 GHz and the para-$H_2{}^{16}O$ 1113 GHz lines, see e.g., Meijerink et al. 2009; Woitke et al. 2009b; Banzatti et al. 2012; Antonellini et al. 2015, 2016).

4.2. *Results*

4.2.1. *The velocity profiles of sub-millimeter water emission lines*

Figures 40 and 41 show the velocity profiles for representative characteristic para-$H_2{}^{16}O$ lines at 183 GHz (top left) and 1113 GHz (bottom left), and para-$H_2{}^{18}O$ lines at 203 GHz (top right) and 1102

[17] $<\sigma v>$ is the collisional rates for the excitation of H_2O molecules by electrons and H_2 molecules for an adopted value of the collisional temperature of 200K (Faure & Josselin 2008).

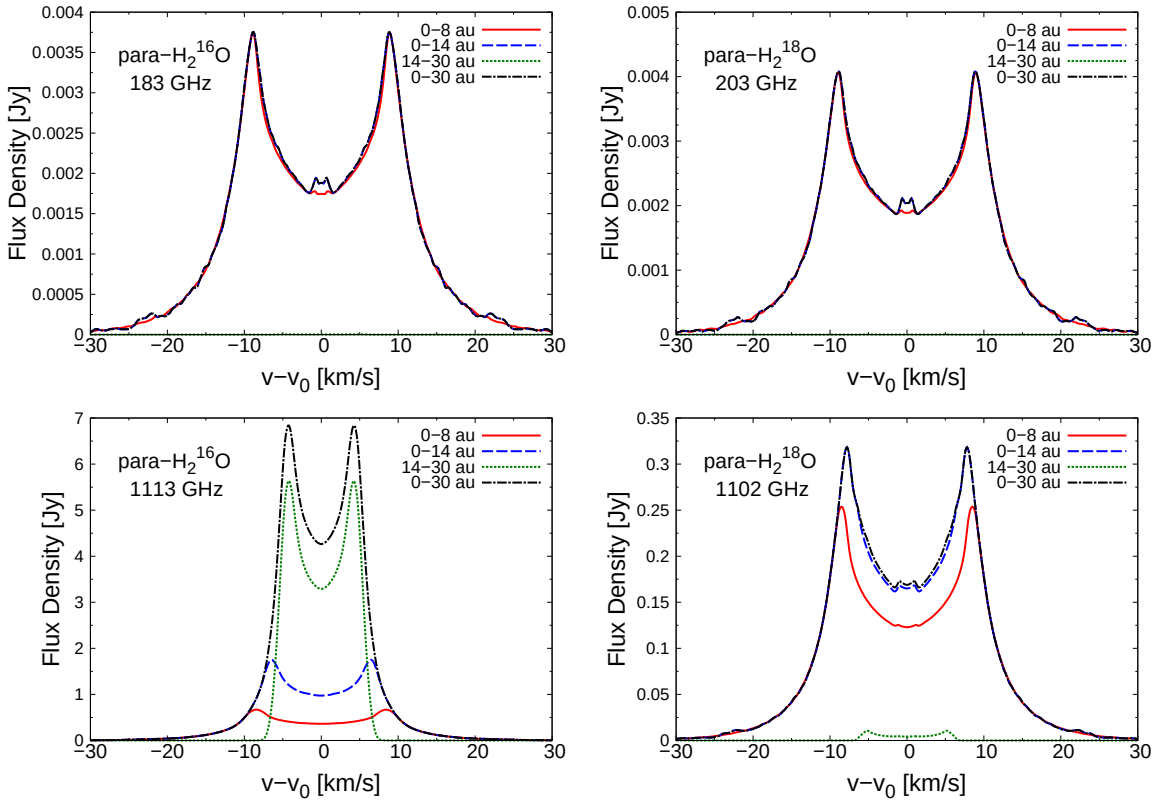

Figure 40. The profiles of para-$H_2{}^{16}O$ lines at 183 GHz (top left) and 1113 GHz (bottom left), and para-$H_2{}^{18}O$ lines at 203 GHz (top right), and 1102 GHz (bottom right) for the Herbig Ae disk. In these line profiles, we ignore dust emission and adopt a disk inclination, $i = 30$ deg and the distance to the object, $d = 140$ pc. The line profiles from inside 8 au (=the inner high temperature region) are displayed with *red solid lines*, those from within 14 au (∼within the H_2O snowline) are *blue dashed lines*, those from 14−30 au (∼outside the H_2O snowline) are *green dotted lines*, and those from the total area inside 30 au are *black dashed dotted lines*. In the top two panels, the flux densities outside the H_2O snowline (*green dotted lines*, $< 10^{-4}$ Jy) are much smaller than those inside 8 au (*red solid lines*). Therefore, the *red solid lines*, *blue dashed lines*, and *black dashed dotted lines* are almost completely overlapped (see also Figure 47).

GHz (bottom right) from the Herbig Ae disk and the T Tauri disk, respectively. The para-$H_2{}^{16}O$ 183 GHz line and the para-$H_2{}^{18}O$ 203 GHz line are the same transition levels and fall in ALMA Band 5 (Immer et al. 2016; Humphreys et al. 2017). The detailed parameters, such as transition quantum numbers ($J_{K_aK_c}$), wavelength λ, frequency, $A_{\rm ul}$, $E_{\rm up}$, and total fluxes of lines are listed in Tables 8

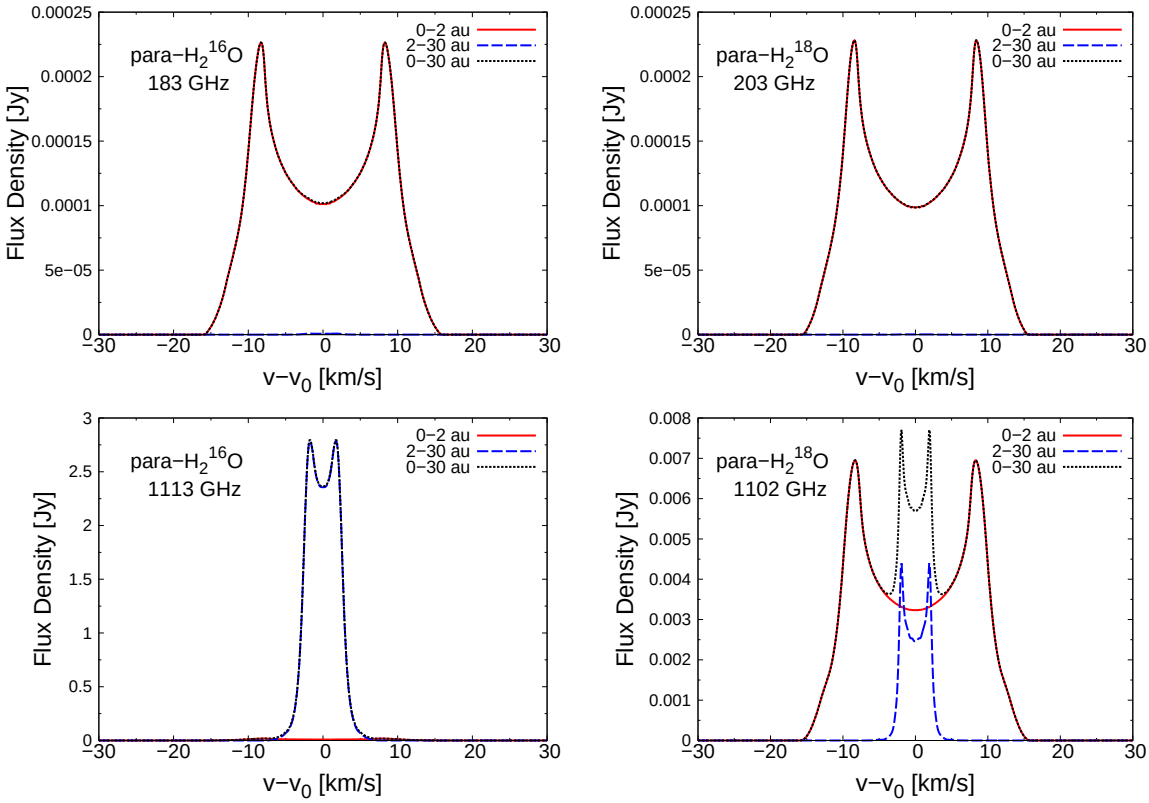

Figure 41. The same as Figure 40 but for the T Tauri disk. The line profiles from inside 2 au (∼within the H_2O snowline) are displayed with *red solid lines*, those from $2-30$ au (∼outside the H_2O snowline) are *blue dashed lines*, and those from the total area inside 30 au are *black dotted lines*. In the top two panels, the flux densities outside the H_2O snowline (*blue dashed lines*, $< 10^{-5}$ Jy) are much smaller than those inside the H_2O snowline (*red solid lines*). Therefore, the *red solid lines* and *black dotted lines* are almost completely overlapped. Moreover in the bottom left panels, the flux densities outside the H_2O snowline (*blue dashed lines*) are much larger than those inside the H_2O snowline (*red solid lines*). Therefore, the *blue dashed lines* and *black dotted lines* are almost completely overlapped.

and 9. In calculating the line profiles in Figures 40 and 41 (also Figures 46 and 47, see Section 4.2.4), and total fluxes in Tables 8 and 9, we do not include dust emission, although we do include both gas and dust absorption. We discuss the effects of dust emission in Section 4.3.1. In calculating line profiles and total fluxes in this work (see Figures 40, 41, 46, 47, 48 and 49, and Tables 8 and 9), we adopted the inclination angle of the disk, $i = 30$ deg and the distance to the object d =140 pc (∼ the

distance of Taurus molecular cloud).

The position of the H_2O snowline in the T Tauri disk (r ∼1.6 au, T_g ∼150K, see paper I) is closer to the central star than that in the Herbig Ae disk (r ∼14 au, T_g ∼120K, see paper II), in agreement with previous studies (e.g., Woitke et al. 2009b; Walsh et al. 2015). Table 7 shows the regional classifications in the disk midplane with different water fractional abundances (for more details, see also papers I and II). Inside the H_2O snowline (regions A_{TT}, A_{HA} and B_{HA}, see also Table 7), the temperature exceeds the sublimation temperature under the pressure conditions of the midplane and most of the H_2O molecules are released into the gas-phase through thermal desorption. Thus the column densities of water vapor become larger ($> 10^{16}$ cm^{-2}, see Figure 3 of paper II) than those of the outer disk ($\sim 10^{14}$ cm^{-2}). In the case of Herbig Ae disks, the gas-phase chemistry to form H_2O molecules is efficient in the inner region at a higher temperature (region A_{HA}, see Table 7), and the column densities of gaseous water molecules become much larger ($\sim 10^{20} - 10^{22}$ cm^{-2}, see Figure 28 of this thesis). Since the radial temperature profile in the midplane of the T Tauri disk is steeper than that of the Herbig Ae disk, the T Tauri disk does not have B_{HA} like transition region with relarively large fractional abundance of water vapor ($\sim 10^{-8}$). Thus in the cases of candidate water lines with smaller Einstein A coefficients (A_{ul}=10^{-6} $\sim$ 10^{-3} s^{-1}) and relatively high upper state energies (E_{up}∼1000K), the contribution to the line emission of the optically thick hot midplane inside the H_2O snowline is much higher than that of the outer optically thin surface layer.

In the top panels of Figures 40 and 41, the contributions from the inner disk within the H_2O snowline (regions A_{TT}, A_{HA} and B_{HA}, see also Table 7) are very large compared with the contributions from the outer disk (regions B_{TT}, C_{HA}, see also Table 7), and they have the characteristic Keplerian rotationally broadened double-peaked profiles. Moreover, in the line profiles from the Herbig Ae disk, most of the emission fluxes come from the high H_2O gas abundance region (region A_{HA}). The two peak positions and the rapid flux density drop between the peaks contains information on the hot H_2O vapor distribution inside the H_2O snowline. The spread in the wings of the emission profile

(high velocity regions) represents the inner edge of the H_2O gas distribution in the disk. This is because emission from each radial region in the disk is Doppler shifted due to the Keplerian rotation (see also Equations (13) and (14)). Comparing sub-millimeter water lines having the same transition quantum numbers ($J_{K_aK_c}$), the total flux of the para-$H_2{}^{16}O$ 183 GHz line tends to be 0.8 times larger than that of the para-$H_2{}^{18}O$ 203 GHz line (see Tables 8 and 9).

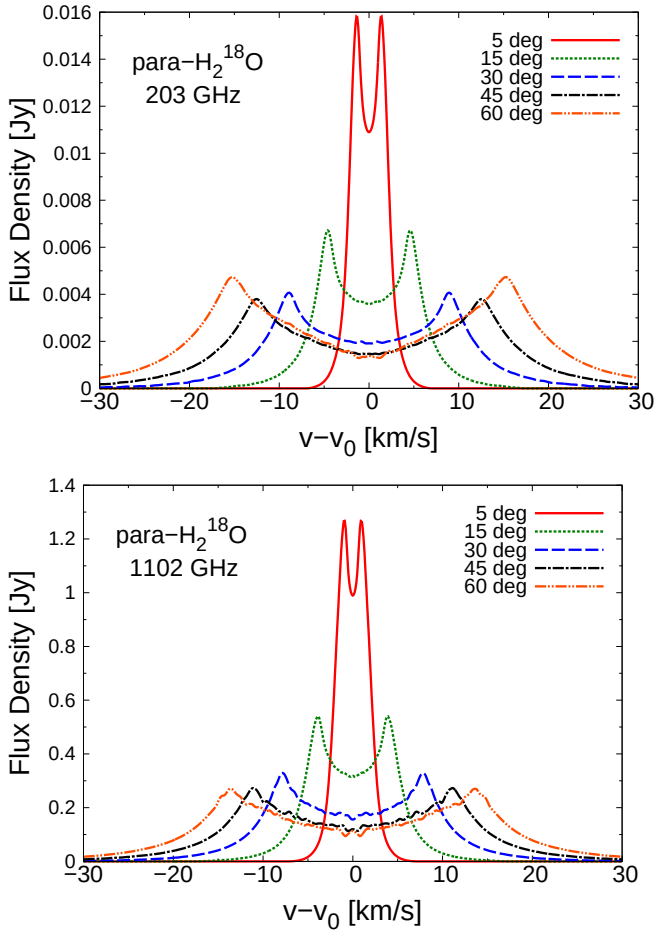

Figure 42. The velocity profiles for the para-$H_2{}^{18}O$ lines at 203 GHz (top panel) and 1102 GHz (bottom panel) from the Herbig Ae disk inside 30 au with different inclination angles, i = 5 deg (*red solid lines*), 15 deg (*green dotted lines*), 30 deg (*blue dashed lines*), 45 deg (*black dashed dotted lines*), and 60 deg (*orange dashed double dotted lines*).

Figure 42 shows the velocity profiles for the para-$H_2{}^{18}O$ lines at 203 GHz (top) and 1102 GHz (bottom) from the Herbig Ae disk inside 30 au with different inclination angles (i = 5, 15, 30, 45, 60 deg). If we observe objects with smaller/larger disk inclination angles than those of our original model value (i =30 deg), the widths of the line peaks become smaller/larger. This is because the projected Keplerian velocity is proportional to $\sin i$. If the object is nearly face on ($i \sim 0$ deg), the shape of the line profile is close to that expected from thermal broadening only, and the flux densities at the line peaks become larger. In contrast, in objects with larger disk inclination angles, the line emission components from various places in the disks are dispersed at various velocities due to the effect of Doppler shift. Thus the flux densities at the line peaks tend to be smaller as the disk inclination angles become larger. Here we note that the flux densities at the line peaks are similar in the cases of much larger inclination angles ($i > 45$ deg). Since the line width depends on central star mass and inclination angle of the disk, we have to know these values in advance through other observations (e.g., resolved imaging of strong molecular lines like CO lines) in order to locate the H_2O snowline from the profiles of water line emission.

In the bottom panels of Figures 40 and 41, except for the para-$H_2{}^{18}O$ 1102 GHz line for the Herbig Ae disk, the outer disk contributions (regions B_{TT}, C_{HA}, see Table 7) are large compared with that from the inner disk within the H_2O snowline (regions A_{TT}, A_{HA} and B_{HA}, see Table 7). In addition, the widths between the line double peaks are about $2-3$ times narrower than those of candidate water lines (see top panels of Figures 40 and 41), although the values of A_{ul} are not so high. This is because these water lines are the ground-state rotational transitions and have much smaller values of E_{up} ($\sim$50K) compared to those of other lines. The fluxes of these lines mainly come from the water reservoir in the outer cold photodesorption region.

4.2.2. *The local intensity and optical depth distributions*

Figure 43 shows the water line local intensity (emissivity times line-of-sight extinction and local length, $\eta_{ul}e^{-\tau_{ul}}$ds; see also Equation (16)) for the Herbig Ae disk. In the left panels of Figure 43, the total (gas and dust) optical depth contours (τ_{ul} =0.1, 1, and 10) are plotted on top of the line local

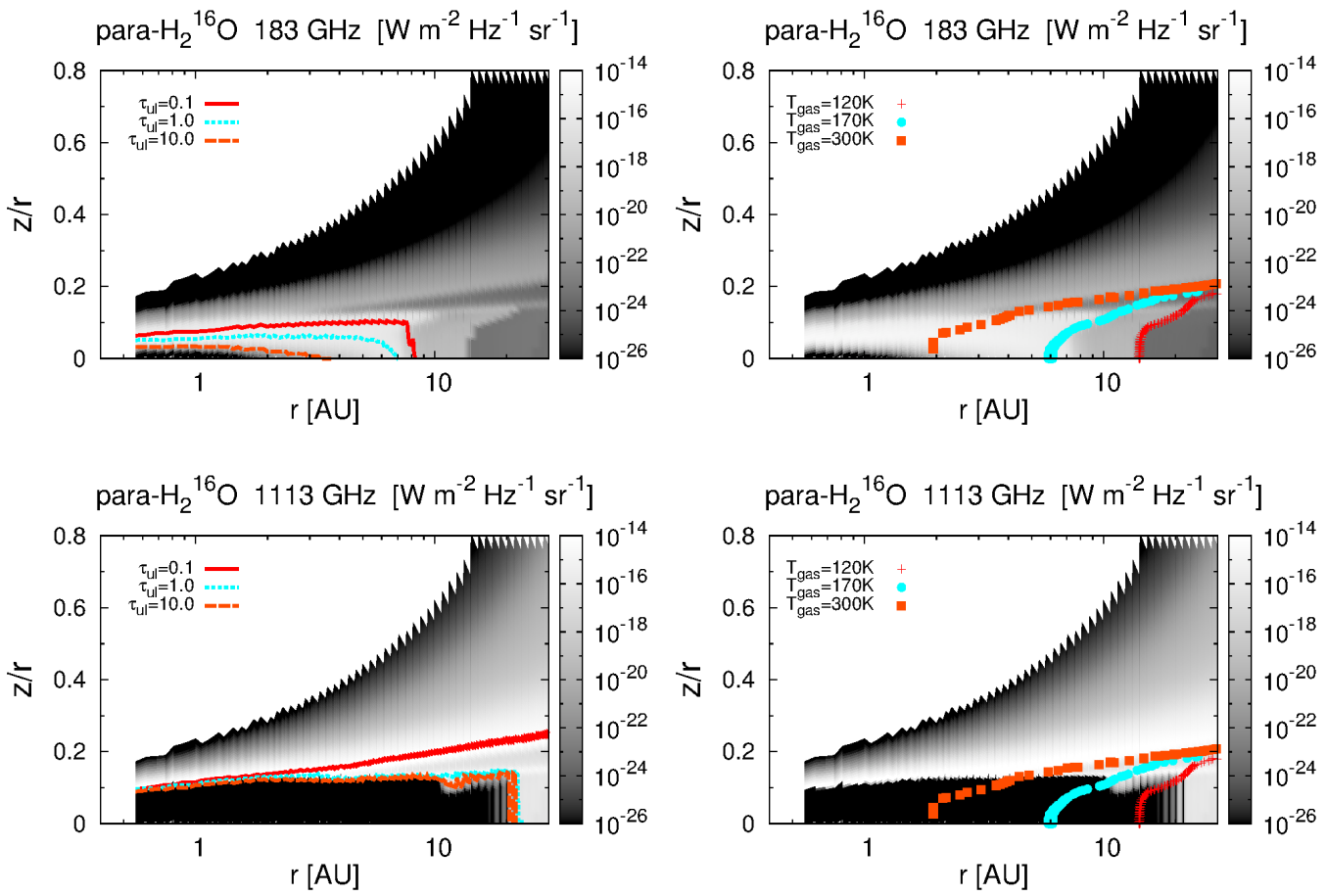

Figure 43. The local intensity distributions along the line-of sight direction of para-$H_2{}^{16}O$ lines at 183 GHz (top panels) and 1113 GHz (bottom panels) for the Herbig Ae disk. In the left panels, the total (gas and dust) optical depth contours for τ_{ul} =0.1 (red solid lines), 1 (cyan dotted lines), and 10 (orange dashed lines) are plotted on top of the line local intensities. The gas temperature contours for T_g =120K (red cross points), 170K (cyan circle points), and 300K (orange square points) are plotted in the right panels. The units of the local intensity are W m^{-2} Hz^{-1} sr^{-1}.

intensities. The gas temperature contours ($T_g = 120, 170, 300$K) are plotted in the right-hand panels. The line-of-sight direction corresponds to $z = +\infty$ to $-\infty$ at each disk radius, thus the inclination angle is assumed to be 0 deg. In calculating the values of τ_{ul}, we consider the contributions of both line absorption by the water gas and absorption by dust grains. Here we note that the units in Figures 40, 41, and 42 are Jy (= 10^{26} W m^{-2} Hz^{-1}) and the values are those observed on Earth.

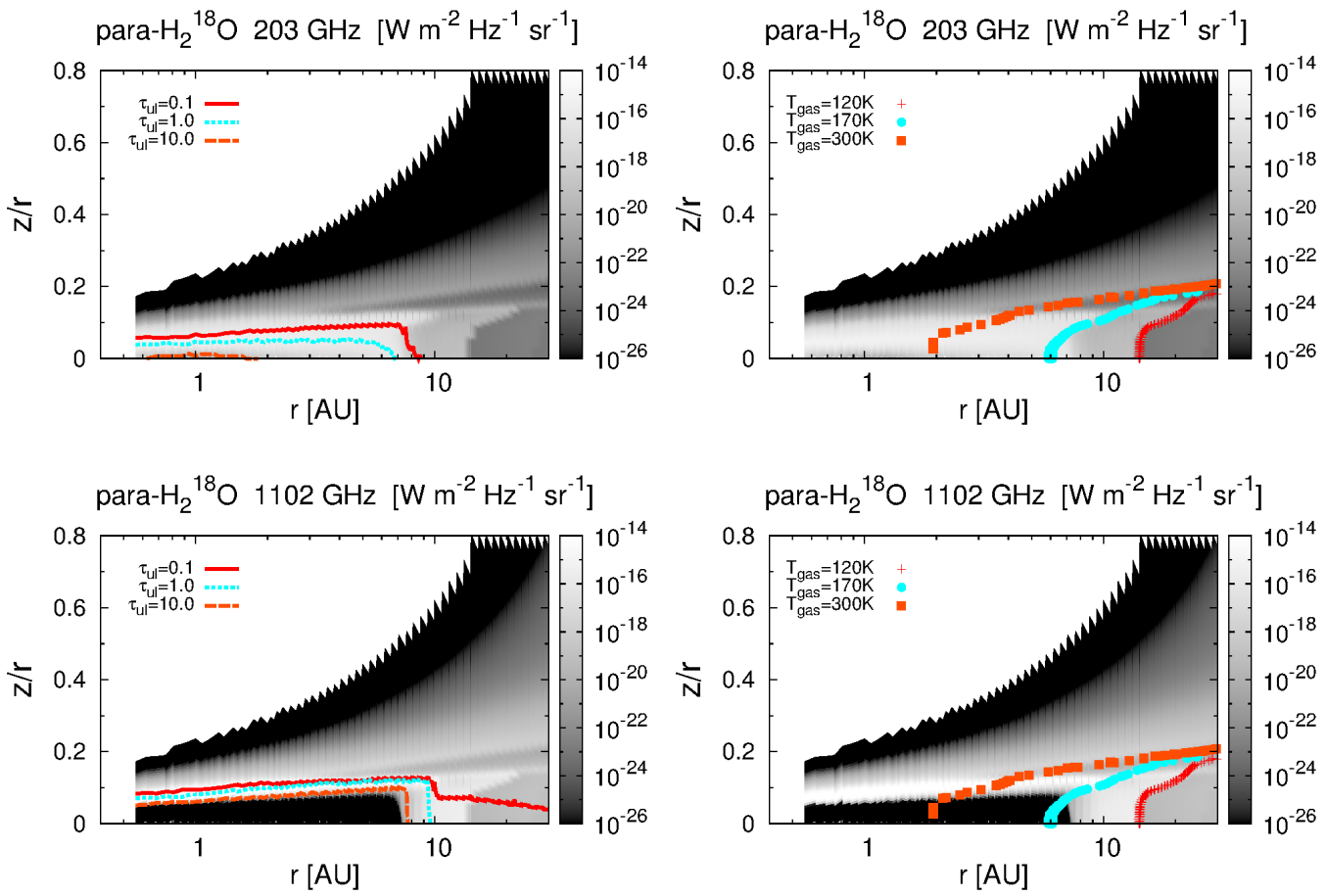

Figure 43. (Continued.) The local intensity distributions along the line-of sight direction of para-$H_2{}^{18}O$ lines at 203 GHz (top panels) and 1102 GHz (bottom panels) for the Herbig Ae disk.

In contrast, we plot the "local intensity" (not "flux density") of each grid in the disk in Figure 43, and the units in this figure are W m^{-2} Hz^{-1} sr^{-1} (see also papers I and II). Figure 44 shows the normalized cumulative line local intensity distributions along the vertical direction at r =5 au (top panels), r =10 au (middle panels), and r =30 au (bottom panels), along with the gas temperature T_g in K. In Figure 44, we also plot the para-$H_2{}^{16}O$ 325 GHz line and the para-$H_2{}^{18}O$ 322 GHz line, which are the same transition levels and fall in ALMA Band 7. Here we note that the detailed profiles of these two lines are shown in Figure 47.

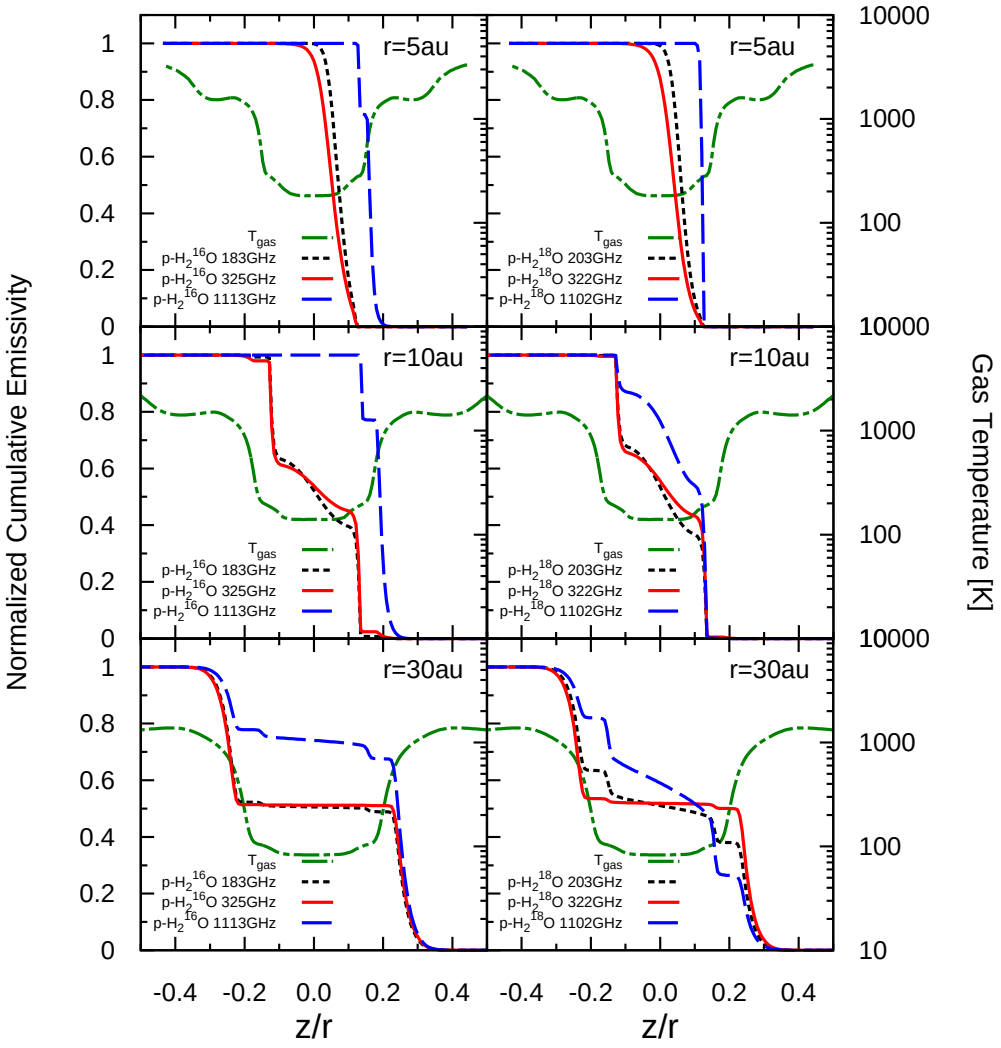

Figure 44. The normalized cumulative line local intensity distributions along the vertical direction at r =5 au (top panels), r =10 au (middle panels), and r =30 au (bottom panels), and the vertical distribution of the gas temperature T_g [Kelvin] (*green dashed dotted lines*). The distributions for three para-$H_2{}^{16}O$ lines at 183 GHz (*black dotted lines*), 325 GHz (*red solid lines*), 1113 GHz (*blue dashed lines*) from a Herbig Ae disk are shown in the left three panels. The distributions for three para-$H_2{}^{18}O$ lines at 203 GHz (*black dotted lines*), 322 GHz (*red solid lines*), 1102 GHz (*blue dashed lines*) from a Herbig Ae disk are shown in the right three panels. The cumulative local intensities are normalized using the values at $z = -\infty$.

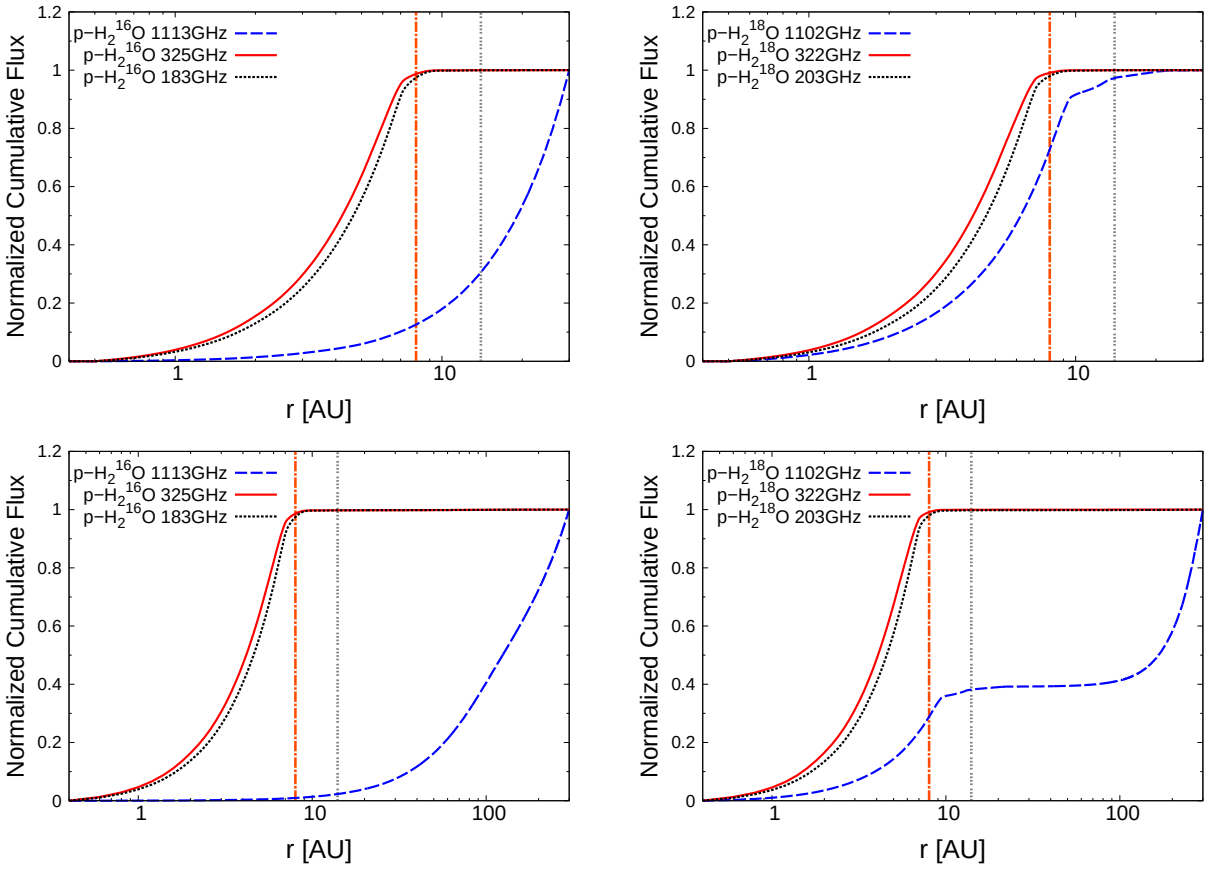

Figure 45. (Left two panels): The distributions of the normalized cumulative fluxes along the radial directions of three para-$H_2{}^{16}O$ lines at 183 GHz (*black dotted lines*), 325 GHz (*red solid lines*), and 1113 GHz (*blue dashed lines*) from a Herbig Ae disk. (Right two panels): The radial distributions of the normalized cumulative fluxes of three para-$H_2{}^{18}O$ lines at 203 GHz (*black dotted lines*), 322 GHz (*red solid lines*), and 1102 GHz (*blue dashed lines*) from the Herbig Ae disk. The vertical straight lines display the positions of r=14 au (*grey dotted line*) and 8 au (*orange dashed dotted line*), respectively. The cumulative fluxes are normalized using the values at $r = 30$ au (top panels) and at $r = 300$ au (bottom panels).

Looking at the top panels of Figures 43 and all panels of Figure 44, the value of local intensities within r <14 au (= the position of the H_2O snowline), T_g >120K, and $z/r \lesssim 0.1$ are larger than those from the outer optically thin hot surface layer and the photodesorption region. In particular, the local intensities from the high H_2O vapor abundance region (region A_{HA}) and $z/r \lesssim 0.1$ are much larger (see also Section 3.2.3 of this thesis). Here we note that these sub-millimeter lines have

smaller A_{ul} values ($\sim 10^{-5} - 10^{-6}$ s^{-1}), and relatively smaller E_{up} values ($\sim 200 - 500$K) compared with candidate ortho-$H_2{}^{16}O$ lines which were discussed in papers I and II ($A_{ul}\sim 10^{-3} - 10^{-6}$ s^{-1}, $E_{up}\sim 700 - 2100$K). For the sub-millimeter $H_2{}^{18}O$ and para-$H_2{}^{16}O$ lines, since the values of A_{ul} tend to be smaller (typically $<10^{-4}$ s^{-1}) than those of infrared candidate ortho-$H_2{}^{16}O$ lines (see paper II), and the number densities of $H_2{}^{18}O$ and para-$H_2{}^{16}O$ molecules are smaller (OPR=3, $^{16}O/^{18}O$=560, see also Section 4.1.2) than those of ortho-$H_2{}^{16}O$ molecules, contributions from the outer optically thin surface region become much smaller. In the sub-millimeter candidate water line cases, the local intensity from the outer optically thin disk is around 10^4 times smaller than that for the infrared candidate water line cases (see paper II). Therefore, we recommend that sub-millimeter $H_2{}^{18}O$ and para-$H_2{}^{16}O$ lines with relatively small values of E_{up} ($\sim$200K) can be used for locating the position of the H_2O snowline.

The optical depths become larger as E_{up} becomes smaller (see Figure 44), because the absorption by lines is stronger even in the colder region of the disk (see also paper II). The dust opacity at sub-millimeter wavelengths is small compared with those at infrared wavelengths. Hence, for the case of candidate sub-millimeter lines, line absorption by excited molecules mainly determines the emitting regions of lines and total optical depth profiles in the disk midplane of the inner disk with a high H_2O gas abundance (region A_{HA}). On the other hand, dust absorption mainly controls the line opacity in the disk surface and colder midplane in the outer disk. Therefore, using candidate sub-millimeter lines, we can detect H_2O vapor closer to the midplane ($z = 0$) inside the H_2O snowline, compared with infrared lines. In the cases of the para-$H_2{}^{16}O$ lines (see Figures 43 and 44), emission from $z < 0.03$ at $r \lesssim 3$ au is not detectable. This is because the optical depth of the innermost disk midplane is high due to absorption by excited water molecules and dust grains in the upper disk layer.

Since the number densities of the para-$H_2{}^{16}O$ molecules are one third smaller than that of ortho-$H_2{}^{16}O$ molecules, the former can trace deeper into the disk than the latter. Furthermore, because the

number densities of the $H_2{}^{18}O$ molecules are around 560 times smaller than that of $H_2{}^{16}O$ molecules, $H_2{}^{18}O$ lines can trace much deeper into the disk (down to $z = 0$) than $H_2{}^{16}O$ lines, and thus $H_2{}^{18}O$ lines are better targets to extract the position of the H_2O snowline at the disk midplane. If the dust opacity of the object is much larger than that of our disk model, however, the $H_2{}^{16}O$ lines are preferred targets. We also discuss in detail the impact of dust emission in Section 4.3.1.

In the Herbig Ae disk (see paper II), there was a difference between the exact H_2O snowline location ($r \sim$14 au) and the outer edge of the hot water vapor area ($r \sim 8$ au), although there was no difference between them in a T Tauri disk with the radial steeper temperature profile in the disk midplane (see also paper I). This is because the water formation rate by gas-phase reactions strongly depends on the gas temperature. Such a water vapor distribution in the Herbig Ae disk midplane was discussed in Woitke et al. (2009b). Here we point out that this distribution will depend on the adopted chemical model. Eistrup et al. (2016) calculated the chemical evolution in a disk midplane under both initial atomic and molecular abundances. They reported that for molecular initial abundances, the water gas and ice fractional abundances around the H_2O snowline ($\sim 10^{-4}$) are larger than that for atomic initial abundances ($\sim 10^{-6}$).

According to our model calculations, some sub-millimeter candidate ortho-$H_2{}^{16}O$ lines (e.g., see also paper II) can trace the position of the exact H_2O snowline location. In contrast, sub-millimeter candidate para-$H_2{}^{16}O$ lines and para-$H_2{}^{18}O$ lines discussed in this subsection mainly trace the position of the outer edge of the hot water vapor area (see Figures 40, 43, 45). The differences in the line properties come from the differences in $A_{\rm ul}$ and number densities among the lines.

Here we note that van Kempen et al. (2008) conducted the calculations of far-infrared $H_2{}^{16}O$ and $H_2{}^{18}O$ lines within the *Herschel*/HIFI frequency coverage for Class 0 protostar models, and suggested that higher excitation lines ($E_{\rm up}$>150 K) are usually dominated by emission coming from the warm inner region.

According to Figures 43 and 44, the local intensities of the para-$H_2{}^{16}O$ 1113 GHz line are similar both outside and inside the H_2O snowline for the Herbig Ae disk. However, most disk-integrated line emission comes from the outer disk on account of the larger surface area. Moreover, the line opacity in the outer disk midplane is about $10^3 - 10^4$ times higher than those of the candidate water lines with similar line wavelengths and thus similar dust opacities.

Here we note that in the case of the para-$H_2{}^{18}O$ line at 1102 GHz for the Herbig Ae disk, the contribution from the inner optically thick layer within the H_2O snowline is still dominant (see Figure 43). This is because the number densities of para-$H_2{}^{18}O$ molecules are much smaller than those of $H_2{}^{16}O$ molecules. However, the emitting region of this line extends farther into the outer disk. Thus the contribution of the outer disk is expected to be larger if we integrate emission components within a larger disk radius (e.g., $r \lesssim$ hundreds au). Therefore, we see that these two lines are not appropriate to detect the hot water emission inside the H_2O snowline, as concluded also for the ortho-$H_2{}^{16}O$ 557 GHz line (see papers I and II).

4.2.3. *The normalized radial cumulative line fluxes*

The top two panels of Figure 45 show the normalized cumulative fluxes in the radial directions of three para-$H_2{}^{16}O$ lines at 183 GHz, 325 GHz, and 1113 GHz, and the bottom two panels show those of para-$H_2{}^{18}O$ lines at 203 GHz, 322 GHz, and 1102 GHz, for the Herbig Ae disk. For the candidate $H_2{}^{16}O$ and $H_2{}^{18}O$ lines, most line flux is emitted from the region with a high water vapor abundance ($\sim 10^{-5} - 10^{-4}$, r <8 au). For the para-$H_2{}^{16}O$ 1113 GHz line case, the line emitting region is much further out from the position of H_2O snowline ($r \sim 50 - 300$ au), and it is similar to that of the ortho-$H_2{}^{16}O$ 557 GHz line (see paper II).

Here we point out that line emission from the para-$H_2{}^{18}O$ 1102 GHz line is both from the region inside (r <14 au) and much further out (r >100 au) than the position of H_2O snowline. We also discussed this line property in the last paragraph of Section 4.2.2.

4.2.4. *The properties of all other sub-millimeter water emission lines*

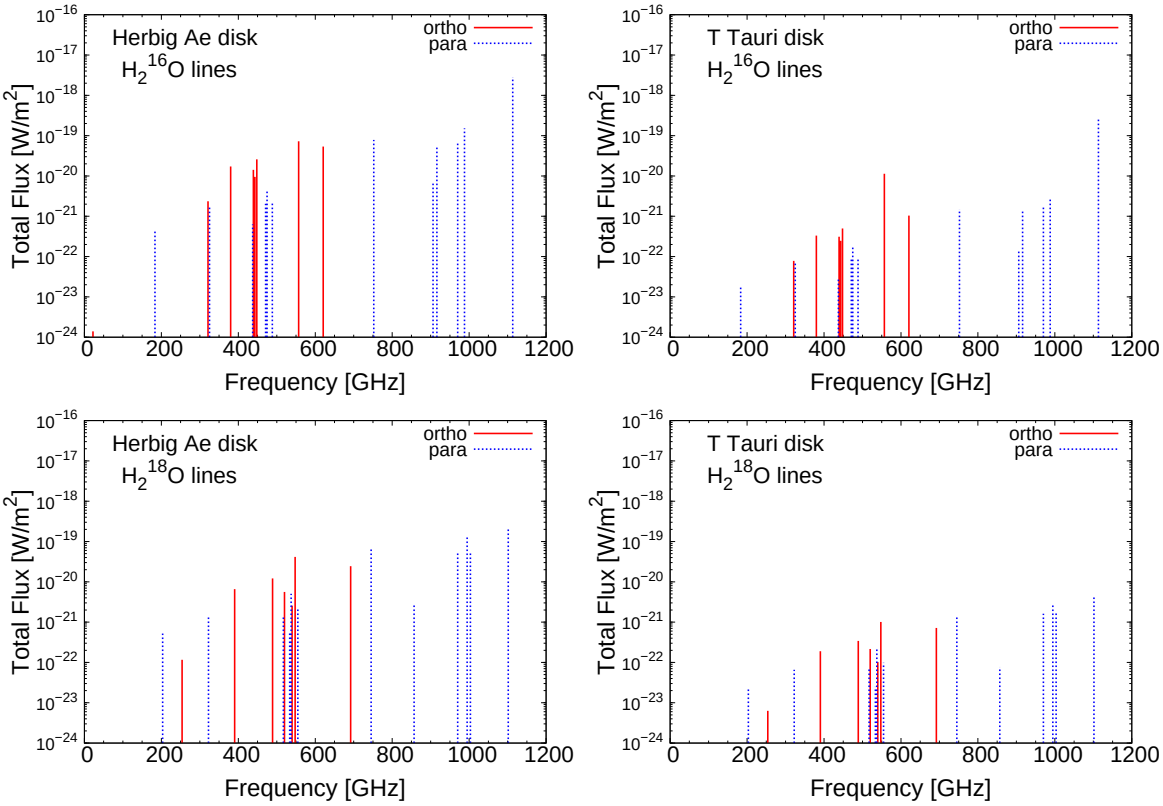

Figure 46. The disk integrated emergent fluxes of sub-millimeter ortho- and para-$H_2{}^{16}O$ lines (top panels), and ortho- and para-$H_2{}^{18}O$ lines (bottom panels), from a Herbig Ae disk (left panels) and a T Tauri disk (right panels). The ortho- and para- water lines are plotted with *red solid lines* and *blue dotted lines*, respectively. These water lines are selected on the basis of their excitation energies, $0 < E_{\rm up} < 2000$K, and lower frequencies, $\nu = 0 - 1003$ GHz ($\lambda > 297\mu$m). In these panels, we also plot the total fluxes of the ground-state rotational transitions of the para-$H_2{}^{16}O$ 1113 GHz line and para-$H_2{}^{18}O$ 1102 GHz line.

Figure 46 shows the total fluxes of calculated all sub-millimeter ortho- and para-$H_2{}^{16}O$ lines and ortho- and para-$H_2{}^{18}O$ lines from a Herbig Ae disk (left panels) and a T Tauri disk (right panels). The detailed line parameters and total line fluxes of $H_2{}^{16}O$ lines and $H_2{}^{18}O$ lines in Figure 46 are listed in Tables 8 and 9, respectively. In calculating the total fluxes in Figure 46 and Tables 8 and 9, we do not include dust emission, although we do include both gas and dust absorption. In Figure

46 and Tables 8 and 9, we calculated the two ground-state rotational transitions of the para-$H_2{}^{16}O$ and para-$H_2{}^{18}O$ lines (at 1113 GHz and 1102 GHz, respectively). We also include all sub-millimeter ortho- and para-$H_2{}^{16}O$ lines and ortho- and para-$H_2{}^{18}O$ lines with $E_{\rm up} < 2000$ K and with a frequency of $\nu \leq 1003$ GHz ($\lambda \geq 297$ μm).

On the basis of Figure 46 and Tables 8 and 9, the values of these line fluxes from the Herbig Ae disk are about $1-5\times10^2$ larger than those of the T Tauri disk. This is because the H_2O snowline position in the T Tauri disk is at a smaller radial distance than that in the Herbig Ae disk. The total line fluxes tend to be larger as the values of $E_{\rm up}$ are smaller and $A_{\rm ul}$ are larger. In addition, they tend to be smaller as the wavelengths of these water lines are longer, because mid-infrared wavelengths are the peak wavelengths of the Planck function at the gas temperatures around the H_2O snowline ($T_g\sim$ 100-200 K). Furthermore, comparing water lines with the same transition quantum numbers ($J_{K_aK_c}$), the total fluxes of $H_2{}^{16}O$ lines tend to be $0.5-10^2$ times larger than those of $H_2{}^{18}O$ lines, and the flux ratios tend to be larger in the cases of ortho-$H_2{}^{16}O$ lines. The differences in flux ratios are mainly due to the differences in emitting regions.

Table 8. Calculated parameters and total fluxes for all sub-millimeter ortho- and para-$H_2{}^{16}O$ lines

$J_{K_aK_c}$	λ[a]	Frequency	$A_{\rm ul}$	$E_{\rm up}$	HAe flux[b]	TT flux[c]	Comments[d]
	[μm]	[GHz]	[s^{-1}]	[K]	[W m^{-2}]	[W m^{-2}]	
			ortho-$H_2{}^{16}O$ lines				
6_{16}-5_{23}	13482.8594	22.23508	1.835×10^{-9}	643.5	1.4×10^{-24}	4.5×10^{-26}	
10_{29}-9_{36}[e]	933.2767	321.22568	6.165×10^{-6}	1861.2	2.3×10^{-21}	7.8×10^{-23}	ALMA Band 7
4_{14}-3_{21}	788.5180	380.19736	3.083×10^{-5}	323.5	1.7×10^{-20}	3.3×10^{-22}	
6_{43}-5_{50}[e]	682.6641	439.15079	2.816×10^{-5}	1088.7	1.4×10^{-20}	3.1×10^{-22}	ALMA Band 8
7_{52}-6_{61}[e]	676.7044	443.01835	2.231×10^{-5}	1524.8	9.5×10^{-21}	2.5×10^{-22}	ALMA Band 8

Table 8 continued on next page

Table 8 *(continued)*

$J_{K_aK_c}$	λ[a]	Frequency	$A_{\rm ul}$	$E_{\rm up}$	HAe flux[b]	TT flux[c]	Comments[d]
	[μm]	[GHz]	[s^{-1}]	[K]	[W m^{-2}]	[W m^{-2}]	
4_{23}-3_{30}	669.1780	448.00108	5.462×10^{-5}	432.1	2.6×10^{-20}	5.0×10^{-22}	ALMA Band 8
1_{10}-1_{01}[e]	538.2889	556.93599	3.497×10^{-3}	61.0	7.2×10^{-20}	1.1×10^{-20}	*Herschel*/HIFI
5_{32}-4_{41}[e]	482.9902	620.70095	1.106×10^{-4}	732.1	5.4×10^{-20}	1.0×10^{-21}	ALMA Band 9
			para-$H_2{}^{16}O$ lines				
3_{13}-2_{20}	1635.4389	183.31009	3.653×10^{-6}	204.7	4.4×10^{-22}	1.8×10^{-23}	ALMA Band 5
5_{15}-4_{22}	922.0046	325.15290	1.168×10^{-5}	469.9	1.9×10^{-21}	7.6×10^{-23}	ALMA Band 7
7_{53}-6_{60}	685.4802	437.34666	2.146×10^{-5}	1524.6	6.3×10^{-22}	2.8×10^{-23}	ALMA Band 8
6_{42}-5_{51}	636.6522	470.88890	3.483×10^{-5}	1090.3	2.0×10^{-21}	8.8×10^{-23}	ALMA Band 8
5_{33}-4_{40}	631.5554	474.68911	4.815×10^{-5}	725.1	4.5×10^{-21}	1.8×10^{-22}	ALMA Band 8
6_{24}-7_{17}	613.7112	488.49113	1.382×10^{-5}	867.3	2.1×10^{-21}	9.5×10^{-23}	ALMA Band 8
2_{11}-2_{02}	398.6426	752.03314	7.130×10^{-3}	136.9	7.8×10^{-20}	1.5×10^{-21}	
9_{28}-8_{35}	330.8216	906.20590	2.221×10^{-4}	1554.4	6.9×10^{-21}	1.5×10^{-22}	ALMA Band 10
4_{22}-3_{31}	327.2230	916.17158	5.743×10^{-4}	454.3	5.7×10^{-20}	1.5×10^{-21}	ALMA Band 10
5_{24}-4_{31}	308.9640	970.31505	9.071×10^{-4}	598.8	6.5×10^{-20}	1.7×10^{-21}	
2_{02}-1_{11}	303.4562	987.92676	5.912×10^{-3}	100.8	1.5×10^{-19}	2.9×10^{-21}	
1_{11}-0_{00}	269.2723	1113.34301	1.863×10^{-2}	53.4	2.8×10^{-18}	2.6×10^{-19}	*Herschel*/HIFI

[a] In calculating the line wavelength values λ from the values of line frequencies, we adopt the speed of light value c=2.99792458 $\times$ 10^8 m s^{-1}.

[b] The total line flux for a Herbig Ae disk. When we calculate these line fluxes, we do not include dust emission.

[c] The total line flux for a T Tauri disk. When we calculate these line fluxes, we do not include dust emission.

[d] "ALMA Band" means that the line is within the current ALMA Band coverage. "*Herschel*/HIFI" means that the line was detected from protoplanetary disks by previous *Herschel*/HIFI observations (e.g., Hogerheijde et al. 2011; Podio et al. 2013; van Dishoeck et al. 2014; Salinas et al. 2016; Du et al. 2017).

[e] We have already reported the values for these ortho-$H_2{}^{16}O$ lines in paper II.

Table 9. Calculated parameters and total fluxes for all sub-millimeter ortho- and para-$H_2{}^{18}O$ lines

$J_{K_aK_c}$	λ[a]	Frequency	$A_{\rm ul}$	$E_{\rm up}$	HAe flux[b]	TT flux[c]	Comments[d]
	[μm]	[GHz]	[s^{-1}]	[K]	[W m^{-2}]	[W m^{-2}]	
			ortho-$H_2{}^{18}O$ lines				
6_{16}-5_{23}	53295.0158	5.62515	2.988×10^{-11}	640.7	1.6×10^{-27}	1.3×10^{-28}	
10_{29}-9_{36}	1180.7587	253.89816	2.806×10^{-6}	1853.5	1.2×10^{-22}	6.3×10^{-24}	ALMA Band 6
4_{14}-3_{21}	767.5026	390.60776	3.160×10^{-5}	322.0	6.6×10^{-21}	1.9×10^{-22}	ALMA Band 8
4_{23}-3_{30}	613.0045	489.05426	6.951×10^{-5}	429.6	1.2×10^{-20}	3.4×10^{-22}	ALMA Band 8
6_{43}-5_{50}	576.3718	520.13732	4.609×10^{-5}	1080.6	5.6×10^{-21}	2.2×10^{-22}	
7_{52}-6_{61}	555.2782	539.89596	3.982×10^{-5}	1512.4	2.6×10^{-21}	1.0×10^{-22}	
1_{10}-1_{01}	547.3897	547.67644	3.257×10^{-3}	60.5	4.2×10^{-20}	1.0×10^{-21}	
5_{32}-4_{41}	433.1766	692.07914	1.511×10^{-4}	727.6	2.4×10^{-20}	7.2×10^{-22}	ALMA Band 9
			para-$H_2{}^{18}O$ lines				
3_{13}-2_{20}	1473.8514	203.40752	4.813×10^{-6}	203.7	5.2×10^{-22}	2.3×10^{-23}	ALMA Band 5
5_{15}-4_{22}	929.6894	322.46517	1.060×10^{-5}	467.9	1.4×10^{-21}	6.6×10^{-23}	ALMA Band 7
6_{24}-7_{17}	579.6653	517.18196	1.491×10^{-5}	865.0	1.5×10^{-21}	7.4×10^{-23}	
7_{53}-6_{60}	561.9372	533.49817	3.841×10^{-5}	1512.1	5.9×10^{-22}	2.5×10^{-23}	
5_{33}-4_{40}	557.9220	537.33757	6.870×10^{-5}	720.2	5.0×10^{-21}	2.1×10^{-22}	
6_{42}-5_{51}	540.3030	554.85987	5.616×10^{-5}	1082.2	2.2×10^{-21}	9.8×10^{-23}	
2_{11}-2_{02}	402.2331	745.32020	6.759×10^{-3}	136.4	6.8×10^{-20}	1.4×10^{-21}	
9_{28}-8_{35}	349.8796	856.84463	1.711×10^{-4}	1548.0	2.8×10^{-21}	7.7×10^{-23}	ALMA Band 10
4_{22}-3_{31}	308.9777	970.27204	6.759×10^{-4}	452.4	5.5×10^{-20}	1.6×10^{-21}	
2_{02}-1_{11}	301.3974	994.67513	5.970×10^{-3}	100.6	1.4×10^{-19}	2.9×10^{-21}	

Table 9 continued on next page

Table 9 *(continued)*

$J_{K_aK_c}$	λ[a]	Frequency	$A_{\rm ul}$	$E_{\rm up}$	HAe flux[b]	TT flux[c]	Comments[d]
	[μm]	[GHz]	[s^{-1}]	[K]	[W m^{-2}]	[W m^{-2}]	
5_{24}-4_{31}	298.8131	1003.27760	9.714×10^{-4}	595.9	5.7×10^{-20}	1.7×10^{-21}	
1_{11}-0_{00}	272.1185	1101.69826	1.769×10^{-2}	52.9	2.1×10^{-19}	4.4×10^{-21}	

[a]In calculating the line wavelength values λ from the values of line frequencies, we adopt the speed of light value c=2.99792458 $\times$ 10^8 m s^{-1}.

[b]The total line flux for a Herbig Ae disk. When we calculate these line fluxes, we do not include dust emission.

[c]The total line flux for a T Tauri disk. When we calculate these line fluxes, we do not include dust emission.

[d]"ALMA Band" means that the line is within the current ALMA Band coverage. $H_2{}^{18}O$ lines have not been detected from protoplanetary disks by previous *Herschel*/HIFI observations (e.g., Hogerheijde et al. 2011; Podio et al. 2013; van Dishoeck et al. 2014; Salinas et al. 2016; Du et al. 2017).

Figure 47 shows the velocity profiles of several water lines in the frequency range 300−700 GHz for the Herbig Ae disk. The values of $E_{\rm up}$ ($\sim 300-700$K) of lines in Figure 47 are relatively smaller than those of candidate ortho-$H_2{}^{16}O$ lines discussed in papers I and II ($E_{\rm up}$ $\sim$1000K). In these cases contributions from the relatively high water vapor abundance region ($\sim10^{-8}$, $r\sim8-14$ au) dominate. By contrast, in the case of para-$H_2{}^{16}O$ and $H_2{}^{18}O$ lines, most of the flux comes from the high H_2O gas vapor abundance region ($\sim10^{-5}-10^{-4}$, r <8 au), since the number densities of $H_2{}^{18}O$ and para-$H_2{}^{16}O$ molecules are smaller than those of ortho-$H_2{}^{16}O$ molecules.

4.3. *Discussions*

4.3.1. *Influence of dust emission on water line properties*

Figure 48 shows the velocity profiles of several para-$H_2{}^{16}O$ and para-$H_2{}^{18}O$ lines for a Herbig Ae disk inside 30 au. In the line profiles with *red solid lines*, we do not include dust emission components (see also Figures 40 and 47). In the line profiles with *blue dashed lines*, we include both dust and gas emission components, and then we subtract dust emission components (the values of fluxes at

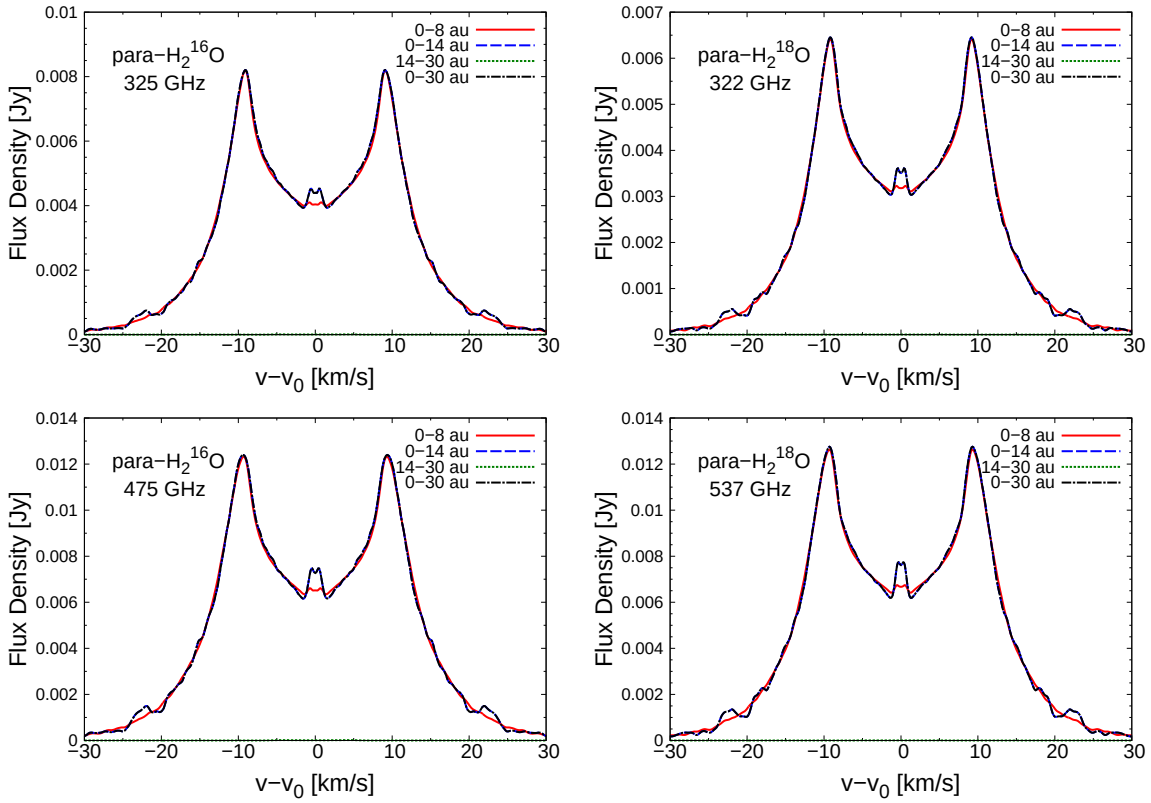

Figure 47. The profiles of para-$H_2{}^{16}O$ lines at 325 GHz (top left) and 475 GHz (bottom left), and para-$H_2{}^{18}O$ lines at 322 GHz (top right), and 537 GHz (bottom right) from the Herbig Ae disk. The parameters and total fluxes of these H_2O lines are listed in Tables 8 and 9. In these profiles, we do not include dust emission. The line profiles from within 8 au, the inner high temperature region, are displayed with *red solid lines*, those from within the H_2O snowline, 14 au, with *blue dashed lines*, those from 14−30 au, outside the H_2O snowline, with *green dotted lines*, and those from the total area inside 30 au, with *black dashed dotted lines*. In the panels of para-$H_2{}^{16}O$ and para-$H_2{}^{18}O$ line profiles, the flux densities outside the H_2O snowline (*green dotted lines*, $< 10^{-4}$ Jy) are much smaller than those inside 8 au (*red solid lines*). Therefore, the *red solid lines*, *blue dashed lines*, and *black dashed dotted lines* are almost completely overlapped (see also Figure 40).

$v - v_0 = \pm\infty$) after the calculation to show the line emission more clearly.

According to the *red solid lines* and *blue dashed lines* in Figure 48, if we do not include dust emission,

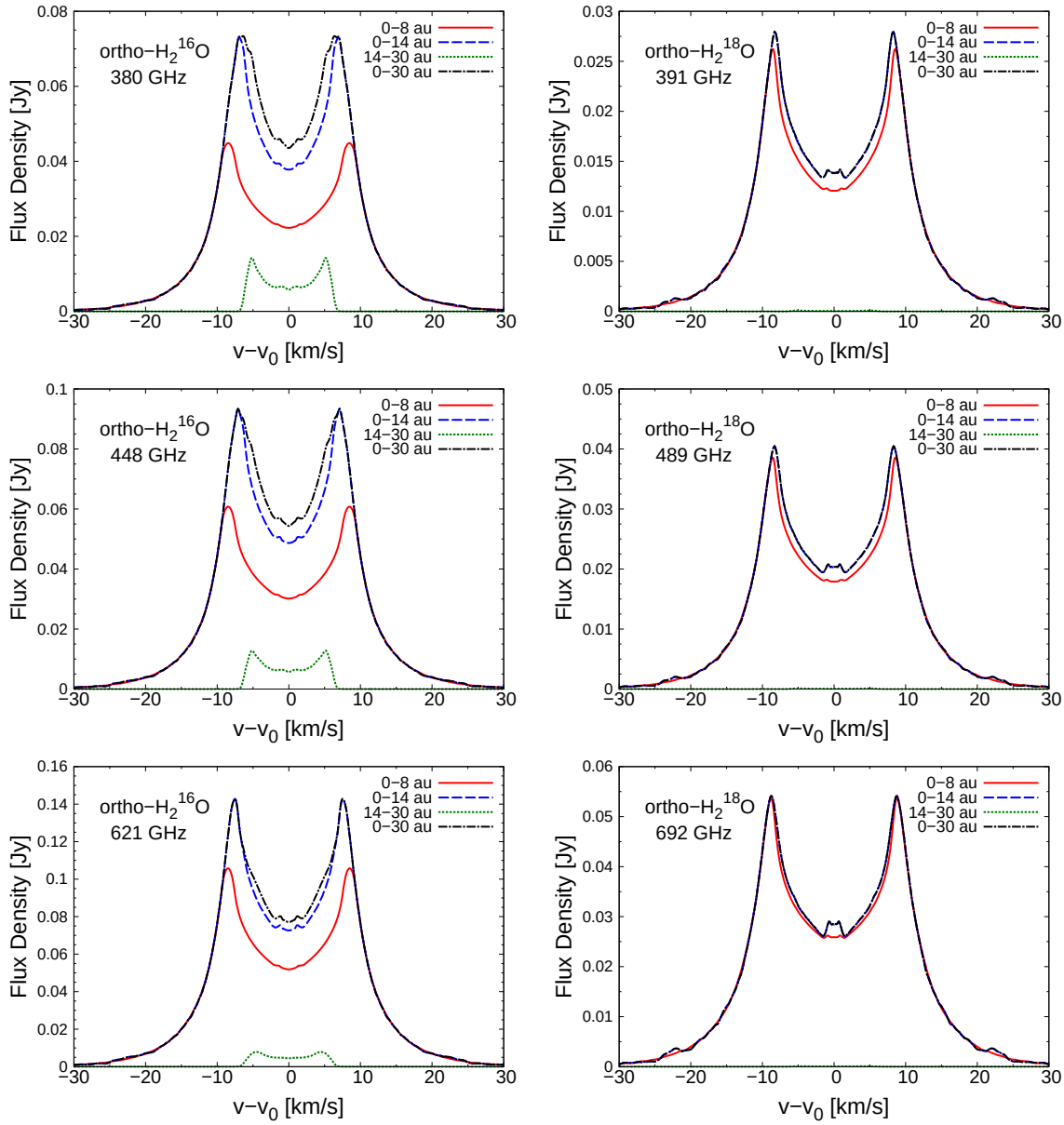

Figure 47. (Continued.) The profiles of ortho-$H_2{}^{16}O$ lines at 380 GHz (top left), 448 GHz (middle left), and 621 GHz (bottom left), ortho-$H_2{}^{18}O$ lines at 391 GHz (top right), 489 GHz (middle right), and 692 GHz (bottom right) from the Herbig Ae disk. The parameters and total fluxes of these H_2O lines are listed in Tables 8 and 9. In the panels of ortho-$H_2{}^{18}O$ line profiles, the flux densities outside the H_2O snowline (*green dotted lines*, $< 10^{-3}$ Jy) are much smaller than those inside 8 au (*red solid lines*). Therefore, the *red solid lines*, *blue dashed lines*, and *black dashed dotted lines* are almost completely overlapped (see also Figure 40).

the values of line peak flux densities become $1.1-2$ times larger. This is because the column density of the inner disk is very high so that the line becomes optically thick. The position of τ_{ul}=1 at the line center in the z direction is higher than those at line-free frequencies, and the total intensity of dust emission is smaller at the line center than those at line-free frequencies. Therefore, the line flux density relative to the flux density of dust emission becomes lower, compared with the case in which both the line and dust continuum emission are optically thin, such as found for molecular clouds. Here we note that in the inner hot disk midplane at $r < 7-8$ au, the vertically integrated column densities of gaseous water molecules are $\sim 10^{20}-10^{22}$ cm^{-2} (see also Figure 3 of paper II), and the values of dust optical depth at $z \sim 0$ are around $0.05-0.4$ at 183 GHz, and around $0.1-0.8$ at 325 GHz. The shapes of line profiles are similar among Figures 40, 47, and 48.

In the line profiles with *black dotted lines* in Figure 48, we also include both dust and gas components in the same way as those with *blue dashed lines*, but we artificially increase the values of dust opacity κ_{ul} by a factor of ten in order to investigate the influence of dust opacity on line properties. We note that the dust opacity at sub-millimeter wavelengths changes by a factor of around ten, depending on the properties of the dust grains (e.g., Miyake & Nakagawa 1993; Draine 2006). In our fiducial disk model, dust opacities appropriate for the dark cloud model are used and they are relatively small at sub-millimeter wavelengths, compared with the model with grain growth (see e.g., Nomura & Millar 2005; Aikawa & Nomura 2006, and paper I). We again subtract dust emission components to show the line emission more clearly. The disk physical structure is the same as the original reference model. In these cases with larger values of dust opacity (see *black dotted lines* in Figure 48), the effect of the dust emission becomes stronger and the values of peak line flux densities become around $0.1-0.6$ times smaller.

The differences in line flux densities are larger in the cases of Band 7 water lines when compared with Band 5 water lines (see Figure 48). This is because the dust opacity becomes larger as the line frequency increases (e.g., Miyake & Nakagawa 1993; Nomura & Millar 2005; Draine 2006). In addition,

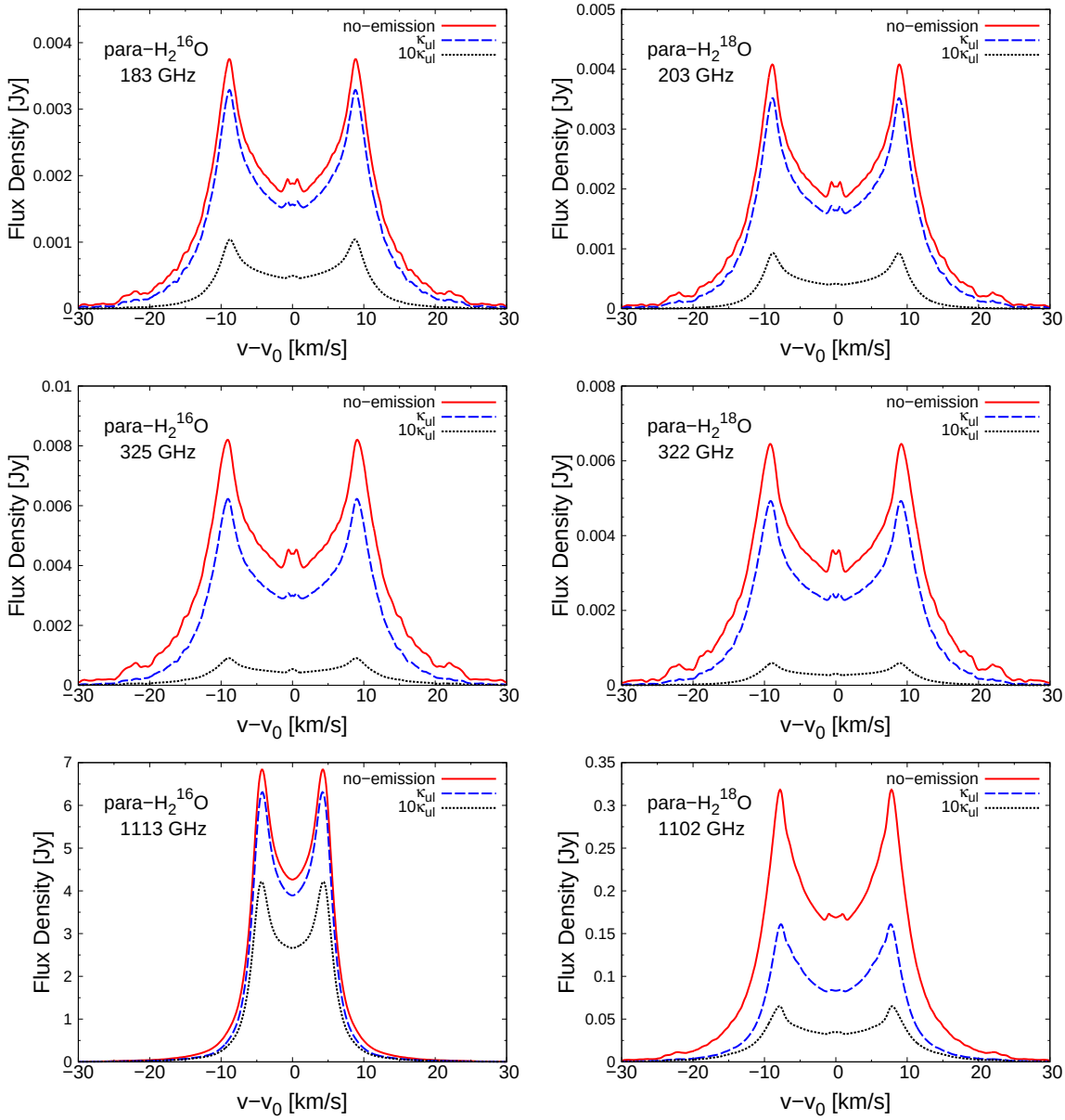

Figure 48. The profiles of para-$H_2{}^{16}O$ lines at 183 GHz (top left), 325 GHz (middle left), 1113 GHz (bottom left), and para-$H_2{}^{18}O$ lines at 203 GHz (top right), 322 GHz (middle right), 1102 GHz (bottom right) from a Herbig Ae disk inside 30 au. In the line profiles with *red solid lines*, we do not include dust emission components (see also Figures 40 and 47). In the line profiles with *blue dashed lines* and *black dotted lines*, we include both dust and gas emission components, and we subtract dust emission components (the values of fluxes at $v - v_0 = \pm\infty$) after the calculation to show the line emission component more clearly. In the line profiles with *black dotted lines*, we set the values of dust opacity κ_{ul} ten times larger in order to investigate the influence of dust opacity on line properties.

the differences in line flux densities are also larger in the cases of $H_2{}^{18}O$ lines, compared with $H_2{}^{16}O$ lines. The emitting regions of $H_2{}^{18}O$ lines are closer to the disk midplane (down to $z = 0$) than those of $H_2{}^{16}O$ lines. The temperature is higher as the disk height is higher (see Figure 44) and thus the temperature around $\tau_{ul} \sim 1$ of $H_2{}^{16}O$ lines is higher than those of $H_2{}^{18}O$ lines. Therefore, the line intensities are larger in the cases of $H_2{}^{16}O$ lines, compared with the cases of $H_2{}^{18}O$ lines. Thus, if the dust opacity of the disk is much larger than that of our disk model, the $H_2{}^{16}O$ lines and Band 5 lines are better candidates for sub-millimeter detection of the inner water reservoir. Moreover, the differences in line flux densities of para-$H_2{}^{16}O$ 1113 GHz and para-$H_2{}^{18}O$ 1102 GHz are smaller than other water lines. This is because the main line emitting region of these lines is the cold water vapor of the outer photodesorption region where the dust opacity is much smaller than that in the inner disk, and where also the line intensity is greater. Since all $H_2{}^{16}O$ and $H_2{}^{18}O$ lines treated here are optically thick (see Figure 43) and the temperature is higher as the disk height is higher (see Figure 44), line emission is stronger than dust emission, even for the case with an assumed large dust opacity.

We point out that previous mid- and near-infrared observations for Herbig Ae disks have not yet detected water line emission from the inner disk surface (Pontoppidan et al. 2010a; Fedele et al. 2011; Salyk et al. 2011), although far-infrared water lines have been detected for a few bright Herbig Ae disks (Fedele et al. 2012, 2013; Meeus et al. 2012), which are classified as group II Herbig Ae stars (e.g., Honda et al. 2015). Several explanations (e.g., inner holes/gaps, strong UV radiation fields in the disk surface, and strong infrared dust emission in the infrared wavelengths, see Section 3.3.4 of this thesis and Antonellini et al. 2015, 2016) have been considered responsible for this non-detection toward Herbig Ae disks. In contrast, since the dust continuum fluxes in the sub-millimeter wavelengths are low, the possibility of water line detections from protoplanetary disks is expected to be higher.

Here we note that the para-$H_2{}^{16}O$ 1113 GHz line and ortho-$H_2{}^{16}O$ 557 GHz line were detected from

disks around two T Tauri stars, TW Hya and DG Tau, and a Herbig Ae star, HD 100546 through space spectroscopic observations with *Herschel*/HIFI (e.g., Hogerheijde et al. 2011; Podio et al. 2013; Zhang et al. 2013; van Dishoeck et al. 2014; Salinas et al. 2016; Du et al. 2017). Du et al. (2017) reported the upper limit flux values of these ground level $H_2{}^{16}O$ lines for disks around two other T Tauri stars (AA Tau, DM Tau) and a Herbig Ae star (HD163296). From the properties of lines detected by previous observations and other modeling works (e.g., Meijerink et al. 2008; Woitke et al. 2009b; Antonellini et al. 2015), the main line emitting region is the cold outer disk, consistent with our results. The number of detections is smaller than those expected from previous modeling works (e.g., Antonellini et al. 2015). Du et al. (2017) discussed the reasons for the low detection rate, and proposed that gas-phase oxygen bearing molecules (such as water and CO) were removed from the line emitting layers of the outer disk by freeze-out of onto dust grains followed by grain growth and settling/migration.

4.3.2. *Influence of different snowline positions and velocity resolution of line profiles*

Our model, which has a continuous disk in the radial direction and no inner gap and/or hole, is applicable to group II Herbig Ae stars (e.g. Honda et al. 2015). For a model having an inner hole (i.e., group I Herbig Ae stars), the fluxes of the H_2O lines, especially from the hot water gas within the H_2O snowline, are expected to decrease. In addition, if we adopt different values of dust opacities (due to dust evolution), mass accretion rates (which determine the effects of viscous heating), and central star temperatures, the position of H_2O snowline is also changed (e.g., Oka et al. 2011; Harsono et al. 2015; Piso et al. 2015). In Sections 2.3.1, 3.3.1 and 3.3.3, the uncertainties in predictions of our model were presented in detail, and the water line properties for some cases in which we artificially changed of H_2O vapor distribution were discussed (see Figures 24 and 25 of this thesis). If the H_2O snowline is farther from the star, and the fractional water vapor abundance in the surface of the outer disk is lower than that in the original disk model, the line fluxes from the hot region within the H_2O snowline are larger than those from the cooler outer disk.

In the cases of sub-millimeter para-$H_2{}^{16}O$ lines and $H_2{}^{18}O$ lines, the emission fluxes from the optically

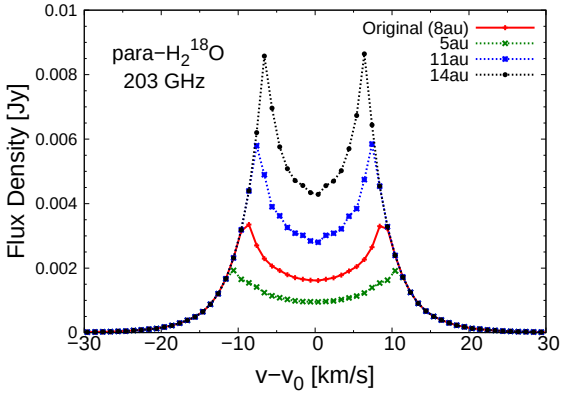

Figure 49. The profiles of the para-$H_2{}^{18}O$ line at 203 GHz from a Herbig Ae disk inside 30 au with a reduced velocity resolution (dv =1.0 km s^{-1}). When we calculate these line profiles, we include both dust and gas emission components, and we subtract dust emission components (the values of fluxes at $v - v_0 = \pm\infty$) after calculations to show the line emission component more clearly. The red solid line with cross symbols is the line profile of our original Herbig Ae disk model (see also Figure 48). In other plots, we artificially change the outer edge of the region with a high H_2O water vapor abundance ($\sim 10^{-5} - 10^{-4}$) region to 5 au (the green dotted line with cross symbols), 11 au (the blue dotted line with filled square and cross symbols), and 14 au (the black dotted line with circle symbols).

thin disk surface and photodesorption region are smaller than those of ortho-$H_2{}^{16}O$ lines. Therefore, the variations in fractional water abundances in those regions will have little impact on the profiles of the para-$H_2{}^{16}O$ lines and $H_2{}^{18}O$ lines with smaller values of $A_{\rm ul}$ ($< 10^{-4}$ s^{-1}) and relatively higher values of $E_{\rm up}$ ($\gtrsim$200K). Here we discuss the behavior of these lines in which we reduce the velocity resolution and artificially change the distribution of water vapor in the disk midplane, and test the validity of our model predictions.

In Figure 49, we display the profiles of the para-$H_2{}^{18}O$ line at 203 GHz from a Herbig Ae disk inside 30 au with a reduced velocity resolution (dv =1.0 km s^{-1}). This velocity resolution we adopted in this figure is ten times larger than those of other line profiles in this work and our previous papers (dv =0.1 km s^{-1}, see also papers I and II), and a velocity resolution of $0.1 - 1.0$ km s^{-1} is often adopted for ALMA observations. The red solid line with cross symbols is the line profile of our

original Herbig Ae disk model (see also Figure 48). In other plots, we artificially change the outer edge of the region with high H_2O water vapor abundance ($= 10^{-5}$) to 5 au ($T_g \sim 180$K), 11 au ($T_g \sim 135$K), and 14 au ($T_g \sim 120$K). Since this line is mainly emitted from the region with a high water vapor abundance ($\sim 10^{-5} - 10^{-4}$, see also Figures 43, 45, 47, and 48) in the Herbig Ae disk, we changed the outer edge of the region with a high H_2O water vapor abundance (originally 8 au, see also Table 7).

According to Figure 49, as the region with a high water vapor abundance becomes larger, the flux density of the line peaks becomes larger, and the line width, especially the width between the two peaks becomes narrower. In the outer disk the changes in local velocity widths are smaller, since the velocity widths are inversely proportional to the square root of the radial distance of the emitting region from the central star (see also Equations (13) and (14)). The figure shows that we will be able to distinguish the differences of the outer edge positions (or the positions of the H_2O snowline) with the resolution of of a few au through observing the separation between the two peaks in the line profile with the velocity resolution of dv =1.0 km s^{-1} for the Herbig Ae disk with the inclination angle of 30 deg. Future detailed calculations, which consider the noise expected in actual observations and the errors of physical parameters such as central star masses and disk inclination angles (obtained by other previous observations), are also important to investigate the observational possibilities with ALMA.

Here we note that the disk physical structure is the same as the original reference model (see Section 4.1.1), because calculating several different disk physical structures and chemical structures self-consistently is computationally demanding and beyond the scope of this work. Even if we adopt self-consistent models, we expect that the line widths will not be affected; however, we do expect that line fluxes will be affected by about 0.5-4 times since the temperature of line emitting regions will be about 0.7−1.2 times different, on the basis of the differences in gas temperatures around the outer edges of high water vapor abundance regions (see also Section 2.3.1 of this thesis).

4.3.3. *Requirement for the future observations*

In order to trace the hot water gas inside the H_2O snowline, high-dispersion spectroscopic observations (R=$\lambda/\delta\lambda$ > tens of thousands) of the water candidate lines in Tables 8 and 9 are needed. This is because the velocity width between the peaks is $\sim 15-20$ km s^{-1}. The para-$H_2{}^{16}O$ 183 GHz line and para-$H_2{}^{18}O$ 203 GHz line, which have the same transition levels, are in the frequency coverage of ALMA Band 5 (Immer et al. 2016; Humphreys et al. 2017), and the para-$H_2{}^{16}O$ 325 GHz line and the para-$H_2{}^{18}O$ 322 GHz line, which have the same transition levels, are in ALMA Band 7. The candidate ortho-$H_2{}^{16}O$ 321 GHz line (see paper II) is also in ALMA Band 7. Since their line fluxes are larger than those of other water lines at similar wavelengths and the atmospheric conditions of ALMA Bands 5 and 7 are usually better than Bands at shorter wavelengths, they are suitable for tracing the hot water vapor inside the H_2O snowline. Because of the small values of $E_{\rm up}$, the para-$H_2{}^{16}O$ lines at 183 GHz and 325 GHz are strongly affected by atmospheric absorption. By contrast, the effects of atmospheric absorption are less in the cases of $H_2{}^{18}O$ lines, and $H_2{}^{16}O$ lines with larger values of $E_{\rm up}$ ($\sim$1000-2000K).

Other sub-millimeter ortho- and para-H_2O lines that trace the H_2O snowline exist in ALMA Bands 8, 9 and 10 ($\sim 275-950$GHz, see also Figures 7 and 8, Tables 8 and 9). The number of candidate water lines is largest in ALMA Band 8, and which has three ortho-$H_2{}^{16}O$ lines, four para-$H_2{}^{16}O$ lines, and one ortho-$H_2{}^{18}O$ lines. The values of $A_{\rm ul}$ are around $1-7\times10^{-5}$ s^{-1}, and the values of $E_{\rm up}$ range from 300K to 1600K. The ortho-$H_2{}^{16}O$ 621 GHz and the ortho-$H_2{}^{18}O$ 692 GHz lines are transitions from the same energy levels and both fall in Band 9. Two candidate para-$H_2{}^{16}O$ lines and one para-$H_2{}^{18}O$ line fall in ALMA Band 10. Here we note that the $H_2{}^{16}O$ lines with small values of $E_{\rm up}$ (< 1000K) are strongly affected by atmospheric absorption.

There are no candidate $H_2{}^{16}O$ and $H_2{}^{18}O$ lines within the frequency coverage of ALMA Bands 3 and 4. The ortho-$H_2{}^{18}O$ 254 GHz line is in Band 6 and it has the same transition energy level of ortho-$H_2{}^{16}O$ 321 GHz line (see paper II), although it has a relatively larger value of $E_{\rm up}$ (= 1853.5K)

and its fluxes are relatively smaller than those of Bands 5 and 7 lines.

Although we predict that the fluxes of the sub-millimeter candidate lines are too small in T Tauri disks ($\sim 10^{-23} - 10^{-22}$ W m^{-2}) to detect with a reasonable integration time with current ALMA sensitivity ($\sim 10^{-21} - 10^{-20}$ W m^{-2}; 5σ, 1 hour), the fluxes are relatively strong and a greater possibility of successful detections are expected in Herbig Ae disks, in T Tauri disks with younger ages (e.g., HL Tau, ALMA Partnership et al. 2015; Banzatti et al. 2015; Harsono et al. 2015; Zhang et al. 2015; Okuzumi et al. 2016), and in disks around FU Orionis type stars (e.g., V883 Ori, Cieza et al. 2016; Schoonenberg et al. 2017). The predicted fluxes of the para-$H_2{}^{16}O$ 183 GHz (Band 5), para-$H_2{}^{18}O$ 203 GHz (Band 7), para-$H_2{}^{16}O$ 325 GHz (Band 7), and para-$H_2{}^{18}O$ 322 GHz (Band 7) lines are around $4 \times 10^{-22} - 10^{-21}$ W m^{-2} (see Tables 8 and 9). In addition, the fluxes of some water lines in Bands $8 - 9$ are also estimated to be around $10^{-21} - 10^{-20}$ W m^{-2} for a Herbig Ae disk (see also Tables 8 and 9).

Here we mention that the ortho-$H_2{}^{16}O$ 321 GHz line has been detected in the disk and outflow around the massive protostar candidate, Source I in Orion KL (Hirota et al. 2014), using ALMA, and around the embedded low mass Class I protostar, HL Tau, using SMA (Kristensen et al. 2016). The interstellar para-$H_2{}^{16}O$ 183 GHz and the para-$H_2{}^{18}O$ 203 GHz lines were detected for the first time in the Orion and DR21(OH) molecular clouds (e.g., Phillips et al. 1978). Some previous observations reported the detections of the thermal para-$H_2{}^{18}O$ 203 GHz line towards hot molecular cloud cores and high mass protostars (Jacq et al. 1988; van der Tak et al. 2006). Resolved detections of the thermal para-$H_2{}^{18}O$ 203 GHz line were reported towards the deeply embedded low mass Class 0 protostars NGC 1333-IRAS4B (Jørgensen & van Dishoeck 2010), NGC 1333-IRAS2A, and NGC 1333-IRAS4A (Persson et al. 2012), using the IRAM Plateau de Bure Interferometer. They suggested that the water emission comes from the inner disk.

4.4. *Conclusion*

In this work (paper III, Notsu et al. 2018), we extended our previous works (papers I and II, Notsu et al. 2016, 2017) on using the profiles of ortho-$H_2{}^{16}O$ lines for tracing the location of the H_2O snowline in a Herbig Ae disk and a T Tauri disk, to include sub-millimeter para-$H_2{}^{16}O$ and ortho- and para-$H_2{}^{18}O$ lines.

The number densities of the para-$H_2{}^{16}O$ molecules are around one third smaller than that of ortho-$H_2{}^{16}O$, thus the para-$H_2{}^{16}O$ line can trace deeper into the disk than the ortho-$H_2{}^{16}O$ lines. Since the number densities of $H_2{}^{18}O$ molecules are around 560 times smaller than those of $H_2{}^{16}O$, they can probe deeper into the disk than the $H_2{}^{16}O$ lines (down to $z = 0$) and thus they are better candidates for detecting water emission within the H_2O snowline at the disk midplane. If the dust opacity of the disk is much larger than that adopted in our disk model, the $H_2{}^{16}O$ lines and lines with longer wavelengths are better candidates for sub-millimeter detection of the inner water reservoir. This is because the dust opacity becomes larger as the line frequency increases. In addition, the temperature is higher as the disk height is higher and thus the temperature around $\tau_{ul} \sim 1$ of $H_2{}^{16}O$ lines is higher than those of $H_2{}^{18}O$ lines. Therefore, the line intensities are larger in the case of $H_2{}^{16}O$ lines, compared with the case of $H_2{}^{18}O$ lines. The values of the Einstein A coefficients of sub-millimeter candidate water lines tend to be smaller (typically $<10^{-4}$ s^{-1}) than infrared candidate water lines (see paper II). Thus, in the case of sub-millimeter candidate water lines, the local intensity from the outer optically thin region in the disk is around 10^4 times smaller than that in infrared candidate water line cases (see paper II). Therefore, in the case of sub-millimeter lines, especially for $H_2{}^{18}O$ and para-$H_2{}^{16}O$ lines with relatively smaller upper state energies ($\sim$ a few 100 K) can also be used to trace the location of the water snowline. The values of candidate water line fluxes of the T Tauri disk are around $1 - 5 \times 10^2$ smaller than those of the Herbig Ae disk, because the location of the H_2O snowline in the T Tauri disk exists at a smaller radius from the star than that in the Herbig Ae disk.

There are several candidate water lines that trace the hot water gas inside H_2O snowline in ALMA

Bands $5 - 10$. The successful detection of candidate water lines in Herbig Ae disks and younger T Tauri disks could be achieved with current ALMA capabilities.

5. ALMA OBSERVATION OF THE PROTOPLANETARY DISK AROUND HD 163296 (NOTSU ET AL. 2019)

5.1. *Observation*

5.1.1. *Observational setup and data reduction*

The high spatial-resolution continuum and water line observations at Band 7 (λ $\sim$0.9 mm) with ALMA was carried out in Cycle 3 on 2016 September 16 (2015.1.01259.S, PI: S. Notsu). In the observation period, 40 of the 12m antennas were operational and the maximum baseline length was 2483.5m. The correlater was configured to detect dual polarizations in four spectral windows with a bandwidth of 1.875 GHz and a resolution of 1953.125 kHz each, resulting in a total bandwidth of 7.5 GHz. The spectral windows were centered at 320.844 GHz (SPW1), 322.740 GHz (SPW2), 332.844 GHz (SPW3), and 334.740 GHz (SPW4), covering ortho-$H_2{}^{16}O$ 321 GHz, para-$H_2{}^{18}O$ 322 GHz, and HDO 335 GHz lines (see also Table 10). The first local oscillator frequency (LO1) was tuned at 327.72597 GHz in order to avoid a strong atmospheric absorption around 325 GHz. The integration time on source (HD 163296) is 0.723 hours (43.35 min.). This integration time is around 20 % of our requested time in our Cycle 3 proposal for the clear detection of water lines.

The phase was calibrated by observations of J1742-1517 and J1751-1950 approximately every 10 minutes, and J1733-1304 was used for absolute flux calibration. The observed passbands were calibrated by J1924-2914. The visibility data were reduced and calibrated using the Common Astronomical Software Application (CASA) package, version 4.7.2. The corrected visibilities were imaged using the CLEAN algorithm with briggs weighting with a robust parameter of 0.5 after calibration of the bandpass, gain in amplitude and phase, and absolute flux scaling, and then flagging for aberrant data. The *uv* sampling of our Band 7 data is relatively sparse. Since in this observation we focused on the water emission lines from the hot region inside the H_2O snowline ($\lesssim$ 14 au), we do not have good *uv* coverage at shorter baselines. From previous observations, it is known that the dust emission extends to >100 au. Thus, in order to recover the missing flux, especially in the outer disk, we have combined Band 7 archival ACA (Atacama Compact Array) data (2016.1.00884.S, PI: V. Guzman) with

our Band 7 data in our dust continuum imaging after applying a phase shift to account for proper motion and different input phase centers. In addition to the usual CLEAN imaging, we performed self-calibration of the continuum emission to improve the sensitivity and image quality. The obtained solution table of the self-calibration for the continuum emission was applied to the visibilities of the lines. The spatial resolutions of the final image is 0.174 × 0.124 arcsec with a position angle (PA) of 76.799 deg for Band 7, corresponding to 17.7 au × 12.6 au. The noise level (rms) of the Band 7 image is around 0.1 mJy beam^{-1}.

We also used ALMA Band 6 calibrated archival data (2013.1.00601.S, PI: A. Isella) of this object which was obtained in ALMA Cycle 2 to compare the dust continuum image between Bands 6 and 7. We generate the Band 6 image with briggs weighting at a robust parameter of 0.5. The spatial resolution of the final image is 0.278 × 0.184 arcsec with a position angle (PA) of -87.987 deg for Band 6, corresponding to 28.2 au × 18.7 au. The spatial resolution of this calibrated archival data is ∼1.7 times larger than that reported in Isella et al. (2016) (0.22 × 0.14 arcsec, corresponding to 22.3 au × 14.2 au), in which they generate the self-calibrated continuum image with different briggs weighting parameter of -1 (uniform weighting). The noise level (rms) of the calibrated archival data of Band 6 image is around 0.5 mJy beam^{-1}.

The total disk fluxes are 1.85Jy in Band 7, and 0.68Jy in Band 6, giving spectral index $\alpha_{\rm mm}$ of ~ 2.7. This is in reasonable agreement with that measured by Pinilla et al. (2014) (2.73 ± 0.44) and Guidi et al. (2016), and a bit larger than that mesured by Dent et al. (2019) (2.1 ± 0.3).

5.1.2. *Targets*

Our target HD163296 is an isolated, young (∼5 Myr), and intermediate mass ($\sim 2.3 M_{\odot}$) Herbig Ae star and has no evidence of a stellar binary companion. It is relatively nearby, and it is surrounded by a well-studied gas-rich disk with no hint of an inner hole (group II, e.g., Honda et al. 2015). Here

we note that according to the recent Gaia data release 2 [18], the distance obtained by Hipparcos measurement in the past (d ∼122 pc, e.g., Perryman et al. 1997; van den Ancker et al. 1997) was corrected to d ∼101.5 pc (Gaia Collaboration et al. 2018). In this work, we adopt this new distance value (101.5 pc) obtained by Gaia. It has a relatively large inclination angle (i ∼42 deg, Isella et al. 2016), and thus we expected the characteristic double-peaked velocity profiles of gas in Keplerian rotation with large velocity widths (∼30 km s^{-1}) due to the compact emitting area, which was suitable to detect the position of the H_2O snowline. In addition, this object has been observed in many transitions at various wavelengths. The spectrally resolved CO lines in the sub-millimeter show the characteristic double-peaked profiles of gas in Keplerian rotation (e.g., Dent et al. 2005; Akiyama et al. 2011).

The CO snowline of this object is resolved directly using $C^{18}O$, N_2H^+, and DCO^+ line data obtained by ALMA (e.g., Qi et al. 2011, 2015; Mathews et al. 2013; Salinas et al. 2017, 2018). Previous ALMA observations showed that the continuum emission has a local maximum near the location of the CO snowline (Guidi et al. 2016; Zhang et al. 2016). The CO snowline position is around 75 au, using the new Gaia data. In addition, the measurements of the spectral index α indicated the presence of large grains and pebbles (∼ 1 cm) in the inner regions of the disk (inside 40 au) and smaller grains, consistent with ISM sizes, in the outer disk (beyond 125 au), which would suggest a grain size distribution consistent with an enhanced production of large grains at the CO snowline and consequent transport to the inner regions (Guidi et al. 2016). Boneberg et al. (2016) suggested by combining their $C^{18}O$ line modelings, previous CO snowline observations, and spectral energy distributions, that the gas to dust mass ratio g/d would be low (< 20) within the CO snowline, the disk gas mass is $\sim (8-30) \times 10^{-3} M_{\odot}$, and the mm dust opacity $\kappa_{\rm mm}$ is ~ 3 cm^2 g^{-1}, assuming the values of $C^{18}O$ abundances reported in star-forming clouds ($\sim 10^{-7} - 10^{-6}$). They also suggested that the value of g/d would be larger (up to ISM-like value, ∼100) if they assume lower $C^{18}O$ abundance

[18] https://www.cosmos.esa.int/web/gaia/dr2

because of CO depletion.

According to (Reboussin et al. 2015), the C atoms generated through CO photodissociation in the upper layers can be effectively removed through formation of species other than CO (e.g., CO_2 and CH_4). Photodissociation is normally localized in the disk surface, and the $C^{18}O$ abundance may be affected only if the CO dissociating photons penetrate to the disk midplane, or if the surface continued to be depleted of CO over very long time-scales. In addition, significant depletion of CO will occur in disks with a high cosmic-ray rate (Schwarz et al. 2018). Here we note that in one relatively old disk around TW Hya, the abundances of of CO and its isotopologues are observed as about 100 times lower than their ISM values (Favre et al. 2013; Schwarz et al. 2016).

The position of the H_2O snowline of a disk around a Herbig Ae star with stellar luminosity of $36L_{\odot}$ is $\sim$14 au from the central star, on the basis of our calculations (Notsu et al. 2017, 2018). Previous infrared observations of HD163296 detected far-infrared H_2O lines. Meeus et al. (2012) and Fedele et al. (2012, 2013) reported that three far-infrared ortho-$H_2{}^{16}O$ emission lines (63.32, 71.95, 78.74 μm) are detected at slightly above 3σ with Herschel/PACS. These lines have large Einstein A coefficients ($A_{ul}\sim$ 1 s^{-1}) and the spectral resolving power of the data was not high ($R\sim\lambda/\Delta\lambda$ $\sim$1000-3000). They argued that these H_2O lines are emitted from an upper hot water layer at radial distances $\sim$20 au, where water formation is driven by high-temperature neutral-neutral reactions. This arguments are consistent with the results of our model calculations of lines with large Einstein A coefficients (Notsu et al. 2016, 2017, 2018).

The origins of these multiple gap and ring patterns are still under-discussion (see also Section 5.3), and the disk around HD 163296 is a great example of a disk that shows planet induced structures at multiple wavelengths. Isella et al. (2016) observed the 232 GHz (1.3mm, Band 6) dust continuum

emission of the disk around HD 163296 with a spatial resolution of around 20 au using ALMA and revealed three dark concentric rings that indicate the presence of dust depleted gaps at about 50, 83, and 137 au from the central star (see also Zhang et al. 2016; Dent et al. 2019; Liu et al. 2018; Teague et al. 2018; Andrews et al. 2018; Isella et al. 2018). Pinte et al. (2018) presented the detection of a large, localized deviation from Keplerian velocity in the ^{12}CO J= 2 − 1 and J= 3 − 2 emission lines of this object obtained by ALMA, and the observed velocity pattern is consistent with the dynamical effect of a two-Jupiter-mass planet orbiting at a radius ∼260 au from the star. In addition, Teague et al. (2018) found that the rotation curves of ^{12}CO, ^{13}CO, and C^{18}O J= 2−1 emission lines of this object obtained by ALMA had substantial deviations caused by local perturbations in the radial pressure gradient, which they explained by local perturbations due to two Jupiter-mass planets at 83 and 137 au. Several near-infrared dust scattered light observations (Monnier et al. 2017; Guidi et al. 2018) for this object also detected ringed emission around 65 au, a position consistent with the first bright dust continuum ring observed by ALMA.

Here we note that the recent observation of ALMA DSHARP with the 1.3mm dust continuum ($\Delta r \sim$ 4au) for the disk around HD 163296 found new small-scale structures, such as a dark gap at 10 au, a bright ring at 15 au, a dust crescent at a radius of 55 au, and several fainter azimuthal asymmetries (Andrews et al. 2018; Isella et al. 2018, see also Figure 7).

5.2. *Water line emission*

5.2.1. *Upper limit of the water line fluxes*

Figure 50 shows the observed flux densities around the line centers of the ortho-$H_2{}^{16}O$ line at 321 GHz, the para-$H_2{}^{18}O$ line at 322 GHz, and the HDO line at 335 GHz of the disk inside 20 au around HD163296, with a velocity resolution dv =1.9 km s^{-1}. The detailed parameters, such as transition quantum numbers ($J_{K_aK_c}$), wavelength λ, frequency, $A_{\rm ul}$, $E_{\rm up}$, 3σ[19] peak flux densities, and 3σ line total fluxes of lines are listed in Table 10. These lines have not been detected, and we obtained the

[19] the σ value is the root-mean-square value of peak flux density

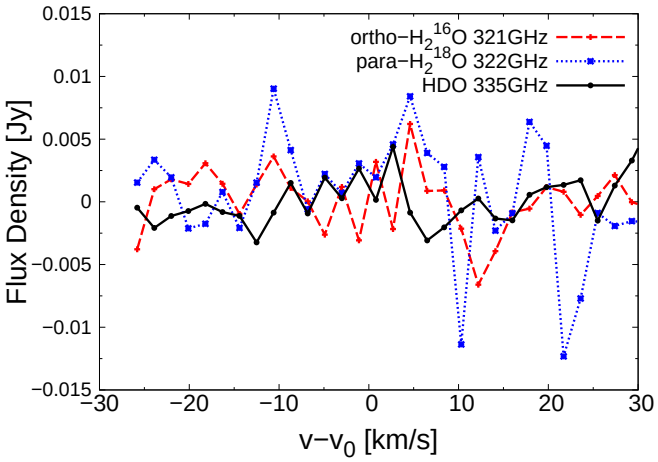

Figure 50. The observed flux densities around the line centers of the ortho-$H_2{}^{16}O$ line at 321 GHz (*red dashed line with cross symbols*), the para-$H_2{}^{18}O$ line (*blue dotted line with filled square and cross symbols*) at 322 GHz, and the HDO line at 335 GHz (*black solid line with circle symbols*) of the disk inside 20 au around HD 163296, with a velocity resolution dv =1.9 km s^{-1}. In obtaining the observed line flux densities, we adopted the circular aperture whose radius is 20 au.

upper limit values of peak flux densities and total fluxes. In calculating the upper limit values of total fluxes, we assume the velocity width of the double peaked profiles as 30 km s^{-1}, on the basis of the velocity width of model calculated line profiles (see Figures 51 and 52). Depending on the shapes of model line profiles, the actual velocity widths could be smaller than 30 km s^{-1}, especially in the cases with large snowline positions. Therefore, in these cases the upper limit values of line fluxes would be over-estimated.

Therefore in Figures 51 and 52, we compare the upper limit fluxes with the values from our model water line calculations with dust emission (Notsu et al. 2015, 2016, 2017, 2018), to constrain the dust opacity and the line emitting region, respectively, and to estimate the necessary observation time for a future clear detection. We calculate the model line profiles with different dust opacity values and different outer edges of the region with a high water vapor abundance. When we calculate these model line profiles, we include both dust and gas emission components, and we subtract the dust

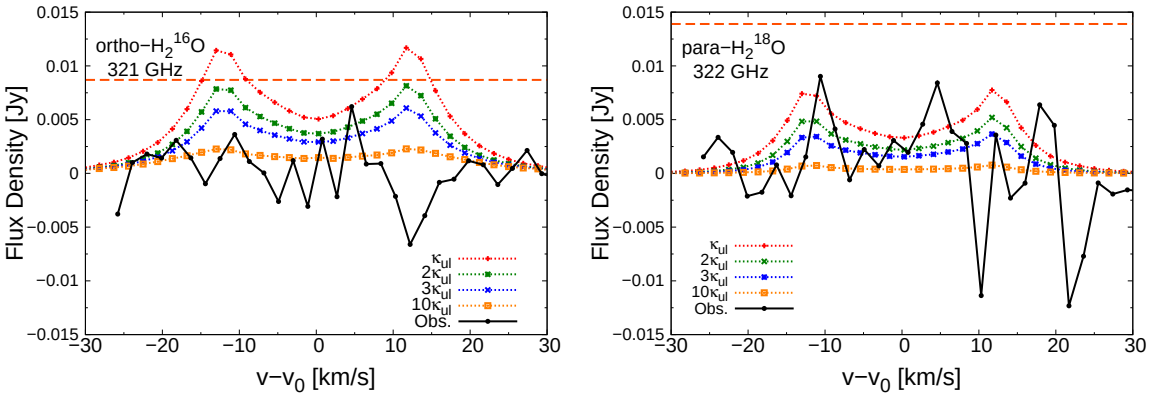

Figure 51. The profiles of the ortho-$H_2{}^{16}O$ line at 321 GHz (left panel) and the para-$H_2{}^{18}O$ line (right panel) at 322 GHz inside 20 au, with a velocity resolution dv =1.9 km s^{-1}. The *black solid line with circle symbols* is the observed flux density of the disk around HD 163296. Other lines are the results of our Herbig Ae disk model calculations (see also Notsu et al. 2017, 2018). The *red dotted lines with cross symbols* are the line profiles of our original Herbig Ae disk model. In the line profiles with *green dotted lines with cross symbols*, *blue dotted lines with filled square and cross symbols*, and *orange dotted lines with square symbols*, we set the values of dust opacity κ_{ul} 2, 3, and 10 times larger than our original value. The horizontal vermilion dashed lines show the values of observed 3σ peak flux densities around line centers (see also Table 10).

continuum emission component (the values of the calculated fluxes at $v - v_0 = \pm\infty$) to show the line emission component more clearly.

In our models, we first adopted the physical model of a steady, axisymmetric Keplerian accretion disk with a viscous parameter α=10^{-2}, a mass accretion rate $\dot{M}$=$10^{-8} M_\odot$ yr^{-1}, and gas-to-dust mass ratio $g/d = 100$ surrounding a Herbig Ae star with stellar mass M_*=$2.5 M_\odot$, stellar radius R_*=$2.0 R_\odot$, and effective temperature T_*=10,000K (Nomura & Millar 2005; Nomura et al. 2007; Walsh et al. 2015). Next we calculated the water gas and ice distributions in the disk using chemical kinetics. The large chemical network (Woodall et al. 2007; Walsh et al. 2010, 2012, 2015) we use to calculate the disk molecular abundances includes gas-phase reactions and gas-grain interactions (freeze-out, and thermal and nonthermal desorption). Using these data, we calculated the profiles of water emission

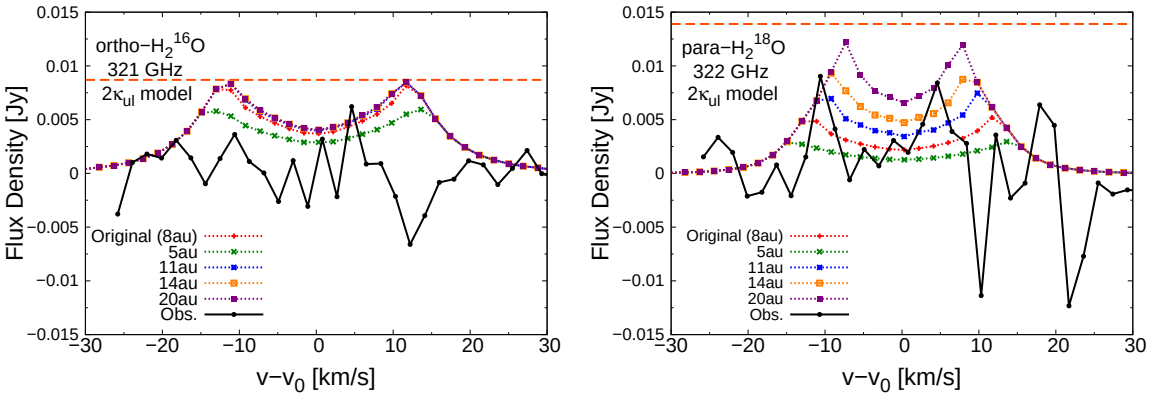

Figure 52. The profiles of the ortho-$H_2{}^{16}O$ line at 321 GHz (left panel) and the para-$H_2{}^{18}O$ line (right panel) at 322 GHz inside 20 au, with a velocity resolution dv =1.9 km s^{-1}. The *black solid line with circle symbols* is the observed flux density of the disk around HD 163296. Other lines are the line profiles which are obtained by our Herbig Ae disk model calculations (see also Notsu et al. 2017, 2018). The *red dotted lines with cross symbols* are the line profile with our original water vapor abundance distributions. In other line profiles, we artificially change the outer edge of the region with a high H_2O water vapor abundance ($\sim 10^{-5} - 10^{-4}$) region to 5 au (*green dotted lines with cross symbols*), 11 au (*blue dotted lines with filled square and cross symbols*), 14 au (*orange dotted lines with perforated square symbols*), and 20 au (*purple dotted lines with square symbols*). We set the values of dust opacity two times larger than our original value (see also Figure 51). The horizontal vermilion dashed lines show the values of observed 3σ peak flux densities around line centers (see also Table 10).

lines. For more details, see e.g., Notsu et al. (2015, 2016, 2017, 2018).

For the calculation of line profiles, we modified the 1D code RATRAN[20] (Hogerheijde & van der Tak 2000). The data for the line parameters are adopted from the Leiden Atomic and Molecular Database LAMDA[21] (Schöier et al. 2005) for the $H_2{}^{16}O$ lines and from the HITRAN Database[22] (e.g., Rothman et al. 2013) for the $H_2{}^{18}O$ lines. Here we note that HDO/H_2O ratio is considered to be sensitive to the temperature in the disk (van Dishoeck et al. 2014). However, deuterium chem-

[20] http://home.strw.leidenuniv.nl/~michiel/ratran/
[21] http://home.strw.leidenuniv.nl/~moldata/
[22] http://www.hitran.org

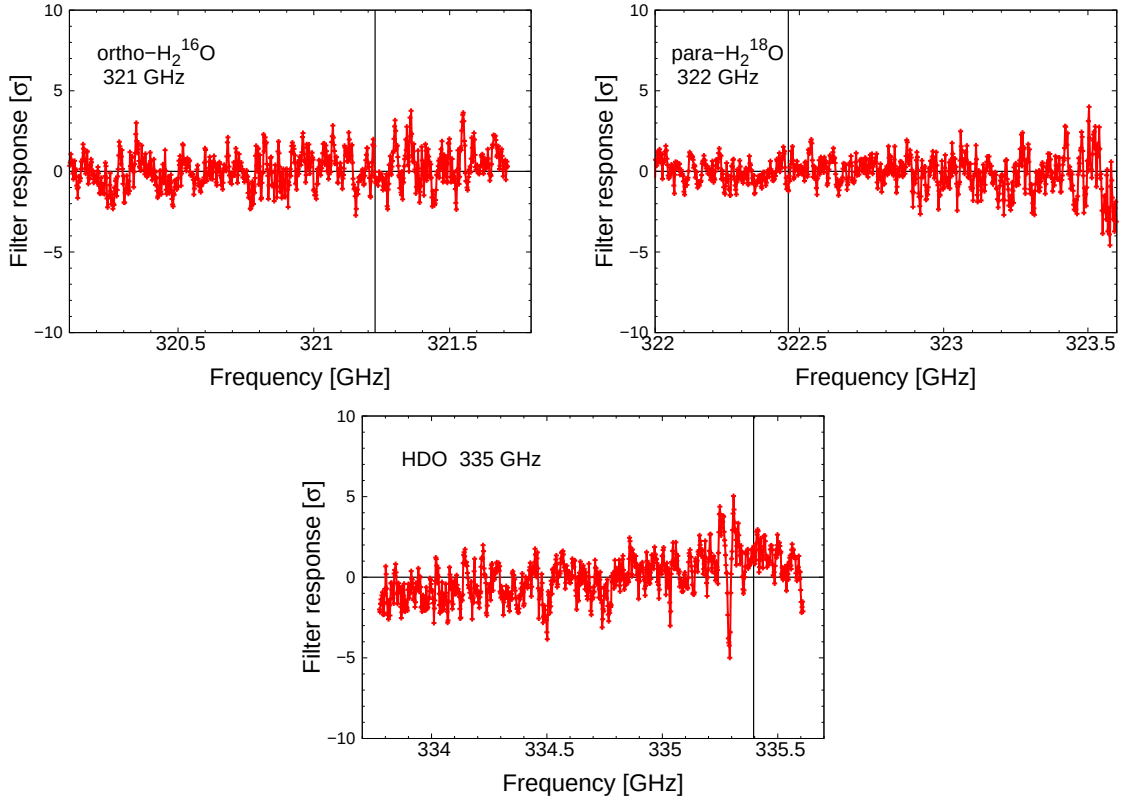

Figure 53. The matched filter response functions of the ortho-$H_2{}^{16}O$ line at 321 GHz (top left panel), the para-$H_2{}^{18}O$ line (top right panel) at 322 GHz, and HDO 335 GHz (bottom panel). The filter response is normalized by its standard deviation, σ (see also Loomis et al. 2018).

istry is not included in our chemical network, thus we only calculated the $H_2{}^{16}O$ and $H_2{}^{18}O$ line profiles. We set the ortho-to-para ratio (OPR) of water to its high-temperature value of 3 throughout the disk (Mumma et al. 1987; Hama & Watanabe 2013; Hama et al. 2016, 2018). We set the isotope ratio of oxygen $^{16}O/^{18}O$ to 560 throughout the disk, as Jørgensen & van Dishoeck (2010) and Persson et al. (2012) adopted. This $^{16}O/^{18}O$ value is determined by the observations of the local interstellar medium (Wilson & Rood 1994). We do not include emission from jet components and disk winds in calculating the line profiles.

First, we fix the location of the water vapor abundant region inside the H_2O snowline and change

the dust opacity. The original position of the outer edge of the water vapor abundant region is 8 au, and that of the water snowline is 14 au. In Figure 51, we plot the model profiles of the ortho-$H_2{}^{16}O$ 321 GHz line and the para-$H_2{}^{18}O$ 322 GHz line with four dust opacity values. The *red dotted lines with cross symbols* are the line profile of our original Herbig Ae model (Notsu et al. 2017, 2018). In this model, the value of mm dust opacity $\kappa_{\rm mm}$ is 1.0 cm^2 g^{-1}. In the line profiles with *green dotted lines with cross symbols*, *blue dotted lines with filled square and cross symbols*, and *orange dotted lines with perforated square symbols*, we set the values of dust opacity 2, 3, and 10 times larger than our original value in order to investigate the influence of dust opacity on line properties, respectively. The calculated line fluxes are listed in Table 11. We note that the dust opacity at sub-millimeter wavelengths can vary by a factor of around 10, depending on the properties of the dust grains (e.g., Miyake & Nakagawa 1993; Draine 2006). In our fiducial disk model, dust opacities appropriate for the dark cloud model are used and are relatively small at sub-millimeter wavelengths, compared to models with grain growth (see e.g., Nomura & Millar 2005; Aikawa & Nomura 2006, and paper I). In our model calculations, the emission of our observed Band 7 water lines is optically thick in the disk midplane within the H_2O snowline. In contrast, the sub-millimeter dust emission is marginally optically thick. The dust emission becomes stronger as the value of the dust opacity becomes larger, and the line emission becomes obscured by the dust emission. As a result, the apparent line intensities obtained by subtracting dust continuum emission become smaller (for more details, see (Notsu et al. 2017, 2018)).

According to Figure 51 and Tables 10 and 11, the observed 3σ upper limit peak flux density of para-$H_2{}^{18}O$ 322 GHz line is larger than model calculated value with original dust opacity, and that of ortho-$H_2{}^{16}O$ 321 GHz line is close to the calculated value for the model with two times larger dust opacity. Here we note that in the cases of our target water lines, most of the line emission comes from the region with a high water gas abundance ($\gtrsim 10^{-5}$) in the Herbig Ae disk (Notsu et al. 2017, 2018). Therefore, we consider that the mm dust opacity $\kappa_{\rm mm}$ is larger than 2.0 cm^2 g^{-1} to explain the water line upper limit, if the outer edge of the water vapor abundant region and also the position of the wa-

ter snowline is located at or beyond 8 au (see also Figure 52). Previous dust continuum observations of this object (e.g., Boneberg et al. 2016) show that $\kappa_{\rm mm}$∼3.0 cm^2 g^{-1}. In the cases with three times larger dust opacity, the model peak flux density corresponds to around 2σ for ortho-$H_2{}^{16}O$ 321 GHz line and around 1σ for para-$H_2{}^{16}O$ 322 GHz line. Therefore, the observation time executed (20% of our proposed time in our Cycle 3 proposal) was not enough to test our model. Here we note that the dust optical depth τ_d is ∼0.2 at r∼5 au for the model with the original dust opacity ($\kappa_{\rm mm}$ = 1.0 cm^2 g^{-1}). Meanwhile, previous ALMA and VLA observations with lower spatial resolution suggests τ_d∼0.55 at r<50 au (Guidi et al. 2016), which is a few times larger than our original value at r∼5 au.

In Figure 52, we fix the dust opacity and artificially change the outer edge of the region with a high H_2O vapor abundance (10^{-5}) from 8 au (Notsu et al. 2017, 2018), to 5 au (T_g ∼180K), 11 au (T_g ∼135K), 14 au (T_g ∼120K, the exact water snowline position), and 20 au (T_g ∼100K). We set the values of dust opacity two times larger than that of our original Herbig Ae model ($\kappa_{\rm mm}$ = 2.0 cm^2 g^{-1}, see also Table 11 and Figure 51). The calculated line fluxes are listed in Table 12. As the region with a high water gas abundance becomes larger, the flux density of the line peaks becomes larger, and the width between the two line peaks becomes narrower. As the region with a high water gas abundance becomes larger, the flux density of the line peaks becomes larger, and the line width, and the width between the two peaks becomes narrower. Since the $E_{\rm up}$ of para-$H_2{}^{18}O$ 322 GHz line is smaller than that of the ortho-$H_2{}^{16}O$ 321 GHz line, the former line profile is expected to be more sensitive to the position of the change of position of the water snowline. According to the right-hand panel of Figure 52, the position of the water snowline will be inside 20 au, if the mm dust opacity $\kappa_{\rm mm}$ is 2.0 cm^2 g^{-1} (see also Figure 51). If $\kappa_{\rm mm}$ is larger than 2.0 cm^2 g^{-1}, the position of H_2O snowline can be larger than 20 au.

As we explained in Section 2.1, the integration time on source is 0.723 hours, which is around 20% of the requested time in our Cycle 3 proposal. Future observations of sub-millimeter water lines

with longer observation time are required to confine the water line fluxes and the position of the H_2O snowline in the disk midplane in detail for the disk around HD163296. The values of peak flux densities from our model calculations suggest that in order to obtain significant detection (5σ) of ortho-$H_2{}^{16}O$ 321 GHz line, around 3 times greater integration time would be needed if $\kappa_{\rm mm}$ is 2.0 cm^2 g^{-1} and the outer edge of the region with a high H_2O vapor abundance (10^{-5}) is larger than 8 au, and around 5 times greater integration time (similar to the requested time in our Cycle 3 proposal) would be needed if $\kappa_{\rm mm}$ is 3.0 cm^2 g^{-1} and the outer edge of the region with a high H_2O vapor abundance (10^{-5}) is larger than 8 au. Moreover, to obtain 3σ and 5σ detections of para-$H_2{}^{18}O$ 322 GHz line, around 6 and 16 times greater integration time would be needed, respectively, if $\kappa_{\rm mm}$ is 2.0 cm^2 g^{-1} and the outer edge of the region with a high H_2O vapor abundance (10^{-5}) is larger than 8 au. In these time estimations, we assume the similar observational conditions, such as weather and numbers of antenna.

Here we note that Carr et al. (2018) reported tentative detection ($2-3\sigma$) of these two water lines with ALMA toward the disk around a T Tauri star, AS 205N, which has high mass accretion rate ($\dot{M}$=$3\times10^{-7}M_\odot$ yr^{-1}). The 3σ flux density at 321 GHz of their observation is around 3 mJy.

5.2.2. *Matched filtering analysis*

Loomis et al. (2018) recently proposed a new method to detect the weak line emissions from Keplerian rotating disks using observed visibility data. In this method, first we have to generate the *uv* plane Keplerian filter which approximates the expected emission pattern using parameters obtained by previous strong emission observations. We used the data of previous CO J= $2-1$ line observation (Isella et al. 2016) to make such Keplerian filter. Then we make cross-correlation of this filter with the visibilities data obtained by our observation (see also Carney et al. 2017, 2018, 2019; Booth et al. 2018a).

Figure 53 shows the matched filter response functions of the ortho-$H_2{}^{16}O$ 321 GHz line (top left

Table 10. Parameters and observed upper limits of our target water lines in ALMA Band 7

isotope	$J_{K_aK_c}$	λ[a]	Frequency	A_{ul}	E_{up}	3σ peak flux density[b]	3σ total flux[b,c]
		[μm]	[GHz]	[s^{-1}]	[K]	[mJy]	[W m^{-2}]
ortho-$H_2{}^{16}O$	10_{29}-9_{36}	933.2767	321.22568	6.17×10^{-6}	1861.2	< 8.7	$< 5.3\times10^{-21}$
para-$H_2{}^{18}O$	5_{15}-4_{22}	929.6894	322.46517	1.06×10^{-5}	467.9	< 13.9	$< 8.5\times10^{-21}$
HDO	3_{31}-4_{22}	893.8476	335.39550	2.61×10^{-5}	335.3	< 7.3	$< 6.3\times10^{-21}$

[a]In calculating the line wavelength values λ from the values of line frequencies, we adopt the speed of light value c=2.99792458 $\times$ 10^8 m s^{-1}.

[b]In calculating the upper limit values of peak flux densities and total fluxes, we integrate the line flux components within 20 au (circular aperture) from the central star. In addition, the σ value is the root-mean-square value of peak flux density.

[c]In calculating the upper limit values of total fluxes, we set the velocity width of the double peaked profiles as 30 km s^{-1}, according to the velocity width of model calculated line profiles (see Figures 51 and 52).

Table 11. Calculated peak flux densities and total fluxes of our target water lines in ALMA Band 7 with different values of dust opacity

isotope	Frequency	Peak flux density[a,b] [mJy]				Total flux[a,b] [W m^{-2}]			
	[GHz]								
		κ_{ori}	$2\kappa_{ori}$	$3\kappa_{ori}$	$10\kappa_{ori}$	κ_{ori}	$2\kappa_{ori}$	$3\kappa_{ori}$	$10\kappa_{ori}$
ortho-$H_2{}^{16}O$	321.22568	12.6	8.9	6.6	2.5	2.4×10^{-21}	2.4×10^{-21}	1.3×10^{-21}	6.4×10^{-22}
para-$H_2{}^{18}O$	322.46517	8.5	5.7	4.1	0.87	1.9×10^{-21}	1.8×10^{-21}	8.4×10^{-22}	1.9×10^{-22}

[a]When we calculate these model line fluxes, we include both dust and gas emission components, and we subtract dust emission components after calculations. We set the four values of dust opacity κ (original value, 2, 3, and 10 times larger values). in order to investigate the influence of dust opacity on line properties.

[b]In calculating these model line fluxes, we integrate the flux components within 20 au (circular aperture) from the central star.

Table 12. Calculated peak flux densities and total fluxes of our target water lines in ALMA Band 7 with different outer edge of high water vapor abundance region

isotope	Frequency	Peak flux density[a,b] [mJy]					Total Flux[a,b] [W m^{-2}]				
	[GHz]	5 au	8 au	11 au	14 au	20 au	5 au	8 au	11 au	14 au	20 au
ortho-$H_2{}^{16}O$	321.22568	5.9	8.9	9.1	9.2	9.2	2.0×10^{-21}	2.4×10^{-21}	2.6×10^{-21}	2.6×10^{-21}	2.6×10^{-21}
para-$H_2{}^{18}O$	322.46517	3.0	5.7	8.7	10.9	14.4	1.1×10^{-21}	1.8×10^{-21}	2.5×10^{-21}	3.0×10^{-21}	3.7×10^{-21}

[a] When we calculate these model line fluxes, we include both dust and gas emission components, and we subtract dust emission components after calculations. We set the values of dust opacity κ two times larger than that of our original Herbig Ae model (see also Figure 51 and Table 11). We set the five values of outer edge of high water vapor abundance region in the inner disk (5 au, original value 8 au, 11 au, 14 au, and 20 au).

[b] In calculating these model line fluxes, we integrate the flux components within 20 au (circular aperture) from the central star.

panel), the para-$H_2{}^{18}O$ 322 GHz line (top right panel), and HDO 335 GHz line (bottom panel). The filter response is normalized by its standard deviation, σ (see also Loomis et al. 2018). We confirm the non-detection of all three lines as also found in the image-plane analyses.

5.3. *Dust continuum image and radial profiles*

Figure 54 shows the dust continuum emission map of the disk around HD 163296 at ALMA Band 7. The positions of bright rings and dark gaps in our observed Band 7 data are consistent with those indicated by the previous Cycle 2 observation of the Band 6 dust continuum emission (Isella et al. 2016), and the resolution of the Band 7 image is $\sim$1.4 times smaller than that of Band 6 image reported in Isella et al. (2016), and $\sim$2.4 times smaller than that of our Band 6 image. In addition, Dent et al. (2019) recently reported the Band 7 dust continuum image of this object, and the positions of rings and gaps in dust continuum emissions are consistent in both data.

To confirm the multiple ring and gap structures in detail, we plot the azimuthally-averaged radial profiles of the dust continuum emission in Figure 55. There are three prominent gaps at around 50, 83 and 137 au, which had been already reported using recent observations (Isella et al. 2016, 2018;

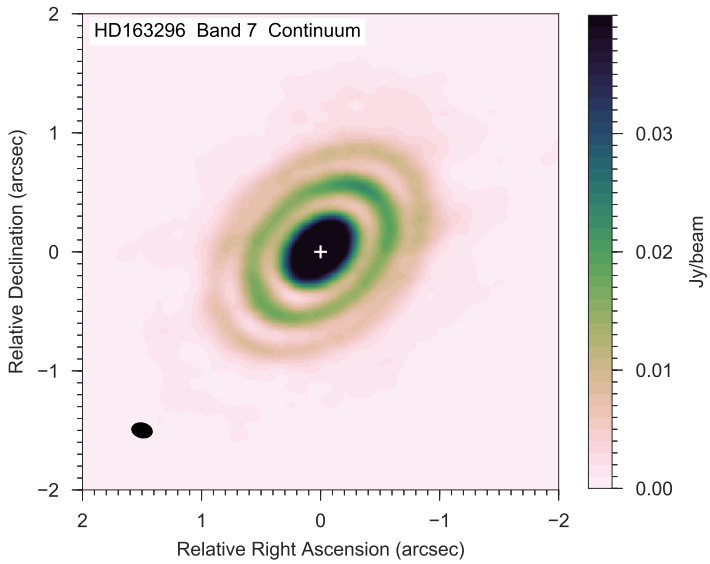

Figure 54. ALMA continuum image of the disk around HD163296 at 0.9 mm (Band 7). The black ellipse at the bottom left corner shows the synthesized beam (0.174×0.124 arcsec).

Andrews et al. 2018; Dent et al. 2019). The gap depths in Band 7 data appear deeper than those of the gaps at our Band 6 data, because of the difference of the spatial resolutions.

These multiple gaps and rings have been also found for several protoplanetary disks, such as HL Tau (e.g., ALMA Partnership et al. 2015; Akiyama et al. 2016; Carrasco-González et al. 2016; Pinte et al. 2016) and TW Hya (e.g., Akiyama et al. 2015; Rapson et al. 2015; Andrews et al. 2016; Nomura et al. 2016; Tsukagoshi et al. 2016; van Boekel et al. 2017; Huang et al. 2018a). Recently, according to the observations of the DSHARP (Disk Substructures at High Angular Resolution Project), the continuum substructures are ubiquitous in disks (see also Figure 7). The most common substructures are narrow emission rings and depleted gaps, although large-scale spiral patterns and small arc-shaped azimuthal asymmetries are also present in some cases (e.g., Andrews et al. 2018; Huang et al. 2018b,c; Isella et al. 2018). The origins of multiple gap and ring patterns are still debated. Sev-

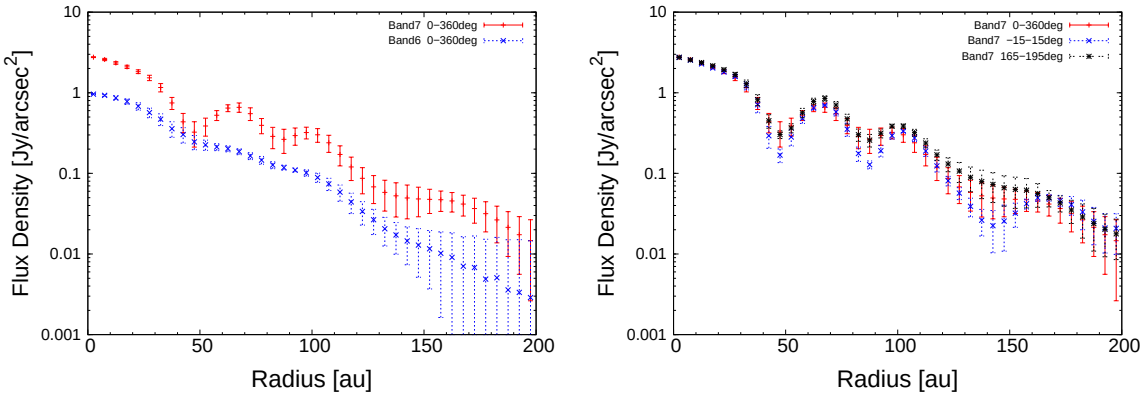

Figure 55. (Left panel): Radial profiles of the flux densities in Jy/arcsec^2 averaged over full azimuthal angle (0-360 deg) for Band 7 (*red cross points*) and Band 6 (*blue cross points*). (Right panel): Band 7 radial profiles of the flux densities in Jy/arcsec^2 averaged over 0-360 deg (*red cross points*), $-15 \sim 15$ deg (*blue cross points*), and $-165 \sim 195$ deg (*black asterisk points*). The error bar is determined from the standard deviation through the azimuthal averaging. We determine the 0 deg as the south-east direction of the major axis.

eral theoretical studies proposed that the planet-disk interaction causes material clearance around the orbits of the planets (e.g., Kanagawa et al. 2015a,b, 2016, 2018; Jin et al. 2016; Dong et al. 2018). There are another scenarios to explain these patterns without planets, such as efficient particle growth and fragmentation of dust grains around snowlines (e.g., Ros & Johansen 2013; Banzatti et al. 2015; Zhang et al. 2015; Okuzumi et al. 2016; Pinilla et al. 2017), particle trapping at the pressure bump structures in the disk surface density close to the outer edge of the dead-zone (e.g., Flock et al. 2015; Pinilla et al. 2016; Ruge et al. 2016), zonal flows from magneto-rotational instability (e.g., Béthune et al. 2016), secular gravitational instability (e.g., Takahashi & Inutsuka 2014, 2016; Tominaga et al. 2017), or baroclinic instability triggered by dust settling (Lorén-Aguilar & Bate 2015). Future observations of the dust continuum emission and gas emission (e.g., CO lines) at higher angular resolution with longer observation time are required to clarify the origins of these structures (e.g., van der Marel et al. 2018).

5.4. *Conclusion*

In this work (paper IV, Notsu et al. 2019), we used ALMA to obtain upper limit fluxes of sub-millimeter ortho-$H_2{}^{16}O$ 321 GHz, para-$H_2{}^{18}O$ 322 GHz, and HDO 335 GHz lines from the protoplanetary disk around the Herbig Ae star, HD 163296. The targeted lines are considered to be the prime candidate water lines at sub-millimeter wavelengths to locate the position of the H_2O snowline. These lines have not been detected, and we obtained the upper limit values of peak flux densities and total fluxes. We compared the upper limit fluxes with the values calculated by our model water line calculations with dust emission (Notsu et al. 2015, 2016, 2017, 2018). We constrained the line emitting region and the dust opacity from the observations. We find that the mm dust opacity $\kappa_{\rm mm}$ is larger than 2.0 $\rm cm^2\ g^{-1}$ to explain the water line properties, if the outer edge of the water vapor abundant region and also the position of the water snowline is beyond 8 au. In addition, the position of the water snowline will be inside 20 au, if the mm dust opacity $\kappa_{\rm mm}$ is 2.0 $\rm cm^2\ g^{-1}$. We also report multiple ring and gap patterns in 0.9 mm (Band 7) dust continuum emission with 15 au resolution. The positions of bright rings and dust depleted dark gaps are consistent with those indicated by the previous observations (Isella et al. 2016, 2018; Andrews et al. 2018; Dent et al. 2019). Future observations of the dust continuum emission at higher angular resolution and sub-millimeter water lines with longer observation time are required to clarify the detailed structures and the position of the H_2O snowline in disk midplane.

6. SUMMARY AND FUTURE WORKS

In this thesis, we proposed a means to identify the position of the H_2O snowline more directly by analyzing the Keplerian profiles of water lines which can be obtained by high dispersion spectroscopic observations across a wide range of wavelengths (from mid-infrared to sub-millimeter, e.g., ALMA, SPICA) and selected based on specific criteria. Most contents of this thesis is based on our refereed papers which have been published (Notsu et al. 2016, 2017, 2018), and was submitted recently (Notsu et al. 2019), and our unrefereed paper (Notsu et al. 2015).

6.1. *Modeling studies I, II. (Notsu et al. 2016, 2017)*

First we calculated the chemical structures of the protoplanetary disk using the self-consistently derived physical models of a typical T Tauri disk (Section 2, see also Notsu et al. 2016) and a typical Herbig Ae disk (Section 3, see also Notsu et al. 2017) to investigate the abundance distributions of H_2O gas and ice, and the positions of the H_2O snowline. We confirm that the abundance of H_2O gas is high not only in the hot disk midplane within the H_2O snowline but also in the hot surface layer and photodesorption region of the outer disk.

Next, on the basis of our calculations of disk chemical structures and water line profiles, we concluded that lines with small Einstein A coefficients (A_{ul}=$10^{-6} \sim 10^{-3}$ s^{-1}) and relatively high upper state energies ($E_{up}\sim$ 1000K) are dominated by emission from the the hot water vapor within the H_2O snowline, and can locate the position of the H_2O snowline. In these candidate water lines, the contribution of the optically thick hot midplane inside the H_2O snowline is large compared with that of the outer optically thin surface layer. This is because the intensities of lines from the optically thin region are proportional to the Einstein A coefficient. Moreover, the contribution of the cold water reservoir outside the H_2O snowline is also small, because lines with high excitation energies are not emitted from the regions at a low temperature.

We also investigated the properties of water lines which have been detected by previous spectroscopic

observations (e.g., ortho-$H_2{}^{16}O$ 63.32μm, 538.29μm). These lines are less suited to locate the H_2O snowline, because they are not dominated by emission from the region within the H_2O snowline. The properties of near-, and mid-infrared water emission lines which do not trace emission from the hot water vapor within the H_2O snowline are also discussed.

The position of the H_2O snowline of a Herbig Ae disk exists at a larger radius compared with that around less massive and cooler T Tauri stars. In addition, the position of H_2O snowline migrates closer to the star as the disk becomes older and mass accretion rate to the central star becomes smaller. Therefore, it is expected to be easier to observe the candidate water lines, and thus identify the location of the H_2O snowline, in Herbig Ae disks and younger T Tauri stars.

6.2. *Modeling studies III. (Notsu et al. 2018)*

We extended our previous work (papers I and II, Notsu et al. 2016, 2017) on using the profiles of ortho-$H_2{}^{16}O$ lines for tracing the location of the H_2O snowline in a Herbig Ae disk and a T Tauri disk, to include sub-millimeter para-$H_2{}^{16}O$ and ortho- and para-$H_2{}^{18}O$ lines.

The number densities of the para-$H_2{}^{16}O$ molecules are around one third smaller than that of ortho-$H_2{}^{16}O$, thus the para-$H_2{}^{16}O$ line can trace deeper into the disk than the ortho-$H_2{}^{16}O$ lines. In addition, since the number densities of the ortho- and para-$H_2{}^{18}O$ molecules are about 560 times smaller than their ^{16}O analogues, they trace deeper into the disk than the ortho-$H_2{}^{16}O$ lines (down to $z = 0$), and thus they are better candidates for detecting water emission within the H_2O snowline at the disk midplane. If the dust opacity of the disk is much larger than that adopted in our disk model, the $H_2{}^{16}O$ lines and lines with longer wavelengths are better candidates for sub-millimeter detection of the inner water reservoir. This is because the dust opacity becomes larger as the line frequency increases. Thus these $H_2{}^{18}O$ lines are potentially better probes of the position of the H_2O snowline at the disk midplane, depending on the dust optical depth. In addition, the temperature is higher as the disk height is higher and thus the temperature around $\tau_{ul} \sim 1$ of $H_2{}^{16}O$ lines is higher than those of $H_2{}^{18}O$ lines. Therefore, the line intensities are larger in the case of $H_2{}^{16}O$ lines,

compared with the case of $H_2{}^{18}O$ lines.

The values of the Einstein A coefficients of sub-millimeter candidate water lines tend to be smaller (typically $<10^{-4}$ s^{-1}) than infrared candidate water lines. Thus, in the case of sub-millimeter candidate water lines, the local intensity from the outer optically thin region in the disk is around 10^4 times smaller than that in infrared candidate water line cases. Therefore, in the case of sub-millimeter lines, especially for $H_2{}^{18}O$ and para-$H_2{}^{16}O$ lines with relatively smaller upper state energies ($\sim$ a few 100 K) can also be used to trace the location of the water snowline.

6.3. *ALMA observation (Notsu et al. 2019)*

There are several candidate water lines that trace the position of the H_2O snowline observable in ALMA Bands $5-10$ and by SPICA. We used ALMA to obtain upper limit fluxes of sub-millimeter ortho-$H_2{}^{16}O$ 321 GHz, para-$H_2{}^{18}O$ 322 GHz, and HDO 335 GHz lines from the protoplanetary disk around the Herbig Ae star, HD 163296. The targeted lines are considered to be the prime candidate water lines at sub-millimeter wavelengths to locate the position of the H_2O snowline. These lines have not been detected, and we obtained the upper limit values of peak flux densities and total fluxes. We compared the upper limit fluxes with the values calculated by our model water line calculations with dust emission (Notsu et al. 2015, 2016, 2017, 2018). We constrained the line emitting region and the dust opacity from the observations. We find that the mm dust opacity $\kappa_{\rm mm}$ is larger than 2.0 cm^2 g^{-1} to explain the water line properties, if the outer edge of the water vapor abundant region and also the position of the water snowline is beyond 8 au. In addition, the position of the water snowline will be inside 20 au, if the mm dust opacity $\kappa_{\rm mm}$ is 2.0 cm^2 g^{-1}. We also report multiple ring and gap patterns in 0.9 mm (Band 7) dust continuum emission with 15 au resolution. The positions of bright rings and dust depleted dark gaps are consistent with those indicated by the previous observations (Isella et al. 2016, 2018; Andrews et al. 2018; Dent et al. 2019).

6.4. *Future works*

The wavelengths of such candidate water lines which can locate the position of the H_2O snowline overlap with the capabilities of ALMA (Bands 5−10) and future mid-infrared high-dispersion spectrographs (e.g., SPICA/SMI-HRS). The successful detection in nearby Herbig Ae disks and younger T Tauri disks could be achieved with current ALMA capabilities using several lines.

Mid-infrared instruments such as HRS on SPICA/SMI (see also Roelfsema et al. 2018) would have a high sensitivity in the Q band (e.g., $\sim 16 - 18\mu$m), and we predict not only successful detections for some Herbig Ae disks, but also suggest the possibility of a survey of H_2O snowline locations in many Herbig Ae disks in nearby ($\lesssim$150pc) star-forming regions for the first time. Moreover, since HRS on SPICA/SMI has an especially high sensitivity, successful detections will be expected even for classical T Tauri disks in nearby ($\lesssim$150pc) star-forming regions, as well as Herbig Ae disks in the Orion star-forming region ($\sim$410 pc), with several hours of observations.

We also expect to detect emission from those candidate water lines (some of which are not accessible from the ground) using other high sensitivity mid-infrared and far-infrared instruments on future space telescopes, such as The Mid-Infrared Instrument on board the James Webb Space Telescope (JWST/MIRI), SPICA FAR-infrared Instrument (SPICA/SAFARI), and MRS of SPICA/SMI. Since the spectral resolution of these instruments is not so high ($\sim$ a few thousands), we cannot resolve the velocity profiles of these candidate lines at sufficient resolution to locate the position of the H_2O snowline. However, it will be possible to detect the total fluxes of these candidate lines with these high sensitivity instruments. Our results suggest that these lines mainly trace emission from the hot water vapor within the H_2O snowline. Moreover, since the sensitivity of these instruments is very high, meaning that the time necessary for a detection is not very long, we expect to detect emission from the hot H_2O gas inside the H_2O snowline for various protoplanetary disks, which are suitable candidates for high-dispersion spectroscopic observations with future instruments (e.g., ALMA, SPICA/SMI-HRS).

In our future work, we will discuss the possibility of future observations (e.g., ALMA, SPICA) in detail on the basis of our further modeling studies. In addition, we will conduct the further observations to locate the positions of the H_2O snowline for various types of protoplanetary disks using several water lines.

ACKNOWLEDGMENTS

First of all, I sincerely would like to thank Dr. Hideko Nomura for continuous encouragements, supports, and accurate advices. She is an associate professor of Tokyo Institute of Technology, and she has also been my substantial supervisor for my research since when I was a fourth year undergraduate student. Since she is an expert of not only star and planet formation, but also astrochemistry and physics of interstellar medium, I studied a lot of knowledge and important viewpoints from her. According to her, now I have great interests for star and planet formation processes and protoplanetary disks.

I am very grateful to my supervisor Dr. Takanori Sasaki for his daily supports and deeply discussions. Since he is also an expert of planetary sciences, he gave me a lot of ideas and viewpoints for my research and studies. Prof. Shin Mineshige, Dr. Keiichi Maeda, Dr. Shiu-Hang (Herman) Lee, and Dr. Norita Kawanaka are also the staffs of groups which I belong to (the group of theoretical sciences), and gave me a lot of useful and instructive advices.

The whole contents of the research reported in this thesis are on the basis of collaborative researches with Dr. Hideko Nomura, Mr. Daiki, Ishimoto, Dr. Catherine Walsh, Dr. Mitsuhiko Honda, Dr. Tomoya Hirota, Dr. Eiji Akiyama, Dr. Takashi Tsukagoshi, Ms. Alice Booth, Prof. T. J. Millar, and other collaborators (e.g., Notsu et al. 2015, 2016, 2017, 2018, 2019). I would like to thank them very much for discussing with me and giving me a lot of useful ideas and comments. I am grateful to Dr. Ryo Tazaki, Dr. Tomohiro Ono, and other members of past and present planetary science group in Department of Astronomy, Kyoto University, for giving me a lot of useful advices in seminars and daily discussion time.

I am grateful to Prof. Inga Kamp, Dr. Stefano Antonellini, Dr. Itsuki Sakon, Dr. Chris Packham, Dr. Hiroshi Shibai, and Dr. Takao Nakagawa and others for their useful advices about the possibility of infrared high-dispersion spectroscopic observations (e.g., SPICA and TMT/MICHI). I also thank

Prof. Ewine van Dishoeck, Dr. Satoshi Okuzumi, Dr. Akimasa Kataoka, Dr. Satoshi Ohashi, and others for giving me their useful comments about disk structures, calculations of emission lines, and ALMA observations. Our numerical studies were carried out on SR16000 at Yukawa Institute for Theoretical Physics (YITP) and computer systems at Kwasan and Hida Observatory (KIPS) in Kyoto University, and PC cluster at Center for Computational Astrophysics, National Astronomical Observatory of Japan. ALMA Data analysis was carried out on the Multi-wavelength Data Analysis System operated by the Astronomy Data Center (ADC), National Astronomical Observatory of Japan. This work is supported by Grants-in-Aid for JSPS (Japan Society for the Promotion of Science) fellows (Grant Number; 16J06887), and by the Astrobiology Center Program of National Institutes of Natural Sciences (NINS) (Grant Number; AB281013).

Our work makes use of the following ALMA data: ADS/JAO.ALMA #2015.1.01259.S and ADS/JAO.ALMA #2013.1.00601.S. ALMA is a partnership of European Southern Observatory (ESO) (representing its member states), National Science Foundation (USA), and National Institutes of Natural Sciences (Japan), together with National Research Council (Canada), National Science Council and Academia Sinica Institute of Astronomy and Astrophysics (Taiwan), and Korea Astronomy and Space Science Institute (Korea), in cooperation with the Republic of Chile. The Joint ALMA Observatory is operated by ESO, Associated Universities, Inc/National Radio Astronomy Observatory (NRAO), and National Astronomical Observatory of Japan.

Although the contents of this thesis is in the field of the star and planet formation, I have also studied the stellar flares, especially superflares on solar type stars, since 2010 when I was a first year undergraduate student. To join and conduct superflare studies, I have obtained the knowledge for solar and stellar physics, and photometric and spectroscopic observations. Their knowledge is also useful to understand the studies of star and planet formation (for example, the activity of young stars and spectroscopic observations of disks). In addition, there are around 14 papers which I was a first author or a coauthor published so far (e.g., Maehara et al. 2012; Notsu et al. 2013). Furthermore,

the experiences of superflare studies give me a reason and a lot of passions to step forward the way of an astrophysicist. I am very grateful to Prof. Kazunari Shibata, Dr. Daisaku Nogami, Dr. Satoshi Honda, Dr. Hiroyuki Maehara, Dr. Yosuke A. Yamashiki, Mr. Yuta Notsu, Mr. Kosuke Namekata, Mr. Kai Ikuta, Mr. Takuya Shibayama, and others, who are the members of superflare studies. I am grateful to all of the past and current members of Department of Astronomy and Astronomical Observatories, Graduate School of Science, Kyoto University, for their various supports to my research activities.

Finally, I thank my parents, brothers, and grand parents with my deepest gratitude for their sincere understandings and powerful supports. I could not have finished this thesis without their continuous encouragements and supports. I would also like to thank many teachers and friends helping me in my life so far. I am glad if this thesis will be their pleasures.

REFERENCES

Adams, F. C., & Shu, F. H. 1986, ApJ, 308, 836

Aikawa, Y., Furuya, K., Nomura, H., & Qi, C. 2015, ApJ, 807, 120

Aikawa, Y., Miyama, S. M., Nakano, T., & Umebayashi, T. 1996, ApJ, 467, 684

Aikawa, Y., & Nomura, H. 2006, ApJ, 642, 1152

Akimkin, V., Zhukovska, S., Wiebe, D., et al. 2013, ApJ, 766, 8

Akiyama, E., Hasegawa, Y., Hayashi, M., & Iguchi, S. 2016, ApJ, 818, 158

Akiyama, E., Momose, M., Hayashi, H., & Kitamura, Y. 2011, PASJ, 63, 1059

Akiyama, E., Muto, T., Kusakabe, N., et al. 2015, ApJL, 802, L17

ALMA Partnership, Brogan, C. L., Pérez, L. M., et al. 2015, ApJL, 808, L3

Anders, E., & Grevesse, N. 1989, GeoCoA, 53, 197

Andrews, S. M., Huang, J., Pérez, L. M., et al. 2019, ApJL, 869, L41

Andrews, S. M., Wilner, D. J., Zhu, Z., et al. 2016, ApJL, 820, L40

Antonellini, S., Bremer, J., Kamp, I., et al. 2017, A&A, 597, A72

Antonellini, S., Kamp, I., Lahuis, F., et al. 2016, A&A, 585, A61

Antonellini, S., Kamp, I., Riviere-Marichalar, P., et al. 2015, A&A, 582, A105

Armitage, P. J. 2011, ARA&A, 49, 195

Banzatti, A., Meyer, M. R., Bruderer, S., et al. 2012, ApJ, 745, 90

Banzatti, A., Pinilla, P., Ricci, L., et al. 2015, ApJL, 815, L1

Banzatti, A., Pontoppidan, K. M., Salyk, C., et al. 2017, ApJ, 834, 152

Barber, R. J., Tennyson, J., Harris, G. J., & Tolchenov, R. N. 2006, MNRAS, 368, 1087

Benisty, M., Juhasz, A., Boccaletti, A., et al. 2015, A&A, 578, L6

Benisty, M., Tatulli, E., Ménard, F., & Swain, M. R. 2010, A&A, 511, A75

Bethell, T. J., & Bergin, E. A. 2011, ApJ, 739, 78

Béthune, W., Lesur, G., & Ferreira, J. 2016, A&A, 589, A87

Blevins, S. M., Pontoppidan, K. M., Banzatti, A., et al. 2016, ApJ, 818, 22

Boneberg, D. M., Panić, O., Haworth, T. J., Clarke, C. J., & Min, M. 2016, MNRAS, 461, 385

Booth, A. S., Walsh, C., Kama, M., et al. 2018a, A&A, 611, A16

Brandl, B. R., Feldt, M., Glasse, A., et al. 2014, Proc. SPIE, 9147, 914721

Brown, W. A., & Bolina, A. S. 2007, MNRAS, 374, 1006

Carney, M. T., Hogerheijde, M. R., Guzmán, V. V., et al. 2019, arXiv:1901.02689

Carney, M. T., Fedele, D., Hogerheijde, M. R., et al. 2018, A&A, 614, A106

Carney, M. T., Hogerheijde, M. R., Loomis, R. A., et al. 2017, A&A, 605, A21

Carr, J. S., & Najita, J. R. 2008, Science, 319, 1504

Carr, J. S., & Najita, J. R. 2011, ApJ, 733, 102

Carr, J. S., Najita, J. R., & Salyk, C. 2018, Research Notes of the American Astronomical Society, 2, 169

Carrasco-González, C., Henning, T., Chandler, C. J., et al. 2016, ApJL, 821, L16

Caselli, P., & Ceccarelli, C. 2012, A&A Rv, 20, 56

Cieza, L. A., Casassus, S., Tobin, J., et al. 2016, Nature, 535, 258

Davis, S. S. 2005, ApJ, 620, 994

Dent, W. R. F., Greaves, J. S., & Coulson, I. M. 2005, MNRAS, 359, 663

Dent, W. R. F., Pinte, C., Cortes, P. C., et al. 2019, MNRAS, 482, L29

Dent, W. R. F., Thi, W. F., Kamp, I., et al. 2013, PASP, 125, 477

Dominik, C., Ceccarelli, C., Hollenbach, D., & Kaufman, M. 2005, ApJL, 635, L85

Dong, R., Li, S., Chiang, E., & Li, H. 2018, ApJ, 866, 110

Draine, B. T. 2006, ApJ, 636, 1114

Drozdovskaya, M. N., Walsh, C., Visser, R., Harsono, D., & van Dishoeck, E. F. 2014, MNRAS, 445, 913

Dominik, C., Dullemond, C. P., Waters, L. B. F. M., & Walch, S. 2003, A&A, 398, 607

Du, F., & Bergin, E. A. 2014, ApJ, 792, 2

Du, F., Bergin, E. A., & Hogerheijde, M. R. 2015, ApJL, 807, L32

Du, F., Bergin, E. A., Hogerheijde, M., et al. 2017, ApJ, 842, 98

Dullemond, C. P., & Dominik, C. 2004, A&A, 417, 159

Dutrey, A., Semenov, D., Chapillon, E., et al. 2014, Protostars and Planets VI, 317

Edridge, J. L. 2010, Ph.D. Thesis

Espaillat, C., Calvet, N., D'Alessio, P., et al. 2007, ApJL, 670, L135

Eistrup, C., Walsh, C., & van Dishoeck, E. F. 2016, A&A, 595, A83

Faure, A., & Josselin, E. 2008, A&A, 492, 257

Favre, C., Cleeves, L. I., Bergin, E. A., Qi, C., & Blake, G. A. 2013, ApJL, 776, L38

Fedele, D., Bruderer, S., van Dishoeck, E. F., et al. 2012, A&A, 544, LL9

Fedele, D., Bruderer, S., van Dishoeck, E. F., et al. 2013, A&A, 559, AA77

Fedele, D., Pascucci, I., Brittain, S., et al. 2011, ApJ, 732, 106

Flock, M., Ruge, J. P., Dzyurkevich, N., et al. 2015, A&A, 574, A68

Fujiwara, H., Honda, M., Kataza, H., et al. 2006, ApJL, 644, L133

Fukagawa, M., Tamura, M., Itoh, Y., et al. 2006, ApJL, 636, L153

Fukagawa, M., Tsukagoshi, T., Momose, M., et al. 2013, PASJ, 65, L14

Furuya, K., Aikawa, Y., Nomura, H., Hersant, F., & Wakelam, V. 2013, ApJ, 779, 11

Furuya, K., & Aikawa, Y. 2014, ApJ, 790, 97

Gaia Collaboration, Brown, A. G. A., Vallenari, A., et al. 2018, A&A, 616, A1

Garaud, P., & Lin, D. N. C. 2007, ApJ, 654, 606

Garrod, R. T., Weaver, S. L. W., & Herbst, E. 2008, ApJ, 682, 283

Graedel, T. E., Langer, W. D., & Frerking, M. A. 1982, ApJS, 48, 321

Glassgold, A. E., Meijerink, R., & Najita, J. R. 2009, ApJ, 701, 142

Goto, M., Usuda, T., Dullemond, C. P., et al. 2006, ApJ, 652, 758

Guidi, G., Ruane, G., Williams, J. P., et al. 2018, MNRAS, 479, 1505

Guidi, G., Tazzari, M., Testi, L., et al. 2016, A&A, 588, A112

Guilloteau, S., Dutrey, A., Wakelam, V., et al. 2012, A&A, 548, A70

Hamaguchi, K., Yamauchi, S., & Koyama, K. 2005, ApJ, 618, 360

Hama, T., Kouchi, A., & Watanabe, N. 2016, Science, 351, 65

Hama, T., Kouchi, A., & Watanabe, N. 2018, ApJL, 857, L13

Hama, T., & Watanabe, N. 2013, Chemical Reviews, 113, 8783

Harsono, D., Bruderer, S., & van Dishoeck, E. F. 2015, A&A, 582, A41

Hasegawa, T. I., Herbst, E., & Leung, C. M. 1992, ApJS, 82, 167

Hasegawa, T. I., & Herbst, E. 1993, MNRAS, 261, 83

Haworth, T. J., Ilee, J. D., Forgan, D. H., et al. 2016, PASA, 33, e053

Hayashi, C. 1981, Progress of Theoretical Physics Supplement, 70, 35

Hayashi, C., Nakazawa, K., & Nakagawa, Y. 1985, in Protostars and Planets II, ed. D. C. Black & M. S. Matthews (Tucson, AZ: Univ. Arizona Press), 1100

Heinzeller, D., Nomura, H., Walsh, C., & Millar, T. J. 2011, ApJ, 731, 115

Henning, T., & Semenov, D. 2013, Chemical Reviews, 113, 9016

Hirota, T., Kim, M. K., Kurono, Y., & Honma, M. 2014, ApJL, 782, L28

Hogerheijde, M. R., Bergin, E. A., Brinch, C., et al. 2011, Science, 334, 338

Hogerheijde, M. R., & van der Tak, F. F. S. 2000, A&A, 362, 697

Honda, M., Inoue, A. K., Fukagawa, M., et al. 2009, ApJL, 690, L110

Honda, M., Kudo, T., Takatsuki, S., et al. 2016, ApJ, 821, 2

Honda, M., Maaskant, K., Okamoto, Y. K., et al. 2012, ApJ, 752, 143

Honda, M., Maaskant, K., Okamoto, Y. K., et al. 2015, ApJ, 804, 143

Humphreys, E., Biggs, A., Immer, K., et al. 2017, The Messenger, 167, 7

Huang, J., Andrews, S. M., Cleeves, L. I., et al. 2018, ApJ, 852, 122

Huang, J., Andrews, S. M., Dullemond, C. P., et al. 2018, ApJL, 869, L42

Huang, J., Andrews, S. M., Pérez, L. M., et al. 2018, ApJL, 869, L43

Ida, S., & Guillot, T. 2016, A&A, 596, L3

Immer, K., Belitsky, V., Olberg, M., et al. 2016, The Messenger, 165, 13

Inoue, A. K., Honda, M., Nakamoto, T., & Oka, A. 2008, PASJ, 60, 557

Isella, A., Guidi, G., Testi, L., et al. 2016, Phys. Rev. Lett. 117, 251101

Isella, A., Huang, J., Andrews, S. M., et al. 2019, ApJL, 869, L49

Jacq, T., Henkel, C., Walmsley, C. M., Jewell, P. R., & Baudry, A. 1988, A&A, 199, L5

Ishimoto, D., Nomura, H., Heinzeller, D., et al. 2013, New Trends in Radio Astronomy in the ALMA Era: The 30th Anniversary of Nobeyama Radio Observatory, 476, 393

Jin, S., Li, S., Isella, A., Li, H., & Ji, J. 2016, ApJ, 818, 76

Jørgensen, J. K., & van Dishoeck, E. F. 2010, ApJL, 710, L72

Kamp, I., Thi, W.-F., Meeus, G., et al. 2013, A&A, 559, A24

Kanagawa, K. D., Muto, T., Tanaka, H., et al. 2015a, ApJL, 806, L15

Kanagawa, K. D., Muto, T., Tanaka, H., et al. 2016, PASJ, 68, 43

Kanagawa, K. D., Tanaka, H., Muto, T., Tanigawa, T., & Takeuchi, T. 2015b, MNRAS, 448, 994

Kanagawa, K. D., Tanaka, H., & Szuszkiewicz, E. 2018, ApJ, 861, 140

Kastner, J. H., Huenemoerder, D. P., Schulz, N. S., Canizares, C. R., & Weintraub, D. A. 2002, ApJ, 567, 434

Kenyon, S. J., & Hartmann, L. 1995, ApJS, 101, 117

Krijt, S., Ciesla, F. J., & Bergin, E. A. 2016, ApJ, 833, 285

Kristensen, L. E., Brown, J. M., Wilner, D., & Salyk, C. 2016, ApJL, 822, L20

Lahuis, F., van Dishoeck, E. F., Blake, G. A., et al. 2007, ApJ, 665, 492

Leger, A., Jura, M., & Omont, A. 1985, A&A, 144, 147

Li, A., & Draine, B. T. 2001, ApJ, 554, 778

Liedahl, D. A., Osterheld, A. L., & Goldstein, W. H. 1995, ApJL, 438, L115

Liu, S.-F., Jin, S., Li, S., Isella, A., & Li, H. 2018, ApJ, 857, 87

Loomis, R. A., Öberg, K. I., Andrews, S. M., et al. 2018, AJ, 155, 182

Lorén-Aguilar, P., & Bate, M. R. 2015, MNRAS, 453, L78

Maaskant, K. M., Honda, M., Waters, L. B. F. M., et al. 2013, A&A, 555, A64

Maehara, H., Shibayama, T., Notsu, S., et al. 2012, Nature, 485, 478

Mandell, A. M., Bast, J., van Dishoeck, E. F., et al. 2012, ApJ, 747, 92

Martin, R. G., & Livio, M. 2012, MNRAS, 425, L6

Martin, R. G., & Livio, M. 2013, MNRAS, 434, 633

Masuda, K., Takahashi, J., & Mukai, T. 1998, A&A, 330, 773

Mathews, G. S., Klaassen, P. D., Juhász, A., et al. 2013, A&A, 557, A132

Mathis, J. S., Rumpl, W., & Nordsieck, K. H. 1977, ApJ, 217, 425

Matsumura, S., Brasser, R., & Ida, S. 2016, ApJ, 818, 15

McClure, M. K., Espaillat, C., Calvet, N., et al. 2015, ApJ, 799, 162

McClure, M. K., Manoj, P., Calvet, N., et al. 2012, ApJL, 759, LL10

McElroy, D., Walsh, C., Markwick, A. J., et al. 2013, A&A, 550, A36

Meeus, G., Montesinos, B., Mendigutía, I., et al. 2012, A&A, 544, AA78

Meeus, G., Waters, L. B. F. M., Bouwman, J., et al. 2001, A&A, 365, 476

Meijerink, R., Aresu, G., Kamp, I., et al. 2012, A&A, 547, A68

Meijerink, R., Poelman, D. R., Spaans, M., Tielens, A. G. G. M., & Glassgold, A. E. 2008, ApJL, 689, L57

Meijerink, R., Pontoppidan, K. M., Blake, G. A., Poelman, D. R., & Dullemond, C. P. 2009, ApJ, 704, 1471

Men'shchikov, A. B., Henning, T., & Fischer, O. 1999, ApJ, 519, 257

Menu, J., van Boekel, R., Henning, T., et al. 2015, A&A, 581, A107

Min, M., Dullemond, C. P., Kama, M., & Dominik, C. 2011, Icarus, 212, 416

Min, M., Bouwman, J., Dominik, C., et al. 2016, A&A, 593, A11

Miyake, K., & Nakagawa, Y. 1993, Icarus, 106, 20

Monnier, J. D., Harries, T. J., Aarnio, A., et al. 2017, ApJ, 838, 20

Morbidelli, A., Bitsch, B., Crida, A., et al. 2016, Icarus, 267, 368

Morbidelli, A., Chambers, J., Lunine, J. I., et al. 2000, Meteoritics and Planetary Science, 35, 1309

Morbidelli, A., Lunine, J. I., O'Brien, D. P., Raymond, S. N., & Walsh, K. J. 2012, Annual Review of Earth and Planetary Sciences, 40, 251

Mulders, G. D., Ciesla, F. J., Min, M., & Pascucci, I. 2015, ApJ, 807, 9

Mumma, M. J., & Charnley, S. B. 2011, ARA&A, 49, 471

Mumma, M. J., Weaver, H. A., & Larson, H. P. 1987, A&A, 187, 419

Muto, T., Grady, C. A., Hashimoto, J., et al. 2012, ApJL, 748, LL22

Muto, T., Tsukagoshi, T., Momose, M., et al. 2015, PASJ, 67, 122

Najita, J., Bergin, E. A., & Ullom, J. N. 2001, ApJ, 561, 880

Najita, J. R., Carr, J. S., Pontoppidan, K. M., et al. 2013, ApJ, 766, 134

Neufeld, D. A., Wu, Y., Kraus, A., et al. 2013, ApJ, 769, 48

Nomura, H. 2002, ApJ, 567, 587

Nomura, H., & Millar, T. J. 2005, A&A, 438, 923

Nomura, H., Aikawa, Y., Tsujimoto, M., Nakagawa, Y., & Millar, T. J. 2007, ApJ, 661, 334

Nomura, H., Tsukagoshi, T., Kawabe, R., et al. 2016, ApJL, 819, L7

Notsu, S., Honda, S., Notsu, Y., et al. 2013, PASJ, 65, 112

Notsu, S., Nomura, H., Walsh, C., et al. 2019, ApJ, submitted (paper IV)

Notsu, S., Nomura, H., Walsh, C., et al. 2018, ApJ, 855, 62 (paper III)

Notsu, S., Nomura, H., Ishimoto, D., Walsh, C., Honda, M., Hirota, T., & Millar, T. J. 2017, ApJ, 836, 118 (paper II)

Notsu, S., Nomura, H., Ishimoto, D., Walsh, C., Honda, M., Hirota, T., & Millar, T. J. 2016, ApJ, 827, 113 (paper I)

Notsu, S., Nomura, H., Ishimoto, D., et al. 2015, in ASP ASP Conference Series 499, Revolution in Astronomy with ALMA: The Third Year, ed. D. Iono et al. (San Francisco, CA: ASP), 289

Öberg, K. I., Fuchs, G. W., Awad, Z., et al. 2007, ApJL, 662, L23

Öberg, K. I., Furuya, K., Loomis, R., et al. 2015, ApJ, 810, 112

Öberg, K. I., Garrod, R. T., van Dishoeck, E. F., & Linnartz, H. 2009, A&A, 504, 891

Öberg, K. I., Linnartz, H., Visser, R., & van Dishoeck, E. F. 2009, ApJ, 693, 1209

Öberg, K. I., Murray-Clay, R., & Bergin, E. A. 2011, ApJL, 743, L16

Öberg, K. I., van Broekhuizen, F., Fraser, H. J., et al. 2005, ApJL, 621, L33

Öberg, K. I., van Dishoeck, E. F., & Linnartz, H. 2009, A&A, 496, 281

Oka, A., Nakamoto, T., & Ida, S. 2011, ApJ, 738, 141

Okuzumi, S., Momose, M., Sirono, S.-i., Kobayashi, H., & Tanaka, H. 2016, ApJ, 821, 82

Okuzumi, S., Tanaka, H., Kobayashi, H., & Wada, K. 2012, ApJ, 752, 106

Packham, C., Honda, M., Richter, M., et al. 2012, Proc. SPIE, 8446, 84467G

Panić, O., Ratzka, T., Mulders, G. D., et al. 2014, A&A, 562, A101

Perryman, M. A. C., Lindegren, L., Kovalevsky, J., et al. 1997, A&A, 323, L49

Persson, M. V., Jørgensen, J. K., & van Dishoeck, E. F. 2012, A&A, 541, A39

Persson, M. V., Jørgensen, J. K., & van Dishoeck, E. F. 2013, A&A, 549, L3

Phillips, T. G., Scoville, N. Z., Kwan, J., Huggins, P. J., & Wannier, P. G. 1978, ApJL, 222, L59

Pinilla, P., Benisty, M., Birnstiel, T., et al. 2014, A&A, 564, A51

Pinilla, P., Flock, M., Ovelar, M. d. J., & Birnstiel, T. 2016, A&A, 596, A81

Pinilla, P., Pohl, A., Stammler, S. M., & Birnstiel, T. 2017, ApJ, 845, 68

Pinte, C., Dent, W. R. F., Ménard, F., et al. 2016, ApJ, 816, 25

Pinte, C., Price, D. J., Ménard, F., et al. 2018, ApJL, 860, L13

Piso, A.-M. A., Öberg, K. I., Birnstiel, T., & Murray-Clay, R. A. 2015, ApJ, 815, 109

Piso, A.-M. A., Pegues, J., & Öberg, K. I. 2016, ApJ, 833, 203

Podio, L., Kamp, I., Codella, C., et al. 2013, ApJL, 766, L5

Pontoppidan, K. M., Blake, G. A., & Smette, A. 2011, ApJ, 733, 84

Pontoppidan, K. M., Blake, G. A., van Dishoeck, E. F., et al. 2008, ApJ, 684, 1323

Pontoppidan, K. M., & Blevins, S. M. 2014, Faraday Discussions, 169, 49

Pontoppidan, K. M., Dullemond, C. P., van Dishoeck, E. F., et al. 2005, ApJ, 622, 463

Pontoppidan, K. M., Salyk, C., Bergin, E. A., et al. 2014, Protostars and Planets VI, 363

Pontoppidan, K. M., Salyk, C., Blake, G. A., et al. 2010a, ApJ, 720, 887

Pontoppidan, K. M., Salyk, C., Blake, G. A., K&aumlufl, H. U. 2010b, ApJL, 722, L173

Preibisch, T., Kim, Y.-C., Favata, F., et al. 2005, ApJS, 160, 401

Qi, C., D'Alessio, P., Öberg, K. I., et al. 2011, ApJ, 740, 84

Qi, C., Öberg, K. I., Andrews, S. M., et al. 2015, ApJ, 813, 128

Qi, C., Öberg, K. I., & Wilner, D. J. 2013, ApJ, 765, 34

Qi, C., Öberg, K. I., Wilner, D. J., et al. 2013, Science, 341, 630

Rapson, V. A., Kastner, J. H., Millar-Blanchaer, M. A., & Dong, R. 2015, ApJL, 815, L26

Rau, U., & Cornwell, T. J. 2011, A&A, 532, A71

Raymond, S. N., & Izidoro, A. 2017, Icarus, 297, 134

Reboussin, L., Wakelam, V., Guilloteau, S., Hersant, F., & Dutrey, A. 2015, A&A, 579, A82

Riviere-Marichalar, P., Ménard, F., Thi, W. F., et al. 2012, A&A, 538, LL3

Roelfsema, P. R., Shibai, H., Armus, L., et al. 2018, PASA, 35, e030

Ros, K., & Johansen, A. 2013, A&A, 552, A137

Rothman, L. S., Gordon, I. E., Babikov, Y., et al. 2013, JQSRT, 130, 4

Ruge, J. P., Flock, M., Wolf, S., et al. 2016, A&A, 590, A17

Rybicki, G. B., & Lightman, A. P. 1986, Radiative Processes in Astrophysics, by George B. Rybicki, Alan P. Lightman, pp. 400. ISBN 0-471-82759-2. Wiley-VCH, June 1986

Salinas, V. N., Hogerheijde, M. R., Bergin, E. A., et al. 2016, A&A, 591, A122

Salinas, V. N., Hogerheijde, M. R., Mathews, G. S., et al. 2017, A&A, 606, A125

Salinas, V. N., Hogerheijde, M. R., Murillo, N. M., et al. 2018, A&A, 616, A45

Salyk, C., Lacy, J. H., Richter, M. J., et al. 2015, ApJL, 810, L24

Salyk, C., Pontoppidan, K. M., Blake, G. A., et al. 2008, ApJL, 676, L49

Salyk, C., Pontoppidan, K. M., Blake, G. A., Najita, J. R., & Carr, J. S. 2011, ApJ, 731, 130

Sandford, S. A., & Allamandola, L. J. 1993, ApJ, 417, 815

Sato, T., Okuzumi, S., & Ida, S. 2016, A&A, 589, A15

Schöier, F. L., van der Tak, F. F. S., van Dishoeck, E. F., & Black, J. H. 2005, A&A, 432, 369

Schoonenberg, D., Okuzumi, S., & Ormel, C. W. 2017, A&A, 605, L28

Schwarz, K. R., Bergin, E. A., Cleeves, L. I., et al. 2016, ApJ, 823, 91

Schwarz, K. R., Bergin, E. A., Cleeves, L. I., et al. 2018, ApJ, 856, 85

Semenov, D., & Wiebe, D. 2011, ApJS, 196, 25

Shakura, N. I., & Sunyaev, R. A. 1973, A&A, 24, 337

Strom, K. M., Strom, S. E., Edwards, S., Cabrit, S., & Skrutskie, M. F. 1989, AJ, 97, 1451

Takahashi, S. Z., & Inutsuka, S.-i. 2014, ApJ, 794, 55

Takahashi, S. Z., & Inutsuka, S.-i. 2016, AJ, 152, 184

Teague, R., Bae, J., Bergin, E. A., Birnstiel, T., & Foreman-Mackey, D. 2018, ApJL, 860, L12

Tennyson J., Zobov. N. F., Williamson R., Polyansky O. L., Bernath P. F. 2001, J. Phys. Chem. Ref. Data, 30, 735

Terada, H., & Tokunaga, A. T. 2017, ApJ, 834, 115

Terada, H., Tokunaga, A. T., Kobayashi, N., et al. 2007, ApJ, 667, 303

Tilling, I., Woitke, P., Meeus, G., et al. 2012, A&A, 538, A20

Tominaga, R. T., Inutsuka, S.-i., & Takahashi, S. Z. 2018, PASJ, 70, 3

Tsukagoshi, T., Nomura, H., Muto, T., et al. 2016, ApJL, 829, L35

van Boekel, R., Henning, T., Menu, J., et al. 2017, ApJ, 837, 132

van den Ancker, M. E., The, P. S., Tjin A Djie, H. R. E., et al. 1997, A&A, 324, L33

van der Marel, N., Williams, J. P., & Bruderer, S. 2018, ApJL, 867, L14

van der Marel, N., van Dishoeck, E. F., Bruderer, S., et al. 2013, Science, 340, 1199

van der Marel, N., van Dishoeck, E. F., Bruderer, S., et al. 2016, A&A, 585, A58

van der Tak, F. F. S., Walmsley, C. M., Herpin, F., & Ceccarelli, C. 2006, A&A, 447, 1011

van Dishoeck, E. F., Bergin, E. A., Lis, D. C., & Lunine, J. I. 2014, in Protostars and Planets VI, ed. H. Beuther et al. (Tucson, AZ: Univ. Arizona Press), 835

van Dishoeck, E. F., Herbst, E., & Neufeld, D. A. 2013, Chemical Reviews, 113, 9043

van Dishoeck, E. F., Jonkheid, B., & van Hemert, M. C. 2006, Faraday Discussions, 133, 231

van Dishoeck, E. F., Kristensen, L. E., Benz, A. O., et al. 2011, PASP, 123, 138

van Kempen, T. A., Doty, S. D., van Dishoeck, E. F., Hogerheijde, M. R., & Jørgensen, J. K. 2008, A&A, 487, 975

van't Hoff, M. L. R., Tobin, J. J., Trapman, L., et al. 2018, ApJL, 864, L23

Vasyunin, A. I., Wiebe, D. S., Birnstiel, T., et al. 2011, ApJ, 727, 76

Veeraghattam, V. K., Manrodt, K., Lewis, S. P., & Stancil, P. C. 2014, ApJ, 790, 4

Wada, K., Tanaka, H., Okuzumi, S., et al. 2013, A&A, 559, AA62

Walsh, C., Harada, N., Herbst, E., & Millar, T. J. 2009, ApJ, 700, 752

Walsh, C., Juhász, A., Pinilla, P., et al. 2014b, ApJL, 791, L6

Walsh, C., Millar, T. J., & Nomura, H. 2010, ApJ, 722, 1607

Walsh, C., Millar, T. J., Nomura, H., et al. 2014a, A&A, 563, AA33

Walsh, C., Nomura, H., Millar, T. J., & Aikawa, Y. 2012, ApJ, 747, 114

Walsh, C., Nomura, H., & van Dishoeck, E. 2015, A&A, 582, A88

Walsh, K. J., Morbidelli, A., Raymond, S. N., O'Brien, D. P., & Mandell, A. M. 2011, Nature, 475, 206

Weingartner, J. C., & Draine, B. T. 2001, ApJ, 548, 296

Westley, M. S., Baragiola, R. A., Johnson, R. E., & Baratta, G. A. 1995, Nature, 373, 405

Willacy, K. 2007, ApJ, 660, 441

Willacy, K., & Langer, W. D. 2000, ApJ, 544, 903

Wilson, T. L., & Rood, R. 1994, ARA&A, 32, 191

Woitke, P., Kamp, I., & Thi, W.-F. 2009a, A&A, 501, 383

Woitke, P., Thi, W.-F., Kamp, I., & Hogerheijde, M. R. 2009b, A&A, 501, L5

Woodall, J., Agúndez, M., Markwick-Kemper, A. J., & Millar, T. J. 2007, A&A, 466, 1197

Yamamoto, T., Nakagawa, N., & Fukui, Y. 1983, A&A, 122, 171

Zhang, K., Bergin, E. A., Blake, G. A., et al. 2016, ApJL, 818, L16

Zhang, K., Bergin, E. A., Blake, G. A., Cleeves, L. I., & Schwarz, K. R. 2017, Nature Astronomy, 1, 0130

Zhang, K., Blake, G. A., & Bergin, E. A. 2015, ApJL, 806, L7

Zhang, K., Pontoppidan, K. M., Salyk, C., & Blake, G. A. 2013, ApJ, 766, 82

Zinnecker, H., & Preibisch, T. 1994, A&A, 292, 152